Alma Mater Studiorum - Università di Bologna

DOTTORATO DI RICERCA IN

MECCANICA E SCIENZE AVANZATE DELL'INGEGNERIA

Ciclo 34

DEVELOPMENT AND IMPLEMENTATION OF THE PLASMA FOCUS
TECHNOLOGY FOR RADIATION THERAPY APPLICATIONS

Presentata da: Lorenzo Isolan

Coordinatore Dottorato   **Supervisore**

Marco Carricato   Marco Sumini

Esame finale anno 2022

Abstract

A Plasma Focus (PF) device can confine in a small region a plasma generated during a discharge phenomenon (pinch phase). When the plasma is in the pinch condition it creates an environment that produces several kinds of radiations in dependence from the working parameters. When the filling gas is nitrogen, a self-collimated backwardly emitted electron beam, slightly spread by the coulomb repulsion, can be considered one of the most interesting outputs. That beam can be converted into X-ray pulses able to transfer energy at an Ultra-High (UH) Dose-Rate (DR), up to 1 Gy pulse^{-1} (pulse lasting 20-50 ns), for clinical applications, research, or industrial purposes. The measurements and the simulations of the radiation fields (e.g., the device characterization) are still an open problem and became critical for a clinical use of the particle beams. These issues have been studied with the Plasma Focus Device for Medical Applications #3 (PFMA-3) hosted at the University of Bologna, finding the radiation behavior at different operating conditions and working parameters for a proper tuning of this class of devices in clinical applications. The experimental outcomes have been compared with available analytical formalisms as benchmark and the scaling laws have been proposed. A set of Monte Carlo models have been built with direct and adjoint techniques for an accurate X-ray source characterization and for setting fast and reliable irradiation planning for patients. By coupling deterministic and Monte Carlo codes, a focusing lens for the charged particles has been designed for obtaining a beam suitable for applications as external radiotherapy or intra-operative radiation therapy. The radiobiological effectiveness of the UH PF DR, a FLASH source, has been evaluated by coupling different Monte Carlo codes: firstly, for generating a nucleotide-level map of the cluster

of DNA damages formed by secondary light charged particles; then, to estimate the overall level of DNA damage at the multi-cellular and tissue levels by considering the spatial variation effects as well as the radiation field characteristics. By applying the Repair-Misrepair-Fixation theory, the numerical results have been correlated to the experimental outcomes (Clonogenic assay for Surviving Fraction, SF, evaluation and DNA Double Strand Break). Finally, ambient dose measurements have been performed for tuning the numerical models and obtaining doses for radiation protection purposes. The PFMA-3 technology has been fully characterized toward clinical implementation and installation in a medical facility.

Sommario

Un dispositivo di tipo Plasma Focus è in grado di confinare in una piccola regione di spazio un plasma generato durante un fenomeno di scarica (pinch). Quando il plasma è in fase di pinch può dare luogo a produzione di differenti radiazioni in funzione dei parametri di lavoro. Se il gas di riempimento è azoto, il prodotto più interessante può essere considerato il fascio di elettroni retro-emesso rispetto alla direzione del moto del plasma ed auto-collimato (a parte la divergenza dovuta alle interazioni di repulsione di tipo coulombiano). Il fascio di particelle cariche leggere può essere convertito in impulsi di raggi X capaci di trasferire energia alla materia nel campo del cosiddetto rateo di dose ultraelevato (Ultra-High Dose-Rate) (fino ad 1 Gy impulso^{-1}, con impulsi della durata di 20-50 ns), con possibili applicazioni in ambito clinico, di ricerca o industriale. La misura e le simulazioni di questa tipologia di campi di radiazione sono, ad oggi, ancora problemi di tipo aperto e diventano critiche se si pensa ad un utilizzo clinico dei fasci di particelle generati. Queste problematiche sono state studiate sia dal punto di vista sperimentale sia numerico grazie al Plasma Focus Device for Medical Applications #3, installato presso l'Università di Bologna, ottenendo il comportamento dei campi di radiazione al variare delle condizioni operative (parametri di lavoro) comparando inoltre i risultati con i modelli analitici più noti. In questo modo è possibile definire il setup migliore per le differenti applicazioni mediche. Mediante un set di modelli Monte Carlo, è stata caratterizzata la sorgente di fotoni, sfruttando tecniche di simulazioni di trasporto dirette ed aggiunte, così da prevedere la possibilità di effettuare piani di trattamento rapidi e affidabili dal punto di vista fisico. Successivamente, è stata progettata una lente focalizzante accoppiando tra loro codici deterministici e codici

Monte Carlo, in modo tale da ottenere una macchia focale idonea per applicazioni medicali quali radioterapia esterna o intra-operatoria. L'efficacia radiobiologica del rateo di dose PF, una sorgente FLASH, è stata poi valutata accoppiando diversi codici Monte Carlo: in primo luogo, per generare una mappa a livello dei nucleotidi nei cluster di lesioni del DNA creati dalle particelle secondarie cariche; quindi, per stimare il livello complessivo di danno al DNA a livello multicellulare e tissutale considerando gli effetti di variazione spaziale e le caratteristiche del campo di radiazione. Applicando la teoria Repair-Misrepair-Fixation, i risultati numerici sono stati correlati ai risultati sperimentali (clonogenic assay per la valutazione della frazione sopravvivente, nonché valutazione della rottura di tipo doppio elicoidale al DNA). Sono infine state eseguite misure di dose ambientale per mettere a punto modelli numerici e valutare il rischio radioprotezionistico. Concludendo, la tecnologia è stata caratterizzata verso l'implementazione clinica e l'installazione in una struttura medica.

INDEX

Radiation Therapy

The Radiation Therapy (RT) continues to play a crucial role across the disease spectrum in almost every type of cancer, and oncology cares are becoming increasingly interdisciplinary [Chandra RA., et al., 2021]. Radiation oncology, on the other hand, is still one of the most misunderstood cancer related disciplines although the origins of radiotherapy may be traced back to the 1895 with the discovery of the X-Rays (XR) by Wilhelm Conrad Röntgen [Nusslin F., 2020]. The science of radiation oncology has seen many renaissances over the last decades [Hyun DH. and Seonghoon K., 2020]: many technological and informatics developments coupled with medical research have enabled radiation oncologists to customize treatments for accurate radiation dose delivery based on clinical criteria and anatomical information [Thwaites D., 2013; Malicki J., 2012; Johansson KA., et al., 2003; Isolan L., et al., 2019; Skouboe S., et al., 2019]. Different applications have simultaneously grown as imaging and therapy technologies have been improved until today, where collaboration across oncological domains is critical for upgrading treatments and ensuring the most effective use of radiations. Nowadays, this translation of basic research discoveries into clinical practice [Doroshow J. and Kummar S, 2014]), allow better therapy outcome while maintaining high health-related quality of life [Baumann M., 2016]. From the 2000s, oncological radiation therapy is one of the most adopted therapeutic strategies for the treatment of many types of cancer [Lee et al., 2012; Delaney G., et al., 2005] and it has been estimated that approximately 50% of all cancer patients, at some point during treatment, undergo radiotherapy in a curative or palliative regimen, alone or in combination with surgery or chemotherapy [Chandra RA., et al., 2021; Delaney G., et

al., 2005; Bhide SA. and Nutting CM., 2010]. However, not all patients benefit from radiotherapy treatment. Intrinsic or acquired radio resistance is the main obstacle to the long-term survival of cancer patients treated with radiotherapy [Ogawa K., et al., 2013]. The molecular mechanisms underlying the resistance to radiation damage are multiple and involve the activation of self-renewal pathways or DNA-repair pathways, the reduction of the reactive oxygen species or other possibilities depending on the microenvironment and autophagy processes. The mechanisms must be more deeply clarified but it is known that are associated to a high self-renewal capacity and DNA repair ability to stem cancer cells as well to the ability to reduce damages for instance by reducing the oxygen related to radical reactions and species (ROS) [Ogawa K., et al., 2013]. It has therefore been observed that these mechanisms and involved molecules, mostly kinases, aberrantly activated, give the cancer cell the ability to effectively repair DNA damage, inactivate the large amount of ROS, regulate cell cycle progression and therefore to survive [Begg A., et al., 2011]. In recent years, research aimed at solving the problem of radio resistance has mainly followed two plans: a) one related to sensitization of the tumor cell through selective inhibition of oncoproteins with molecularly targeted drugs, thus combining radiotherapy and targeted therapy [Selzer E. and Kornek G., 2013] (targeted treatment is a method of fight diseases by selectively targeting and manipulating the molecules considered to be responsible for the disease itself; in oncology, targeted drugs are often characterized as being directed against specific chemicals that are unique to tumor cells, as opposed to traditional chemotherapeutic treatments, which are generally unable to distinguish between normal and malignant cells [Hebar A., et al., 2013]); b) another focused on the generation of more intense or differently modulated radiation beams [Sterzing F., et al., 2005; Deasy JO., et al., 2001; Matsuya et al., 2019] and on Ultra-High (UH) Dose Rate

(DR) [Wilson R., 2004] with i.e. the so called FLASH sources [Favaudon V., et al., 2014 ; Buontempo F., et al., 2016; Buontempo F., et al., 2018; Hall EJ., 1972]. The dose rate, that is the amount of energy from ionizing radiation absorbed in the unit of mass and time, is one of the main factors determining the biological consequences of an absorbed dose [Rühm W., et al., 2016]. It is well known that the induced effects therefore depend not only on the dose, but also on the dose rate and on the quality of the radiation and the radiosensitivity of the tissue [Rühm W., et al., 2016; ICRP, 2007]:

1) Dose: there is a dose threshold value such that if it is not exceeded the effects are called sub-clinical;

2) Dose rate: at the same dose, the time with which it is received plays a fundamental role on the effects that will arise. Generally speaking, if the dose is distributed over a very long time the damage will be less because biological tolerance will increase, and the cells will have time to activate repair mechanisms;

3) Radiation quality: different radiations (e.g. $\alpha, e, \beta, \gamma, X, p, n$) have different weight in terms of hazard on living tissues, (e.g. α radiations release a large quantity of energy in an extremely short distance unlike γ rays do the opposite). For this reason, radiations can be divided into high-LET radiations, such as neutrons, protons and alpha particles, or low-LET radiations, like photons, i.e., X and gamma rays but also electrons. The biological effects caused by these two types of radiation are very different and this difference is expressed by the so-called quality factor.

4) Radiosensitivity: the radiosensitivity of the tissues plays a fundamental role in the appearance and type of induced deterministic effects, which are proportional to the reproductive activity of the tissue in question. Therefore, if the tissue has

excellent regeneration capacities, the effects will be less important. The reproductive activity of the cells is proportional to the inverse of the degree of differentiation of the cells themselves.

It is then well known that, at parity of target and type of radiation, the higher the DR (and therefore the shorter the exposure time), the more relevant could be the radiobiological effectiveness of the exposure, as the tumor cells do not have the time to activate those mechanisms of repair of the sub-lethal damage, notoriously underlying of the radio resistance [Mitchell JB. and Bedford JS., 1973; Bedford JS, Mitchell JB., 1977; Virelli A., et al., 2015]. On the contrary, since radiotherapy is one of the most frequently used and effective anti-tumors adopted strategy, it can also harm healthy tissues both acutely (deterministic effects) and late in life (stochastic effects [Choudhary S., 2018], e.g., inducing solid tumors and/or leukemia) as consequence of medical exposure [Ulanowski A., et al., 2019]. As a result of the toxicity to neighboring healthy tissue, the dose supplied to the tumor is restricted; this might imply that a tumor cannot be fully eliminated, and the efficacy of radiation treatment is therefore reduced. Thus, avoiding or minimizing radiation-induced healthy tissue harm has long been a focus of radiotherapy research: FLASH RT or Pulsed Low-Dose RT can be good candidates.

"FLASH" sources for radiation therapy

With the aim to minimize the secondary effects on healthy tissues and also possibly maximize the damages to cancer tissues [Buontempo F., et al., 2016; Buontempo F., et al., 2018], the Flash Radiation Therapy (FLASH-RT) is currently under investigation by the scientific community and can represent a very good candidate for reaching the mentioned goal: it consists in a revolutionary radiotherapy treatment that exploits UH DR (> 40 Gy s^{-1}) radiation beams for a single radiotherapy session [Binwei L., et al., 2021]. Flash sources could probably be able to spare healthy tissues with respect to conventional irradiations (e.g., 0.1 Gy s^{-1}), with potential benefits in cancer treatment due to different effects that have already to be fully explained i.e. on oxygen deprecation and ROS production [Vozenin MC., et al, 2019; Durante M., et al., 2018], while probably also compromising cancer cells more than conventional irradiations [Buontempo F., et al., 2016; Buontempo F., et al., 2018] (or, at least, with an iso-effect). The preliminary results available in literature suggest that in the conducted experiments, the reduction of the Normal Tissue Complication Probability (NTCP, [Trott KR., et al., 2012]) associated with FLASH irradiation is quite considerable with potential therapeutic benefit. Then, even if dose rate would not have effect on Tumor Control Probability (TCP, [Nuraini R. and Widita R., 2019]), FLASH radiation would continuously enlarge the therapeutic window TCP-NTCP, permitting dose escalation in hypofractionation [Marcu LG., et al., 2021]. Not unexpectedly, these considerations piqued the interest of the radiation medical physics community and sparked a debate concerning the importance of dose rate in radiotherapy. Of course, prudence is warranted since as of now no basic radiobiological clarification for these discoveries is available [Durante M., et al., 2018]. Despite the difficulties in understanding radiobiological mechanisms behind the FLASH effects, radiation flashing devices used as source for radiotherapy applications, while gaining a growing attention from the scientific community, could become the next generations of radiotherapy machines [Vozenin MC., et al, 2019; Durante M., et al., 2018; Kim YE., et al., 2020; Abolfath R., et al., 2020]. In particular, an intense scientific debate on the role of UH DR produced by FLASH irradiators (see the works of Durante M., et al., 2018 and Favaudon V., et al., 2014 and reference therein) in medical applications such as

classical external radiotherapy [Binwei L., et al., 2021, Vozenin MC., et al., 2019; Delaney G., et al., 2005; Bhide SA. and Nutting CM., 2010], brachytherapy [Yavas G., 2019; Mendez LC and Morton GC, 2019; Lazzaro G., 2005; Brenner DJ. and Hall EJ., 1991] or intra-operative radiation therapy (IORT) [Wilson D W., et al., 2020] is growing and is making its way in this field of application [Chow R., et al., 2021].

A Bit of history

Despite the topic is not new [Dewey DL. and Boag JW., 1959], research on UH DR and consequently on the jargon-called FLASH irradiators (FLASH-RT, as coined by Favaudon V., et al., 2014), is just at the beginning due to the controversial results which have been obtained in the past years. Dewey DL. and Boag JW., 1959 reported that biological materials, including bacteria, used to be more easily damaged when the cells have oxygen at the time of irradiation than when it is absent. Serratia Marcescens [Khanna A., et al., 2013], a human pathogen, exhibited this increased sensitivity to radiation (the so-called "oxygen effect") almost to the maximum when a suspension was saturated with a gas mixture containing 1% oxygen and 99% nitrogen, against 1.5 MeV photon beam emitted at normal DR (of about 10 Gy min^{-1}) generated from a LINAC. However, using the intense electron beam produced from the same linear accelerator, a dose rate of approximately 100 Gy in 2 µs could be delivered and Dewey DL. and Boag JW., 1959, claimed that in a nitrogen-oxygen mixture containing 1% oxygen, the pathogen resulted more sensitive at UH DR than when exposed to a normal DR in 100% nitrogen. However, when using an UH DR, the pathogen in the same nitrogen-oxygen mixture exhibited lower radiosensitivity, corresponding to anaerobic radiation. In summary, the Dewey DL. and Boag JW., 1959 work firstly showed different responses between the two explored DR (conventional and UH), concluding that higher dose rates protected the pathogens compared with low DR irradiation as consequence of the oxygen effect [Binwei L., et al., 2021]: if the radiation can be delivered at sufficiently high dose rates, the oxygen will be consumed. This produced the so-called 'hockey stick' shaped survival curves, with a steeper initial slope of the

aerobic response at doses lower than those at which all oxygen was consumed, and a lower slope of the hypoxic response above this point. These results paved the way to a research line which aimed to explore the protective effect on healthy tissues that FLASH-RT could potentially provide. It is also worth to cite that oxygen in molecules has long been recognized as a potent radiosensitizer able to boosts the cell-killing efficiency of ionizing radiation [Liu C., et al., 2015]. Usually, the half-maximum oxygen radiosensitization occurs at low concentrations (typically, the half-maximum value is at 3 mmHg). At oxygen concentrations below 15 mmHg, robust hypoxia-signals can be induced, producing a wide range of cellular responses that affect both therapy and malignant cells proliferation (as such hypoxia condition has been shown to suppress the expression of genes involved in the major repair pathways). The unanswered question is why hypoxic cells exhibit increased radioresistance despite a general down-regulation of various DNA repair genes (see Liu C., et al., 2015 for further information). Only not long ago, new works such as the one proposed by Boscolo D., et al., 2021, re-discussed the oxygen role in UH DR irradiation: the Authors proposed a "state of the art" radiation chemistry model which did not support the oxygen depletion and the radiation-induced transient hypoxia as the main mechanisms behind the FLASH effect. In that work it has also been stated that magnitude and dependence of the oxygen effects are not consistent with the actual observed biological effects, admitting however that oxygenation plays an undoubted role in mediating the FLASH effect (as stated from the 50s thanks to experimental observations and models).

The work of Town C., 1967 showed the effects on a biological system constituted by a sub-clone (a sub-population of cells that descended from a different clone but then

diverged by accumulating another mutation, as stated in Chowell D, 2018) of HeLa S-3 cells (mammalian cells), obtained from the Oxford's Radiobiology Laboratory, when irradiated by pulsed dose rate up to 3.5E+07 Gy sec^{-1} with single or double pulses of 1.3 μs but reaching the same total doses. The single-pulse data followed the two-pulse line closely up to 9 Gy, but the cells irradiated with a single pulse showed a reduced sensitivity for larger doses. The Authors stated that the biphasic nature of the single pulse survival curve could be produced by the removal of oxygen from the site during irradiations. As the dose of a pulse is increased, the concentration of oxygen decreases, but the cells remain sensitive until about 90% of the oxygen has been removed. On the other hands, the results were contentious as the "hockey-stick" shaped curves seemed to have the inflection at a too low dose for being produced by radiochemical utilization of oxygen.

Todd P., et al., 1968 irradiated human kidney cells with a 10 MV X-rays up to 10^{11} Gy min^{-1} delivering doses in single pulses of about 10^{-8} seconds and compared the results with irradiation from Cobalt-60 sources which generated 0.15 Gy min^{-1}. The results suggested that the experiment did not obtain desired anoxic conditions, since the ratio of doses in nitrogen compared to those in air needed to obtain equivalent survival was less than expected under complete anoxia. In other words, they tried to reproduce the FLASH effect but failed to observe hockey-stick shaped survival curves as well as reported by other Authors.

Berry RJ. and Stenford JBH., 1972 stated that their results on P.388 murine leukemia cells demonstrated that only the ones with low oxygen levels could be affected by nanosecond pulses of radiation. This raised the prospect that using short radiation pulses for radiotherapy could be more difficult than was thought earlier.

Also, in the work of Berry RJ., 1973, the same opinion was declared, contributing to destabilize the birth and the growth of this research/clinical sector: it was stated that such a survival curve was obtained only when the short pulses were applied to cells that were already partially hypoxic (oxygen concentration <1%). This was predicted from the radiochemical consumption of the remaining oxygen, just as in the case of bacteria. Therefore, exposures to single pulses at low and high dose rates produced very little differences in survival curves for the studied mammalian cell lines. They concluded that this field of application did not seem to offer any potential therapeutic advantage and appears to be destinate to remain a tool for radiation chemist, but "a mere laboratory curiosity for the radiobiologist and radiotherapist".

Weiss H., et al., 1973 presented their results in measuring the Surviving Fraction (SF) for Escherichia Coli bacteria irradiated by γ-rays at conventional dose-rate and with electrons at UH DR, produced with an average energy of 450 keV and 3 ns pulses. It was clearly observed that at UH DR and low oxygen concentrations the survival curve shown and unexpected behavior. The Authors explanation involved the presence of an oxygen active transport mechanism. Indeed, the quantity of oxygen dissolved in the biological material was established at higher levels respect what was expected by the usual Henry's Law. Nevertheless, they concluded that such considerations should be taken as unexplainable and required further investigation.

In the Field SB. and Beweli DK., 1974 work on anaesthetized rats' skin, reactions, and late deformities after irradiation of the paws with 7 MeV electrons were measured at dose rates from 2 Gy min^{-1} to 5000 Gy min^{-1}. At dose rates up to 700 Gy min^{-1}, there was no change in radiation effectiveness. Increasing the dose rate to 5000 Gy min^{-1} significantly reduced the effectiveness. This means that oxygen was depleted at high

dose rates and at 500 Gy min^{-1} provided under aerobic conditions, a withdrawal point occurred at about 20 Gy, above which the skin reaction was similar to the anoxic one.

A new push on this topic was provided in late 2010, by Favaudon V., et al., 2014 which irradiated in vitro lung fibrogenesis in C57BL/6J mice with sub-millisecond pulses ($\geq$ 40 Gy s^{-1}) and compared the results with irradiation on the same biological system but with a conventional dose rate (≤ 0.03 Gy s^{-1}), in single doses. The Authors found that conventional treatments at doses of 15 Gy induced lung fibroses while FLASH treatments permitted to not have complications for more than 36 weeks of follow-up after the radiations. Moreover, FLASH-RT spared normal muscles and epithelial cells from the usual radiation-induced acute effects, protected blood vessels and bronchi from radiation-induced acute apoptosis, controlled the xenografted human tumors as well as conventional irradiations and controlled the syngeneic and orthopic lung tumors. As both conventional and FLASH treatments were able to reduce the tumor growth, the Authors concluded that the results suggested that FLASH-RT could possibly eradicate lung tumors while reducing manifestation and severity of radiation induced complications on normal tissues. The molecular mechanisms behind such results have been deeply investigated (see Favaudon V., et al., 2014 for further information) but no clear evidence has been reported. Usually, it is quite accepted that the induction of the transient hypoxia by trapping the oxygen as consequence of reducing radicals after large doses could result in a drop of the radiation susceptibility in low oxygen tissues. On the other hands, as in the case of lungs, this may be not applicable to high oxygenated tissues. A possible explanation has been provided, for the differential response between normal and tumor tissues, in relation to the damaged DNA which might be different in FLASH regimen respect to conventional dose rates.

Montay-Gruel P., et al., 2017 clearly explained that the FLASH radiation therapy, if compared to conventional radiation therapy, could enhance the differential response (e.g., a RT treatment exploits the clinical observation that healthy tissues are able to recover from the harmful effects of IR to a higher extent than tumors) between normal tumor tissues in lung models and allows dose escalation. The Authors performed experiments with two accelerator (6 MeV and 4.5 MeV) able to drive electrons up to 1000 Gy s^{-1} and irradiated a population of 95 female C57BL/6J mice. What was evaluated was the dose rate effect on neuroprotection two months post-irradiation where 10 Gy were delivered. As a results, the damage to normal brain tissue in mice was reduced by passing from conventional to FLASH dose rates by maintaining the anti-tumor effect.

Following what has been reported by Buontempo F., et al., 2018, on very radioresistant melanoma cell lines (A375 and SK-MEL28) irradiated with X-ray pulses generated by a pulsed plasma device (Plasma Focus device for Medical Applications #3, hosted at the University of Bologna, Italy) and comparing the results with a conventional source characterized by the same photon spectrum and total treatment time, the UH DR showed more capacity in killing cancer cells (or, at least, strongly impairing proliferation).

Other studies achieved similar results of Montay-Gruel P., et al., 2017 by testing the FLASH-RT also on more complex in-vivo models such as cats and mini-pigs [Vozenin MC., et al., 2019].

Bourhis J., et al., 2019a studied how to approach in practice the so-called clinical translation of FLASH-RT, which uses the ultra-fast transfer of radiations at DR several thousand times higher than what used in routinary clinical practice. The Authors

pointed out that the definition of FLASH-RT is more complex than conventional RT because involves many physical parameters as repetition-rate, pulse characteristics, total duration of exposure and others. The clinical translation of FLASH-RT can be supported by results related on the normal tissue protection among different species, the level of this advantage, the outstanding anti-tumor effects and more: these astonishing previously presented results suggested that the FLASH-RT could probably be reproduced in human patients and inspired the examination of this theory in clinical trials. A background encouraging the clinical translation of FLASH-RT is given by the pre-clinical data firstly obtained from micro-organisms such as bacteria passing from cell lines to different animal species (mice tested on skin, lung, gut and brain, mini-pigs, cats, and others). The previous studied case showed, most of the time, that FLASH-RT remarkably reduces healthy tissue unwanted effects while offering an effective anti-tumor effect. Another consideration that supported the clinical implementation of FLASH-RT is represented by the order of magnitude of the healthy tissue protection. The results on mini-pigs provided the most important results when scaling the dose rate on their skin with single irradiations from 22 to 34 Gy applicated on beam field size of 2.6 cm. What has been observed was that the same necrosis level after 9 month as endpoint was reached with 24 Gy by conventional DR and 34 Gy with FLASH irradiations suggesting a dose modifying factor of nearly 1.3. 28 months after from irradiation, the skin appeared normal. Extra benefits could rise the interest of UH DR in clinical practice: short time of exposure could strongly help to make irrelevant the intra-fraction motion of the patient. Moreover, since FLASH treatments works well at high doses per session, the number of irradiation sessions could be decreased. Then, radiation-oncology divisions could benefit from logistical assets, since the treatments would be shorter and less [Bourhis J., et al., 2019a].

The very first human patient was treated in 2019 [Bourhis J., et al., 2019b], where 15 Gy in 90 ms were successfully provided using a prototype LINAC on a 75-year-old man affected by a cutaneous lymphoma.

New type of results, sometimes countercurrent, are also emerging from literature. In the Venkatesulu BP., et al., 2019 work, where the immune system in models of radiation induced lymphopenia were evaluated, the results can be summarized as follows:

1) UH DR seems to causes higher apoptosis and clonogenic cell death with respect to standard DR;

2) UH DR and standard DR are equally powerful in killing lymphocytes ex vivo;

3) UH DR does not seems to spare the immune cells irradiated by cardiac irradiation experiments;

4) UH DR does not seems to spare immune cells irradiated by splenic irradiation experiments;

5) UH DR (> 40 Gy s^{-1}) causes more gastrointestinal mucosal toxicity than conventional DR (usually in the order of 0.1 Gy s^{-1}).

Lately, also Griffin RJ., et al., 2020 (see also reference therein), reported that in some cases, the FLASH-RT resulted to be superior in terms of tumor killing when compared to conventional radiation therapy, as already stated in the Buontempo F., et al., 2018 and other works.

Nowadays, even other particles than photons and electrons are under investigation for exploring the FLASH effect such as protons or carbon ions, that it is well known have other potential benefits in dose conformation, radiobiological efficacy and "intrinsic"

healthy tissue sparing as consequence of the Bragg-peak [Zakaria AM., et al., 2020; Kim MM., et al., 2021], improving the therapeutic power with tumor greater toxicity.

Possible mechanisms of action induced by FLASH-RT

The biological mechanisms behind the FLASH radiation therapy (as coined by Favaudon V., et al., 2014) are very complex but mainly rely on a local oxygen depletion that is much faster than tissue re-oxygenation, which could result in short-lived radiation induced hypoxia (as it has been seen in bacteria and, in general, in vitro). It must be also stated that the mechanism that produces the differential responses between healthy tissues and tumor tissues, in vivo, remains vague and the elucidatory hypotheses need other experimental verification, as it not clear when the FLASH effects arise [Binwei L., et al., 2021]. What has also been seen is that hyper oxygenation conditions can possibly eliminate the FLASH effect, at least in mouse models [Bourhis J., et al., 2019a]. For describing the biological system evolution after an irradiation, the cell's Surviving Fraction (SF) model described by the Linear Quadratic (LQ) formalism can be considered the state of the art [Brenner DJ. and Hall EJ., 1991]. This is based on a representation of the DNA damaged species (two species, for a DSB) that could be created by the same track of an interacting radiation or by two different tracks (namely α and β parameters, see Brenner DJ. and Hall EJ., 1991 for details). Since FLASH-RT could change DNA repair and intrinsic radiosensitivity, when a normal tissue is irradiated, its radiobiological parameters might change differently on what expected with conventional irradiations. An accurate description of the biological mechanisms behind such FLASH-RT behavior is therefore provided by the recent work of Friedl A., et al., 2021.

The Pulsed Low Dose Radiotherapy

An important novelty in this sector (e.g., the FLASH sources applications) could be provided by Pulsed Low Dose Radiotherapy (PLDR) (see the Chen L., 2021 work and references therein), that although the name would seem to suggest otherwise, is a very recent technique that could potentially exploit the capabilities of FLASH sources, both from the point of view of radiation generators and from dosimetry and laboratory analysis techniques. The idea behind PLDR is to take advantage from the radiosensitivity of a tumor cell below its transition dose (TS, Transition Switching, e.g., the lack of DNA repair below a given dose, which is cell type dependent and is usually observed in the fraction of sub-Gy range (0.2-0.6 Gy) usually greater for tumor than the dose of normal/healthy tissues), and the increased normal tissue repair at low dose rates. Contrary on the FLASH techniques, where the dose is given by a single pulse or at least in a very small amount of time, the way to apply the PLDR consists in dividing the radiation dose in multiple pulses (or fractions), each of which has a whole dose less than the tumor transition dose but greater than the normal tissue transition dose, to trigger radiation repair in normal tissues rather than tumor cells. Such results can be achieved by irradiating biological material with short pulses, with every pulse providing a dose lower than the tumor transition dose and delivering the irradiations at certain time interval in such a way to obtain a low/conventional "real/averaged" dose rate (averaged between short pulses due to a cooling down period). This strategy induces the so-called Low Dose Hyper-Radiosensitivity (LDHR): this phenomenon has been observed in cancer cell lines, healthy cells, and metastatic tumors but not in innately radiosensitive cells (on the contrary, it is worth to mentions that LDHR was found to be higher in radiation resistant cells) [Chen L., 2021].

New insight and recent evidence in PLDR inducing LDHR with ultra-fast sources

An extensive review of the techniques is proposed by Rogacki K., et al., 2018, since recurrent cancer after initial standard treatment is devastating to patients, families and physicians/medical staff. In particular, post-recurrence treatment options are often not well defined and may contain minimal data to support one approach more than another. In addition, the use of reirradiation to treat recurrent cancer is often avoided due to concerns that it may exceed normal tissue tolerance in previous treated areas. Finally, re-irradiation is often employed in palliative situations, using doses lower than the definitive dose that should be provided for killing cancer. Therefore, there is often a lack of data on tumor control after re-irradiation. Pulse-reduced dose rate is a re-irradiation technique that potentially overcomes volume and dose limitations in the setting of recurrent tumors.

Jie L., et al., 2019 argued that re-irradiation after radiation therapy is a common treatment for some locally recurrent type of cancers. However, the side effects of repeated exposure could be serious in repeated irradiation, and they can manifest themselves as perforation of tissues and bleeding. Since studies have shown that low dose rate radiation therapy induces a hypersensitivity effect on tumor tissue and a hyper-reparation effect on normal tissue (which can simultaneously reduce damage to normal tissue and enhance a therapeutic effect on tumor), the PLDR can be considered as a good candidate for clinical application with also fast sources (fast pulses distant in time at doses suitable for stimulating the TS).

Jain. J., et al., 2021 clearly demonstrated the application of the PLDR by inducing LDHR taking advantages by irradiating colorectal (DLD-1 and HCT-116) and breast (MCF-7) human cancer cell lines (monolayer setup, in vitro) with short X-ray pulses (90 ns) with each pulse providing doses of 0.025 Gy. The particle source was a 2 kJ dense Plasma Focus pulsed device. The cell death from LDHR in the DLD-1 line resulted to be 3 times higher respect from a conventional continuous X-ray source with two times higher doses. The LDHR effect has also been observed in HCT-116 and MCF-7 lines exposed respectively to 10 and 20 pulses, while no LDHR effect emerged with conventional continuous X-ray sources. These preliminary results suggested a selective effect of low dose pulsed ultra-fast X-Rays on cancer cells.

Possible mechanisms of action induced by PLDR

When referring to the LDHR effect from PLDR treatment, one possible biological explanation can be found in the lack of DNA repair below a given threshold dose, which is cell type dependent and is usually observed in the range of the fraction of Gy (0.2-0.6 Gy as order of magnitude) [Chen L., 2021]. In contrast to repairing sublethal DNA damage while preserving normal tissue during low dose rate irradiation, when the dose rate is reduced, an increase in the radiosensitivity of tumor cells is observed. This so-called inverse dose rate effect can be observed in cells displaying LDHR at dose rates below 1 Gy h^{-1}. In the case of single-strand or double-strand breaks, increased DNA repair occurs over a longer treatment period, which leads to a lower biologically effective dose. At doses above the transition dose, which is generally lower for normal tissue than for tumor cells, increased DNA repair will compromise tumor control and further reduce damage to normal tissue. In addition, slowly proliferating normal tissues may be relatively insensitive to low dose radiation because more sublethal damage is repaired before cell division than malignant cells during lengthy treatment. To take advantage of both low-dose high-radiosensitivity to tumors and increased normal tissue repair at low dose rates, PLDR is designed to provide a total daily dose with a small amount of subfractions (pulses) within a limited time frame achieving effective low dose rates.

As also stated in the Chen L., 2021 work, a dose of 2 Gy can be provided with ten subfractions (e.g., in pulses) within a 3-minute time in between, resulting in an effective dose rate of 0.067 Gy min^{-1}. According to the classic cell survival curve, hypersensitivity is observed in tumor cells that have been exposed to radiation at a low

dose rate with a steeper slope of the survival curve than the one due to radiation at higher dose. When the dose reached higher values, radiation sensitivity began to shift from sensitivity to radiation resistance, but sufficient interval time can promote repair of normal tissue and reduce side effects on normal tissue, thereby increasing the therapeutic effect on tumors and reducing side damages.

In vivo, PLDR causes less vascular damage and preserves the vascular network possibly also improving the oxygen supply to the tumor while normal tissue can be repaired during the treatment interval.

Clinical studies on recurrent breast cancer, head and neck tumors and gliomas after radiation therapy have further demonstrated the efficacy and safety of repeat PLDR radiation therapy (the Joiner MC., et al., 2001 work provide a solid literature basis of cases and example of treatments).

Novel fast radiation sources

Commercial FLASH sources are currently not easily available, but already existing irradiators can be modified for producing an UH DR: some examples can be represented by customized X-ray devices [Rezaee M., et al., 2021], LINACs [Lempart M., et al., 2019], Synchrotrons [Smyth LML., et al., 2018] or proton or ion accelerators [Rama N., et al., 2019]. In common, at least in principle, for being easily suitable as FLASH devices these apparatuses should be modified quickly, with no intersection with the clinical treatments and in a reversable way.

For instance, with the aim of a UH DR, in an electron linear accelerator the customization can include:

- the distance from the focal spot (that can be reduced for exploit the inverse square law of distance),
- the gun current modification
- the modulator charge rate modification
- the beam steering values modification,
- the control of the micro pulses,
- the removal of the scattering foils (can be moved or eliminated) [Lempart M., et al., 2019].

Taking a look at what the market currently offers, just a few products such as the one described in the Bourhis J., et al., 2019 work are starting to become a reality.

Also new technologies based on laser-plasma interaction (promising to be able to carry significant doses in the nanoseconds or even less time scales, towards femtoseconds or

even picoseconds pulses [Kraft SD., et al., 2010; Zlobinskaya O., et al., 2012; Labate L., et al., 2016; Sinigardi S., 2013]) are currently under investigation.

Another promising source can be represented by the Plasma Focus (PF) technology [Filippov NV., et al., 1962; Mather JW., 1971; Mather JW., 1965], which can provide UH DR [Sumini M., et al., 2019a; Jain. J., et al., 2021] and being even suitable for PLDR [Jain J., et al., 2021].

The Plasma Focus technology

A PF is a plasma device which is able to produce a so hot and so dense short-lived plasma that it could become a multiple source for different ionizing radiations, non-ionizing radiations and products [Sumini M., et al., 2006; Sumini M., et al., 2015; Sumini M., et al., 2017]. The plasma is confined at thermonuclear temperature and densities in a small volume, in the so-called pinch-phase, which rest in life for a short time (tens of nanoseconds) before that the onset of low-order Magneto-Hydro-Dynamic (MHD) instabilities starts the disruption of the confinement. Thanks to the pinch-phase and depending on the working gas filling the PF vacuum chamber, different particles or reactions can be generated such as neutron generation (Deuterium or Deuterium-Tritium as filling), radioisotopes of medical interest production (e.g. F18 with He3-O16 as filling) or charged particle production (e.g. Argon or Nitrogen as filling). When filling the plasma vacuum chamber with Nitrogen no nuclear reactions occur and aside an isotopic bremsstrahlung X-ray emission and positive ions peaked on the device's axis, an appealing phenomenon is the emission of self-guided and self-collimated backward electron bunch. In general, the PF flexibility lets its use in different applications as generation of neutrons [Niranjan R., et al., 2018], analysis through nuclear activation techniques [Gribkov VA., et al., 2017], fusion reaction production or plasma astrophysics applications [Pouzo JO. and Milanese MM., 2003], fusion systems wall damage [Chernyshova M., et al., 2019], charged and uncharged particles generation [Damideh V., et al., 2019; Rawat RS., et al., 2004], deposition or modification or processing of materials [Inestrosa-Izurieta MJ., et al., 2016; Hassan M., et al., 2006; Werner Z., et al., 2001], fabrication of nano-materials [Saw SH., et al.,

2014] and radiation biology [Jain et al., 2017]. The PF are effortlessly scalable in size and in particle production yield [Soto L., et al., 2010]. As presented, when the operating gas is Nitrogen or Argon, no reactions involving the nuclei take place and two beams of charged particles (if neglecting low-energy X-Rays from bremsstrahlung emitted from the focus point, the pinch) are emitted in opposed directions: electrons and ions [Sumini M., et al., 2019a, 2019b]. Thanks to particular physical [Pavez C., et al., 2014; Gribkov VA., et al., 2015] and radiobiological features [Virelli A., et al., 2011; Sumini M., et al., 2015; Buontempo F., et al., 2016; Jain J., et al., 2016; Jain J., et al., 2018; Bennett N., et al., 2018; Buontempo F., et al., 2018], recently the attentiveness on these devices moved on the quasi-relativistic electron's applications, implicating that a deep and further investigation is required. Such electron bunches could be of the order of magnitude of 0.1 mC pulse^{-1} for a class of capacitors in the kJ of stored bank energy. They are generated in few µm as the pinch diameter and are released in tens of ns, during the pinch-phase lifetime of confinement (consequently, generating currents ranging from 100 to 400 A, as can be registered by Rogowski coils). The electron beams can be converted in X-rays by interaction with a suitable target (e.g. a high Z material) in the 50-100 keV as centered in the energy range. Such fast-emission and high-intensity could make the PF generated X-ray pulses of strong interest in the frame of biological target irradiation such as cell cultures, tissues and cancer therapy. The proposed beams can be characterized by an UH DR (order of magnitude of 0.1-1 Gy pulse^{-1} or 10^7 Gy s^{-1} considering the effective pulse length). Thanks to these features, the PF device can be considered in the radiation therapy field, for example for surface or IORT applications [Sumini M., et al., 2019a, 2019b]. As stated in the Sumini M., et al., 2019a work, the research in this field has been experiencing a new push, gaining new momentum, thanks to the recently really fast improvement of the PF technology

respect to traditional X-ray or charged particle sources but also of the recent development of new technologies based on laser-plasma interaction (promising to be able to carry significant doses in the nanoseconds or even less time scales, towards femtoseconds or even picoseconds pulses [Kraft SD., et al., 2010; Zlobinskaya O., et al., 2012; Labate L., et al., 2016; Sinigardi S., 2013]). As it is known, the prospective of these technological achievements would be to carry out a radiation therapy treatment involving less doses to kill cancer cells sparing also healthy tissues and consequently contributing to protect patients from supplementary risks due to unwanted damages. Research on this theme is mainly based on radiobiological analyses (e.g., on cell's cultures) [Kraft SD., et al., 2010], while very few clinical results started to appear [Ciocca M., et al., 2003; Sinigardi S., 2013, Bourhis J., et al., 2019b], however not so many as expected. The restrictive aspect for the research's progression in this topic has been typically due to the high-technological efforts required for building radiation sources able to generate the UH DR.

The PF technology, which is quite simple and cost-effective, could play a pivotal role in this game (see the very recent and complete review about this class of devices as provided in the Auluck S., et al., 2021 work).

The Plasma Focus device for Medical Applications #3: an overview

At the Montecuccolino Laboratory of the Industrial Engineering Department of the University of Bologna, the applicability of the PF technology for irradiating superficial skin cancers or for intra-operatorial irradiation of a tumor bed (IORT) has been recently proved through a deep investigation of the pattern of the dose deposition and response to the cells against irradiation [Ceccolini E., 2012; Ceccolini E., et al., 2012; Sumini M., et al., 2015; Buontempo F., et al., 2016; Buontempo F., et al., 2018]. The Plasma Focus device for Medical Applications #3 (PFMA-3) hosted at the Montecuccolino Laboratory has been designed for delivering up to 1 Gy pulse^{-1} as X-rays to cells samples, after a conversion of an electron beam on a suitable target, with each pulse lasting about 50 ns (i.e., the time of the plasma confinement in the pinch phase) [Sumini M., et al., 2017] and a 3 cm as max focal spot (specifically designed for irradiating cell holders). The device's geometry can be seen in Figure 1 and Figure 2.
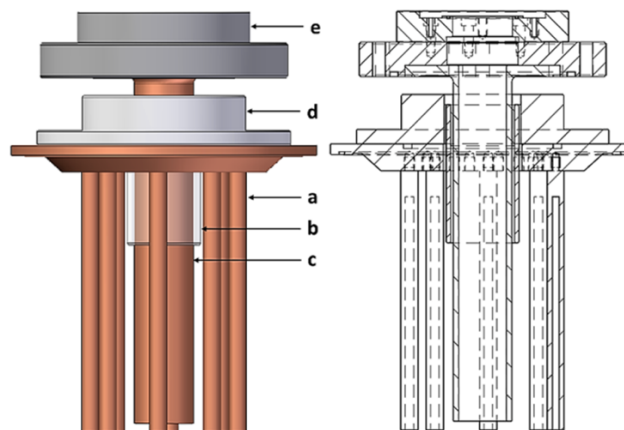
Figure 1. PFMA-3 central unit, rendering and axial section. External squirrel cage electrode (a), pyrex axial insulator (b), hollow inner electrode (anode) (c), delrin insulator (d). The upper flange (e) hosts the target, defining the limit of the electron extraction channel that starts at the hollow anode [Sumini M., et al., 2019a].
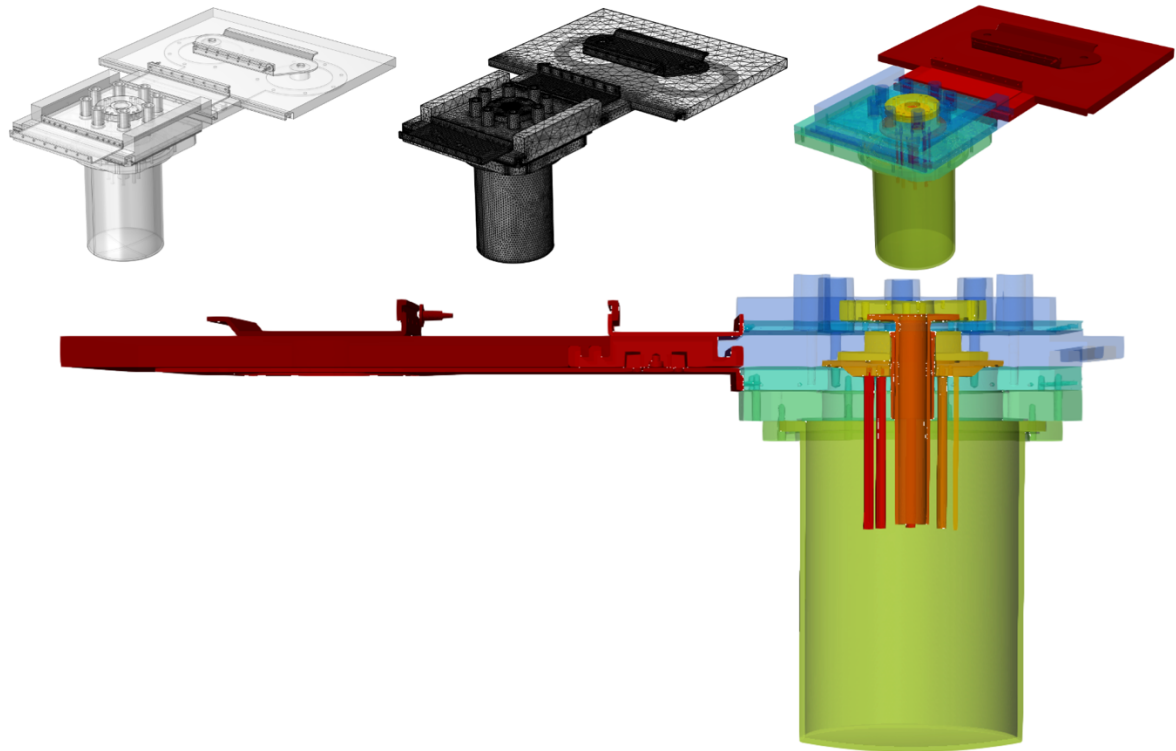
Figure 2. MCNP Unstructured Mesh model of the PFMA-3 device. Above-left, CAD model isometric view; Above-Centre, Unstructured Mesh model isometric view; Above-Right, rendering of Monte Carlo model isometric view. Below, Unstructured Mesh Monte Carlo model cut view.

The light charged particle beams generated at each pinch phase [Sumini M., et al., 2019a] and the option of their conversion in ultra-short X-ray pulses [Sumini M., et al., 2019b], have been tested from physical and radiobiological effectiveness point of view [Virelli A., et al., 2011; Buontempo F., et al., 2018].

The PFMA-3 is a Mather-type PF that is set up in a configuration that provides a minimum electron extraction channel length (along the axis of the hollow anode), for optimizing the self-collimation of the electron beam from the pinch volume to the target in such a way to minimize the repulsive effects.

The target has a diameter of 2 or 3 cm diameter (brass, lead, tungsten has been evaluated so far – the effective diameter depends on the use of a built lead collimator).

The actual working gas is nitrogen with a reference pressure of 0.40 mbar, a capacitor bank of 22 μF and an overall inductance of 150 nH. The latter is the main parameter that defines the "optimization" of the PF device. This relatively high value (optimized equipment should be characterized by 30-50 nH) indicates that the entire setup has great improvement's margin in the design of future medical application tools, because higher inductance will reduce the available energy of the plasma and related phenomena (see the new Yasar A., 2021 work for the optimization main parameters and laws). The discharge current is approximately 200 kA. The electrodes are made of copper, nearly 15 cm long, and has a squirrel cage on the outside. The first thing to be emphasized is that the entire PF discharge phenomenon is characterized by chaotic behavior.

In particular, during the last years different experiments with different tumor cell lines, comparing the damages produced by the PFMA-3 device and by a conventional X-Ray Tube (XRT) type BALTEAU CSC320/70 (COMECER S.p.A.- ACCREDIA LAT 065)) with a similar photon spectrum have been performed [Virelli A., et al., 2011; Sumini M., et al., 2015; Buontempo F., et al., 2016; Buontempo F., et al., 2018] (see Table 1). The PFMA-3 has been found to be generally strongly more effective than the XRT.

Starting from 2010, retracing the more recent history of the technical and radiobiological experiments conducted at the PFMA-3, the first experimental campaigns was conducted in early 2011 on human fibroblast and glioma cell lines (T98G) in collaboration with and AIRC supported project (AIRC, Italy's Association for Cancer Research, 'Analysis of characteristics of Plasma Focus beams: its future

oncological applications', Investigator Grant IG10559, 2010, P.I.: Roberto Orecchia, IEO) [Virelli A., et al., 2011; Ceccolini E., 2012; Ceccolini E., et al., 2012]. The cells were irradiated with the PF device and, in comparison, with a standard X-ray source characterized by a similar photon spectrum (ISO-H60). The results coming from irradiated cells were encouraging, suggesting a specific answer probably related to the UH DR. Due to the obtained achievements, the PF source has been considered of interest as candidate reference radiation source for the radiobiological effectiveness studies on UH DR with respect to their RBE and other parameters. The scientific debate on these topics is actually just at the very beginning, because just recently new sources are becoming technically practicable in this range of DR.

Moreover, in 2017 [Sumini M., et al., 2017], spurred on by wanting to achieve better results in terms of precision in controlling delivered radiation, a way to carefully check the dose to the samples has been also developed, analyzing the current signal registered by a Rogowsky coil [Samimi M., et al., 2015] connected to the device and correlating such signal to a dose read in passive dosimeters with a possible machine learning implementation for an online dose monitoring.

In 2018 [Buontempo F., et al., 2018], continuing a series of experiments started in 2016 [Buontempo F., et al., 2016] and craving at skin cancer clinical applications, a comprehensive analysis on the effects of the PMFA-3 on melanoma cell lines A375 and SK-Mel28 has been carried out. Such cultures have been chosen for their strong ability of recovering from radiation damages representing an effective benchmark. The obtained results have been successful, increasing the interest for this topic.

While the consequences of UH DR for low-LET radiations have extensively reported, limited recent biological outcomes have been made available in literature on UH DR

effects in tumor. In Buontempo F., et al., 2018, the authors also theorized that the delivered PFMA-3 UH DR delivered impaired radiation resistance of models of metastatic melanomas, one of the most aggressive and, to date, difficult to treat with success. The weight of such preliminary data exists in a chance for future preclinical characterizations, since such UH DR could potentially compromise tumor cells more than conventional DR and also sparing healthy tissues: see Table 1 for details.

Table 1. Data and caption from Sumini M., 2019a. Radiobiological experiments conducted (in-vitro) on different cell lines. The dose rate (DR) effect has been highlighted in comparison with a conventional X-ray tube (XRT) BALTEAU CSC320/70 X-ray device, calibrated to reproduce the PFMA-3 photon energy.

Cell lines	Cancer type	Assays and evaluations	Effects
SK-Mel28 and A375	Human skin melanoma	Clonogenic power	Reduced
		DNA double-strand brake damage	Increased
		Apoptosis	Not induced
		Mitotic catastrophe	Observed
		Cell cycle distribution	Blocked in G2/M phase
		Senescence	Increased
		Oxidative stress	Increased
		Migratory capacity	Reduced
MCF-7	Human breast adenocarcinoma	Morphology, shape and density evaluation	Compromised
		Vitality	Reduced
		Damage and death evaluation	Increased
T98G	Glioblastoma	Cell proliferation	Reduced
		Oxidative stress	Increased

Then, in 2019 [Isolan L., et al., 2019], the in-vivo irradiation starting from a micro tomography of a mouse has been planned at the Montecuccolino Laboratory. The produced DICOM file has been converted in a 3D unstructured tetrahedral mesh Abaqus [ABAQUS Analysis User's Guide] model and tested against the PFMA-3 photon beam with the Monte Carlo [Dunn WL. and Shultis JK., 2011] code MCNP

[Goorley, T., et al., 2012; Goorley T., 2014; Booth TE., et al., 2003; Pelowitx DB., 2011; Martz RL., 2014] (Figure 3). The numerical results have also been experimentally benchmarked relying mainly to micro-silica beads Thermo-Luminescent Dosimeters [Jafari SM., et al., 2014a; Jafari SM., et al., 2014b], classical TLD and Gafchromic© films [Karsch, L., et al., 2012] (Figure 4). See the [Isolan L., et al., 2019] work for further details.
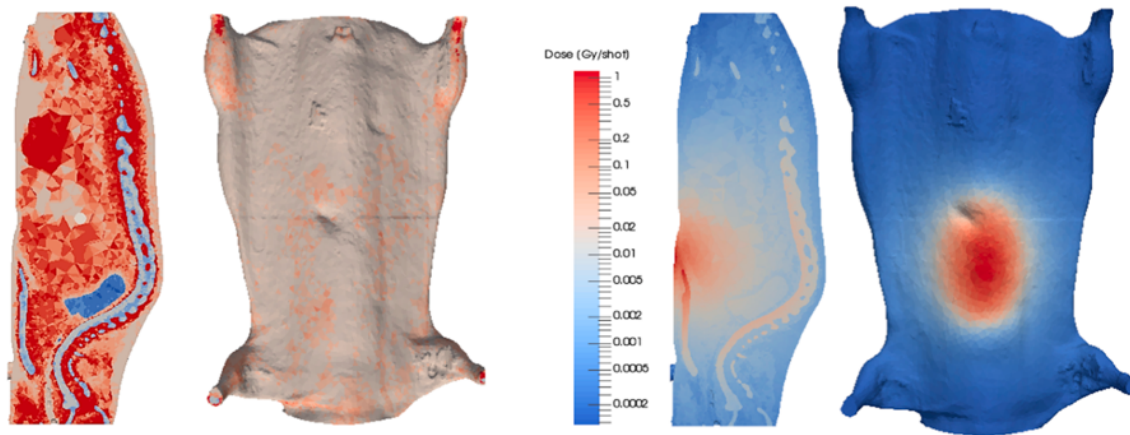
Figure 3. UM MCNP model derived from the micro-CT scan of a mouse. Left, segmented mouse UM structure from a CT scan. Right, dose distribution [Isolan L., et al., 2019].
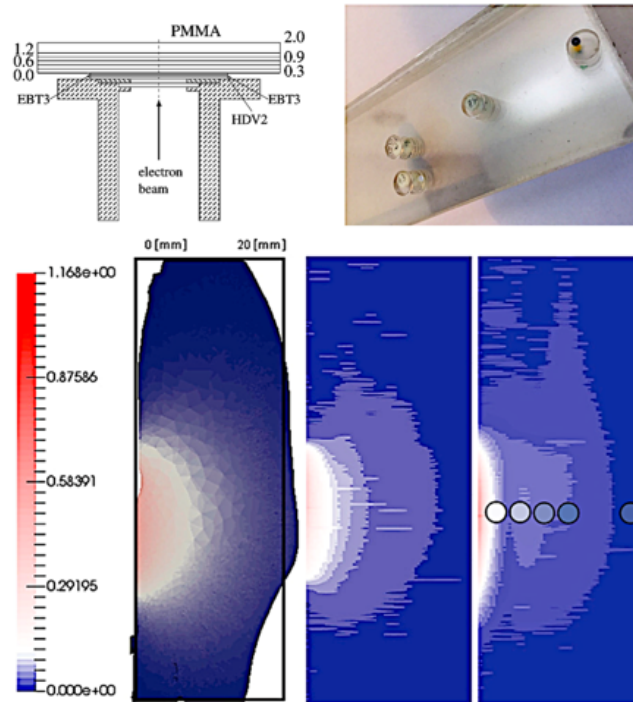
Figure 4. Above, Left, mouse phantom setup, cm. Above, right, PMMA hosting TLD and micro-silica beads. Centre, from left: comparison between the PMMA mouse UM model and the experimental irradiation with and without lead collimator; circular spots, dose registered by the beads [Isolan L., et al., 2019]. Below, left, EBT3 holder for in-air irradiations. Below, right, PMMA slabs before manufacturing and dosimeters.

At this point, one aspect that has been considered of fundamental importance was to get more insight into the various aspects of whole physical process of this pulsed source generation toward clinical applications.

The PhD research path: overview

Generally speaking, the PF are poorly controllable machines whose details and behavior of the source term are not fully known or predictable (electrons for the PFMA-3) due to the chaotic behavior of the discharges: this is the starting point. If the aim is to obtain a final product that is reliable and suitable for radiation therapy, it is necessary to know the behavior of the generated electron beam under variating operating conditions (through direct measurements and through the semiempirical-analytical models available in literature). This serves to understand the control mechanisms and, after appropriate and future engineering, to give the future medical physicist the possibility to choose the best energies and setups. For these reasons, the electron spectra were measured, and characteristics were compared with analytical models.

The electrons, however, are "the vector" with which the X-rays are generated. By carrying out a numerical study on the production of photons when not only the operating parameters of the machine vary (therefore, the electron spectra and current), but also parameterizing the material and the thickness of the target, further different "knobs" were obtained for the future radiotherapists for controlling the beam (which allow to modulate energy, spectrum, dose, etc.).

Subsequently, the attention moved to the dosimetry properties of the primary beam and the effects in materials, studied in particular with the aid of a tissue equivalent PMMA phantom and carrying out analog measurements and Monte Carlo simulations in such a way to estimate the doses for a potential patient.

Having obtained this result, the need to have a calculation system that would allow to obtain treatment plans quickly and reliably for this type of radiation beam has become of primary importance. On the other hand, an analog Monte Carlo simulation is too slow for routine applications and the usual variance reduction techniques do not always ensure the maintenance of good physics in the model with a simultaneous increase in performance. Taking as reference the well-known Weight Windows biasing method, it must be noted that it is characterized by the risk of a poor estimation of the importance function caused by the statistical nature of the generator itself. This means that if there is a phase-space region that is not properly sampled, an unreliable importance estimation can be generated. The solution to this problem was obtained by the inverse calculation with the solution of the adjoint transport problem and finally on the generation of importance maps obtained with external tools (set for other technological fields and transposed to the actual problem).

However, for clinical applications, the focal spot designed for cell irradiations (2-3 cm as diameter) is too large and therefore a magnetic focusing system has been modeled for its reduction to levels consistent with those required for human treatments (e.g., ~0.5 cm), comparable with other technologies on the market. In particular, the design of the quadrupolar focusing triplet was studied both for focusing the electron beam and simultaneously obtaining a hardening of the primary beam with consequent hardening of the X beam (optimizing the dose deposition).

Lastly, the reasons that make the radiobiological potential of the PF so high are being evaluated, by using different calculation codes to replicate the experimental measurements on RBE shown in past experimental campaigns.

Conclusively, (see Appendix A), the focus has shifted to the possibility of installing the equipment in a medical center or laboratory, studying the radiation protection issues related of these pulsed devices.

Point by point, the PFMA-3 has been fully characterized toward a clinical implementation of the technology and several milestones have been achieved:

1) Electron measurements: source beam spectral and spatial characteristics in function of the operating parameters for an effective way to optimize the technology toward clinical applications;

2) Analytical modeling of the PFMA-3: analytical modeling of the PFMA-3 discharges for validating the electron beam measurement for validation the electron beam data due to uncertainties in measuring ultra-fast quantities;

3) Monte Carlo photon transport simulations: parametric Monte Carlo simulations using the measured electron characteristics as model sources and optimizing thickness and material of the target: for confirming that the pulsed X-ray source was able to deliver one Gy pulse^{-1}, well characterized and technically feasible; the experimental measurements became a link between the "Lab. reality" and the numerical models;

4) Direct and adjoint Monte Carlo transport simulations: punctual dose measurements in PMMA phantoms and MCNP benchmark with numerical optimization and acceleration through adjoint importance functions and CADIS approach (through the ADVANTG [Mosher SW., et al., 2015] tool) to physically optimize the weight windows to bias the forward calculations performances toward clinical applications;

5) Magnetic lens design for focusing the measured electron beams: focusing the primary electron beam for satisfying the clinical irradiation requirements;

6) Radiobiological Effectiveness evaluation: RBE of the flashing photon beam against melanoma cell lines to find an evaluation process considered as a new approach for the implementation of simulation models suitable for the prediction of biological effects induced by FLASH source irradiation;

7) Radiation protection issues at the PFMA-3: RP from experimental and numerical point of view as milestone when managing FLASH sources, due to the not almost unknown response to the dosimeters and often the impossibility to use active instrumentation (see Appendix A for details).

Electron source beam spectral and spatial characteristics in function of the operating parameters

The electron spectral characteristics of the PFMA-3 have been deeply evaluated under a parametric study performed by varying the operational condition of the device and registering the results through a Thomson spectrometer and a Rogowski coils in such a way to better explore the irradiation capability [Sumini M., et al., 2019a]. The characteristic that was intended to be deeply investigated was the existence of one or more scaling laws that could be helpful in the upcoming design of a dedicated device: the aim has been to drive the technology's evolution from "conceptual viability" to a prototype of an effective clinical application device. The analysis was conducted in order to check the possible enhancing of the electron beam source (electron charge bunches and energy spectrum and, consequently, X-ray pulses and dose delivery capabilities). Due to the fact that the focus on the backward-emitted electron streams can be considered quite "non-standard" (with respect to classical applications of the PF devices which are born mainly for being studied as compact neutron sources but also with respect to standard sources, e.g., X-ray tubes or linear accelerators) the specific output could not yet be linked to the common and already modeled pinch yields (as the classical PF applications is being a compact neutron source, there is a limited literature regarding such devices as electron beam generator as primary beam and only few empirical models related to specific devices are available; see f.i. the Patran A., et al., 2005 work). The spots obtained from a short sequence of pulses on Gafchromic™ HDV2 films stack interacting directly with the electron bunches (dosimeters used as closure of the hollow anode instead of the usual metal target) shown the stochastic behavior of the interaction of the different light charged particle streams (Figure 5) and

also the saturation effect (e.g., when the dosimeter does not respond anymore [Casolaro P, 2021]; see f.i., Figure 5, panel 1) due to the extremely high doses delivered (by light charged particles). See the Sumini M., et al., 2019a, 2019b and references therein for further details.
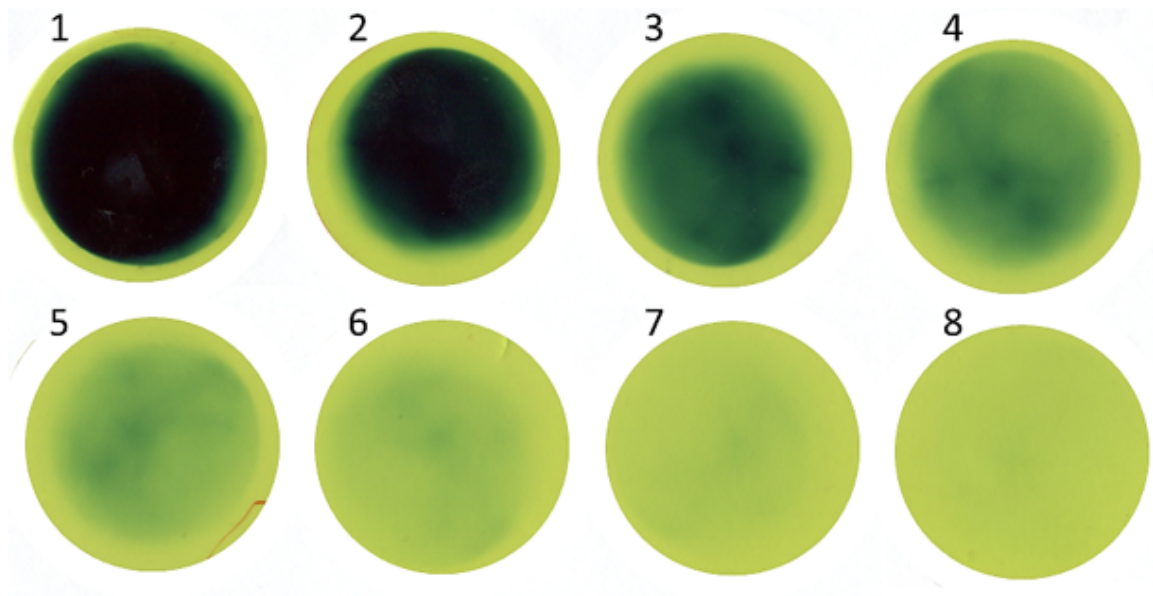
Figure 5. Outcomes of a 3 pulse sequence irradiation set at 18 kV as power supply charging voltage, 3 kJ as capacitor's stored energy, stack of eight HDV2 Gafchromic™ films (used for closing the central unit of the extraction channel) [Sumini M., et al., 2019a].

Gafchromic™ films setup

Due to the extremely short time scale of the electron pulses, passive methods of dose recording can be used for measurement [Sumini M., et al., 2019a]. So far, Gafchromic™ films have mainly been used to obtain a dose assessment and the associated spatial distribution. Due to their high spatial resolution, tissue-equivalent properties, self-developing technology and low energy dependency, these films are often used as reliable dosimeter systems for both clinical and research applications. Three types of Gafchromic™ films have been historically used for PFMA-3 experiments: EBT3, HDV2 and XR-QA2 (Figure 6).

The EBT3 is symmetric and consists of a 25 μm active layer between two 125 μm polyester backings. The recommended dose range for use is from 0.1 cGy to 40 Gy. Because it is equivalent to human tissue (similar atomic number), it is considered as primary reference dosimeter for PFMA-3 experiments for evaluating the integral of the effective energy transfer of an X-ray beam.

HDV2 film consists of a 97 μm transparent polyester backing and 8 μm active material. Self-developing HDV2 films have a dose range of 10 to 1000 Gy. The spatial resolution is quite high, in fact, they can resolve details 5 microns in size. The active layer can be directly exposed to radiation in order to detect photons or even low energy electrons. It has been used to stop electrons, which, thanks to their energy, could eventually (statistically) pass through the metal target.

XR-QA2 films are composed from different substrates and the active layer is about 25 μm. The films are dose sensitive from 0.1 cGy to 20 cGy. The response is almost linear

in the range from 20 to 200 keV. It has been used in evaluating the high energy fraction of electron beams [Sumini M., et al., 2019a, 2019b].
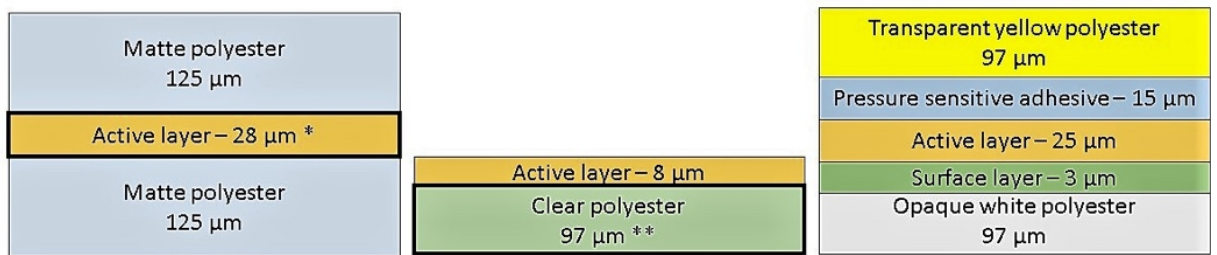
Figure 6. Layered structure of the Gafchromic™ films used in the experiments, in sequence EBT3, HDV2 and XRQA2, scale not preserved (see Sumini M., et al., 2019b and reference therein for insights).

Energy distribution characterization with the Magnetic spectrometer setup

The discharge process characteristics of each pulse in PF equipment are usually coded by a set of standard parameters, namely: the energy stored in the capacitor bank; plasma vacuum chamber gas pressure; due to the spark gap (actually a "rail gap" for PFMA-3), the discharge current obtained when the circuit is closed; measurable yields at pinch and the "pinch current" recorded due to the Rogowski coil signal embedded in the device (Figure 7 and raw data below). Therefore, it is being considered to study electron streams in terms of energy distribution and current using signals recorded in various pulses through a magnetic spectrometer (Figure 8) and a Rogowski coil (Figure 9). The backward-emitted electrons can be characterized in terms of energy distribution in several ways, relying primarily on magnetic spectrometers. It consisted of two permanent magnets that generated a magnetic field of 0.18 T, able to bend the electron stream toward the Gafchromic™ film, and was capable of applying robust and reliable range-energy method. The calibration curve of the magnetic spectrometer correlates the electron energy with the distance traveled by the electrons under the action of a magnetic field before storing the energy in the films (28 x 31 mm), see Figure 10 and Figure 11. Indeed, the larger the radius of curvature, the higher the particle energy. To check the calibration curve, different thicknesses of mylar were placed on top of the Gafchromic™ film placed on the spectrometer (Table 2). Thus, only electrons with energies in excess of the energy required to achieve their range in the mylar (at any given thickness) could transfer a dose to the film (Table 3). By calculating the energy of the particles required to pass the Mylar of various thicknesses and measuring where the film began to amplify the resulting pattern, the two different quantities could be correlated. Mylar thicknesses of 50, 100 and 200 microns were placed on top of another

HDV2 instead of the 450 microns mounted on the XR-QA2 to study the high-energy part of the beam [Sumini M., et al., 2019a]. After calibration processes, the spectrometer has been used for recording electron spectra.

Figure 7. Potential and its derivative (current) as registered by embedded Rogowski coil.

The raw data as registered by the Rogowski coil and displayed in Figure 7 are as follows:

```
Model,DPO4032
Firmware Version,2.30
Point Format,Y,,Point Format,Y
Horizontal Units,S,,Horizontal Units,S
Horizontal Scale,4e-06,,Horizontal Scale,4e-06
Sample Interval,4e-10,,Sample Interval,4e-10
Record Length,100000,,Record Length,100000
Gating,0.0% to 100.0%,,Gating,0.0% to 100.0%
Probe Attenuation,1,,Probe Attenuation,1
Vertical Units,V,,Vertical Units,NONE
Vertical Offset,0,,Vertical Offset,0
Vertical Scale,10,,Vertical Scale,1e-05
Label,,,Label,
TIME,CH1,,TIME,MATH
-3.70800e-06,0,,-3.70800e-06,0
…
-3.70120e-06,-0.4,,-3.70120e-06,-1.5625e-09
…
3.62916e-05,-0.4,,3.62916e-05,2.90156e-06
```
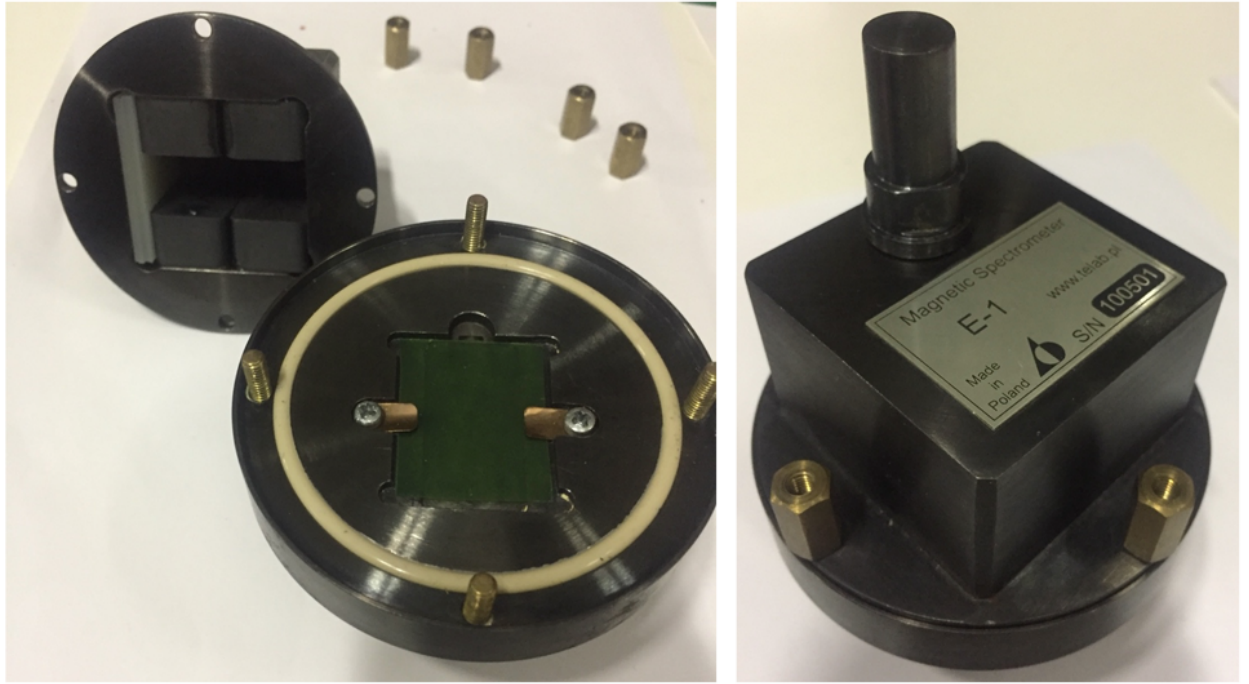
Figure 8. Thomson Spectrometer. An HDV2 film is also visible (left panel).
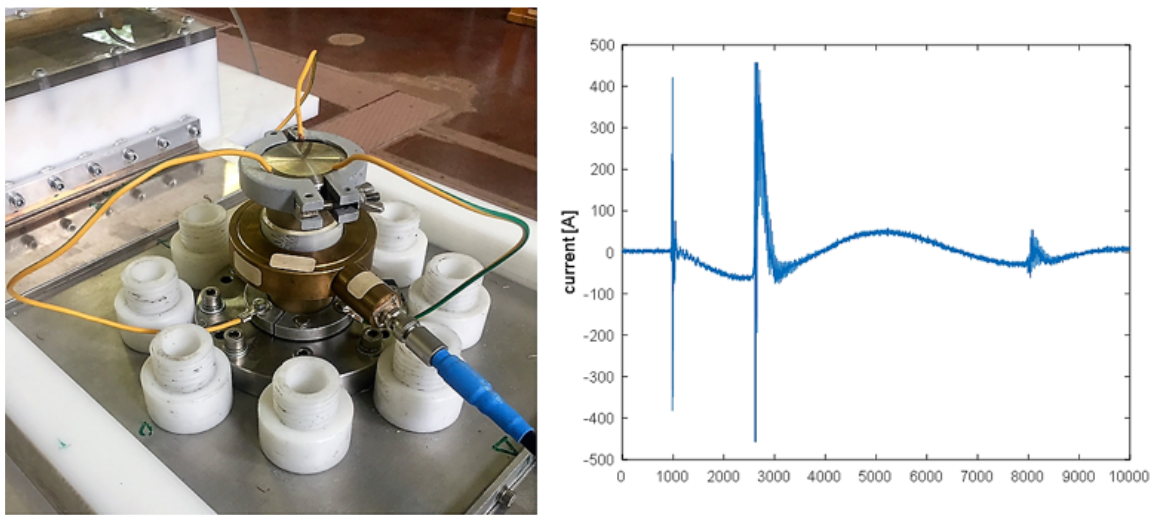
Figure 9. Experimental setup for electron current direct registration (left). The external Rogowski coil, the oscilloscope connecting cable (blue) and the three connectors that make the components at the same potential are clearly visible. On the right, the registered electron current signal, power supply 18 kV, pressure 0.4 mbar. Each point on the horizontal scale corresponds to 0.2 nanosec. The main signal lasts 40 nanosec. It is possible to see as background the harmonic related to the equivalent circuit parameters [Sumini M., et al., 2019a].

Figure 10. Example of passive dosimeters introduced in the Thomson spectrometer for calibration, covered by different mylar layers (not shown) and exposed to the electron beam. It can clearly be seen that the energy is deposed in different positions as a function of the curvature radius (e.g., the energy required to "pass through" the mylar), see also Figure 11.

Table 2. Calibration process.

n. shots	Mylar thickness s [μm]	Spectral 2D distribution	Spectrum along the middle film line
5	50	8 mm	
5	100	11 mm	

5	200
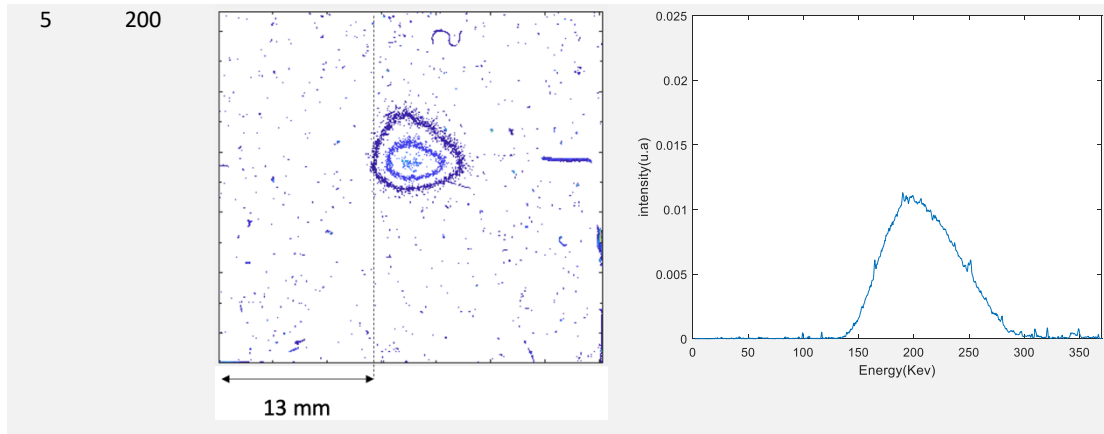
Table 3. Correlation between thickness of material interposed in front of the films, the minimum particle energy required for passing through and distance reached after the curvature.

Thickness [µm]	Minimum electron energy [keV]	Reached distance [mm]
50 mylar	60	8
100 mylar	95	11
200 mylar	140	13
450 mylar + 97 polyesters	270	20
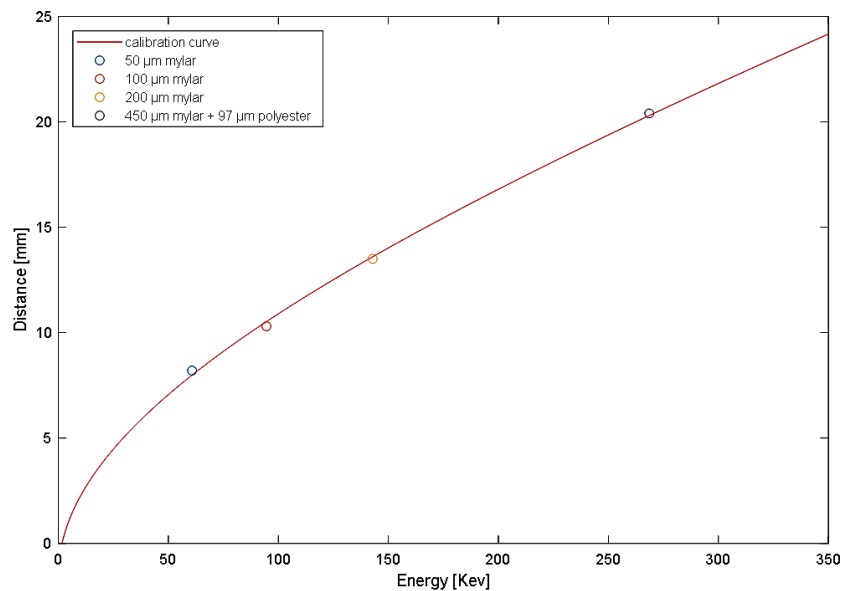
Figure 11. Energy-range magnetic spectrometer calibration curve based on the Larmor radius evaluation. Experimental data can be fitted with a polynomial with a correlation factor R2 = 0.9989. The uncertainty is only due to the HDV2 film scanning spatial resolution (<0.05 mm) [Sumini M., et al., 2019a].

52

Rogowski coil for electron current measurement setup

By putting a Rogowski coil outside the extraction channel, coaxially with the hollow anode, it has been possible to experimentally record and evaluate the induced currents, namely the effective electronic current flowing from the pinch point. Telab (Poland) cables correctly designed and calibrated for the Rogowski coil have been used for these experiments. The cable is manufactured by Huber+Suhner (Sucoflex cable) and has strict shielding standards to avoid interference with the main electromagnetic signal from the pinch point. See Figure 12 for configuration details.
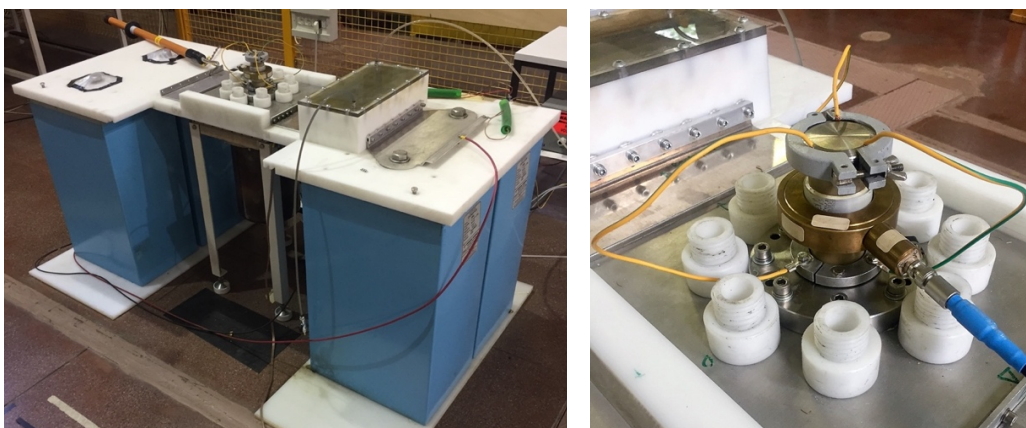
Figure 12. PFMA-3 global view. The external Rogowski coil is also visible.

The energy stored in the capacitor's bank, the gas filling pressure, the discharge current obtained thanks to a spark gap, the measurable yields at the pinch, and the "pinch current" as registered thanks to a Rogowski coil signal imbedded in the device have been used to code the characteristics of the discharge process at each pulse in a PF device. The electron streams are highly "uncharacteristic," at least in comparison to traditional sources (as the electrons resulted self-directed and self-collimated differently to classical quite isotropic distributions as in the other particles cases) and, for the time being, cannot be related to conventionally predicted pinch yields: due to that, dedicated scaling laws has also been modelled [Sumini M., et al., 2019a]. Relying mainly to the results coming from the magnetic spectrometer and the signal recorded at various pulses through the Rogowski coil was the starting point, Table 4 shows the findings in terms of electron energy spectra obtained at a constant working pressure of 0.40 mbar for various power supply settings and capacitor bank energy. Table 5 depicts the impact of various gas filling pressures on the energy spectrum. The PF discharge current signal were measured as well as the impacts beam deviation as imprinted on the Gafchromic™ films thanks to the magnetic spectrometer for each pulse. The beam energy spectrum might be reconstructed by analyzing the gray levels. The spectrum was shaped by averaging at least five different pulses. Different "averaged" spectra for the backward emitted electron streams result from the examination of the different patterns observed under varying power supply settings and stored energy. The set of current signals captured by the inner Rogowski coil during the discharge is presented in the left column. The pinch and the effects recorded by the HDV2 Gafchromic™ films on the magnetic spectrometer are clearly visible (and fairly repeatable) (center). The

reference grey level and the related energy scale utilized in the study are defined by the vertical dash line. As previously stated, there will be some stochastic effects, as well as some asymmetry (see i.e. for 12, 22, 24 kV). The "reference" electron energy, which is connected to the electron bunch originating from the primary pinch, is defined by the peak of the spectrum. The presence of contributions due to different bunches is easily recognizable in some of them, such as the 12 kV pattern, and they can be thought of as the superposition of different Maxwellian-like distributions centered on the average energy (or "kinetic temperature") of each electron beam (the Maxwellian-like distributions comes from a Local Thermodynamic Equilibrium model, LTE, that can be considered valid when the electron density is "high" [Akel M., et al., 2013]). The results suggest that expanding the capacitor's bank energy can be translated in a slight shift toward higher values (the electron energies in correspondence of the highest probability of the diverse spectra move from 43.92 keV at 1.6 kJ to 89.38 keV at 6.39 kJ, see Figure 13). Such results suggest also a decreasing of the secondary pinches (that vanishes at higher control supply values) related to the secondary electron beams, getting a much more unequivocal range that looks "constrained" to a legitimate Maxwellian distribution. The information also recorded in Figure 13 recommends a scaling law with a dependence from the energy bank stored as shown in Figure 14. The data in Figure 15 shows a scaling law related to stored energy. This scaling law hypothesis is currently only based on experimental results and seems to cover a fairly wide range, from 12 to 30 kV. The data indicates that increasing the gas pressure will provide a high energy contribution to the electron spectrum. This may be because more plasma is confined to the pinch point at higher pressures. The electron beam carries more energy, but the flattening of the spectrum in the range of up to 200 keV or higher also means that from the perspective of conversion to X-ray pulses, more freedom's

degrees in the target material and thickness may be available. A linear correlation was obtained between both peak and pinch currents and the capacitor's bank energy. The existence of patterns and scaling laws for PF devices, both in Mather and Filippov configuration has been widely acknowledged in the literature since the very beginning of the development of this technology. These scaling criteria were designed to optimize nuclear reactions and the nuclear conditions (mostly the power and voltage) involved. The PFMA-3 cannot be considered yet optimized since it has a very high inductance of 150 nH. This makes difficult to encase the actual PF in the complex configuration space as defined in several references. Moreover, the reverse-emitted electrons are a sort of by-product of the pinch conditions. It is difficult to determine whether electron streams' characteristics are linked to the commonly-considered pinch yield parameters. The trends that come from the experimental results, gives the perspective of the possible evolution of this class of devices with respect to the specific goal of an enhancement of the PF as electron source. In Figure 15 and Figure 16 the electron current has been directly measured and analyzed, in terms of intensity, by an external Rogowski coil setup. The measurements confirmed that the pulse was short as expected. As it can be seen, the energy carried by the electron streams, evaluated taking into account the whole spectrum, changes very little with the capacitor bank energy. This probably means that the phenomenon is strictly correlated with pinch conditions, but not with standard pinch yield. The electron current can be measured and used to characterize the beams with respect to energy, charge and current. The 12 kV voltage must be considered with care, because in the device, the voltage is a "threshold" at which a pinch is not produced. See Sumini M., et al., 2019a for further details.

Table 4. Samples from the data sets used for the definition of the averaged electron energy spectra obtained for different power supply voltages [Sumini M., et al., 2019a]. Left, derivative of the PF discharge current, time scale in Tektronix™ oscilloscope units, each lasting 0.04 nanosec. Center, Gafchromic™ film impressed by the electron impact in the magnetic spectrometer with the scale showing the electron energies according to the calibration curve. On the right, the electron spectrum evaluated along that scale; the dash line defines the "reference energy", i.e. the peak of the distribution.
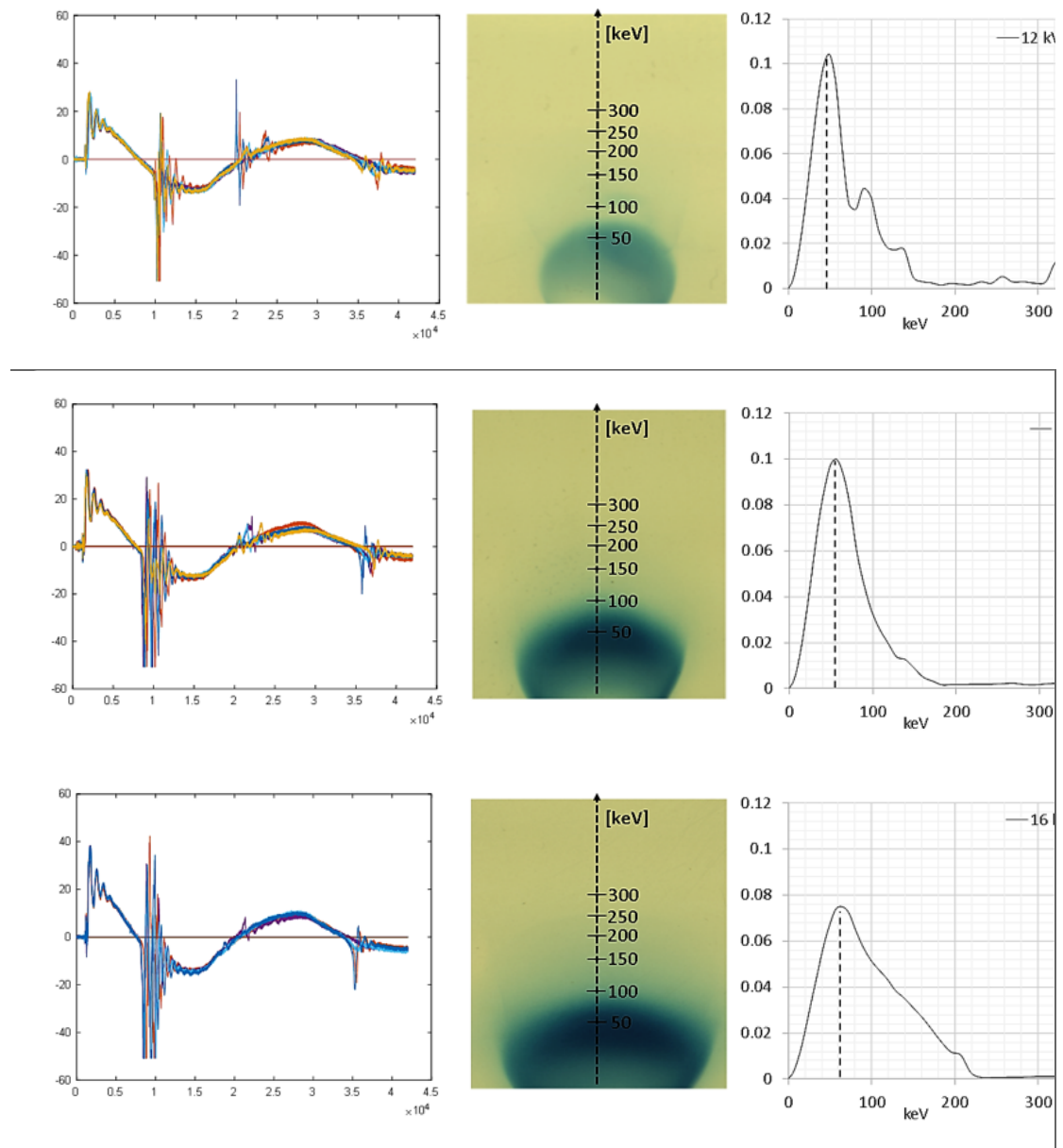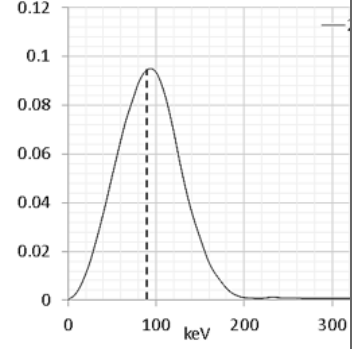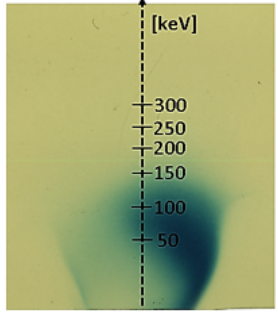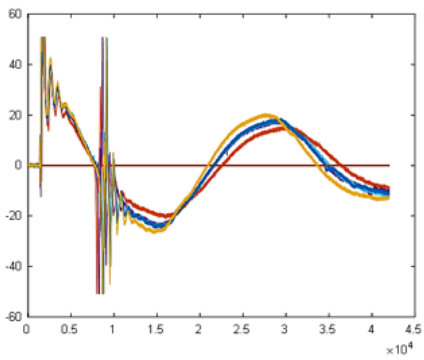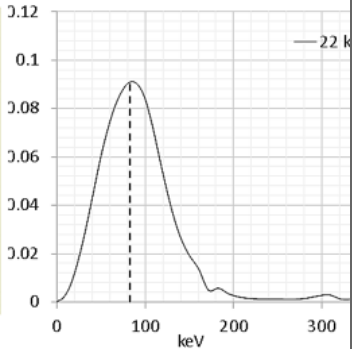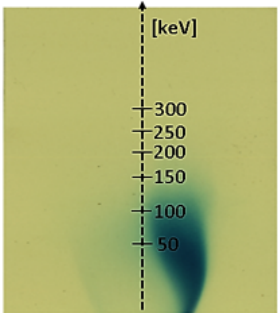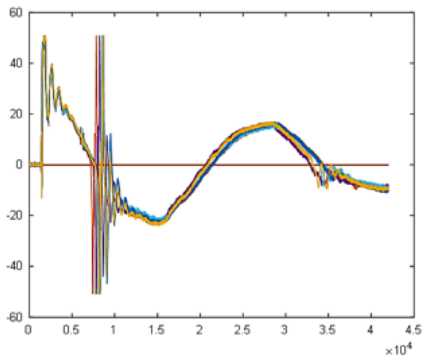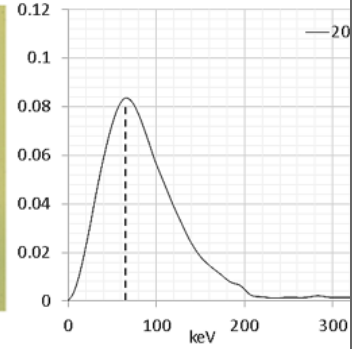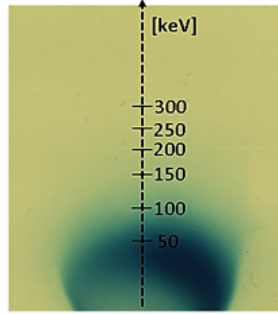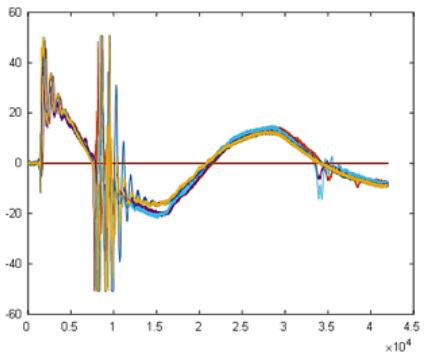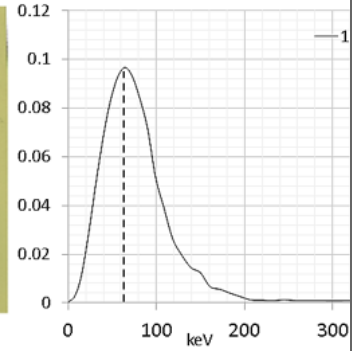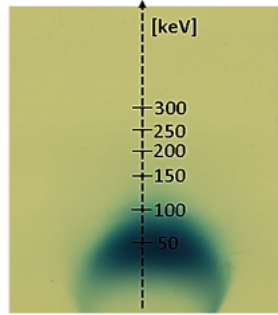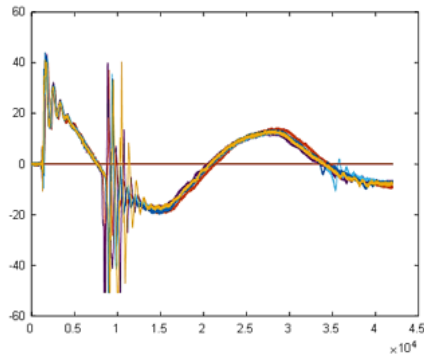
Table 5. Effects of the N$_2$ pressure in the chamber. Results collected from several pulses for each pressure value, with the power supply at 18 kV. The main pinch maintains its regularity. Time scale in Tektronix™ oscilloscope units, each lasting 0.04 nanosec. The spectrum at 0.40 mbar is reported for comparison with a dashed line [Sumini M., et al., 2019a].
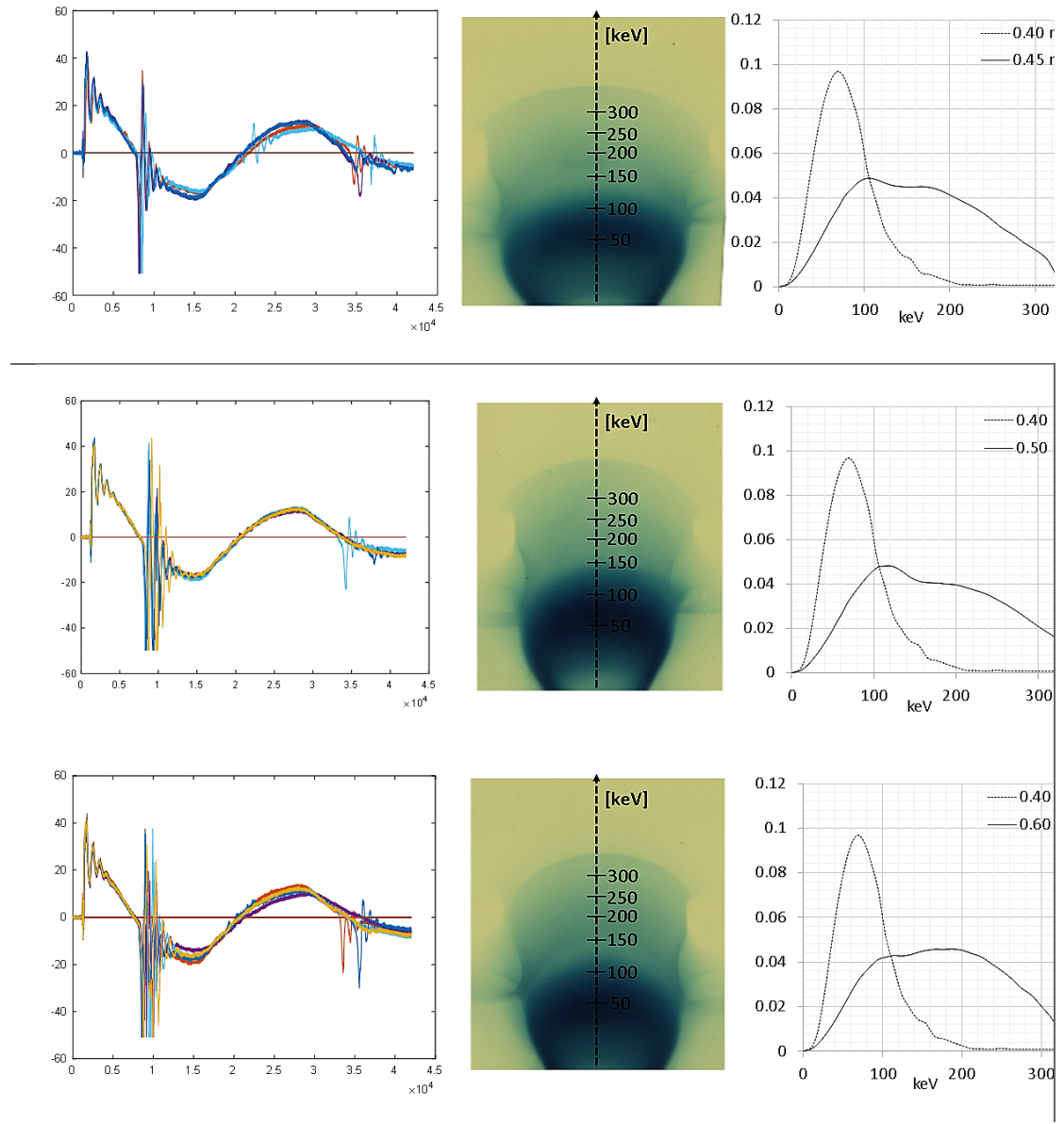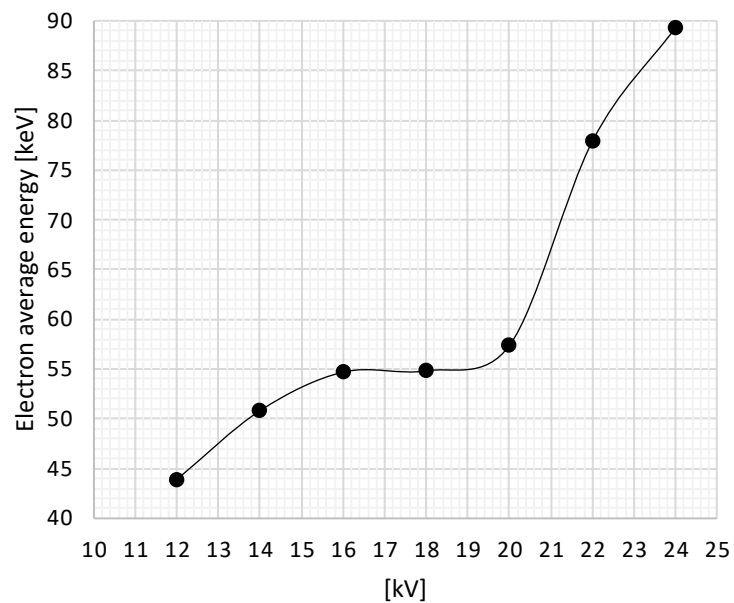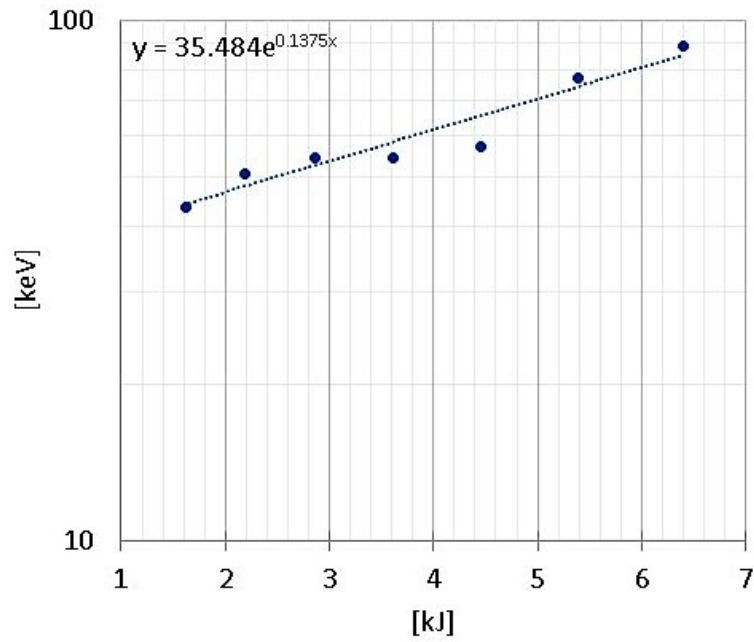
Figure 13. Above, correlation between the reference electron energy and capacitor's bank stored energy (R^2 equal to 0.9278). The gas filling chamber pressure has been kept constant at 0.40 mbar [Sumini M., et al., 2019a]. Below, calculated electron averaged energy. Errors in evaluations related to the HDV2 sensitivity, OD reading system, numerical analysis performed, power supply and components settings. The expected experimental errors are mainly related to the PF discharge variability and on the basis of laboratory experiences can be estimated to be under the 20%.
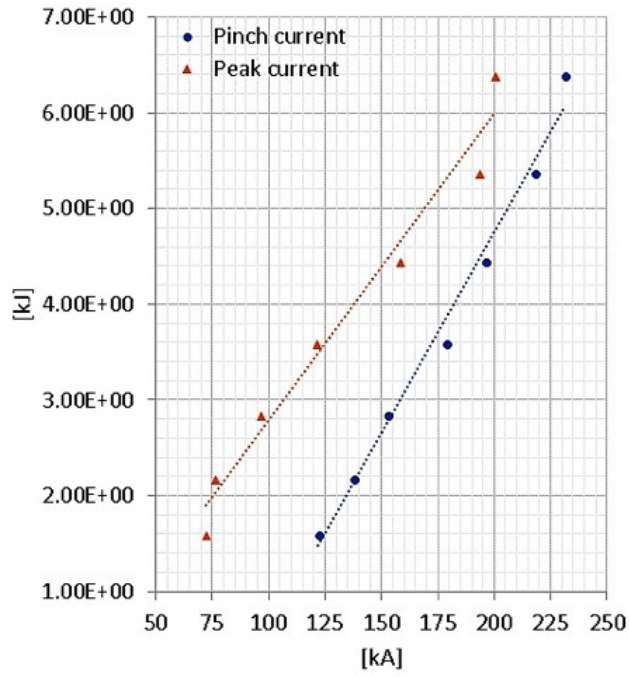
Figure 14. Correlation between peak/pinch current (respectively R^2 of 0.9711 and 0.9863) and capacitor's bank energy [Sumini M., et al., 2019a].
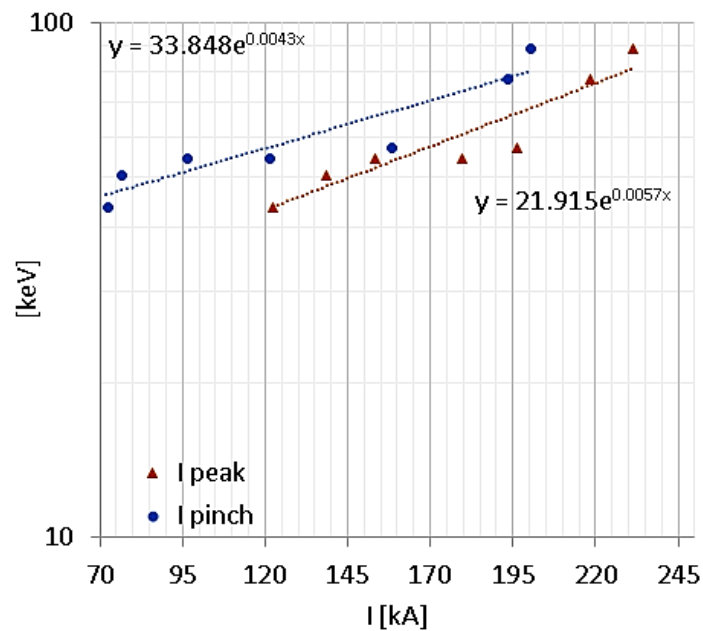
Figure 15. Correlation between peak/pinch current and the reference electron beam energy from Figure 5, right column [Sumini M., et al., 2019a].
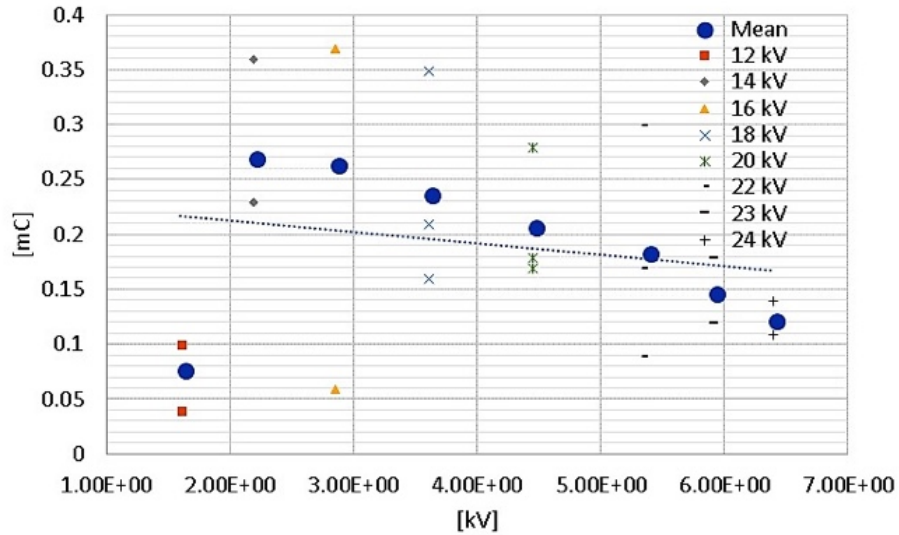
Figure 16. Distribution of the charge carried by the electron bunches for different capacitor's bank energy. Interpolating linear trend displayed [Sumini M., et al., 2019a].

The PF electron source that has been characterized so far has shown both stability and coherence, which could lead to a technological evolution towards a dedicated tool for medical applications. The PFMA-3 device's pinch phase produces an electron stream that is primary source for ultra-short X-rays. The results obtained not only confirmed our previous findings but suggested a possible path towards a new class of X-ray pulsed generators in the perspective of the potential interest about this source in medical applications. For the next steps, an analytical validation of the achieved results has been performed before moving to the X-ray production evaluation based on Monte Carlo simulations [Sumini M., et al., 2019a, 2019b].

Analytical modeling of the PFMA-3 discharges for validating the electron beam measurement

Experimental results of the Sumini M., et al., 2019a work have been analytically validated when operated at 18 kV and 0.4 mbar with a simple model [Lee S., 2014] that estimated peak and pinch currents as 188 kA and 132 kA against measures of 180 kA and 126 kA (based on the HDV2 characteristics and the experimental setup, the expected errors are mainly related to the PF discharge variability and on the basis on laboratory experiences evaluated to be under the 20%). The flux has been derived as $1.42E+15$ # cm^{-2} pulse^{-1} with 18 kA electron current. Such fluence rate corresponds to a calculated transported bunch of electrons of total charge equal to 0.27 mC which is nearly compliant with the measured quantity of 0.23 mC [Sumini M., et al., 2019a]. The validation of the electron beam data was required due to uncertainties in measuring ultra-fast "quantities". Lee's model describes the behavior of a Plasma Focus and the gas within it, whether it is of the Filippov type or the Mather type. The model relates the electrical (Figure 17), thermodynamic, radiative, and fluid dynamic characteristics of the machine and the gas operator, to provide information for the optimization of the same, or to serve as a theoretical basis for the confirmation of experimental experiences. The events concerning a single Plasma Focus discharge are summarized in the 5 classical phases [Lee S., 2014].
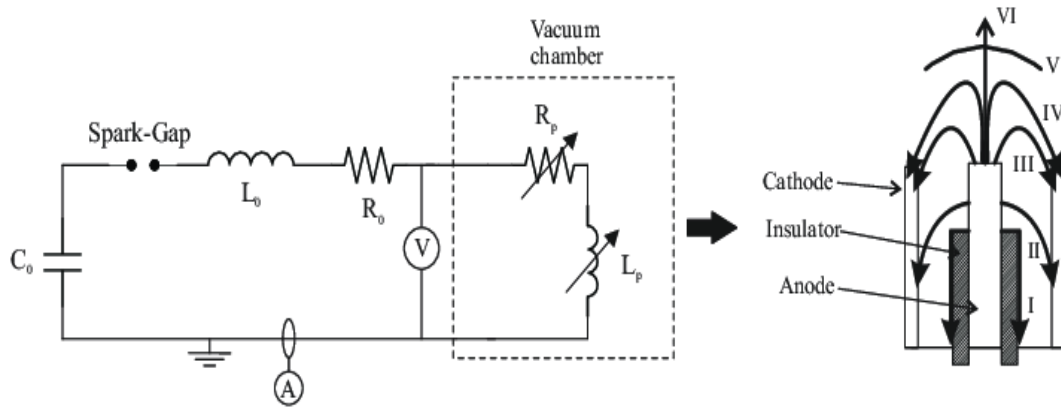
Figure 17. PF equivalent circuit as shown in the Ceccolini E., 2012 work.

Axial phase

This phase is described by the so-called snow-plow model (as coined by Rosenbluth M., et al., 1954), where an equation of motion is coupled with a circuit dynamic. The equation of motion incorporates within it the characteristic factors of this phase, that is mainly described by the mass factor f_m which takes into account all the effects that result in the increase or decrease of the moving mass. The current factor f_c that defines the fraction of current actually present in the motion in the axial phase is also considered (details and derivation procedures in Lee S., 2014).

Defining:

- z, position of the current sheet (e.g., the number of charges which flows in plasma);
- f_m, mass factor;
- f_c, current factor (or current sheet, CS);
- $c = b/a$, cathode radius/anode radius;
- ρ_0, ambient density;
- μ, permeability;
- V_0, capacitor voltage;
- C_0, capacitance;
- L_0, inductance;
- t_a, caracteristic axial transit time of the CS;
- v_a, characteristic axial transit speed [Lee S., 2014];

The motion equation, derived combining the rate of change of momentum of current sheet and the magnetic force on current sheet equations is:

$$\frac{d^2z}{dt^2} = \frac{\left[\frac{f_c^2}{f_m}\frac{\mu\ln(c)}{4\pi^2\rho_0(c^2-1)}\left(\frac{I}{a}\right)^2 - \left(\frac{dz}{dt}\right)^2\right]}{z} \qquad (1)$$

And the circuital equation is:

$$\frac{dI}{dt} = \frac{\left[V_0 - \int \frac{I dt}{C_0} - r_0 I - I f_c \frac{\mu}{2\pi}(\ln(c))\frac{dz}{dt}\right]}{\left[L_0 + \frac{f_c \mu}{2\pi}(\ln(c))z\right]} \tag{2}$$

The time and the axial propagation velocity of the current sheet can be obtained as:

$$t_a = \left[\frac{4\pi^2(c^2 - 1)}{\mu \ln(c)}\right]^{0,5} \frac{f_m^{0,5}}{f_c} \frac{z_0 \rho_0^{0,5}}{(I_0/a)} \tag{3}$$

$$v_a = \frac{z_0}{t_a} \tag{4}$$

Radial inward shock phase

This phase is described by four concentrated equations using an "elongating slug-model". The first equation (5.1) computes the radial characteristics of the magnetic pressure wave and its velocity. The second equation (6) calculates the elongation velocity of the column, while the third (7) calculates the speed of the Current Sheet (CS), also called magnetic piston, which allows the CS to separate from the shock wave by an adiabatic approximation. The fourth (8) is the circuit equation. The thermodynamic effects due to the pushed ionization of the operator gas and excitation are included in these equations. It is at this stage that the characteristic density and temperature values of the discharge are calculated. Also, for this phase, mass factors f_{mr} and current f_{cr} are defined, which define respectively the amount of mass and current that actually drive the process. r_p, r_s and γ can be defined as the piston radius (in motion), shock-front radius and specific heat (5/3 for atomic gases and 7/3 for molecular gases [Lee S., 2014]. Using the following definitions:

- P, shock pressure;
- ρ_0, ambient gas density;
- v_s, shock speed;
- γ, specific heat ratio of the gas;
- r_s, position of the inward moving shock front driven by the piston at position;
- r_p, CS position;
- f_{mr}, radial phase mass swept-up;
- f_{cr}, current factor;
- z_f, posizion of the axial CS (see [Lee S., 2014] for additional information);

The shock-front equation, from shock wave propagation theory is

$$P = \frac{2\rho_0 v_s^2}{(\gamma + 1)} \qquad (5)$$

From which can be derived that

$$\frac{dr_s}{dt} = -\left[\frac{\mu(\gamma + 1)}{\rho_0}\right]^{0,5} \frac{f_c}{f_{mr}^{0,5}} \frac{1}{4\pi r_p} \quad (5.1)$$

Then, along the z axis, the elongation velocity (of the current sheet) is

$$\frac{dz_f}{dt} = -\left(\frac{2}{\gamma + 1}\right) \frac{dr_s}{dt} \quad (6)$$

The piston radial motion equation

$$\frac{dr_p}{dt} = \frac{\frac{2}{\gamma + 1} \frac{r_s}{r_p} \frac{dr_s}{dt} - \frac{r_p}{\gamma I}\left(1 - \frac{r_s^2}{r_p^2}\right)\frac{dI}{dt} - \frac{r_p}{z_f}\left(1 - \frac{r_s^2}{r_p^2}\right)\frac{dz_f}{dt}}{\frac{\gamma - 1}{\gamma} + \frac{1}{\gamma}\frac{r_s^2}{r_p^2}} \quad (7)$$

And the circuital equation

$$\frac{dI}{dt} = \frac{V_0 - \frac{\int I \, dt}{C_0} - r_0 I - f_c \frac{\mu}{2\pi}\left(\ln\left(\frac{b}{r_p}\right)\right) I \frac{dz_f}{dt} + f_c \frac{\mu}{2\pi} \frac{z_f}{r_p} I \frac{dr_p}{dt}}{L_0 + f_c \frac{\mu}{2\pi}(\ln(c))z_0 + f_c \frac{\mu}{2\pi}\left(\ln\left(\frac{b}{r_p}\right)\right)z_f} \quad (8)$$

Combining, it is possible to calculate the time and the velocity of axial crossing (of the current sheet along the electrode axis), e.g., t_r, characteristic radial transit time (between the two coaxial electrodes); v_r, characteristic speed of the radial inward shock to focus axis [Lee S., 2014];

$$t_r = \frac{4\pi}{[\mu(\gamma + 1)]^{0,5}} \frac{f_{mr}^{0,5}}{f_c} \frac{a}{\frac{\left(\frac{I_0}{a}\right)}{\rho^{0,5}}} \quad (9)$$

$$v_r = \frac{a}{t_r} \quad (10)$$

Radial reflected shock phase

When the inward shock phase impacts the central axis, being the process collisional, a shock wave is always generated in the radial direction, outwards, although the CS continues to move inwards. For this phase the same factors apply as for the previous phase f_{mr} and f_{cr}. The temperature behind the r_s rises by two orders of magnitude [Lee S., 2014]. Introducing: r_r, Reflected Shock (RS) position [Lee S., 2014];

The motion piston equation is

$$\frac{dr_r}{dt} = -0,3\left(\frac{dr_s}{dt}\right) \tag{11}$$

While its velocity assumes the form

$$\frac{dr_p}{dt} = \frac{\frac{-r_p}{\gamma I}\left(1 - \frac{r_s^2}{r_p^2}\right)\frac{dI}{dt} - \frac{r_p}{z_f}\left(1 - \frac{r_s^2}{r_p^2}\right)\frac{dz_f}{dt}}{\frac{\gamma - 1}{\gamma} + \frac{1}{\gamma}\frac{r_s^2}{r_p^2}} \tag{12}$$

The elongation velocity is

$$\frac{dz_f}{dt} = -\left(\frac{2}{\gamma + 1}\right)\left(\frac{dr_s}{dt}\right) \tag{13}$$

And the circuit equation became

$$\frac{dI}{dt} = \frac{V_0 - \frac{\int I dt}{C_0} - r_0 I - f_c\frac{\mu}{2\pi}\left(\ln\left(\frac{b}{r_p}\right)\right)I\frac{dz_f}{dt} + f_c\frac{\mu}{2\pi}\frac{z_f}{r_p}I\frac{dr_p}{dt}}{L_0 + f_c\frac{\mu}{2\pi}(\ln(c))z_0 + f_c\frac{\mu}{2\pi}\left(\ln\left(\frac{b}{r_p}\right)\right)z_f} \tag{14}$$

Pinch phase

When the position of the inward moving shock front driven by the piston collides with the magnetic piston, the compression is such that it enters a radiative state. For heavier gases (i.e., Argon, Xenon, Neon, etc.), this emission of highly energetic radiation increases the degree of compression itself. The three equations describing this phase include the energy loss/gain effects in the form of radiation escaping and joule heating. These equations are on the motion in the radial direction of the piston, on the elongation of the column and on the circuit.

This stage of the discharge is the one in which almost all the ionizing radiation is released, it is therefore obvious to refer at this moment to the computation of radiation yields (which take into account the effect of self-absorption by the plasma) and of neutrons (particularly important if the operator gas turns out to be Deuterium). Also, the thermonuclear components and the target beam-gas are calculated here, as they belong to the Fast Ion Beam (FIB) and the Fast Plasma Streams (FPS), both coming out of the pinch phase [Lee S., 2014].

The column elongation

$$\frac{dz_f}{dt} = \left[\frac{\mu}{4\pi^2(\gamma+1)\rho_0}\right]^{1/2} \frac{If_c}{r_p} \qquad (15)$$

The circuit equation

$$\frac{dI}{dt} = \frac{V_0 - \frac{\int I dt}{C_0} - \frac{\mu}{2\pi}\left(\ln\left(\frac{b}{r_p}\right)\right)\frac{dz_f}{dt}If_c + \frac{\mu}{2\pi}\frac{z_f}{r_p}\frac{dr_p}{dt}If_c - I(Rf_c + r_0)}{L_0 + \frac{\mu}{2\pi}f_c\left((\ln(c))z_0 + \left(\ln\left(\frac{b}{r_p}\right)\right)z_f\right)} \qquad (16)$$

The piston motion equation

$$\frac{dr_p}{dt} = \frac{-\frac{r_p}{\gamma I}\frac{dI}{dt} - \frac{1}{\gamma+1}\frac{r_p}{z_r}\frac{dz_f}{dt} + \frac{4\pi(\gamma-1)}{\mu\gamma z_f}\frac{r_p}{f_c^2 I^2}\frac{dQ}{dt}}{\frac{\gamma-1}{\gamma}} \qquad (17)$$

With,

- Q, the sum of the power in input for joule effect and the power in output for the bremsstrahlung and the line radiation;
- $\frac{dQ}{dt}$, total power gains/loss of the plasma column
- $\frac{dQ_j}{dt}$, Joule term;
- $\frac{dQ_b}{dt}$, bremsstrahlung term;
- $\frac{dQ_l}{dt}$, linear (or "line") loss term;
- I_{p-b}, Pease-Braginskii current;
- Z_{eff}, effective nuclear charge;

$$\frac{dQ}{dt} = \frac{dQ_j}{dt} + \frac{dQ_b}{dt} + \frac{dQ_l}{dt} \qquad (18)$$

It should be emphasized that depending on the sign of the upper equation, the thrust of the piston is respectively outwards, if the sign is positive, or inwards, if the sign is negative [Lee S., 2014]. If the terms of loss prevail, the thermonuclear plasma will collapse very quickly inwards (r_p tends to very small values very quickly), becoming opaque to radiation, and then stopping it. The equilibrium value for which the heating by joule effect and the losses for linear Radiation and Bremsstrahlung are equivalent,

is concretized in a current value called Pease-Babinski Current (1.6 MA in Deuterium). This parameter is to be considered a threshold value for achieving plasma stability. For operating gases such as Deuterium, Hydrogen, and Nitrogen, and thanks to the temperatures reached in the plasma chamber, it is correct to neglect the contribution of Line Radiation when calculating the I_{p-b}.

$$\frac{dQ_j}{dt} = \frac{dQ_b}{dt} \tag{19}$$

And by using the Bennet relation,

$$I_{p-b}^2 \propto \frac{1}{\pi b^2 Z_{eff}^2}(1 + Z_{eff})^2 \tag{20}$$

Z_{eff} is the effective nuclear charge, i.e., the charge from which an orbital electron is affected by the nucleus. For PFMA-3 operations, since the gas in the plasma chamber is almost totally ionized, it is legitimate to consider the Z_{eff} as a constant.

$$Z_{eff} = 6{,}65$$

In accordance with Slater's rules ($Z_{N2} = 7$).

The effective nuclear charge, in a poly-electronic atom, consists in the charge of which an electron, taken as a reference, is affected by the nucleus. For example, an electron that moves in the outermost orbitals, will be affected by a much lower charge than an electron that orbits closer to the nucleus, because of the shielding effect, hence also the correlation with the amplitude of the orbit (increasing as it moves away from the nucleus).

In the literature, in addition to numerical codes that plot the effective nuclear charge as the temperature changes (Corona Models, [Rashid NA., et al., 2015], Figure 18), there empirical method can be found, e.g., the Slater rules [Reed JL., 1999]. Almost total ionization of the operating gas in the plasma chamber at operating temperatures can be achieved. A gas composed of Nitrogen is completely ionized at temperatures that are corresponding to 800 eV (even if in "reality" it begins to be in a state of ionization starting from 190 eV). The kinetic temperature of the particles in the PFMA-3 is around 10^7 K, or 870 eV: due to that, it is licit to assume the total ionization of the operating gas and its relative effective nuclear charge. Slater's rules allow to calculate the effective nuclear charge starting from the overall charge of the nucleus (atomic number) and subtracting a screen factor, variable depending on which electron and which orbital for which to calculate the Z_{eff}. The procedure for calculating the effective nuclear charge for Nitrogen, in particular for the innermost orbital (1s).

From electronic configuration of Nitrogen: screen constant for each electron occupying an orbital (n-1) = 0.85; screen constant for each electron occupying the same orbital as the reference electron = 0.35;

Z_{eff} = Z-screen constant;

Z_{eff} (2p) = 7-(0,85×2)-(0,35×4) = 3,90;

Z_{eff} (1s) = 7-(1×0,35) = 6,65.
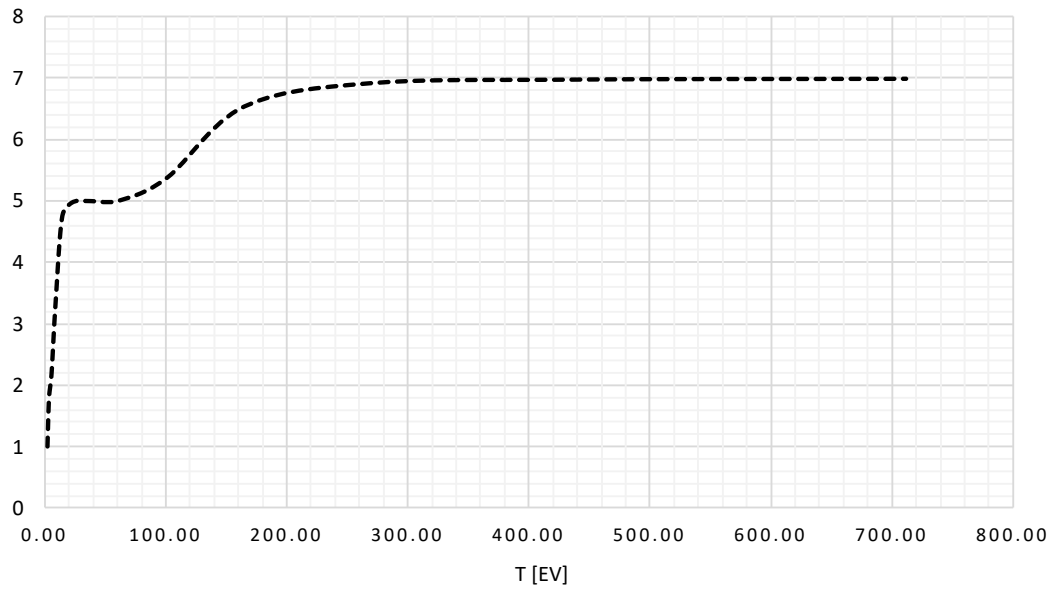
Figure 18. Z_{eff} for N_2 calculated with Corona Model.

Expanded column phase

This phase, which is not of particular relevance, follows closely the Pinch phase, and corresponds to the phase of "breaking" of the thermonuclear confinement. In fact, an observer is witnessing a sudden cooling (the Bremsstrahlung prevails) and there is a separation of the plasma structure into many small hot spots, which rapidly collapse.

Pinch and peak current calculation

For the calculation of the Peak and Pinch currents, that are, respectively, the maximum current flowing in a shot of the Plasma Focus, and the fraction of it that actually starts the Pinch phase, the Haghani S. et al., 2013 work (see the reference for details) can be followed with the following notation:

- I_{peak}, peak current;
- f, multiplier factor for pinch current calculation;
- I_{pinch}, pinch current;
- T, characteristic period of the shot measured in μs;

$$I_{peak} = \frac{\pi C V (1 + f)}{T} \tag{21}$$

With

$$f = 0{,}76 \tag{22}$$

$$I_{pinch} = 0{,}7 I_{peak} \tag{23}$$

Electrons and ions flux calculation

It is possible to estimate the extent of the flow of ions that are released in the pinch phase thanks to the Lee S. and Shaw SH., 2013 work. In this article the derivation from the Lee model described in the previous sections to equations to determine the number of ions and electrons that are released in a single shot can be found.

Assuming,

- J_b, particle flux;
- M, mass number of gas;

the flux equation can be represented as

$$J_b \propto 2,75 * 10^{15} \left(\frac{1}{(MZ_{eff})^{1/2}} \right) \left\{ \frac{\left(\ln \left(\frac{b}{r_p} \right) \right)}{r_p^2} \right\} \tag{24}$$

Once in possession of this data, other important properties of the flux can be calculated

1. Energy carried by the beam $J_b * Z_{eff} U [\text{W/m}^2]$

2. Current density $J_b * e Z_{eff} [\text{A/m}^2]$

3. Total current $J_b * e Z_{eff} * (\pi r_p^2) [\text{A}]$

4. The number of electrons, considering that the ions are completely ionized $J_b *$ 6,65 $[1/\text{m}^2\text{s}]$ [Lee S. and Saw H., 2013].

Pinch time and radius calculation

Two other important parameters are the Pinch Time and the Pinch Radius, the duration of the pinch phase and the radius of the plasma respectively [Lee S, 2003; Lee S. and Shaw SH., 2011; Haghani S. et al., 2013] .

For the calculation of pinch time in the literature there are two approaches: a purely semi-empirical one, which tends to link the duration of the pinch phase with the radius of the internal electrode ("a"), leading to a law of scale adaptable to each Plasma Focus; another approximates the duration of the pinch phase with the duration of the radial phase.

Defining,

- t_p, pinch time;
- $pinch_{radius}$, radius of the pinch;

the reference equations are:

$$t_p = 2 \times 10^{-6} \times (a), [a] \text{ m} \tag{25}$$

$$t_p = 8 \div 14 \times a, [a] \text{ cm}, [t_p] \text{ nanosec} \tag{26}$$

With

$$pinch_{radius} = 0.12 \times a \tag{27}$$

Below are presented the calculations made on the Montecuccolino device, adapting the equations previously presented [Lee S., 2014] to the operating parameters of PFMA-3, and, where possible, connecting the results with the experimental outcomes from Sumini M., et al., 2019a. See Table 6, Table 7, Table 8.

Table 6. Peak and pinch currents. Errors roughly estimated as 20%.

[kV]

				Pinch [kA]		
	Calculated	Sumini M, et al 2019a	Diff. %	Calculated	Sumini M, et al 2019a	Diff. %
12	125	122	2.4	88	85	3.4
14	146	139	4.7	102	97	4.9
16	167	155	7.1	117	108	7.6
18	188	180	4.2	132	126	4.5
20	209	197	5.7	146	138	5.4
22	230	218	5.2	161	152	5.5
24	251	232	7.5	176	162	7.9

Table 7. Axial and radial plasma propagation time.

[kV]	t_a [μs]	v_a [cm μs^{-1}]	t_r [μs]	v_r [cm μs^{-1}]
12	3.329	6.189	0.182	9.355
14	2.853	7.220	0.156	10.914
16	2.496	8.252	0.136	12.473
18	2.219	9.283	0.121	14.032
20	1.997	10.315	0.109	15.591
22	1.816	11.346	0.099	17.150
24	1.664	12.378	0.091	18.709

The Pease-Braginskii current is derived as 1.6 MA, while the pinch time and radius were $t_p = 8 \div 14 \ [ns] \times a = 18.7 \ [ns]$ and $pinch_{radius} = 0.12 \times a = 0.23 \ [cm]$ respectively.

Table 8. Ion flux, areal power, power, energy transported by electrons, electron current density, electron current, electron bunch intensities. See also Figure 13, Figure 14, Figure 15, Figure 16 for comparison.

[kV]	[ion cm^{-2} pulse^{-1}]	[W cm^{-2}]	[W]	[J]	[A cm^{-2}]	[kA]	[mC]
12	8.80E+14	2.63E+09	4.76E+08	8.91	5.02E+04	9.075	0.17
14	1.05E+15	4.11E+09	7.43E+08	13.90	5.95E+04	10.775	0.20
16	1.22E+15	5.98E+09	1.08E+09	20.25	6.97E+04	12.621	0.24
18	1.42E+15	8.28E+09	1.50E+09	28.02	8.07E+04	14.607	0.27
20	1.62E+15	1.10E+10	2.00E+09	37.37	9.23E+04	16.695	0.31
22	1.83E+15	1.43E+10	2.59E+09	48.34	1.04E+05	18.897	0.35
24	2.06E+15	1.80E+10	3.26E+09	61.02	1.17E+05	21.202	0.40

The results obtained are largely in good agreement with the measured results presented in Sumini M., et al., 2019a (see also Figure 14). It should be pointed out, however, that with regard to the fluence of ions (J_b) and for all the quantities related to it, such as the number of charges released by pulse and the energy carried by them, there is only a partial agreement (same order of magnitude and partial overlap), Figure 16. In fact, the trend that is expected at the theoretical level, based on the equations presented, would be a monotonic increase as the operating voltage rises, since its increase is realized in a higher value of the peak and pinch currents and consequently of all the quantities in relation of direct proportionality with them (J_b; number of charges; energy etc.). This does not seem to happen at the experimental level, in fact for both the quantities mentioned above, a flattening and a consequent collapse of the curve is observed, exceeding the threshold value of 14 kV. This behavior could be attributed mainly to three factors: Inductance value (L_0) too high in the current configuration of PFMA-3 (leads to a time lag between pinch phase and peak phase of the current); limits of sensitivity of measuring instruments, which beyond a certain voltage may not have a sufficient degree of reliability for the purpose, given the extremely fast time behavior of the phenomena to be investigated. While some dissonances remain, the calculations

based on the current state of the art, agree in large part with the experimental experiences, acting as partial confirmation for them.

A further experimental parametric investigation which is worth to be cited besides Sumini M., et al., 2019a is the Jain J., et al., 2021b work.

Monte Carlo photon transport simulations

A Monte Carlo study has been conducted to search an optimum configuration in terms of bremsstrahlung yield and characteristic line intensities, by testing the X-rays coming from the different measured electron spectra against different material and thickness of the metal interaction targets [Sumini M., et al., 2019b]. Even if the PFMA-3 device has already been employed as an ultra-fast source in cell culture irradiations, it is useful to get some insight into the target conversion process that switches primary electron beams into an X-ray ultra-short, pulsed source suitable for radiotherapy. This type of source should primarily be considered for superficial X-ray therapy, 10-50 keV range for skin cancer applications, or for deeper or orthovoltage X-ray therapy, up to 300 keV. An accurate investigation of various metal targets conversion performances and related processes was carried out mostly using computational models and experimental benchmarks. The X-ray spectra produced from the research provide a more in-depth understanding of the possibilities associated with future clinical application of this class of devices.

The modeling of coupled electron-photon transport via the target that closes the PF device electron extraction channel (the hollow anode) was primarily based on the use of Monte Carlo codes. Monte Carlo methods can rigorously take into account system geometry, the various types of scatterings in which electron beams are involved, coupled electron-photon transport phenomena, and accurately describe the interactions that give rise to the build-up of the photon spectrum, allowing for an efficient interpretation of experimental results. Monte Carlo codes also have limitations because they need to convert all physical models or data in the "scoring" processes with respect

to certain probability distribution functions and map any type of interaction in "collision" (for example, this is especially true for Bremsstrahlung).

However, in order to analyze and enhance the application perspectives of PF technology, the Monte Carlo codes of the MCNP family was first used to fully study the X-ray pulse generation from the interaction between the electron beam and the metal target, and then benchmark tests were also performed, whenever possible, with experimental activities.

Such work confirmed the effectiveness of the irradiation experiments performed in [Isolan L., et al., 2019] and put into evidence also the possibility of control the source for different applications (e.g., orthovoltage applications, intraoperative radiation therapy, direct electron superficial irradiations).

Experimental setup

Figure 19 shows the reference experimental setup for X-ray field characterization in terms of energy distribution and energy deposition (dose) utilized in this study: a thin metal conversion layer (50 microns brass) put at the end of the hollow anode and a stack of Gafchromic™ films on top of it.

One HDV2 and four EBT3 films composes the stack. The initial HDV2 layer is provided to halt any remaining electron following the beam-target conversion, assisting in the formation of an electronic equilibrium situation.

Following irradiation, the films were scanned with a scanner (Epson Perfection V370 PHOTO) in accordance with the Picodose™ sw's specifications, and the grey levels were assessed using a calibration curve modified from the one used by the BALTEAU CSC320/70 X-ray equipment.

The grey levels of the fourth EBT3 were used to assess the impact on tissue or cell culture irradiations, using a well-established approach that has proved to be extremely successful [Ceccolini E., et al., 2012; Sumini M., et al., 2017; Buontempo F., et al., 2018]. The first three EBT3 just block the lower energy region of the spectrum, useless for clinical applications needs. Furthermore, the effects of source anisotropy due to electron electrostatic repulsion, electron scattering, and bremsstrahlung emission on the X-ray distribution induced by the same 50-micron brass target were tested experimentally by evaluating the grey level on a Gafchromic™ film, as shown also in Figure 19 and studied with the Figure 19 (below) setup [Sumini M., et al., 2019b].
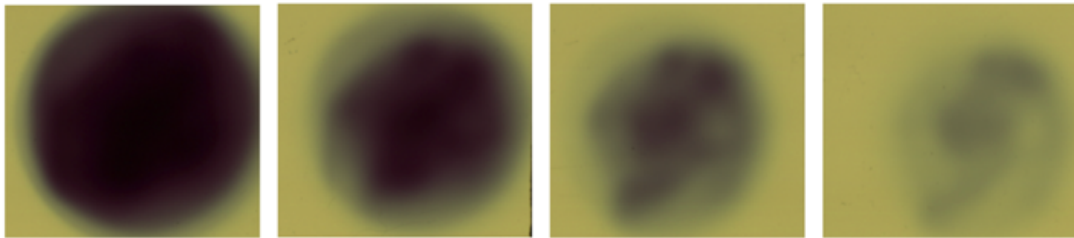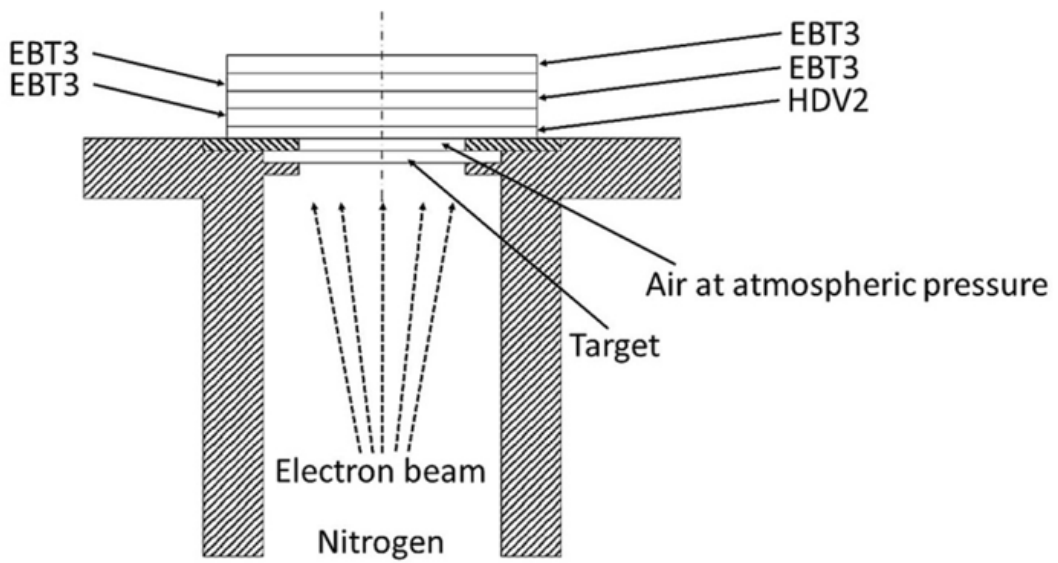
Figure 19. Above, experimental setup for the X-ray field characterization. The same geometry has been implemented as input for the MC codes. [Sumini M., et al., 2019b]. Center, example of PFMA-3 X-ray pulse effects on a stack of EBT3. HDV2 not shown. Below, left, rendering of the experimental setup with the XRQA2 Gafchromic™ films (the green cylinder coaxial with the hollow anode) for anisotropy emission evaluation. Below, center, experimental application of the setup. Below, right, example of PFMA-3 pulse effects.

Monte Carlo simulations setup

The analyses of the components have been based on a series of simulations using the Monte Carlo MCNPX/6 codes. The electron beam passed through the hollow anode and the target and then the Gafchromic™ film stack was positioned to evaluate the intensity and spectrum of the X-ray pulse. The models taken into account the effective geometry of the hollow anode cavity, the internal environment (i.e., the low-pressure gas content, currently nitrogen, the experimental measured electron spectra as born as point source at the pinch position but letting the repulsive effects playing their role while running toward the target), the targets and the layers of the films. The electron spectra used for the MCNP primary particle's source are the ones which have been measured with the magnetic spectrometer and are detailed in Appendix B [Sumini M., et al., 2019b].

An example of an MCNP input is reported as follow:

```
MCNPX
c
10 101 -7.85 -10 11 -12 20 imp:p=1 imp:e=1 $ extraction channel external cilinder
20 200 -6e-007 -20 11 -30 imp:p=1 imp:e=1 $ extraction channel inner cilinder
300 100 -8.73 -20 30 -12 imp:p=1 imp:e=1 $ brass target
40 101 -7.85 20 -10 -40 12 imp:p=1 imp:e=1 $ drift tube
81 500 -1.2 -601 imp:p=1 imp:e=1 $ HDV2 active layer
82 6 -1.35 -501 imp:p=1 imp:e=1 $ clear polyester
90 6 -1.35 -701 imp:p=1 imp:e=1 $ 1 EBT3 polyester overlaminate
92 500 -1.2 -702 imp:p=1 imp:e=1 $ 1 EBT3 active layer
93 6 -1.35 -703 imp:p=1 imp:e=1 $ 1 EBT3 polyester substrate
94 6 -1.35 -801 imp:p=1 imp:e=1 $ 2 EBT3 polyester overlaminate
96 500 -1.2 -802 imp:p=1 imp:e=1 $ 2 EBT3 active layer
97 6 -1.35 -803 imp:p=1 imp:e=1 $ 2 EBT3 polyester substrate
98 6 -1.35 -901 imp:p=1 imp:e=1 $ 3 EBT3 polyester overlaminate
99 500 -1.2 -902 imp:p=1 imp:e=1 $ 3 EBT3 active layer
100 6 -1.35 -903 imp:p=1 imp:e=1 $ 3 EBT3 polyester overlaminate
101 6 -1.35 -904 imp:p=1 imp:e=1 $ 4 EBT3 polyester overlaminate
102 500 -1.2 -905 imp:p=1 imp:e=1 $ 4 EBT3 active layer
103 6 -1.35 -906 imp:p=1 imp:e=1 4 EBT3 polyester overlaminate
30 0 2000:4000:6000:-1000:-3000:-5000 $ rest of the world
imp:p=0 imp:e=0
27 4 -0.001225 -2000 -4000 -6000 1000 3000 5000
(10:-11:12:-20) (20:-11:30)(20:-30:12)
(-20:10:40:-12) 501 601 701 702 703 801
802 803 901 902 903 904 905 906
imp:p=1 imp:e=1

1000 pz -200 $ world surface 1
2000 pz 200 $ world surface 2
3000 px -200 $ world surface 3
4000 px 200 $ world surface 4
5000 py -200 $ world surface 5
6000 py 200 $ world surface 6
```

```
10 1 cz 2.75 $ ext cylinder 1
11 1 pz 0 $ ext cylinder 2
12 1 pz 29.995 $ ext cylinder 2
20 1 cz 1.75 $ inner cylinder
30 1 pz 29.795 $ brass
40 1 pz 30.1 $ external air
501 1 rcc 0 0 30.1 0 0 0.0097 1.75 $ hdv2
601 1 rcc 0 0 30.1097 0 0 0.0008 1.75 $ hdv2
c EBT3 1
701 1 rcc 0 0 30.1105 0 0 0.0125 1.75
702 1 rcc 0 0 30.123 0 0 0.003 1.75
703 1 rcc 0 0 30.126 0 0 0.0125 1.75
c EBT3 2
801 1 rcc 0 0 30.1385 0 0 0.0125 1.75
802 1 rcc 0 0 30.151 0 0 0.003 1.75
803 1 rcc 0 0 30.154 0 0 0.0125 1.75
c EBT3 3
901 1 rcc 0 0 30.1665 0 0 0.0125 1.75
902 1 rcc 0 0 30.179 0 0 0.003 1.75
903 1 rcc 0 0 30.182 0 0 0.0125 1.75
c EBT3 4
904 1 rcc 0 0 30.1945 0 0 0.0125 1.75
905 1 rcc 0 0 30.207 0 0 0.003 1.75
906 1 rcc 0 0 30.21 0 0 0.0125 1.75

mode p e
*tr1 3.70 36.02 3 0 -90 -90 90 -90 0 -90 180 90
m4 7014.  -0.755636 8016.  -0.231475 18036.  -3.9e-005 18038.  -8e-006 18040.  -0.012842
m6 1000. 0.042 6000. 0.625 8000. 0.333
m7 1000. 0.094 6000. 0.651 8000. 0.255
m8 1000. 0.058 3000. 0.063 6000. 0.31 8000. 0.25 17000.   0.319
m100 29000.  -0.873 30000.  -0.12636 82000.  -0.00013 26000.  -0.0001 50000.  -0.00019 28000.  -0.00022 cond=1
m101 6000.  -0.004 25000.  -0.007 28000.  -0.0185 24000.  -0.008 42000.  -0.0025 26000.  -0.96 cond=1
m200 7000.  -1
m500 1000. 0.0978 3000. 0.009 6000. 0.587 7000. 0.0023 8000. 0.28 17000. 0.0175 19000. 0.0064
m256 1001.70c -0.143711 6000.70c -0.856289
c point source collimated into a cone of directions
SDEF PAR=E POS=0 0 0.00001 ERG=d1 VEC=0 0 1 DIR=d2 tr=1
c 18kV. 0.40 mbar electron spectrum
SI1 H 0.0 0.001666215 0.003330301 0.005557767 0.008341365 0.01167221
0.015539918 0.019932758 0.024837815 0.030241166 0.036128049 0.042483037
0.049290204 0.05653328 0.0641958 0.072261235 0.080713111 0.089535113
0.098711176 0.108225563 0.118062923 0.128208346 0.138647401 0.149366164
0.160351238 0.171589769 0.183069443 0.194778497 0.206705703 0.218840368
0.231172317 0.243691879 0.256389872 0.269257586 0.282286762 0.295469575
0.308798615 0.322266864 0.33586768 0.349594781 0.363442217 0.377404363
0.391475895 0.405651776 0.419927239 0.434297773 0.448759108 0.4633072
0.477938221
SP1 D 0.0 0.000819264 0.001039449 0.001771819 0.003519915 0.006790837
0.012589299 0.021726343 0.033174865 0.047102135 0.06095618 0.07439011
0.085498104 0.093449356 0.096708236 0.093085515 0.08405791 0.071727853
0.051528656 0.038864276 0.026202965 0.019598106 0.014401901 0.012310938
0.006588478 0.005493746 0.003898457 0.002462713 0.001088948 0.001016361
0.000731442 0.001147593 0.000825655 0.000746456 0.000792488 0.000724493
0.000708664 0.000850311 0.000712512 0.000833465 0.001289263 0.001967439
0.002239212 0.002306559 0.002035783 0.002455918 0.002594487 0.002966854
0.002208674
SI2 A 0.998 1      $ source information
SP2   1    1      $ source probabilities
bbrem 1. 1. 46I 100. 100
f4:p 82 $ 92 96 97
e4:p 0.001 36i 0.37
nps 100000000
```

The thin layer of air between the target and the first film has also been considered in the simulations (see Figure19). The physics of the transport process from the target to the film, through the target and through the film was considered without biases (to avoid a "forced" score, that would compromise the physical interpretation of the results), besides bremsstrahlung enhancement with respect to photon production in the high energy portion of the electron spectrum. A purely analog simulation requires a higher number of particle's histories to fill the scores, but, even with some limits, at least in

principles, should be free from the risk of unphysical outcomes. As source for the simulations, the spectra obtained in the electron stream characterizations were considered for several power supply values, nitrogen pressure, and different targets [Sumini M., et al., 2019b].

With respect to the specific code used in the simulations, the MODE card, for the choice of the transported particles, has been set to consider both photons and electrons, with a cut-off energy of 1 keV. The bremsstrahlung effect has been enhanced by using the MCNP BBREM card, which allowed a gradual increase in the photon production as the electron energy increases.

This causes electrons/bremsstrahlung conversion to be generated, but it creates a cost in terms of computational load. The results of the calculation were obtained with the default values for the electron transport physics (PHYS CARD) into the target:

- the electron production by photons has been turned on;

- the photon production by electrons has been turned on;

- the full bremsstrahlung tabular angular distribution has been performed;

- the sampled straggling for electron energy loss has been used;

- the analog number of bremmstrahlung photons has been maintained;

- the analog production of electron-induced x-rays has been set;

- the analog number of knock-on electrons productions has been used;

- the analog number of photon-induced secondary electrons has been set).

The Figure Of Merit (FOM) of all these simulations has proven to be stable around the values reported in the Table 9 and Table 10, indicating that an increase of the number of particle's histories would not add more information as the Relative Error (RE) was

well below to the suggested values for considering the results as "reliable" (0.1). The relative error gives a measure of the score distribution variance around the estimated average value.

Table 9. Typical MCNPX code running parameters for photon spectrum calculation tallied (tally F4, average flux on a cell) on lower part of the lowest layer of the HDV2 film. The relative error is <0.05 suggested threshold. [Sumini M., et al., 2019b].

	Brass	W	Brass-Pb
# of histories	1.0E+08	1.0E+08	1.0E+08
Tally type	F4	F4	F4
Relative error	<2.0E-02	<6.0E-03	<5.0E-02
# of collisions	1.2E+11	2.2E+11	1.6E+12
FOM	12	26	11
Computer time [CPU h]	22	48	30

Table 10. Typical MCNP6 code running parameters for photon dose calculation tallied (tally F6, average energy deposition on a cell) on the fourth EBT3 film central active layer. [Sumini M., et al., 2019b].

	Brass	W	Brass-Pb
# of histories	1.5E+07	1.5E+07	1.5E+07
Tally type	F6	F6	F6
Relative error	<4.0E-02	<4.5E-02	<5.0E-02
# of collisions	1.81E+10	3.35E+10	2.67E+10
FOM	9.72	5.23	2.14
Computer time [CPU h]	2.85	5.16	4.92

The MCNP F4 and F6 tallies were used for reaction rates and energy deposition. The F4 is the track-length estimate of a cell flux (the average particle flux in the cell); the F6 is the "track-length flux" (F4, with one bin for the whole energy range) adapted to evaluate reaction rate with an energy-dependent heating function instead of a flux. It was intended to be used with just one energetic bin for the whole dose estimations. The F4 spectra estimations required the definition of an accurate energy grid, where the cutoff energy and 370 keV were sampled with 74 bins 5 keV each. Reference sets of typical parameters for the Monte Carlo runs for the energy spectrum determination and

for dose calculation are summarized in Table 9 and Table 10 for three different target materials, brass, 50 μm, W, 50 μm, and a blend of brass and lead (brass, 25 μm, plus Pb, 27 μm thick: brass first because Pb changes status at 327 °C, and, given the high intensity of the electron pulses, 0.2 mC it should protect the target form potential harmful high temperature spots) to see the effect on the bremsstrahlung emission spectrum. The electron spectral distributions, as recorded with the magnetic spectrometer have been used as source according to the following parameters: power supply, nitrogen pressure (producing a different electron source spectrum), target composition (for now tungsten, brass, brass+lead). The model for the brass target, 18 kV capacitor charge and 0.4 mbar nitrogen pressure, has been benchmarked with experimental results. Furthermore, the effects on the X-ray source induced by the anisotropy of the source due to the electron electrostatic repulsion, electron scattering and bremsstrahlung emission have been checked experimentally through a proper film setup, evaluating the grey level of a Gafchromic™ film [Sumini M., et al., 2019b].

The results of the MC simulations are discussed with respect to the evaluated X-ray energy spectra for tungsten, lead+brass and brass targets for different power supply and pressure (the latter at 18 kV) [Sumini M., et al., 2019b]. For tungsten, the more relevant answer is related to the dominance of the characteristic line, that makes less important other interaction effects like bremsstrahlung emission. The first ones, shown in Figure 20, were obtained from MCNPX simulations at a constant nitrogen pressure of 0.40 mbar for the W spectrum. The effects of the power supply could become of some interest only with respect to the emission in the 10-50 keV range, useful for superficial X-ray applications. In Figure 21 are shown the results of MC simulations for a W target, at different pressures for nitrogen, all with respect to the reference power source of 18 kV. The dominant feature of the X-ray emission remains the W line.
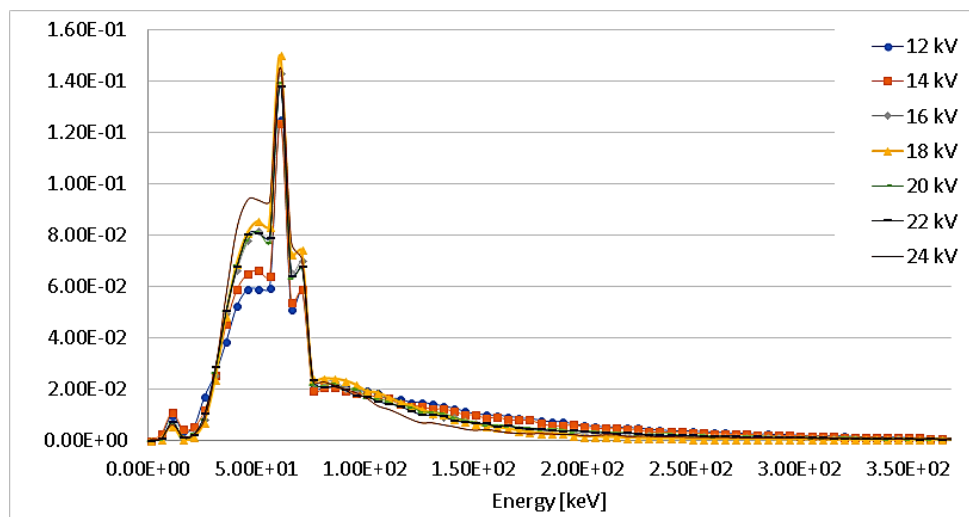
Figure 20. MC simulation of X-ray energy spectra exiting from the tungsten (W) target, 50 μm thick. Constant Nitrogen PF chamber pressure of 0.4 mbar, for different power supply values. [Sumini M., et al., 2019b].
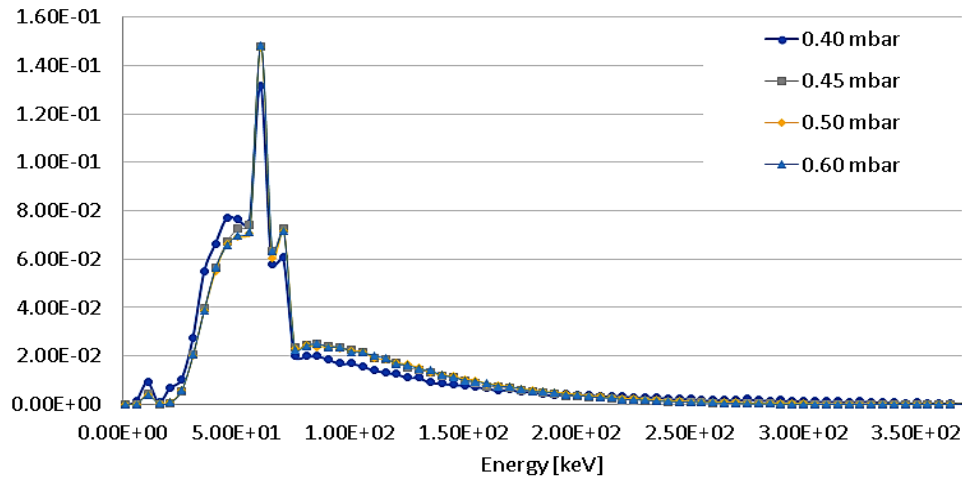
Figure 21. MC evaluation of X-ray energy spectrum as a function of different PF chamber pressures. W target, 50 μm thick, 18 kV. [Sumini M., et al., 2019b].

The MC simulations of the X-ray energy spectrum for a composite target at the same reference chamber pressure as a function of different power supply levels are shown in Figure 22. Even at a high-Z target like lead, the X-ray spectrum is quite smooth. It's clear that the peak related to brass (Cu-Zn) line near 10 keV. The beam's bremsstrahlung component becomes more relevant. The same type of analysis is performed on the simulation results for the electron source with the spectrum at various pressures, as shown in Figure 23.
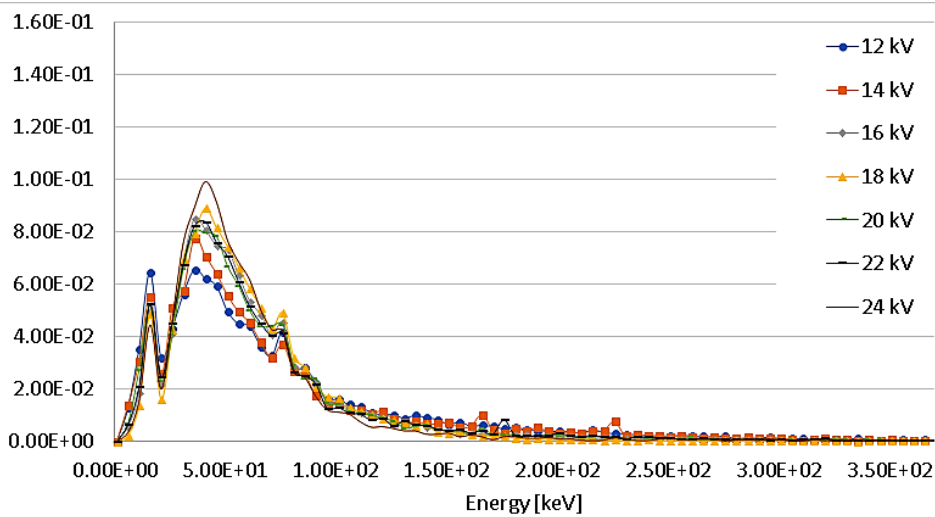
Figure 22. MC simulation of X-ray energy spectrum with a Pb-brass layered target (Pb 27 μm, brass 25 μm), 0.40 mbar constant pressure as a function of different power supply levels. [Sumini M., et al., 2019b].
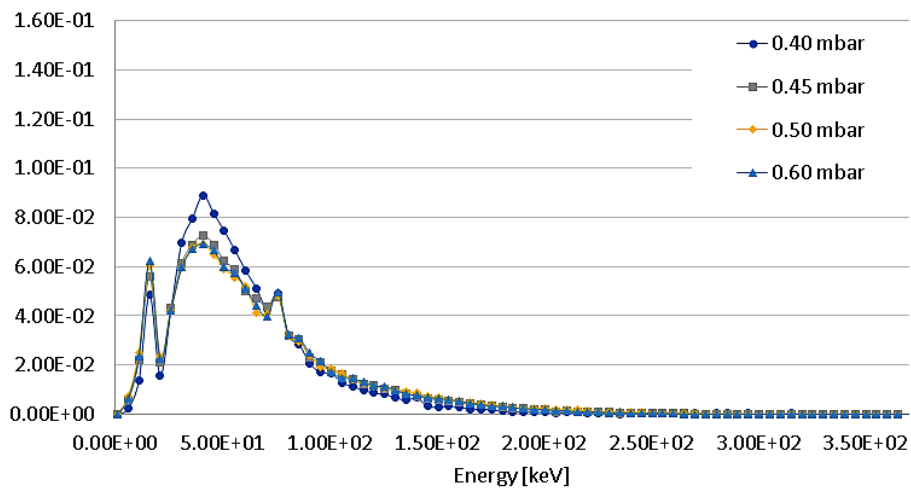
Figure 23. MC simulation of X-ray energy spectrum with a Pb-brass layered target (Pb 27 μm, brass 25 μm), as a function of the PF chamber Nitrogen pressures. [Sumini M., et al., 2019b].

The X-ray spectrum is just a little less peaked because of the less peaked electron spectrum.

The spectra of the beam that was simulated as it interacted with a brass target are shown in Figure 24. This target has the worth of quite strong separation between the Cu-Zn characteristic lines and the bremsstrahlung component of the resulting X-ray spectrum. This spectrum is of interest for surface clinical applications and also for deep X-ray therapy because of its relevant tail running up 200 keV and more. The X-ray device in this study is one of the first in the history of X-ray experimentation in this country, and it is one that has a good equivalence with the spectrum of classical X-ray devices.

The results for the brass target at different pressures are presented in Figure 25. The flattened spectrum of the incoming electron source makes the bremsstrahlung high energy contribution more relevant and useful for deep X-ray therapy.
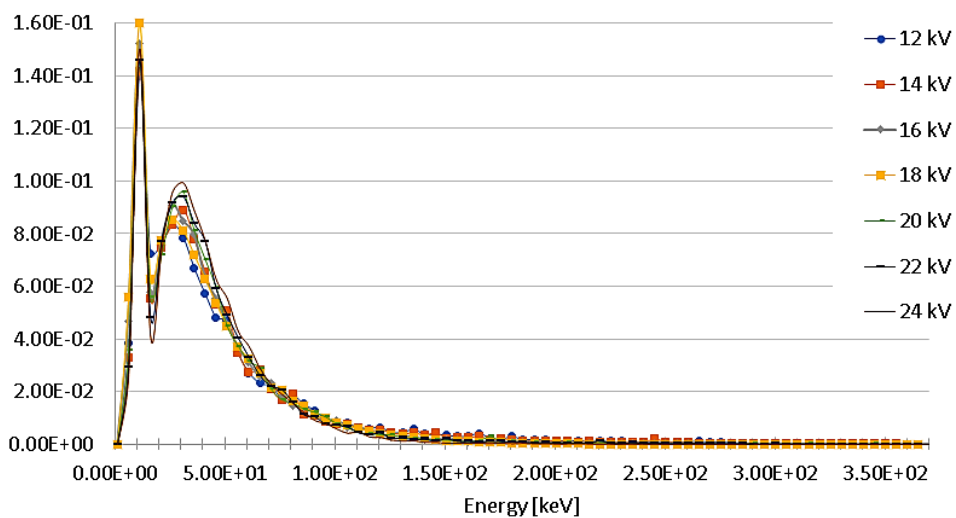
Figure 24. MC simulation of X-ray energy spectra for a brass target as a function of different power supply. [Sumini M., et al., 2019b].
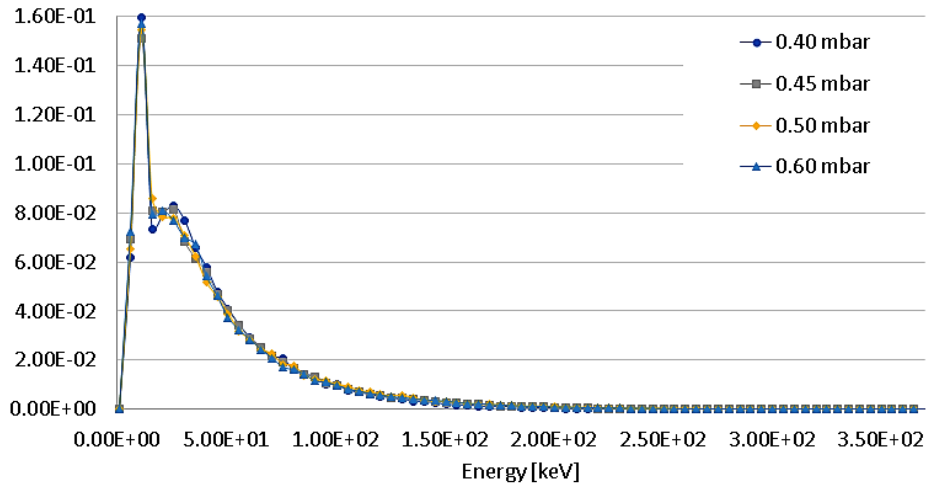
Figure 25. X-ray spectra for a brass target at varying pressure, MC simulations. [Sumini M., et al., 2019b].

Experimental benchmarks

The simulation results were benchmarked with the outcomes of the experiments with the brass target, and the experiments have been fully validated testing the device at 18 kV and 0.40 mbar. The brass target is the most monochromatic, whereas the layered Pb-brass target is probably the most valid target. Moreover, the spectral "anomalies" from the fact that each experimentally evaluated electron source spectrum is a sort of "average" of the outcome of several PF pulses should be considered (and this has a broadening effect on the simulated X-ray spectrum, in particular at higher energies). Each single pulse (not an "averaged" one) can be assumed to produce a cleaner X-ray spectrum but, looking at the effective irradiation process, the "averaged" one gives a coherent picture of the phenomenon, due to the fact that the final delivered dose will be the results of several PF pulses. As far as the dose deposition analysis on the stack of Gafchromic™ films is concerned, at the PFMA-3 the tests relied on the biological tissues equivalence of this kind of detectors. Moreover, the dose associated to the energy deposition on the fourth film (considering the effect of the lower part of the stack as a filtering device) was considered as an acceptable evaluation of the dose transferable in possible irradiation applications. The results of the different doses on the different Gafchromic™ layers are shown in Figure 26. Schematically, the brass target produces a higher dose of radiation in the fourth film. This gives us a quantitative indication of the dose that could be absorbed into cells. The Figure 27 shows the angular distribution of energy deposition from the electron-target (brass) interaction with X-ray pulses of 18 kV and 0.4 mbar as the nitrogen pressure in the PF chamber (see also Figure 20). The X-ray emission pattern is nearly isotropic, as expected for the bremsstrahlung component for brass.
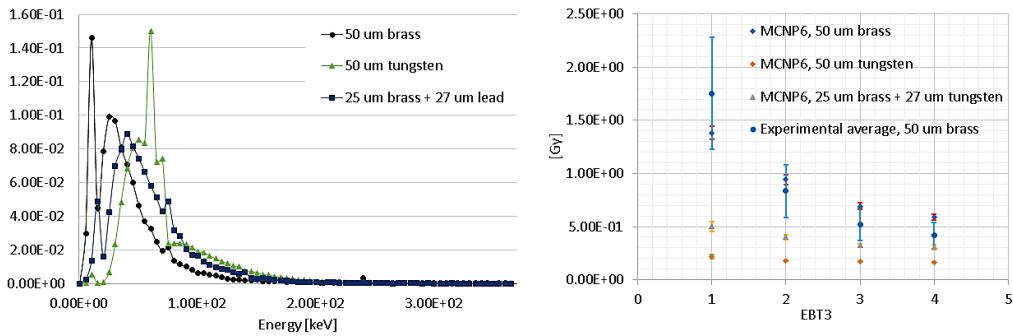
Figure 26. a) MC simulation of X-ray spectra comparison between target conversion models at the reference power supply level, 18 kV, and 0.4 mbar Nitrogen pressure. b) Dose delivered on the four EBT3 films, MC simulations and experimental data (brass only). Uncertainties coming from experiments (due to the small stochastic fluctuations that affect the behavior of the plasma discharges also partially due to the fact that the PFMA-3 is a device still not optimized, the dose delivered in each pulse is slightly variable – moreover, the EBT3 sensitivity has an intrinsic uncertainty of the order of 3%) for brass target and from the MC simulations convergence for the others. [Sumini M., et al., 2019b].
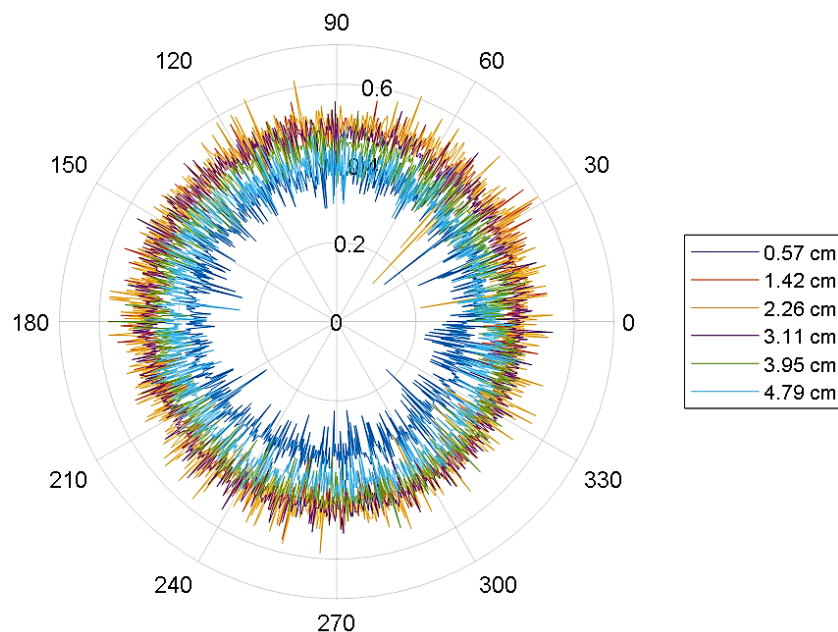
Figure 27. Angular distribution of the energy deposition due to the X-ray pulses, recorded through a Gafchromic™ XRQA2 film. The different colors are related to the distance from the target plane [Sumini M., et al., 2019b].

Punctual dose measurements in PMMA phantoms and MCNP benchmark with numerical optimization and acceleration through adjoint importance functions and CADIS approach

Then, a deep Monte Carlo study of the device from the X-ray field managing point of view has been performed for planning very precise irradiations taking also into account different Variance Reduction Techniques (VRT) such as adjoint importance function implementation, Weight Windows (WW) and solutions based on discrete models with the Consistent Adjoint Driven Importance Sampling (CADIS) [Peplow DE., et al., 2012] approach for a strong simulation acceleration and particle transport optimization, as stated in Isolan L., et al., 2020. In particular, looking at clinical applications, the requirements were to have an upgrade respect the cell's irradiation passing through an animal model [Isolan L., et al., 2019] and, with that aim in mind, starting from a micro-tomography of a mouse to simulate an immune-depressed nude mice with an implanted human melanoma (xeno-graphs), a 3D highly differentiated Monte Carlo Unstructured Mesh model has been built from DICOM data [Isolan L., et al., 2019]: the dose irradiation patterns were obtained, comparing also the results with a PMMA [McConn Jr., et al., 2011] phantom built ad-hoc in laboratory (to mimic the mouse geometry). The phantom was composed by different PMMA slabs filled with Termo-Luminescent Dosimeters (TLDs) and micro-silica Trueinvivo© dosimeters [Isolan L., et al., 2019] as already shown in Figure 4. The results between experiments and Monte Carlo estimations were in good agreement but one serious issue to be solved was the poor convergence (low FOM) of the radiation transport simulations. The issue emerged not only due to the highly complex geometry, but also for the large dimension of the particle field/source respect to the small dimension of the dosimeters (e.g., source of 35 mm of

diameter against 1 mm for the Trueinvivo© dosimeters, also far or decentered to the particle beam axis and "shielded" by the model parts, the PMMA slabs). To optimize the simulation processes with the goal to implement procedure aiming at a quasi-routinely irradiation plan, an investigation on the reliability of the extended application of the adjoint weighting approach to photon transport modeling has been set. As reported in Isolan L., et al., 2020, the solution of the adjoint transport problem has been recognized, as usual, as the "importance function", in the sense of the potential contribution of the detector reading (or response), as explicitly stated by Lewins J., 1965 and comprehensively described by Hoogenboom JE., 1977 and one of its most common applications was historically in Monte Carlo calculations for reactor physics. Alternatively, considering photons, a Monte Carlo bias scheme based on the adjoint weighting approach was exploited to speed up the simulation by De Matteis A. and Simonini R. 1978. The Authors found positive gains in terms of computer time, in particular when estimating the gamma fluence rate at a point from a flat and spatially extended source (as in the case of the PFMA-3 against Trueinvivo© dosimeters). In Drumm CR., et al., 1991, forward and adjoint methods related to Boltzmann's equation were used to determine solutions to increase the yield of bremsstrahlung X-ray FLASH equipment, as in the PFMA-3 field of application, taking into account a deterministic method of coupling of the electron-photon transport problem. In addition, Lawrence LJ., et al. 1995 used adjoint methods to solve Boltzmann-Fokker-Plank equations in different geometries and claimed that compared with traditional techniques, "inverse world" may be the only practical method to obtain solutions (as also in Hoogenboom JE., 1977). About the adjoint transport of photons, Hoogenboom JE., et al., 2000 extended the well-known theory of continuous Monte Carlo adjoint neutrons theory by considering the photoelectric effect and Compton interactions in a similar way to

neutron capture and scattering (for the latter, by deriving in analytical way the adjoint cross sections by starting from the Klein-Nishima function [Klein O. and Nishina Y., 1929]). Finally, it was possible to manage the production of pair, proving the effectiveness of the method also in such applications. In connection with previous considerations, has been considered the full Monte Carlo adjoint transport approach [Wagner JC., et al., 1994], based primarily on the multi-group (MG) version of the MCNP5 code. For the purposes to be investigated in the PFMA-3 project, given the geometry of the PMMA phantom composed by slabs, MCNP5 turned out to be faster and simpler compared to the newest versions of the X and 6/6.1.1 codes on the basis on different tests performed on the codes. See the Isolan L., et al., 2020 and reference therein for further details.

The simulation path is as follows:

- a dose-response curve for TLDs was obtained as a consequence of an experimental PFMA-3 irradiation campaign, performed to evaluate the behavior of glass bead dosimeters and photon-absorbed doses at different locations and depth in the phantom of PMMA slabs (Figure 4);

- the experimental results were estimated by MCNP simulation for validation;

- a pure backward (reverse/inverse) transport was set to estimate the fluxes, perform a sensitivity analysis of the response of the dosimeters against radiation spectrum and investigate the particle collision distribution;

- the inversion procedure, from the real (forward) word to the reversed one, was further validated by considering the overall flux and the flux as a function of the scattering's order;

- the adjoint functions estimated by the backward simulations were "fed" into a new forward computation to obtain a physically biased model characterized with high performances and therefore suitable for fast and accurate simulations toward clinical applications;

- moreover, conclusively, the analysis of weight windows (WW) [Hoogenboom JE. and Legrady D., 2005] obtained with MCNP (WW on model cells and superimposed mesh) and with the application of ADVANTG CADIS (Driven Consistent Sampling) has been performed [Mosher SW., et al., 2015; Wagner JC., et al., 2009] (which is based on a discrete ordinate particle transport techniques applied to the same Monte Carlo geometry - Variance Reduction Techniques, VRT, to improve transport toward deeper and farther micro-silica bead in PMMA).

The results were compared in terms of simulation performances finding that with this approach, a quasi-routinely irradiation plan for patients could be set.

The adjoint method

In the Isolan L., et al., 2020 (and references therein) work, the adjoint method is described and here reported. The Authors reported that, as it is well known, a radiation flux can be determined by solving the forward transport Boltzmann equation. The semi-analytical solution for the photon problem, based on an order of scattering approach, was explained by Fernandez JE., et al., 1989 as a good opportunity for finding an easily extendable and generalized solution for specific interaction models and geometries. Fernandez JE. and Sumini M., 1992   showed that the adjoint formulation of the transport problem for Compton scattering could allow taking into account the characteristics of a detector when an extremely detailed answer is necessary. In the Fernandez JE., et al., (2012) work, as already recalled in Isolan L., et al., 2020, an X-ray spectrum can be obtained by applying the inverse techniques for particle transport, starting from a scattered radiation as measured by a detector. Such work demonstrated the capability of the adjoint method in experimental situations. The Authors determined a usefulness for X-ray spectra evaluations for quality control of the beams for medical or industrial apparatuses, concept easily expandable also to the actual research field.

The well-known photon transport equation, as recalled in the previous literature works [Isolan L., et al., 2020], can be easily written considering

- $f(\boldsymbol{r}, \boldsymbol{\omega}, \lambda)$, angular photon flux;
- $\boldsymbol{\omega}$, direction of flight;
- $\boldsymbol{r}$, position;
- λ, wavelength;
- k, interaction kernel;
- q, particle source distribution

$$\boldsymbol{\omega} \cdot \nabla f(\boldsymbol{r}, \boldsymbol{\omega}, \lambda) + \mu(\lambda) f(\boldsymbol{r}, \boldsymbol{\omega}, \lambda)$$

$$- \int_0^{+\infty} d\lambda' \int_{4\pi} d\overrightarrow{\boldsymbol{\omega}}' k(\boldsymbol{\omega}', \lambda' \to \boldsymbol{\omega}, \lambda) f(\boldsymbol{r}, \boldsymbol{\omega}', \lambda') = q \qquad (28)$$

Assuming

- $\hat{L}$, forward integro-differential operator,

the transport equation can be re-written as

$$\hat{L} f = q \quad (29)$$

With the same philosophy, the adjoint transport equation, for photons, can be obtained

in terms of

- f^+, the adjoint angular flux which has the physical significance of "importance function" of a given particle source [Lewins J., 1965];
- $\hat{L}^+$ is the adjoint integrodifferential operator;
- q^+ is the adjoint source (or the "detector response");

$$\hat{L}^+ f^+ = q^+ \quad (30)$$

$$\hat{L}^+ = \boldsymbol{\omega} \cdot \nabla + \mu(\lambda) - \int_0^{+\infty} d\lambda' \int_{4\pi} d\boldsymbol{\omega}' k(\boldsymbol{\omega}, \lambda, \to \boldsymbol{\omega}', \lambda') \quad (31)$$

Given that the integral of f and g over the 6-dimension phase-space variables represent

the inner product definition

$$(f, g) = \int_V d\boldsymbol{r} \int_0^{+\infty} d\lambda \int_{4\pi} d\boldsymbol{\omega} \, f(\boldsymbol{r}, \boldsymbol{\omega}, \lambda) g(\boldsymbol{r}, \boldsymbol{\omega}, \lambda) \quad (32)$$

the direct and the adjoint integro-differential operators satisfy the condition

$$(\hat{L}f, f^+) = (f, \hat{L}^+ f^+) \quad (33)$$

And, due to the $\hat{L}f = q$ and $\hat{L}^+ f^+ = q^+$ relationship it can be derived that

$$(f^+, q) = (f, q^+) \quad (34)$$

where it is shown that the photons from the particle source weighted by the solution from the adjoint problem is equal to the forward photon flux weighted by the adjoint source (the detector's characteristics). It can be recalled also that the final and initial states in the interaction kernel have been exchanged, e.g. $(\boldsymbol{\omega}', \lambda' \to \boldsymbol{\omega}, \lambda)$ is replaced by $(\boldsymbol{\omega}, \lambda, \to \boldsymbol{\omega}', \lambda')$. Adjoint transport can be simulated by Monte Carlo codes to improve computational efficiency, mainly focusing on the importance of particles. This turned out to be useful because the direct VRT based on WW often fails to fill the energy, space and time intervals due to the statistical nature of the method [Booth TE., et al., 2003]. In the Solomon CJ., et al., 2009 work, it is declared that if a proper variance reduction is applied to the model, usually the importance and the weight of a transported particle vary one inversely to the other (see also Isolan L., et al., 2020). Continuing to follow what is reported in the Isolan L., et al., 2020 work, in MC simulations of particle transport, the weight of a particle increases or decreases as it moves closer to or far from the source, given the appropriate VRT. On the other hand, it becomes more important if the particles are transported closer and contribute to the tally. It has long been known that "useful" importance does not necessarily depend on the full range of each variable throughout the phase-space, but a subset of them can be a good compromise. For example, the "average" importance in a spatial region can be defined by a weighting by particle density. This is the idea behind the WW statistical method, which is a Monte Carlo technique that evaluate scores generated by particles that fall into part of a domain and estimates their importance by considering the weight of each

particle that contributes to it (in a tallying process). For example, for an integrated particle current (F1 tally) on a surface, the code indicates the number of particles that cross the surface as an output (see Booth TE., et al., 2003 for F1 tally details). This means that the F1 tally estimates correspond to the particle weight calculation, which is also strictly related to the importance. Each other's tallies are similarly linked to importance. In a forward Monte Carlo simulation, the particles are emitted from the source, transported through the geometry, and contribute to the tally (which can be changed by the response function). A so-called detector-tally response R, when defining S as the domain part, can be stated [Sheu RJ., et al., 2005] as:

$$R =$$

$$\int_S \int_{4\pi} \int_0^{+\infty} R(\boldsymbol{r}, \boldsymbol{\omega}, E) f(\boldsymbol{r}, \boldsymbol{\omega}, E) \, dE \, d\boldsymbol{\omega} \, d\boldsymbol{r}_S = \qquad (35)$$

$$\int_S \int_{4\pi} \int_0^{+\infty} q(\boldsymbol{r}, \boldsymbol{\omega}, E) f^+(\boldsymbol{r}, \boldsymbol{\omega}, E) \, dE \, d\boldsymbol{\omega} \, d\boldsymbol{r}_S$$

On the contrary, in adjoint calculations, particles are backscattered from the tally cell to the source in space and time, which means that the source of the adjoint simulation is located at the detector position and defined by the forward response function, and the adjoint detector position is in the forward source coordinates. See Figure 28.
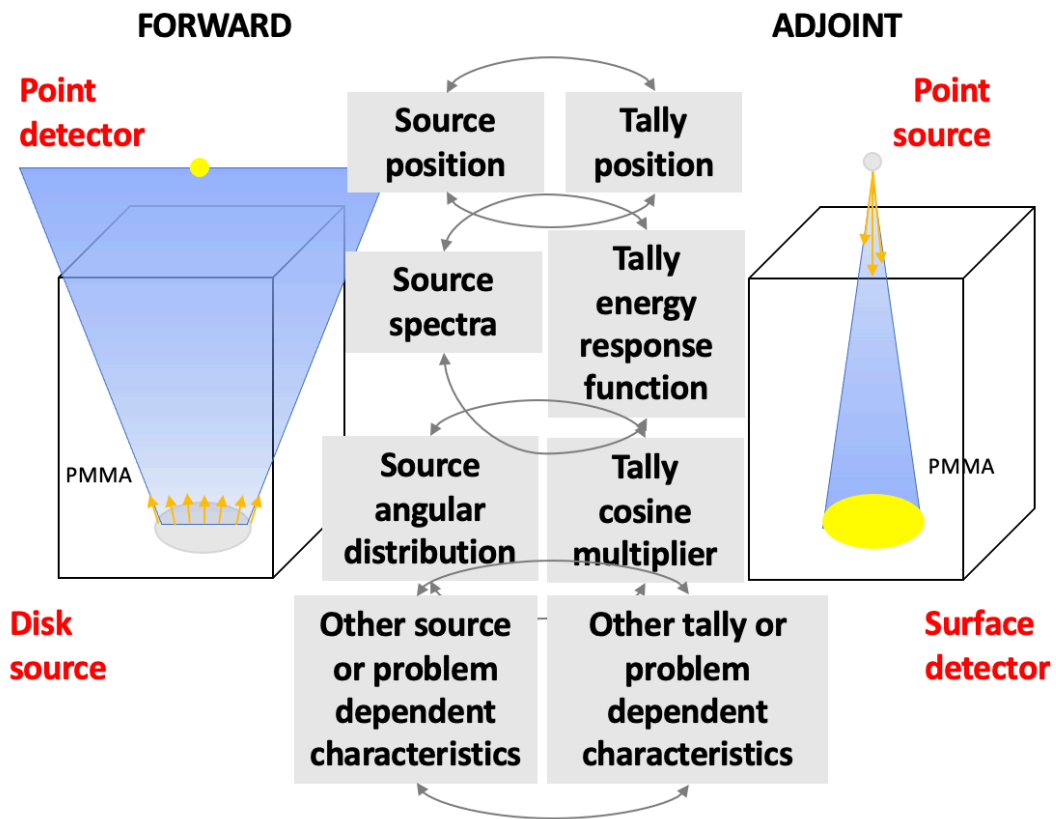
Figure 28. Forward and Adjoint strategies.

Micro-silica beads in PMMA phantom setup

In the Trueinvivo© Microsilica Beads, the thermoluminescent material is silicon oxide, suitable for a variety of applications such as medical physics, research, industrial dosimetry, X, γ, β, protons and neutrons. Dosimeters are characterized by 1 mm spatial resolution, linear response over a wide dose range, and dose rate and field orientation independence. In addition, microsilica beads are non-hygroscopic and inert and can be used in extreme temperature and humidity conditions, making them suitable for in vivo / liquid situations. Dosimeters were introduced in the PMMA phantom, which consists of various slabs. The microsilica beads had central axis depths of 3 mm, 6 mm, 9 mm, 12 mm, and 20 mm [Isolan L., et al., 2020]. See Figure 29. The TLDs were also hosted in other positions outside the central axis (positions B and C, Figure 29) in the PMMA, but in the same depths as positions A. The TLDs were read by the ENEA Radiation Protection Institute thanks to a semi-automatic reader from TOLEDO.
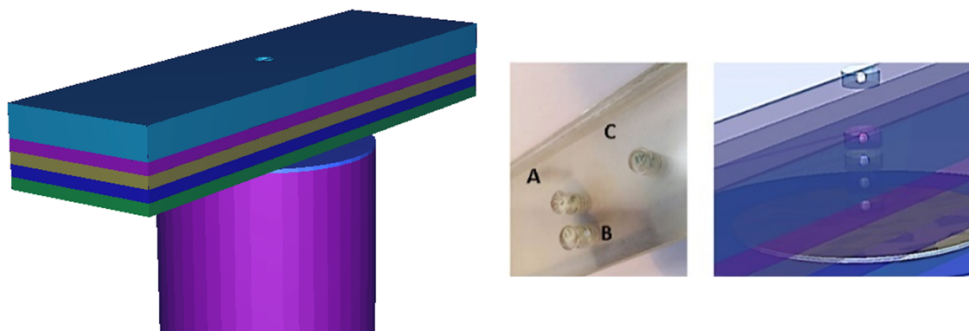
Figure 29. Left, Example of the MCNP geometry rendering under the building process, showing the electron extraction channel and the PMMA phantom in construction on the top. Center: PMMA phantom hosting different TLDs (type GR200A) and micro-silica beads dosimeters at different depth and in different positions. Right: Rendering of the MCNP model of the PMMA slab phantom positioned on top of a stack of circular Gafchromic© films (Devic et al., 2016) (reproducing the experimental irradiation configuration) on the brass target of the PFMA-3 [Isolan L., et al., 2020].

MCNP5 setup and adjoint transport options

As reported in Isolan L., et al., 2020, for the inversion and optimization procedure, a first direct/forward Monte Carlo simulation has been run to estimate the forward scalar flux $f(\boldsymbol{r}, E)$. Then, to generate the adjoint importance functions for a new forward run, the adjoint simulation has been carried out. (f^+, q) means that the detector response in the adjoint flux can be rearranged as follows (P is a point in the phase space $\{r, \omega, E\}$) and $\hat{q}(\boldsymbol{r}, \boldsymbol{\omega}, E)$, the bias source distribution:

$$R = \int_{whole\ phase\ space} f^+(P)q(P)dP \quad (35)$$

$$\hat{q}(\boldsymbol{r}, \boldsymbol{\omega}, E) = \frac{f^+(\boldsymbol{r}, \boldsymbol{\omega}, E)\, q(\boldsymbol{r}, \boldsymbol{\omega}, E)}{R} \quad (36)$$

The adjoint flux weighting the source is representative of the response of the detector due to a particle described by the $(\boldsymbol{r}, \boldsymbol{\omega}, E)$ space, angular and energetic "coordinates", while the denominator is representative of the total response. At this point, defining $w(\boldsymbol{r}, \boldsymbol{\omega}, E)$, particle weight, continuing to adhere to the procedure proposed by Wagner JC., et al., 2009 and as stated in Isolan L., et al., 2020, it can be also shown that the weights of a source of particle must be corrected following the relationship $w(\boldsymbol{r}, \boldsymbol{\omega}, E)\hat{q}(\boldsymbol{r}, \boldsymbol{\omega}, E) = w_o(\boldsymbol{r}, \boldsymbol{\omega}, E)q(\boldsymbol{r}, \boldsymbol{\omega}, E)$ (with $w_o(\boldsymbol{r}, \boldsymbol{\omega}, E)$ initial weight). The latter describes the inverse relationship between response and adjoint function, showing the physical consistency of the statistical weight that are used for transport simulation and source sampling.

The adjoint flux weighting the source is a representation of the response of the detector due to the particle described by the (r, ω, E) space, angular and energetic "coordinates", while the denominator is a representation of the total response. The next formalism can be derived from the following equation

$$w(r, \omega, E)\hat{q}(r, \omega, E) = w_o(r, \omega, E)q(r, \omega, E) \quad (37)$$

with $w_o(r, \omega, E)$ initial weight. Then, it is easy to derive that:

$$w(r, \omega, E) = \frac{R}{f^+(r, \omega, E)} \quad (38)$$

The last describes the inverse relationship between response and adjoint function, showing the physical consistency of the statistical weight that are used for transport simulation and source sampling [Isolan L., et al., 2020; Wagner JC., et al., 2009].

The simulation performances can be compared evaluating the Figure Of Merit (FOM), function of statistical error (σ) and computational time (T),

$$FOM = \frac{1}{\sigma^2 T} \quad (39)$$

The application of the strategy means that the adjoint simulations require the so-called "external calculations" (in the present application the procedure was repeated 6 times to obtain the inverted problem for each of the 6 microsilica beads considered, five on the axis at different depths in PMMA and one not in the axis at a depth of 20 mm – each has then been considered as a new source for the adjoint calculations). The default cross section libraries of MCNP have been applied. The MCAL parameter of the MGOPT card allows to choose a forward or an adjoint simulation (details in Booth TE.,

et al., 2003). Introducing the adjoint calculation input parameter, the code will produce an adjoint treatment of just the collision interactions. For a complete adjoint treatment, the source and tally regions must be completely redefined by switching the source related cards (space, time, angular and the energy dependence of the particles) with the tally related cards (space, time, angular and/or response). In this way, the simulation starts from the original source to the detector. The PFMA-3 Photon Forward Source is a model derived from the measured electron spectra at 18kV and 0.4 mbar of nitrogen, interacting with a 50 μm brass target, and represented by a circular Surface Source of 1.75 cm radius. An energy deposition tally with a single energy bin on the whole X-ray energy spectrum has been firstly used for comparing the experimental results. The SDEF and related cards have been then switched by an F1 tally cards. The point source card is used to score the photon fluence in the different beads. As previously explained, MCNP has proposed two techniques for generating the importance functions, both with the aim of rising the efficiency of the simulations. When the generators are used, there is a manual iterative process before an approximation of the importance functions is made. The steps also require iterations between adjoint and forward simulations to create an ideally optimized importance function. In Figure 30, a map of the systems with cells of interest is shown. In the Table 11 and Table 12 the information related to the forward and Adjoint MG MCNP5 run is shown. In the Figure 31, the geometric importance of the different cells of the MCNP model, derived and normalized from the track entering column of the Table 126 of the output file, are shown. After an iterative process of importance biasing, the new geometric importance is shown (see Table 13 and Table 14). With a constant track entering in each cell, the results are a function of the particle weight in that cell, and not of the "number of particles" entering in them (that will be the same for every geometric portion of the model) (Figure 32).
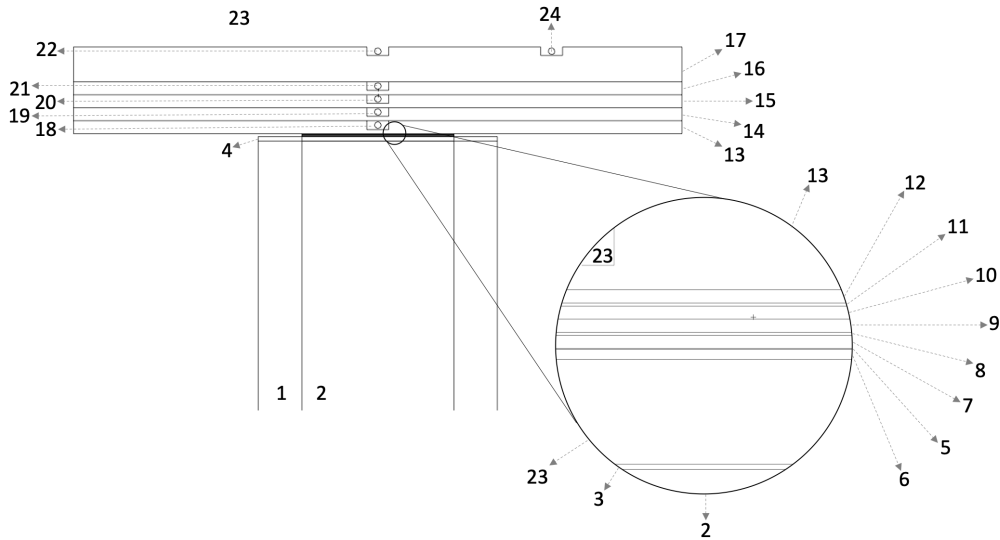
Figure 30. Geometry reporting the relevant MCNP cells.1, electron extraction channel; 2, nitrogen; 3, brass target; 4 iron flange; 5, HDV2 Gafchromic© film active layer; 6, HDV2 Gafchromic© film plastic layer; 7, 8, 9, first EBT3 Gafchromic© film (two plastic layer and one active layer); 10, 11, 12, second EBT3 Gafchromic© film; 13, 14, 15, 16, 17, PMMA slabs; 18, 19, 20, 21, 22, 24, micro sílica beads dosimeters; 23, air filling the ambient [Isolan L., et al., 2020].

Table 11. Example of a Forward MG MCNP5 simulation.

	Cell	Tracks	Popul	Coll	Coll*w *history	N. Weighted Energy	Flux Weighted Energy	Average Track Weight (relative)	Average Track Mfp (cm)
1	1.0E+1	6.5E+5	6.4E+5	7.5E+5	5.8E-1	1.7E-1	1.7E-1	1.0E+0	4.2E-1
2	2.0E+1	9.2E+5	8.9E+5	2.0E+0	1.6E-6	7.2E-2	7.2E-2	1.0E+0	9.5E+6
3	3.0E+2	6.0E+5	5.8E+5	1.1E+5	8.7E-2	7.4E-2	7.4E-2	1.0E+0	1.0E-1
4	4.0E+1	6.2E+4	6.2E+4	5.5E+4	4.3E-2	1.3E-1	1.3E-1	1.0E+0	2.9E-1
5	8.1E+1	5.4E+5	5.1E+5	2.7E+2	2.1E-4	7.2E-2	7.2E-2	1.0E+0	4.1E+0
6	8.2E+1	5.5E+5	5.2E+5	6.4E+3	5.0E-3	7.2E-2	7.2E-2	1.0E+0	2.3E+0
7	9.0E+1	5.5E+5	5.2E+5	8.0E+3	6.2E-3	7.2E-2	7.2E-2	1.0E+0	2.3E+0
8	9.2E+1	5.4E+5	5.1E+5	1.0E+3	7.9E-4	7.2E-2	7.2E-2	1.0E+0	4.1E+0
9	9.3E+1	5.5E+5	5.2E+5	7.8E+3	6.1E-3	7.2E-2	7.2E-2	1.0E+0	2.3E+0
10	9.4E+1	5.5E+5	5.1E+5	7.8E+3	6.0E-3	7.2E-2	7.2E-2	1.0E+0	2.3E+0
11	9.6E+1	5.4E+5	5.0E+5	9.7E+2	7.6E-4	7.2E-2	7.2E-2	1.0E+0	4.1E+0
12	9.7E+1	5.4E+5	5.1E+5	7.8E+3	6.1E-3	7.2E-2	7.2E-2	1.0E+0	2.3E+0
13	8.0E+2	7.4E+5	6.3E+5	9.1E+4	7.1E-2	7.2E-2	7.2E-2	1.0E+0	4.6E+0
14	8.1E+2	6.0E+5	5.2E+5	7.4E+4	5.7E-2	7.2E-2	7.2E-2	1.0E+0	4.6E+0
15	8.1E+2	4.8E+5	4.3E+5	5.7E+4	4.5E-2	7.2E-2	7.2E-2	1.0E+0	4.6E+0
16	8.1E+2	4.0E+5	3.7E+5	4.5E+4	3.5E-2	7.2E-2	7.2E-2	1.0E+0	4.6E+0
17	8.1E+2	3.3E+5	3.2E+5	8.3E+4	6.5E-2	7.2E-2	7.2E-2	1.0E+0	4.6E+0
18	8.1E+2	1.1E+4	1.1E+4	4.9E+2	3.8E-4	7.1E-2	7.1E-2	1.0E+0	2.1E+0
19	8.1E+2	5.2E+3	5.2E+3	2.2E+2	1.7E-4	7.1E-2	7.1E-2	1.0E+0	2.1E+0
20	8.1E+2	2.6E+3	2.6E+3	1.3E+2	9.7E-5	7.0E-2	7.0E-2	1.0E+0	2.1E+0
21	8.1E+2	1.3E+3	1.3E+3	6.6E+1	5.1E-5	6.8E-2	6.8E-2	1.0E+0	2.1E+0
22	8.1E+2	4.5E+2	4.5E+2	2.2E+1	1.7E-5	7.5E-2	7.5E-2	1.0E+0	2.2E+0
24	2.7E+1	1.4E+6	8.5E+5	2.5E+4	1.9E-2	8.3E-2	8.3E-2	1.0E+0	4.6E+3
Tot	1.1E+7	9.4E+6	1.3E+6	1.0E+0					

111

Table 12. Example of an Adjoint MG MCNP5 simulation.

	Cell	Tracks	Popul	Coll	Coll*w	N. Weighted Energy	Flux Weighted Energy	Average Track Weight (relative)	Average Track Mfp (cm)
1	1.0E+1	1.1E+7	1.0E+7	1.4E+7	9.3E+1	3.0E-1	3.0E-1	8.3E+1	7.9E-1
2	2.0E+1	9.7E+6	8.8E+6	4.0E+0	2.6E-5	2.6E-1	2.6E-1	7.9E+1	1.3E+7
3	3.0E+2	9.0E+6	8.9E+6	4.4E+5	2.8E+0	2.6E-1	2.6E-1	7.9E+1	5.4E-1
4	4.0E+1	1.4E+6	1.4E+6	7.4E+5	4.5E+0	2.9E-1	2.9E-1	8.1E+1	7.7E-1
5	8.1E+1	9.8E+6	9.5E+6	2.9E+3	2.0E-2	2.5E-1	2.5E-1	8.0E+1	6.4E+0
6	8.2E+1	9.7E+6	9.5E+6	4.8E+4	3.3E-1	2.5E-1	2.5E-1	8.0E+1	5.3E+0
7	9.0E+1	9.9E+6	9.6E+6	6.4E+4	4.4E-1	2.5E-1	2.5E-1	8.0E+1	5.3E+0
8	9.2E+1	9.9E+6	9.6E+6	1.1E+4	7.8E-2	2.5E-1	2.5E-1	8.0E+1	6.4E+0
9	9.3E+1	1.0E+7	9.7E+6	6.7E+4	4.6E-1	2.5E-1	2.5E-1	8.0E+1	5.3E+0
10	9.4E+1	1.0E+7	9.8E+6	6.8E+4	4.8E-1	2.5E-1	2.5E-1	8.0E+1	5.3E+0
11	9.6E+1	1.0E+7	9.8E+6	1.2E+4	8.4E-2	2.5E-1	2.5E-1	8.0E+1	6.3E+0
12	9.7E+1	1.0E+7	9.9E+6	7.1E+4	5.0E-1	2.5E-1	2.5E-1	8.0E+1	5.3E+0
13	8.0E+2	1.3E+7	1.2E+7	1.1E+6	7.8E+0	2.5E-1	2.5E-1	8.0E+1	6.2E+0
14	8.1E+2	1.3E+6	1.2E+6	1.3E+5	7.9E-1	2.6E-1	2.6E-1	7.2E+1	6.2E+0
15	8.1E+2	1.1E+6	1.0E+6	9.5E+4	5.9E-1	2.6E-1	2.6E-1	7.2E+1	6.2E+0
16	8.1E+2	9.0E+5	8.7E+5	7.6E+4	4.7E-1	2.6E-1	2.6E-1	7.2E+1	6.2E+0
17	8.1E+2	7.8E+5	7.7E+5	1.4E+5	8.9E-1	2.6E-1	2.6E-1	7.3E+1	6.2E+0
18	8.1E+2	1.1E+7	1.1E+7	2.8E+5	2.0E+0	2.5E-1	2.5E-1	8.2E+1	3.2E+0
19	8.1E+2	6.2E+3	6.1E+3	2.0E+2	1.2E-3	2.3E-1	2.3E-1	7.2E+1	3.0E+0
20	8.1E+2	2.7E+3	2.7E+3	9.0E+1	5.5E-4	2.3E-1	2.3E-1	7.0E+1	3.1E+0
21	8.1E+2	1.6E+3	1.6E+3	5.2E+1	3.0E-4	2.4E-1	2.4E-1	7.0E+1	3.1E+0
22	8.1E+2	7.1E+2	7.1E+2	1.8E+1	9.8E-5	2.5E-1	2.5E-1	6.8E+1	3.1E+0
24	2.7E+1	2.7E+7	1.2E+7	1.8E+5	1.3E+0	2.9E-1	2.9E-1	8.2E+1	6.7E+3
Tot	1.7E+8	1.5E+8	1.8E+7	1.2E+2					

Table 13. Example of a Forward MG MCNP5 simulation, crude importance.

	Cell	Tracks	Popul	Coll	Coll*w	N. Weighted Energy	Flux Weighted Energy	Average Track Weight (relative)	Average Track Mfp (cm)
1	1.0E+1	1.0E+1	2.7E+6	2.7E+6	3.2E+6	5.8E-1	1.7E-1	1.7E-1	7.9E-1
2	2.0E+1	2.0E+1	2.7E+6	2.7E+6	4.0E+0	1.1E-6	7.2E-2	7.2E-2	7.9E-1
3	3.0E+2	3.0E+2	2.8E+6	2.7E+6	5.3E+5	8.7E-2	7.4E-2	7.4E-2	7.6E-1
4	4.0E+1	4.0E+1	2.7E+6	2.7E+6	2.4E+6	4.3E-2	1.3E-1	1.3E-1	8.0E-1
5	8.1E+1	8.1E+1	2.8E+6	2.7E+6	1.4E+3	2.1E-4	7.2E-2	7.2E-2	7.7E-1
6	8.2E+1	8.2E+1	2.8E+6	2.7E+6	3.2E+4	4.9E-3	7.2E-2	7.2E-2	7.6E-1
7	9.0E+1	9.0E+1	2.7E+6	2.6E+6	4.1E+4	6.3E-3	7.2E-2	7.2E-2	7.8E-1
8	9.2E+1	9.2E+1	2.7E+6	2.6E+6	5.1E+3	7.7E-4	7.2E-2	7.2E-2	7.8E-1
9	9.3E+1	9.3E+1	2.7E+6	2.6E+6	3.9E+4	6.1E-3	7.2E-2	7.2E-2	7.9E-1
10	9.4E+1	9.4E+1	2.7E+6	2.6E+6	3.9E+4	6.0E-3	7.2E-2	7.2E-2	8.0E-1
11	9.6E+1	9.6E+1	2.7E+6	2.6E+6	4.8E+3	7.5E-4	7.2E-2	7.2E-2	8.0E-1
12	9.7E+1	9.7E+1	2.7E+6	2.6E+6	3.8E+4	5.9E-3	7.2E-2	7.2E-2	8.0E-1
13	8.0E+2	8.0E+2	2.6E+6	2.4E+6	3.3E+5	7.1E-2	7.2E-2	7.2E-2	8.1E-1
14	8.1E+2	8.1E+2	2.6E+6	2.4E+6	3.2E+5	5.8E-2	7.2E-2	7.2E-2	8.3E-1
15	8.1E+2	8.1E+2	2.7E+6	2.5E+6	3.1E+5	4.4E-2	7.2E-2	7.2E-2	8.3E-1
16	8.1E+2	8.1E+2	2.7E+6	2.5E+6	3.0E+5	3.5E-2	7.2E-2	7.2E-2	8.2E-1
17	8.1E+2	8.1E+2	2.7E+6	2.7E+6	6.8E+5	6.4E-2	7.2E-2	7.2E-2	8.1E-1
18	8.1E+2	8.1E+2	2.6E+6	2.6E+6	1.2E+5	3.7E-4	7.1E-2	7.1E-2	7.9E-1
19	8.1E+2	8.1E+2	2.6E+6	2.6E+6	1.2E+5	1.8E-4	7.2E-2	7.2E-2	8.3E-1
20	8.1E+2	8.1E+2	2.6E+6	2.6E+6	1.2E+5	9.7E-5	7.3E-2	7.3E-2	8.3E-1

21	8.1E+2	8.1E+2	2.6E+6	2.6E+6	1.2E+5	4.8E-5	7.1E-2	7.1E-2	8.2E-1
22	8.1E+2	8.1E+2	2.8E+6	2.8E+6	1.3E+5	1.6E-5	7.4E-2	7.4E-2	8.1E-1
24	2.7E+1	2.7E+1	2.9E+6	2.5E+6	4.7E+4	1.9E-2	8.3E-2	8.3E-2	8.1E-1
Tot	6.2E+7	6.0E+7	8.9E+6	1.0E+0					

Table 14. Example of an Adjoint MG MCNP5 simulation, crude importance.

	Cell	Tracks	Popul	Coll	Coll*w	N. Weighted Energy	Flux Weighted Energy	Average Track Weight (relative)	Average Track Mfp (cm)
1	1.0E+1	6.3E+6	5.9E+6	7.9E+6	9.3E+1	3.0E-1	3.0E-1	9.2E+1	7.9E-1
2	2.0E+1	6.3E+6	5.8E+6	0.0E+0	0.0E+0	2.6E-1	2.6E-1	8.6E+1	1.3E+7
3	3.0E+2	6.3E+6	6.2E+6	3.0E+5	2.8E+0	2.6E-1	2.6E-1	8.7E+1	5.4E-1
4	4.0E+1	6.3E+6	6.3E+6	3.3E+6	4.5E+0	2.9E-1	2.9E-1	8.9E+1	7.7E-1
5	8.1E+1	6.3E+6	6.3E+6	1.8E+3	2.0E-2	2.5E-1	2.5E-1	8.8E+1	6.4E+0
6	8.2E+1	6.3E+6	6.3E+6	3.1E+4	3.4E-1	2.5E-1	2.5E-1	8.8E+1	5.3E+0
7	9.0E+1	6.3E+6	6.3E+6	4.1E+4	4.4E-1	2.5E-1	2.5E-1	8.8E+1	5.3E+0
8	9.2E+1	6.3E+6	6.3E+6	7.0E+3	7.8E-2	2.5E-1	2.5E-1	8.8E+1	6.4E+0
9	9.3E+1	6.3E+6	6.3E+6	4.2E+4	4.6E-1	2.5E-1	2.5E-1	8.8E+1	5.3E+0
10	9.4E+1	6.3E+6	6.2E+6	4.2E+4	4.8E-1	2.5E-1	2.5E-1	8.8E+1	5.3E+0
11	9.6E+1	6.3E+6	6.2E+6	7.6E+3	8.6E-2	2.5E-1	2.5E-1	8.8E+1	6.3E+0
12	9.7E+1	6.3E+6	6.2E+6	4.4E+4	5.0E-1	2.5E-1	2.5E-1	8.8E+1	5.3E+0
13	8.0E+2	6.3E+6	6.2E+6	5.5E+5	7.8E+0	2.5E-1	2.5E-1	8.8E+1	6.2E+0
14	8.1E+2	6.3E+6	6.2E+6	6.3E+5	7.9E-1	2.6E-1	2.6E-1	7.9E+1	6.2E+0
15	8.1E+2	6.3E+6	6.2E+6	5.7E+5	5.9E-1	2.6E-1	2.6E-1	7.9E+1	6.2E+0
16	8.1E+2	6.3E+6	6.2E+6	5.3E+5	4.7E-1	2.6E-1	2.6E-1	7.9E+1	6.2E+0
17	8.1E+2	6.3E+6	6.3E+6	1.2E+6	9.0E-1	2.6E-1	2.6E-1	8.0E+1	6.2E+0
18	8.1E+2	6.3E+6	6.3E+6	1.6E+5	2.0E+0	2.5E-1	2.5E-1	9.0E+1	3.2E+0
19	8.1E+2	6.2E+6	6.2E+6	2.1E+5	1.3E-3	2.3E-1	2.3E-1	7.9E+1	3.1E+0
20	8.1E+2	6.6E+6	6.6E+6	2.3E+5	6.1E-4	2.3E-1	2.3E-1	7.7E+1	3.0E+0
21	8.1E+2	6.2E+6	6.2E+6	2.1E+5	3.4E-4	2.3E-1	2.3E-1	7.7E+1	3.0E+0
22	8.1E+2	5.7E+6	5.7E+6	1.9E+5	1.2E-4	2.5E-1	2.5E-1	7.4E+1	3.2E+0
24	2.7E+1	6.3E+6	5.2E+6	4.3E+4	1.3E+0	2.9E-1	2.9E-1	9.0E+1	6.7E+3
Tot	1.4E+8	1.4E+8	1.6E+7	1.2E+2					

An extract of one of the MCNP input file for the forward photons multigroup

calculations is reported as follows:

```
MCNP5
…
c PMMA PHANTOM
804 9 −1.19 −804 805 imp:p=1 imp:e=1
805 9 −1.19 −806 807 imp:p=1 imp:e=1
806 9 −1.19 −808 809 imp:p=1 imp:e=1
807 9 −1.19 −810 811 imp:p=1 imp:e=1
808 9 −1.19 −812 813 imp:p=1 imp:e=1
c beads
809 10 −2.63 −814 imp:p=1 imp:e=1
810 10 −2.63 −815 imp:p=1 imp:e=1
811 10 −2.63 −816 imp:p=1 imp:e=1
812 10 −2.63 −817 imp:p=1 imp:e=1
813 10 −2.63 −818 imp:p=1 imp:e=1
…

c PMMA phantom
804 rpp −7 7 −2 2 30.1665 30.4665
805 rcc 0 0 30.2665 0 0 0.2 0.25
806 rpp −7 7 −2 2 30.4665 30.7665
807 rcc 0 0 30.5665 0 0 0.2 0.25
808 rpp −7 7 −2 2 30.7665 31.0665
```

```
809 rcc 0 0 30.8665 0 0 0.2 0.25
810 rpp −7 7 −2 2 31.0665 31.3665
811 rcc 0 0 31.1665 0 0 0.2 0.25
812 rpp −7 7 −2 2 31.3665 32.1665
813 rcc 0 0 31.9665 0 0 0.2 0.25
c beads
814 s 0 0 30.3665 0.075
815 s 0 0 30.6665 0.075
816 s 0 0 30.9665 0.075
817 s 0 0 31.2665 0.075
818 s 0 0 32.0665 0.075

mode p
MGOPT F 12
*tr1 3.70 36.02 3 0 −90 −90 90 −90 0 −90 180 90
…
SDEF pos= 0 0 29.995 PAR=p  ERG=d1 VEC=0 0 1 EXT=0 RAD=d2 $ tr=1
si1 h 1.00E−03 5.99E−03 1.10E−02 1.60E−02 2.10E−02 2.60E−02 3.09E−02 3.59E−02 4.09E−02 4.59E−02 5.09E−02
5.59E−02 6.09E−02 6.59E−02 7.09E−02 7.59E−02 8.08E−02 8.58E−02 9.08E−02 9.58E−02 1.01E−01      1.06E−01
1.11E−01 1.16E−01 1.21E−01 1.26E−01 1.31E−01 1.36E−01 1.41E−01 1.46E−01 1.51E−01 1.56E−01 1.61E−01 1.66E−
01 1.71E−01 1.76E−01 1.81E−01 1.86E−01 1.91E−01 1.96E−01 2.01E−01 2.06E−01 2.11E−01 2.16E−01 2.21E−01
2.26E−01 2.31E−01 2.36E−01 2.41E−01      2.46E−01 2.51E−01 2.55E−01 2.60E−01 2.65E−01 2.70E−01 2.75E−01
2.80E−01 2.85E−01 2.90E−01 2.95E−01 3.00E−01 3.05E−01 3.10E−01 3.15E−01 3.20E−01 3.25E−01 3.30E−01 3.35E−
01 3.40E−01 3.45E−01 3.50E−01 3.55E−01 3.60E−01 3.65E−01 3.70E−01 3.75E−01 3.80E−01      3.85E−01 3.90E−
01 3.95E−01 4.00E−01 4.05E−01 4.10E−01 4.15E−01
       4.20E−01 4.25E−01 4.30E−01 4.35E−01 4.40E−01 4.45E−01 4.50E−01
       4.55E−01 4.60E−01 4.65E−01 4.70E−01 4.75E−01 4.80E−01 4.85E−01
       4.90E−01 4.95E−01 5.00E−01
sp1 d 0.00E+00 2.99E−02 1.46E−01 4.49E−02 7.86E−02 9.92E−02 9.67E−02
       8.11E−02 7.09E−02 5.99E−02 4.64E−02 3.69E−02 3.26E−02 2.47E−02
       1.95E−02 2.13E−02 1.37E−02 1.15E−02 1.01E−02 8.06E−03 6.11E−03
       6.35E−03 5.27E−03 4.61E−03 3.88E−03 2.91E−03 2.31E−03 2.30E−03
       1.77E−03 2.02E−03 2.18E−03 1.29E−03 1.23E−03 1.39E−03 3.05E−03
       1.04E−03 1.29E−03 1.01E−03 8.54E−04 7.36E−04 7.24E−04 5.59E−04
       7.36E−04 6.12E−04 7.55E−04 5.79E−04 5.20E−04 5.70E−04 3.10E−03
       4.83E−04 4.10E−04 3.75E−04 5.65E−04 4.16E−04 4.21E−04 5.67E−04
       4.20E−04 2.42E−04 3.37E−04 2.54E−04 2.41E−04 3.46E−04 3.50E−04
       1.23E−04 2.19E−04 2.13E−04 1.78E−04 1.86E−04 1.53E−04 1.59E−04
       9.80E−05 1.88E−04 1.50E−04 1.14E−04 8.23E−05 1.33E−04 1.87E−04
       7.08E−05 4.96E−05 1.95E−05 6.37E−05 6.13E−05 5.01E−05 1.89E−05
       3.28E−05 1.07E−04 5.91E−05 2.06E−05 5.93E−06 5.57E−06 0.00E+00
       7.23E−06 0.00E+00 0.00E+00 0.00E+00 0.00E+00 0.00E+00 0.00E+00
       0.00E+00 0.00E+00 0
e0     1.00E−03 5.99E−03 1.10E−02 1.60E−02 2.10E−02 2.60E−02 3.09E−02
       3.59E−02 4.09E−02 4.59E−02 5.09E−02 5.59E−02 6.09E−02 6.59E−02
       7.09E−02 7.59E−02 8.08E−02 8.58E−02 9.08E−02 9.58E−02 1.01E−01
       1.06E−01 1.11E−01 1.16E−01 1.21E−01 1.26E−01 1.31E−01 1.36E−01
       1.41E−01 1.46E−01 1.51E−01 1.56E−01 1.61E−01 1.66E−01 1.71E−01
       1.76E−01 1.81E−01 1.86E−01 1.91E−01 1.96E−01 2.01E−01 2.06E−01
       2.11E−01 2.16E−01 2.21E−01 2.26E−01 2.31E−01 2.36E−01 2.41E−01
       2.46E−01 2.51E−01 2.55E−01 2.60E−01 2.65E−01 2.70E−01 2.75E−01
       2.80E−01 2.85E−01 2.90E−01 2.95E−01 3.00E−01 3.05E−01 3.10E−01
       3.15E−01 3.20E−01 3.25E−01 3.30E−01 3.35E−01 3.40E−01 3.45E−01
       3.50E−01 3.55E−01 3.60E−01 3.65E−01 3.70E−01 3.75E−01 3.80E−01
       3.85E−01 3.90E−01 3.95E−01 4.00E−01 4.05E−01 4.10E−01 4.15E−01
       4.20E−01 4.25E−01 4.30E−01 4.35E−01 4.40E−01 4.45E−01 4.50E−01
       4.55E−01 4.60E−01 4.65E−01 4.70E−01 4.75E−01 4.80E−01 4.85E−01
       4.90E−01 4.95E−01 5.00E−01
em0 0.0 1 99r
SI2 0 1      $ source information
SP2 0    1       $ source probabilities
f6:p 809 810 811 812 813
f5:p 0 0 30.3665 0.0
ft5 inc
fu5 0 1 2 3 4 5 6 7 8 9 10 11 12 13 14 15 16 17 18 19 20 21 22 23
     24 25 26 27 28 29 30 T
fq5 e u
f15:p 0 0 30.6665 0.0
ft15 inc
fu15 0 1 2 3 4 5 6 7 8 9 10 11 12 13 14 15 16 17 18 19 20 21 22 23
     24 25 26 27 28 29 30 T
fq15 e u
f25:p 0 0 30.9665 0.0
ft25 inc
fu25 0 1 2 3 4 5 6 7 8 9 10 11 12 13 14 15 16 17 18 19 20 21 22 23
     24 25 26 27 28 29 30 T
fq25 e u
f35:p 0 0 31.2665 0.0
ft35 inc
fu35 0 1 2 3 4 5 6 7 8 9 10 11 12 13 14 15 16 17 18 19 20 21 22 23
     24 25 26 27 28 29 30 T
fq35 e u
f45:p 0 0 32.0665 0.0
ft45 inc
fu45 0 1 2 3 4 5 6 7 8 9 10 11 12 13 14 15 16 17 18 19 20 21 22 23
     24 25 26 27 28 29 30 T
fq45 e u
f55:p 0 0 30.3665 0.0
f4:p 809 810 811 812 813
print
```

Then, the first adjoint run, for one specific bead, must be done accordingly to

```
…
mode p
MGOPT A 12

SDEF pos= 0 0 30.3665 cel=809 PAR=p  ERG=d1 VEC=0 0 1 dir=d2 wgt=82 $ tr=1
e0    1.00E-03 5.99E-03 1.10E-02 1.60E-02 2.10E-02 2.60E-02 3.09E-02
3.59E-02 4.09E-02 4.59E-02 5.09E-02 5.59E-02 6.09E-02 6.59E-02
7.09E-02 7.59E-02 8.08E-02 8.58E-02 9.08E-02 9.58E-02 1.01E-01
1.06E-01 1.11E-01 1.16E-01 1.21E-01 1.26E-01 1.31E-01 1.36E-01
1.41E-01 1.46E-01 1.51E-01 1.56E-01 1.61E-01 1.66E-01 1.71E-01
1.76E-01 1.81E-01 1.86E-01 1.91E-01 1.96E-01 2.01E-01 2.06E-01
2.11E-01 2.16E-01 2.21E-01 2.26E-01 2.31E-01 2.36E-01 2.41E-01
2.46E-01 2.51E-01 2.55E-01 2.60E-01 2.65E-01 2.70E-01 2.75E-01
2.80E-01 2.85E-01 2.90E-01 2.95E-01 3.00E-01 3.05E-01 3.10E-01
3.15E-01 3.20E-01 3.25E-01 3.30E-01 3.35E-01 3.40E-01 3.45E-01
3.50E-01 3.55E-01 3.60E-01 3.65E-01 3.70E-01 3.75E-01 3.80E-01
3.85E-01 3.90E-01 3.95E-01 4.00E-01 4.05E-01 4.10E-01 4.15E-01
4.20E-01 4.25E-01 4.30E-01 4.35E-01 4.40E-01 4.45E-01 4.50E-01
4.55E-01 4.60E-01 4.65E-01 4.70E-01 4.75E-01 4.80E-01 4.85E-01
4.90E-01 4.95E-01 5.00E-01
em0   0.00E+00 2.99E-02 1.46E-01 4.49E-02 7.86E-02 9.92E-02 9.67E-02
8.11E-02 7.09E-02 5.99E-02 4.64E-02 3.69E-02 3.26E-02 2.47E-02
1.95E-02 2.13E-02 1.37E-02 1.15E-02 1.01E-02 8.06E-03 6.11E-03
6.35E-03 5.27E-03 4.61E-03 3.88E-03 2.91E-03 2.31E-03 2.30E-03
1.77E-03 2.02E-03 2.18E-03 1.29E-03 1.23E-03 1.39E-03 3.05E-03
1.04E-03 1.29E-03 1.01E-03 8.54E-04 7.36E-04 7.24E-04 5.59E-04
7.36E-04 6.12E-04 7.55E-04 5.79E-04 5.20E-04 5.70E-04 3.10E-03
4.83E-04 4.10E-04 3.75E-04 5.65E-04 4.16E-04 4.21E-04 5.67E-04
4.20E-04 2.42E-04 3.37E-04 2.54E-04 2.41E-04 3.46E-04 3.50E-04
1.23E-04 2.19E-04 2.13E-04 1.78E-04 1.86E-04 1.53E-04 1.59E-04
9.80E-05 1.88E-04 1.50E-04 1.14E-04 8.23E-05 1.33E-04 1.87E-04
7.08E-05 4.96E-05 1.95E-05 6.37E-05 6.13E-05 5.01E-05 1.89E-05
3.28E-05 1.07E-04 5.91E-05 2.06E-05 5.93E-06 5.57E-06 0.00E+00
7.23E-06 0.00E+00 0.00E+00 0.00E+00 0.00E+00 0.00E+00 0.00E+00
0.00E+00 0.00E+00 0
si1 h  1.00E-03 5.99E-03 1.10E-02 1.60E-02 2.10E-02 2.60E-02 3.09E-02
3.59E-02 4.09E-02 4.59E-02 5.09E-02 5.59E-02 6.09E-02 6.59E-02
7.09E-02 7.59E-02 8.08E-02 8.58E-02 9.08E-02 9.58E-02 1.01E-01
1.06E-01 1.11E-01 1.16E-01 1.21E-01 1.26E-01 1.31E-01 1.36E-01
1.41E-01 1.46E-01 1.51E-01 1.56E-01 1.61E-01 1.66E-01 1.71E-01
1.76E-01 1.81E-01 1.86E-01 1.91E-01 1.96E-01 2.01E-01 2.06E-01
2.11E-01 2.16E-01 2.21E-01 2.26E-01 2.31E-01 2.36E-01 2.41E-01
2.46E-01 2.51E-01 2.55E-01 2.60E-01 2.65E-01 2.70E-01 2.75E-01
2.80E-01 2.85E-01 2.90E-01 2.95E-01 3.00E-01 3.05E-01 3.10E-01
3.15E-01 3.20E-01 3.25E-01 3.30E-01 3.35E-01 3.40E-01 3.45E-01
3.50E-01 3.55E-01 3.60E-01 3.65E-01 3.70E-01 3.75E-01 3.80E-01
3.85E-01 3.90E-01 3.95E-01 4.00E-01 4.05E-01 4.10E-01 4.15E-01
4.20E-01 4.25E-01 4.30E-01 4.35E-01 4.40E-01 4.45E-01 4.50E-01
4.55E-01 4.60E-01 4.65E-01 4.70E-01 4.75E-01 4.80E-01 4.85E-01
4.90E-01 4.95E-01 5.00E-01
sp1 d 0.0 1 99r
SI2 -1 0 1      $ source information
SP2 0   1 0      $ source probabilities
f6:p 809 810 811 812 813
f1:p 30
ft1 inc
fu1 0 1 2 3 4 5 6 7 8 9 10 11 12 13 14 15 16 17 18 19 20 21 22 23
24 25 26 27 28 29 30 T
fq1 e u
tf1 3j 1
f11:p 30
ft11 scx 2
fu11 0 1 2 3 4 5 6 7 8 9 10 11 12 13 14 15 16 17 18 19 20 21 22 23
24 25 26 27 28 29 30 T
fq11 e u
tf11 3j 1
f5:p 0 0 30.3665 0.0
ft5 inc
fu5 0 1 2 3 4 5 6 7 8 9 10 11 12 13 14 15 16 17 18 19 20 21 22 23
24 25 26 27 28 29 30 T
fq5 e u
f15:p 0 0 30.6665 0.0
ft15 inc
fu15 0 1 2 3 4 5 6 7 8 9 10 11 12 13 14 15 16 17 18 19 20 21 22 23
24 25 26 27 28 29 30 T
fq15 e u
f25:p 0 0 30.9665 0.0
ft25 inc
fu25 0 1 2 3 4 5 6 7 8 9 10 11 12 13 14 15 16 17 18 19 20 21 22 23
24 25 26 27 28 29 30 T
fq25 e u
f35:p 0 0 31.2665 0.0
ft35 inc
fu35 0 1 2 3 4 5 6 7 8 9 10 11 12 13 14 15 16 17 18 19 20 21 22 23
24 25 26 27 28 29 30 T
fq35 e u
```

```
f45:p 0 0 32.0665 0.0
ft45 inc
fu45 0 1 2 3 4 5 6 7 8 9 10 11 12 13 14 15 16 17 18 19 20 21 22 23
24 25 26 27 28 29 30 T
fq45 e u
f111:p 30
ft111 scx 1
fq111 u e
cut:p j 0.5
print
PTRAC NPS=1,1e7 TYPE=P WRITE=pos FILE=asc EVENT=src
```


Figure 31. Example of the typical variable geometric importance that "naturally" characterize the MCNP model cells derived by the track entering column of the Table 126 of the output file (Pelowitz, 2011). Line: forward MG calculation. Dashed line: adjoint (or reversed) calculation for the 3 mm depth Trueinvivo© micro-silica beads (the same behaviour for the other TLDs has been found) [Isolan L., et al., 2020].

With the calculated forward crude importance

```
                                   …
10   101   −7.85 −10 11 −12 20 imp:p=1.131724147
c PMMA PHANTOM
804 9 −1.19 −804 805 imp:p=1
805 9 −1.19 −806 807 imp:p=1.2331574
806 9 −1.19 −808 809 imp:p=1.527815848
807 9 −1.19 −810 811 imp:p=1.829485719
808 9 −1.19 −812 813 imp:p=2.256994294
c beads
809 10 −2.63 −814 imp:p=66.77573062
810 10 −2.63 −815 imp:p=142.5566751
811 10 −2.63 −816 imp:p=278.5819765
812 10 −2.63 −817 imp:p=549.8766816
813 10 −2.63 −818 imp:p=1649.630045
…
mode p
MGOPT F 12
…
```

With the calculated adjoint crude importance

```
                                              ...
10    101   -7.85 -10 11 -12 20 imp:p=1.11519554
c PMMA PHANTOM
804 9 -1.19 -804 805 imp:p=1
805 9 -1.19 -806 807 imp:p=9.826253363
806 9 -1.19 -808 809 imp:p=11.82499363
807 9 -1.19 -810 811 imp:p=13.87635379
808 9 -1.19 -812 813 imp:p=16.13559179
c beads
809 10 -2.63 -814 imp:p=1.100030791
810 10 -2.63 -815 imp:p=2024.51369
811 10 -2.63 -816 imp:p=4615.69553
812 10 -2.63 -817 imp:p=7569.862616
813 10 -2.63 -818 imp:p=17963.59248
...
```
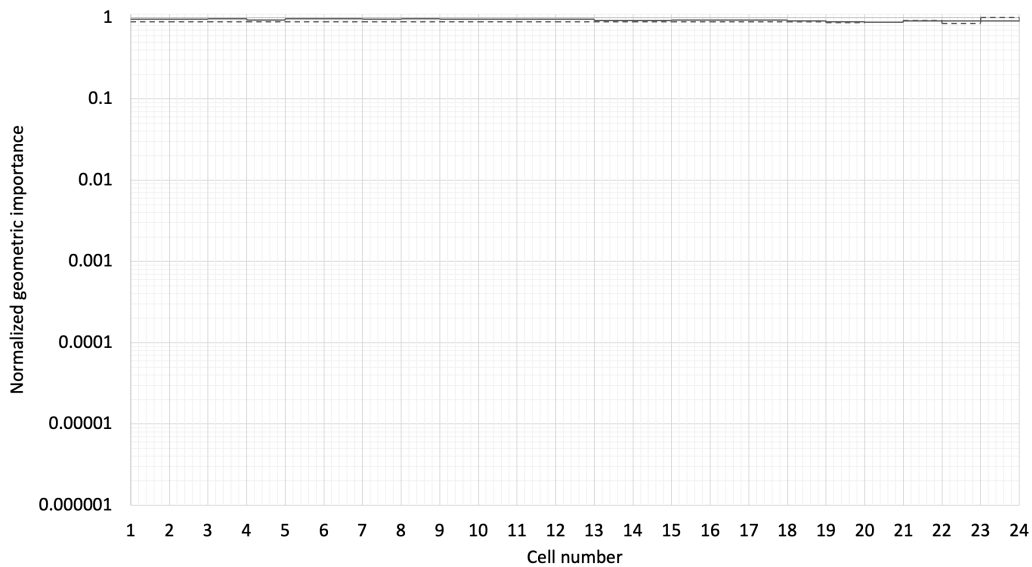

Figure 32. Geometric importance of the MCNP cells of the model derived by the track entering column of the Table 126 of the output file after a strong bias applied to the "imp" card in such a way to obtain a constant number of photons in each cell. In this way the results are a function of the particle weights and not of the "particle number" entering in the cells. Line: forward MG calculation. Dashed line: adjoint calculation [Isolan L., et al., 2020].

At this point, the forward WW can be generated adding the cards in the forward input with crude importance, both fort a cell-based strategy or superimposed mesh.

About the cell-based WW, it should first be noted that in such forward way, to compare the results exactly with the same geometry and not affecting the model, no "supporting" cells have been added to increase the VRT performances. MCNP has a method for

performing geometric splitting based on cells. The method is controlled by the WWG, WWN and WWP cards. MCNP runs typically do not generate WW values. The weights as a function of depth in central axis are shown in Figure 33.

```
…
Wwg 5 300 0.0 j j j j 0
wwge:p 0 0.01 0.1 0.5
....
```
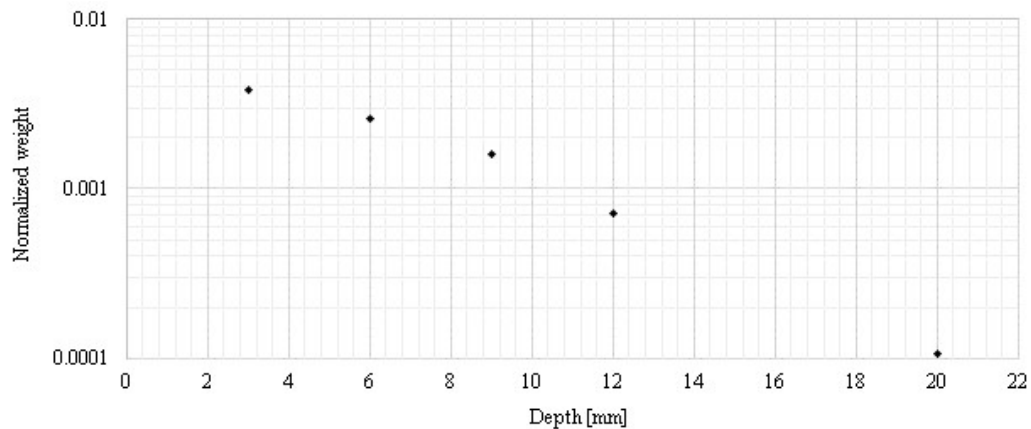

Figure 33. Typical MCNP weight behavior as found with the cell-based technique [Isolan L., et al., 2020].

The mesh-based weight-window generator has a few keywords that define the card. One of the keywords is the GEOM REC. This defines a cartesian mesh geometry and is used to create the normalization constant for the mesh-based weight-window generator. Other keywords are the ORIGIN, the AXS and the VEC, which define the superimposed coordinates system. The IMESH, IINTS, JMESH, JINTS, KMESH, KINTS define the mesh elements number and distribution. See Figure 34.

```
…
WWG 5 0 0 4J 0
WWGE:p $
…
mesh geom=xyz
        ref 0 0 29.995
        origin −41 −41 −41
        imesh 41 iints 5
        jmesh 41 jints 5
        kmesh 41 kints 5
```
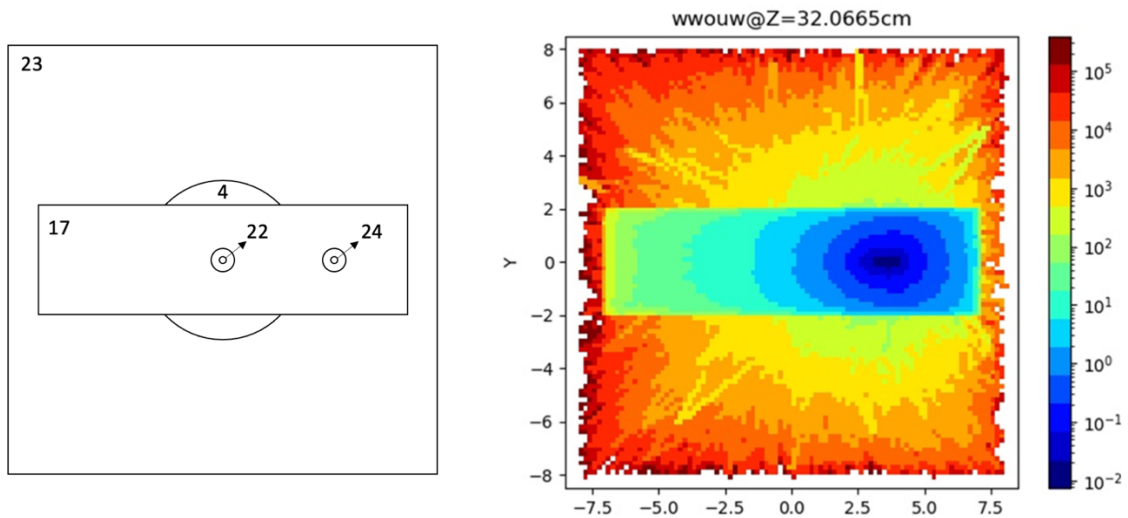
Figure 34. Left, geometry (xy view, see also Figure 30). Right, WW value distribution visualization as estimated by MCNP with 1.0E+06 rectangular elements [Isolan L., et al., 2020]. Not on axis bead. Figure generated with the iWW-GVR tool (https://github.com/Radiation-Transport/iWW-GVR - ©2019 F4E | European Joint Undertaking for ITER and the Development of Fusion Energy ('Fusion for Energy')).

And, extracted from the output file, can be used in a biased new forward input file

```
                                       …
wwe:p  1.0000E-02  1.1000E-02  1.0000E-01  5.0000E-01
wwn1:p     0.0000E+00  0.0000E+00  0.0000E+00  0.0000E+00  0.0000E+00
0.0000E+00  0.0000E+00  0.0000E+00  0.0000E+00  0.0000E+00
0.0000E+00  0.0000E+00  0.0000E+00  0.0000E+00  0.0000E+00
0.0000E+00  0.0000E+00  0.0000E+00  0.0000E+00  0.0000E+00
0.0000E+00  0.0000E+00 -1.0000E+00  0.0000E+00
wwn2:p     0.0000E+00  0.0000E+00  0.0000E+00  0.0000E+00  0.0000E+00
0.0000E+00  0.0000E+00  0.0000E+00  0.0000E+00  0.0000E+00
0.0000E+00  0.0000E+00  0.0000E+00  0.0000E+00  0.0000E+00
0.0000E+00  0.0000E+00  0.0000E+00  0.0000E+00  0.0000E+00
0.0000E+00  0.0000E+00 -1.0000E+00  0.0000E+00
wwn3:p     4.3095E+01  1.5681E-01  5.0000E-01  2.5485E+01  4.3213E-01
3.4746E-01  3.2206E-01  3.9669E-01  3.1409E-01  3.1190E-01
3.8300E-01  3.0694E-01  9.2307E-02  2.2366E-01  9.8993E-01
3.1411E+00  5.3439E+00  2.9439E-03  1.5960E-01  6.6793E-01
2.0101E+00  3.0525E+01 -1.0000E+00  8.4021E-02
wwn4:p     5.1069E+00  1.4435E-01  5.0837E-01  5.1355E+00  5.4559E-01
4.1982E-01  3.8781E-01  5.0220E-01  3.8286E-01  3.7952E-01
4.7539E-01  3.8083E-01  1.0908E-01  2.8399E-01  1.3858E+00
4.8023E+00  7.5599E+00  2.6926E-03  2.1876E-01  6.7222E-01
3.3760E+00  0.0000E+00 -1.0000E+00  1.0900E-01
```

On the other hands, it must be recalled that the purpose was to obtain importance functions to be used in forward calculations instead of classical weight windows. The following input file generates importance function from adjoint run of the problem.

```
…
    10    101    -7.85 -10 11 -12 20 imp:p=1.11519554
c PMMA PHANTOM
804 9 -1.19 -804 805 imp:p=1 vol=23.9607
805 9 -1.19 -806 807 imp:p=9.826253363 vol=23.9607
806 9 -1.19 -808 809 imp:p=11.82499363 vol=23.9607
807 9 -1.19 -810 811 imp:p=13.87635379 vol=23.9607
808 9 -1.19 -812 813 imp:p=16.13559179 vol=63.9607
c beads
809 10 -2.63 -814 imp:p=1.100030791
810 10 -2.63 -815 imp:p=2024.51369
811 10 -2.63 -816 imp:p=4615.69553
812 10 -2.63 -817 imp:p=7569.862616
813 10 -2.63 -818 imp:p=17963.59248
…
mode p
MGOPT A 12 0 2 2 1 1000

…
c TLD
m10 3000 -0.267585 9000 -0.732415
SDEF pos= 0 0 30.3665 cel=809 PAR=p  ERG=d1 VEC=0 0 1 dir=d2 wgt=82 $ tr=1
e0    1.00E-03 5.99E-03 1.10E-02 1.60E-02 2.10E-02 2.60E-02 3.09E-02
      3.59E-02 4.09E-02 4.59E-02 5.09E-02 5.59E-02 6.09E-02 6.59E-02
      7.09E-02 7.59E-02 8.08E-02 8.58E-02 9.08E-02 9.58E-02 1.01E-01
      1.06E-01 1.11E-01 1.16E-01 1.21E-01 1.26E-01 1.31E-01 1.36E-01
      1.41E-01 1.46E-01 1.51E-01 1.56E-01 1.61E-01 1.66E-01 1.71E-01
      1.76E-01 1.81E-01 1.86E-01 1.91E-01 1.96E-01 2.01E-01 2.06E-01
      2.11E-01 2.16E-01 2.21E-01 2.26E-01 2.31E-01 2.36E-01 2.41E-01
      2.46E-01 2.51E-01 2.55E-01 2.60E-01 2.65E-01 2.70E-01 2.75E-01
      2.80E-01 2.85E-01 2.90E-01 2.95E-01 3.00E-01 3.05E-01 3.10E-01
      3.15E-01 3.20E-01 3.25E-01 3.30E-01 3.35E-01 3.40E-01 3.45E-01
      3.50E-01 3.55E-01 3.60E-01 3.65E-01 3.70E-01 3.75E-01 3.80E-01
      3.85E-01 3.90E-01 3.95E-01 4.00E-01 4.05E-01 4.10E-01 4.15E-01
      4.20E-01 4.25E-01 4.30E-01 4.35E-01 4.40E-01 4.45E-01 4.50E-01
      4.55E-01 4.60E-01 4.65E-01 4.70E-01 4.75E-01 4.80E-01 4.85E-01
      4.90E-01 4.95E-01 5.00E-01
em0   0.00E+00 2.99E-02 1.46E-01 4.49E-02 7.86E-02 9.92E-02 9.67E-02
      8.11E-02 7.09E-02 5.99E-02 4.64E-02 3.69E-02 3.26E-02 2.47E-02
      1.95E-02 2.13E-02 1.37E-02 1.15E-02 1.01E-02 8.06E-03 6.11E-03
      6.35E-03 5.27E-03 4.61E-03 3.88E-03 2.91E-03 2.31E-03 2.30E-03
      1.77E-03 2.02E-03 2.18E-03 1.29E-03 1.23E-03 1.39E-03 3.05E-03
      1.04E-03 1.29E-03 1.01E-03 8.54E-04 7.36E-04 7.24E-04 5.59E-04
      7.36E-04 6.12E-04 7.55E-04 5.79E-04 5.20E-04 5.70E-04 3.10E-03
      4.83E-04 4.10E-04 3.75E-04 5.65E-04 4.16E-04 4.21E-04 5.67E-04
      4.20E-04 2.42E-04 3.37E-04 2.54E-04 2.41E-04 3.46E-04 3.50E-04
      1.23E-04 2.19E-04 2.13E-04 1.78E-04 1.86E-04 1.53E-04 1.59E-04
      9.80E-05 1.88E-04 1.50E-04 1.14E-04 8.23E-05 1.33E-04 1.87E-04
      7.08E-05 4.96E-05 1.95E-05 6.37E-05 6.13E-05 5.01E-05 1.89E-05
      3.28E-05 1.07E-04 5.91E-05 2.06E-05 5.93E-06 5.57E-06 0.00E+00
      7.23E-06 0.00E+00 0.00E+00 0.00E+00 0.00E+00 0.00E+00 0.00E+00
      0.00E+00 0.00E+00 0
si1 h  1.00E-03 5.99E-03 1.10E-02 1.60E-02 2.10E-02 2.60E-02 3.09E-02
      3.59E-02 4.09E-02 4.59E-02 5.09E-02 5.59E-02 6.09E-02 6.59E-02
      7.09E-02 7.59E-02 8.08E-02 8.58E-02 9.08E-02 9.58E-02 1.01E-01
      1.06E-01 1.11E-01 1.16E-01 1.21E-01 1.26E-01 1.31E-01 1.36E-01
      1.41E-01 1.46E-01 1.51E-01 1.56E-01 1.61E-01 1.66E-01 1.71E-01
      1.76E-01 1.81E-01 1.86E-01 1.91E-01 1.96E-01 2.01E-01 2.06E-01
      2.11E-01 2.16E-01 2.21E-01 2.26E-01 2.31E-01 2.36E-01 2.41E-01
      2.46E-01 2.51E-01 2.55E-01 2.60E-01 2.65E-01 2.70E-01 2.75E-01
      2.80E-01 2.85E-01 2.90E-01 2.95E-01 3.00E-01 3.05E-01 3.10E-01
      3.15E-01 3.20E-01 3.25E-01 3.30E-01 3.35E-01 3.40E-01 3.45E-01
      3.50E-01 3.55E-01 3.60E-01 3.65E-01 3.70E-01 3.75E-01 3.80E-01
      3.85E-01 3.90E-01 3.95E-01 4.00E-01 4.05E-01 4.10E-01 4.15E-01
      4.20E-01 4.25E-01 4.30E-01 4.35E-01 4.40E-01 4.45E-01 4.50E-01
      4.55E-01 4.60E-01 4.65E-01 4.70E-01 4.75E-01 4.80E-01 4.85E-01
      4.90E-01 4.95E-01 5.00E-01
sp1 d 0.0 1 99r
SI2 -1 0 1      $ source information
SP2 0   1 0     $ source probabilities
f6:p 809 810 811 812 813
f1:p 30
ft1 inc
fu1 0 1 2 3 4 5 6 7 8 9 10 11 12 13 14 15 16 17 18 19 20 21 22 23
    24 25 26 27 28 29 30 T
fq1 e u
tf1 3j 1
f11:p 30
c fs11 -4
ft11 scx 2
fu11 0 1 2 3 4 5 6 7 8 9 10 11 12 13 14 15 16 17 18 19 20 21 22 23
    24 25 26 27 28 29 30 T
fq11 e u
tf11 3j 1
f5:p 0 0 30.3665 0.0
ft5 inc
fu5 0 1 2 3 4 5 6 7 8 9 10 11 12 13 14 15 16 17 18 19 20 21 22 23
    24 25 26 27 28 29 30 T
fq5 e u
f15:p 0 0 30.6665 0.0
ft15 inc
fu15 0 1 2 3 4 5 6 7 8 9 10 11 12 13 14 15 16 17 18 19 20 21 22 23
    24 25 26 27 28 29 30 T
```

```
fq15 e u
f25:p 0 0 30.9665 0.0
ft25 inc
fu25 0 1 2 3 4 5 6 7 8 9 10 11 12 13 14 15 16 17 18 19 20 21 22 23
     24 25 26 27 28 29 30 T
fq25 e u
f35:p 0 0 31.2665 0.0
ft35 inc
fu35 0 1 2 3 4 5 6 7 8 9 10 11 12 13 14 15 16 17 18 19 20 21 22 23
     24 25 26 27 28 29 30 T
fq35 e u
f45:p 0 0 32.0665 0.0
ft45 inc
fu45 0 1 2 3 4 5 6 7 8 9 10 11 12 13 14 15 16 17 18 19 20 21 22 23
     24 25 26 27 28 29 30 T
fq45 e u
f111:p 30
ft111 scx 1
fq111 u e
cut:p j 0.5
print
PTRAC NPS=1,1e7 TYPE=P WRITE=pos FILE=asc EVENT=src
```

Finally, the adjoint importance functions can be used in a new forward calculation

which can be considered physically optimized:

```
MCNP5
…
10    101    −7.85 −10 11 −12 20 imp:p=1.131724147
…
c PMMA PHANTOM
804 9 −1.19 −804 805 imp:p=1
805 9 −1.19 −806 807 imp:p=1.2331574
806 9 −1.19 −808 809 imp:p=1.527815848
807 9 −1.19 −810 811 imp:p=1.829485719
808 9 −1.19 −812 813 imp:p=2.256994294
c beads
809 10 −2.63 −814 imp:p=66.77573062
810 10 −2.63 −815 imp:p=142.5566751
811 10 −2.63 −816 imp:p=278.5819765
812 10 −2.63 −817 imp:p=549.8766816
813 10 −2.63 −818 imp:p=1649.630045
…

mode p
MGOPT F 12
…
…
wwe:p  1.0000E−01  5.0000E−01  1.0000E+00  2.0000E+00  3.0000E+00
4.0000E+00  5.0000E+00  6.0000E+00  7.0000E+00  8.0000E+00
9.0000E+00  2.0000E+01
wwn01:p   2.1101E−01  1.2586E−01  2.9075E−02  6.8705E−02  2.5588E−02
2.5784E−02  2.5410E−02  2.5155E−02  2.4901E−02  2.4430E−02
2.4150E−02  2.3877E−02  6.7864E−02  1.9523E−01  2.2628E−01
2.5507E−01  3.0257E−01  2.0959E−03  5.7817E−02  5.2772E−02
7.4620E−02  1.2078E−01 −1.0000E+00  2.0959E+00
wwn02:p   9.7337E−02  5.7620E−02  1.3333E−02  3.1175E−02  1.2252E−02
1.2320E−02  1.2160E−02  1.2074E−02  1.1971E−02  1.1806E−02
1.1721E−02  1.1611E−02  3.2649E−02  9.5685E−02  1.0853E−01
1.2040E−01  1.4031E−01  1.0000E−03  3.9112E−02  5.1556E−02
8.3460E−02  9.2439E−02 −1.0000E+00  1.0000E+00
wwn03:p   2.0624E−01  1.2209E−01  2.8251E−02  6.6054E−02  2.5959E−02
2.6104E−02  2.5765E−02  2.5583E−02  2.5365E−02  2.5015E−02
2.4835E−02  2.4602E−02  6.9177E−02  2.0274E−01  2.2996E−01
2.5511E−01  2.9730E−01  2.1188E−03  8.2871E−02  1.0924E−01
1.7684E−01  1.9586E−01 −1.0000E+00  2.1188E+00
wwn04:p   4.3698E−01  2.5868E−01  5.9858E−02  1.3996E−01  5.5002E−02
5.5309E−02  5.4592E−02  5.4206E−02  5.3744E−02  5.3003E−02
5.2621E−02  5.2128E−02  1.4657E−01  4.2957E−01  4.8724E−01
5.4054E−01  6.2993E−01  4.4894E−03  1.7559E−01  2.3145E−01
3.7469E−01  4.1500E−01 −1.0000E+00  4.4894E+00
wwn05:p   9.2589E−01  5.4810E−01  1.2683E−01  2.9654E−01  1.1654E−01
1.1719E−01  1.1567E−01  1.1485E−01  1.1387E−01  1.1230E−01
1.1149E−01  1.1045E−01  3.1056E−01  9.1018E−01  1.0324E+00
1.1453E+00  1.3347E+00  9.5122E−03  3.7204E−01  4.9041E−01
7.9390E−01  8.7930E−01 −1.0000E+00  9.5122E+00
wwn06:p   1.9618E+00  1.1613E+00  2.6873E−01  6.2833E−01  2.4693E−01
2.4830E−01  2.4508E−01  2.4335E−01  2.4128E−01  2.3795E−01
2.3624E−01  2.3402E−01  6.5803E−01  1.9285E+00  2.1874E+00
```

```
2.4267E+00  2.8280E+00  2.0155E-02  7.8829E-01  1.0391E+00
1.6821E+00  1.8631E+00 -1.0000E+00  2.0155E+01
wwn07:p    4.1567E+00  2.4606E+00  5.6938E-01  1.3313E+00  5.2319E-01
5.2611E-01  5.1929E-01  5.1562E-01  5.1123E-01  5.0417E-01
5.0054E-01  4.9586E-01  1.3942E+00  4.0862E+00  4.6347E+00
5.1418E+00  5.9920E+00  4.2704E-02  1.6702E+00  2.2016E+00
3.5641E+00  3.9475E+00 -1.0000E+00  4.2704E+01
wwn08:p    7.5604E+00  4.1831E+00  9.7606E-01  2.4212E+00  8.9052E-01
8.9580E-01  8.8402E-01  8.7733E-01  8.6965E-01  8.5690E-01
8.5008E-01  8.4186E-01  2.3517E+00  6.8067E+00  7.7429E+00
8.6064E+00  1.0061E+01  7.4258E-02  2.5838E+00  2.9197E+00
4.3826E+00  5.8187E+00 -1.0000E+00  7.4258E+01
wwn09:p    7.5604E+00  4.1831E+00  9.7606E-01  2.4212E+00  8.9052E-01
8.9580E-01  8.8402E-01  8.7733E-01  8.6965E-01  8.5690E-01
8.5008E-01  8.4186E-01  2.3517E+00  6.8067E+00  7.7429E+00
8.6064E+00  1.0061E+01  7.4258E-02  2.5838E+00  2.9197E+00
4.3826E+00  5.8187E+00 -1.0000E+00  7.4258E+01
wwn10:p    7.5604E+00  4.1831E+00  9.7606E-01  2.4212E+00  8.9052E-01
8.9580E-01  8.8402E-01  8.7733E-01  8.6965E-01  8.5690E-01
8.5008E-01  8.4186E-01  2.3517E+00  6.8067E+00  7.7429E+00
8.6064E+00  1.0061E+01  7.4258E-02  2.5838E+00  2.9197E+00
4.3826E+00  5.8187E+00 -1.0000E+00  7.4258E+01
wwn11:p    7.5604E+00  4.1831E+00  9.7606E-01  2.4212E+00  8.9052E-01
8.9580E-01  8.8402E-01  8.7733E-01  8.6965E-01  8.5690E-01
8.5008E-01  8.4186E-01  2.3517E+00  6.8067E+00  7.7429E+00
8.6064E+00  1.0061E+01  7.4258E-02  2.5838E+00  2.9197E+00
4.3826E+00  5.8187E+00 -1.0000E+00  7.4258E+01
wwn12:p    7.5604E+00  4.1831E+00  9.7606E-01  2.4212E+00  8.9052E-01
8.9580E-01  8.8402E-01  8.7733E-01  8.6965E-01  8.5690E-01
8.5008E-01  8.4186E-01  2.3517E+00  6.8067E+00  7.7429E+00
8.6064E+00  1.0061E+01  7.4258E-02  2.5838E+00  2.9197E+00
4.3826E+00  5.8187E+00 -1.0000E+00  7.4258E+01
```

ADVANTG setup and adjoint transport options

As underlined in the Isolan L., et al., 2020 an efficient alternative to the above outlined procedure is given by the auxiliary tool ADVANTG [Mosher SW., et al., 2015]. The particle transport tool solves the particle transport problem in the same MCNP geometry (by reading the MCNP input file) with a discrete ordinate transport code originally belonging to the SCALE suite, DENOVO [Evans TM., et al., 2010]. The total forward and the adjoint fluxes for the actual simulation geometry are shown in Figure 35. A typical Weight Window is reported in Figure 36. The ADVANTG calculations have been performed on a rectangular mesh of 1,000,000 elements, with 4 Legendre polynomial orders, 8 azimuthal and 8 polar angles per octant of sphere, using the FW-CADIS method, with MG 27n19g library (a library with 27 neutron groups and 19 gamma groups, respectively in the 1.0E-11:2.0E+01 and 1.0E-02:2.0E+01 MeV ranges, evaluated from the ENDF/B-VII.0 and intended as general-purpose shielding libraries based on a weighting function that consists of a fission spectrum, a 1/E slowing down spectrum, and a Maxwellian distribution; details in Mosher SW., et al., 2015 and Wiarda D., et al., 2008), and source sampling on 1,000,000 particles. In order to better understand the comparison between the results of ADVANTG with those directly from the MCNP model, it is therefore helpful to remember that the FW-CADIS approach uses the forward flux to generate the correct physical quantities (e.g. adjoint source) introduced in the adjoint calculation for obtaining the adjoint importance functions for getting a constant track entering. Having a uniform number of particles in all the geometry means having a quite constant uncertainty which can be translated in having an inversely proportional mathematical relationship between the adjoint source and the forward flux. From a technical point of view, then, in MCNP, the Weight Window has

been set with the WWP card applied to the photon transport, and the source has been

biased with the SB card.

$$q^+(\boldsymbol{r}, \boldsymbol{\omega}, E) = \frac{1}{f(\boldsymbol{r}, \boldsymbol{\omega}, E)} \qquad (40)$$

An example of ADVANTG input file

```
method                     fwcadis
mcnp_input                 forward_photons_mg.txt
mcnp_tallies               65
mcnp_material_names         4   Air
                            6   mylar
                          100   brass
                          101   iron
                          200   nitrogen
                          500   gaf
anisn_library              27n19g
denovo_quad_num_azi    8
denovo_quad_num_polar  8
denovo_pn_order            4
# denovo_x_blocks            4
# denovo_y_blocks            4
# denovo_z_blocks            4
mesh_x                     -8.5   8.5
mesh_x_ints                100
mesh_y                     -8.5   8.5
mesh_y_ints                 100
mesh_z                     -1.5  41.5
mesh_z_ints                 100
```

The ADVANTG run generates the lines to be added in the MCNP input files for biasing

the source and using the WW

```
sb1    0.00000e+00 1.69115e-02 8.35268e-02 2.54222e-02 4.45229e-02 5.66592e-02
       5.45128e-02 4.59904e-02 3.98617e-02 4.83540e-02 8.79901e-02 7.00813e-02
       6.19790e-02 4.68734e-02 3.72387e-02 4.05906e-02 2.60269e-02 2.18513e-02
       1.91747e-02 1.52933e-02 1.20142e-02 1.45680e-02 1.20889e-02 1.05848e-02
       8.91208e-03 6.68059e-03 5.29812e-03 5.27494e-03 4.06724e-03 4.63902e-03
       4.99720e-03 2.95886e-03 2.83137e-03 3.19040e-03 7.01224e-03 2.39344e-03
       2.97171e-03 2.31991e-03 1.96107e-03 1.68927e-03 1.68980e-03 1.39856e-03
       1.84369e-03 1.53470e-03 1.88828e-03 1.44989e-03 1.30171e-03 1.42509e-03
       7.75340e-03 1.21025e-03 1.02486e-03 9.38916e-04 1.41656e-03 1.03967e-03
       1.05140e-03 1.41700e-03 1.05083e-03 6.06627e-04 8.43020e-04 6.36176e-04
       6.03824e-04 8.88650e-04 8.97177e-04 3.15486e-04 5.60220e-04 5.46725e-04
       4.55543e-04 4.75779e-04 3.92954e-04 4.08115e-04 2.51537e-04 4.81655e-04
       3.85102e-04 2.92874e-04 2.10865e-04 3.40683e-04 4.79135e-04 1.81285e-04
       1.27244e-04 5.00299e-05 1.63184e-04 1.09310e-04 8.95048e-05 3.37145e-05
       5.85900e-05 1.90835e-04 1.05237e-04 3.66681e-05 1.05819e-05 9.94017e-06
       0.00000e+00 1.28790e-05 0.00000e+00 0.00000e+00 0.00000e+00 0.00000e+00
       0.00000e+00 0.00000e+00 0.00000e+00 0.00000e+00 0.00000e+00
wwp:p 5.0 j 100 j -1 0 1.033522298e+00
```

And the WW are generated in a separate file

```
        1         1        2        10
        0        19
  1.00000e+02  1.00000e+02  1.00000e+02 -8.50000e+00 -8.50000e+00 -1.50000e+00
  1.00000e+02  1.00000e+02  1.00000e+02  1.00000e+00
 -8.50000e+00  1.00000e+00 -8.33000e+00  1.00000e+00  1.00000e+00 -8.16000e+00
  1.00000e+00  1.00000e+00 -7.99000e+00  1.00000e+00  1.00000e+00 -7.82000e+00
…
  3.67457e+01  3.61873e+01  3.55805e+01  3.50476e+01  3.46372e+01  3.43694e+01
  3.42268e+01  3.41598e+01  3.41057e+01  3.40136e+01
```
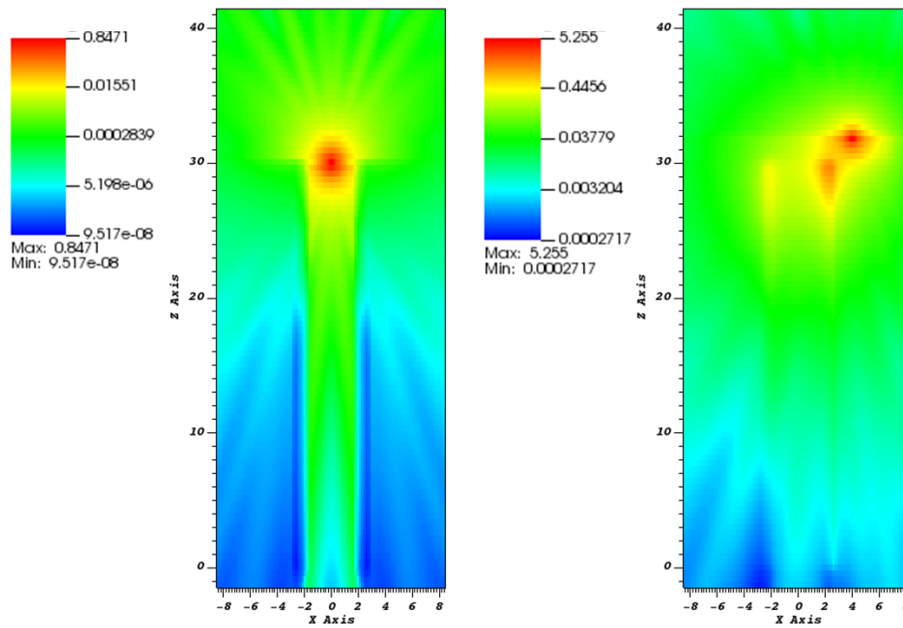
Figure 35. Typical forward and adjoint fluxes as externally calculated by ADVANTG for the WW generation for MCNP. Left, forward flux values from the MCNP input file as sampled from ADVANTG for the WW creation. Right, adjoint photon flux (the importance function) [Isolan L., et al., 2020]. See Figure 30 for geometry details.
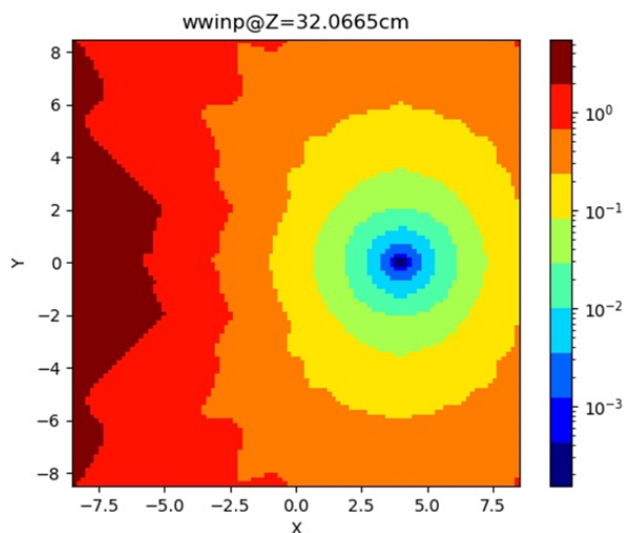
Figure 36. WW value distribution visualization as calculated by ADVANTG [Isolan L., et al., 2020].

The linear dose response behavior of the micro-silica beads has been experimentally evaluated as in Figure 37. The absorbed dose per single PFMA-3 pulse in the micro-silica beads at different depths and positions in the PMMA phantoms can be seen in Table 15.

The experimental benchmark of the setup has been validated through the MCNP5 code with continuous cross-section approach, the multigroup approach, the cell-based WW, the superimposed mesh WW and the ADVANTG tool, as presented in Figure 38, obtaining a good agreement, at least for the purposes of this conceptual work, also proving the effectiveness of the techniques that have been applied [Isolan L., et al., 2020].
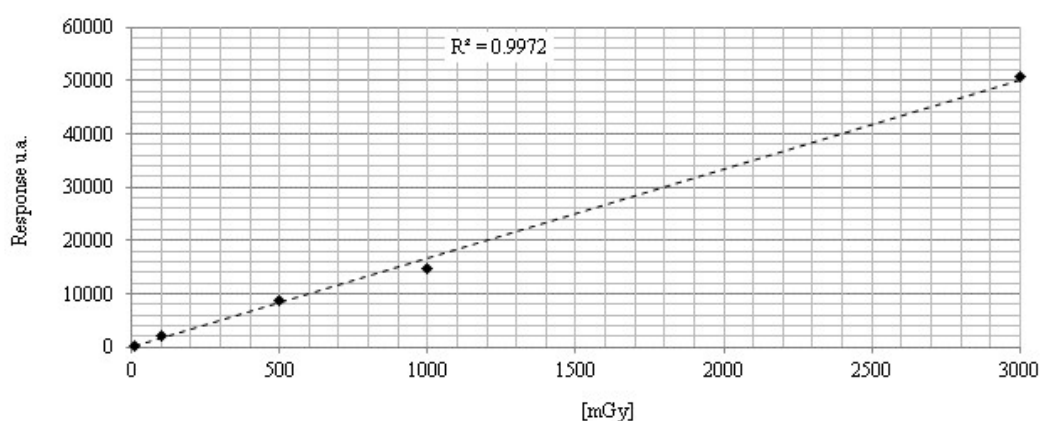
Figure 37. Experimental measurements of the micro-silica beads response at different doses [Isolan L., et al., 2020].

Table 15. Experimentally measured absorbed dose (per PFMA-3 single shot/pulse) in micro-silica beads at different depths and positions in the PMMA phantom [Isolan L., et al., 2020].

Depth in PMMA [mm]	A (Isolan et al., 2019) [Gy pulse^{-1}]	B [Gy pulse^{-1}]	C [Gy pulse^{-1}]
3	0.0895	0.0867	0.0103
6	0.0586	0.0458	0.0046
9	0.0314	0.0239	0.0039
12	0.0202	0.0220	0.0040
20	0.0117	0.0091	0.0027
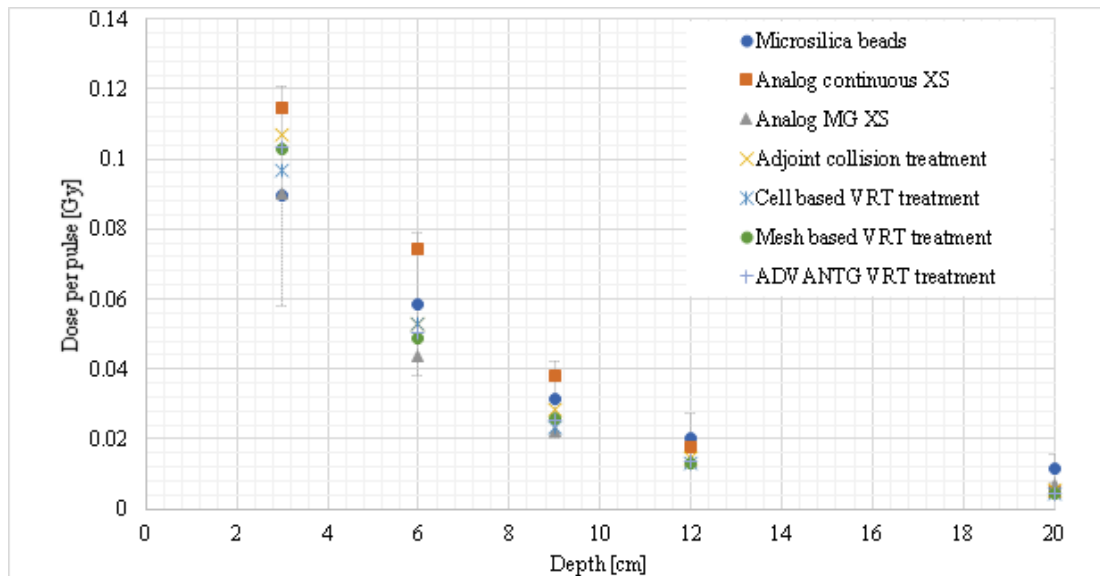
Figure 38. Absorbed dose (per PFMA-3 single pulse) in micro-silica beads at different depths in the PMMA phantom. Comparison between the experimental measurements (35% uncertainty) and the Monte Carlo MCNP5 estimations using both the continuous and the multigroup approaches (with default cross section libraries) and also different VRT [Isolan L., et al., 2020].

In order to verify if the adjoint calculation has been set and executed properly, the results in term of photon fluence have been plotted as a function of the order of scattering, comparing the numerical values between the different forward and backward strategies. The fluence as a function of the order of scattering is very similar in all of the methods, as it should be, proving the correct inversion of the problem procedure. See Figure 39.
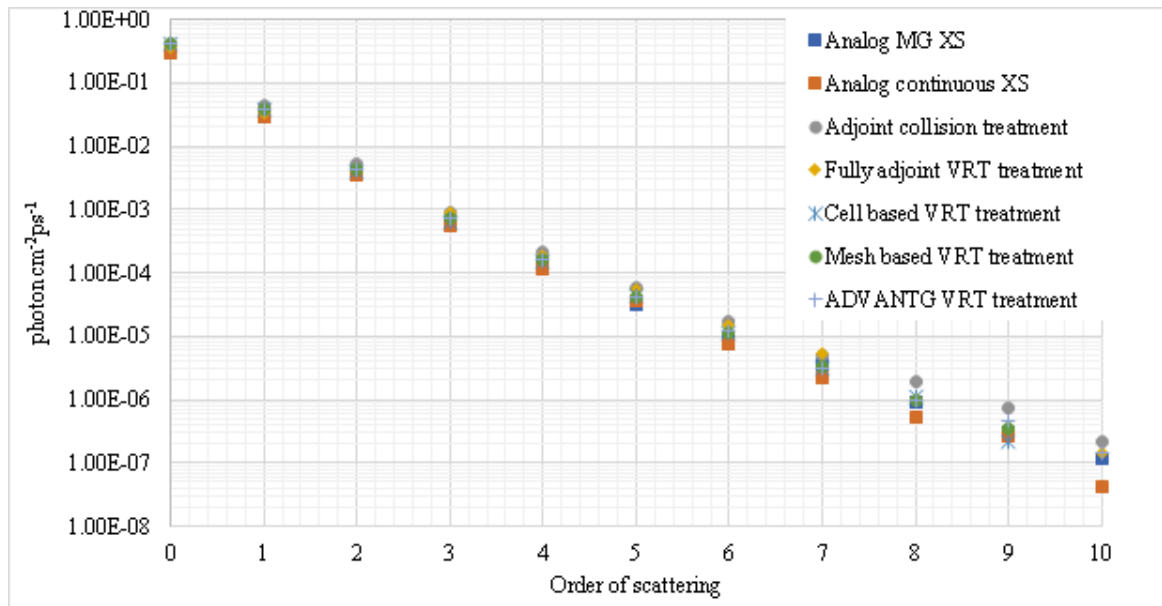
Figure 39. Comparison between the fluence in micro-silica beads in forward continuous, forward multigroup, adjoint collision treatment, fully adjoint treatment, cell based, and mesh based (directly from MCNP or ADVANTG) VRT approaches as a function of the order of scattering. The reported result is related to simulations on the 3 mm depth TLDs. For all the others beads the behavior has been found to be analogous [Isolan L., et al., 2020].

In order to further compare and validate the inversion process, the comparison between the total photon fluence (in a. u.) between the direct (the starting point) and reversed MCNP estimations (the fully adjoint simulation) has been done. The result is that the direct estimation is close to the fully adjoint simulation, but with a small difference of 4.4%.

Sensitivity behavior at PFMA-3 kV energies has been evaluated through MCNP5 and the results are shown in Figure 40, which shows the importance of the micro-silica beads, as a function of depth in the PMMA phantom and estimated on target. The normalized adjoint importance values and flux, as a function of depth, are provided in Figure 41.
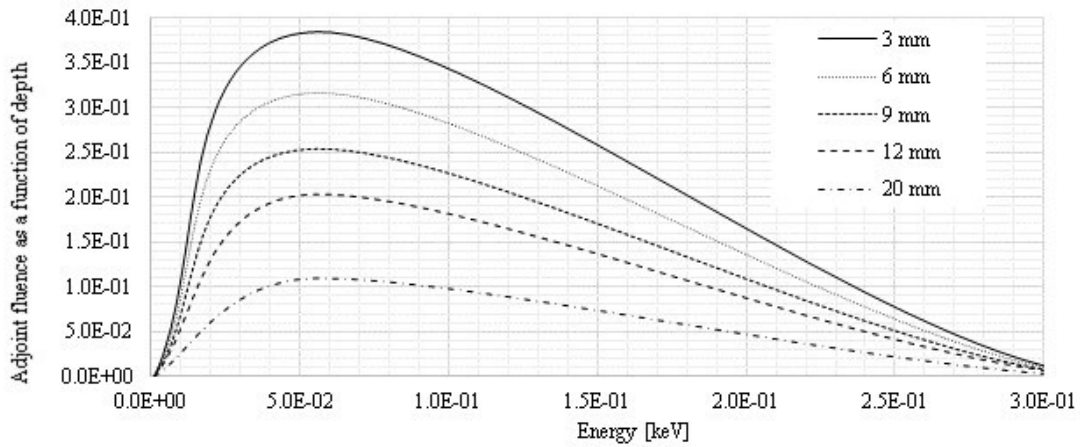
Figure 40. Adjoint photon fluence estimated with MCNP5 at different depth for the different micro-silica beads [Isolan L., et al., 2020].
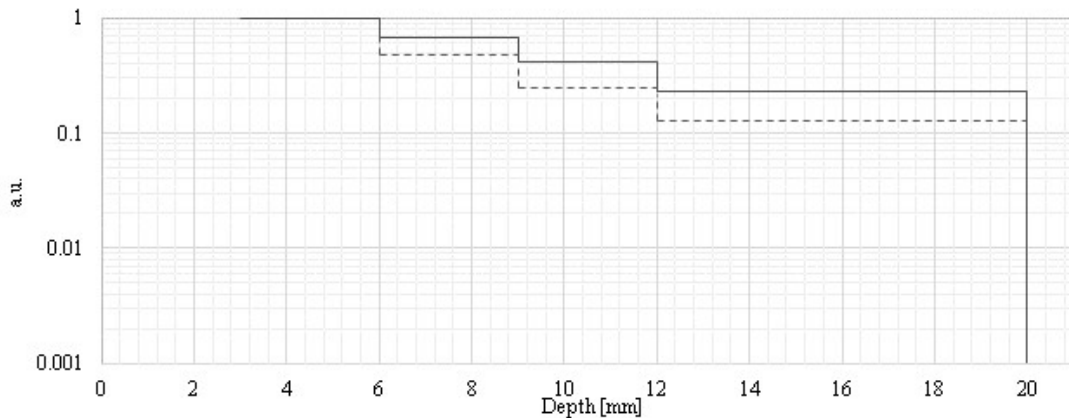
Figure 41. Normalized adjoint importance values (line) as a function of depth in comparison with the photon flux (dashed line) [Isolan L., et al., 2020].

The effects of introducing the adjoint importance functions in such a way to optimize the Monte Carlo tally scoring are presented in Figure 42 as a plot of particle collision. This study is important because it illustrates the different way that the particle transport has been simulated as a result of the adjoint importance function introduction.
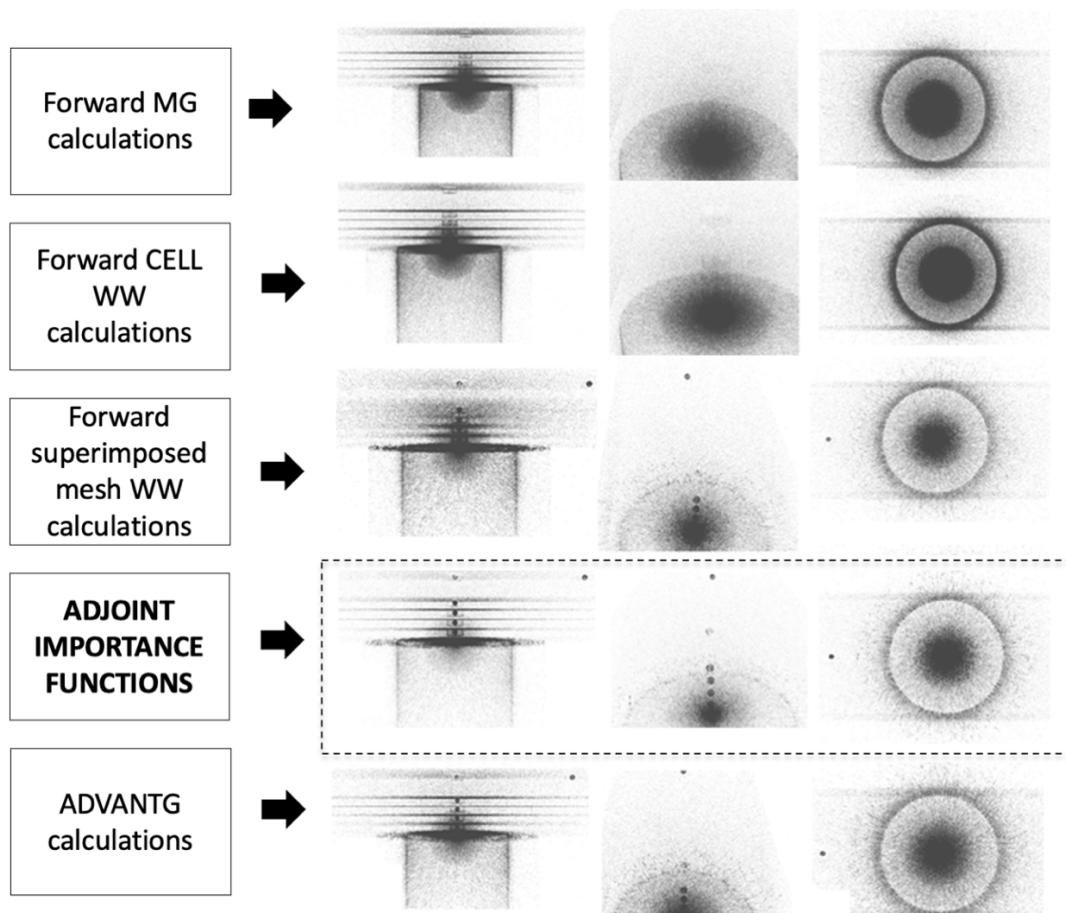
Figure 42. Particle collisions maps in the simulated geometry. First line, MCNP analog simulation (no biasing or VRT techniques). Second line, cell based MCNP WW VRT. Third line, MCNP adjoint importance function (in forward mode when the adjoint importance functions optimized for the micro-silica beads tallies have been applied). Fourth line, ADVANTG WW in MCNP. Fifth line, mesh based MCNP WW VRT. Plot of 1.0E+05 particle collisions [Isolan L., et al., 2020]. Figure generated with the PTRAC_POS2CDSV tool (https://github.com/Radiation-Transport/PTRAC_POS2CSV - ©2019 F4E | European Joint Undertaking for ITER and the Development of Fusion Energy ('Fusion for Energy')).

In Figure 43, the increase in the FOM in the source axis and the increase in the FOM in function of depth are shown for the adjoint importance functions introduced in the forward simulation, with respect to the classical WW techniques and the FW-CADIS approach, and for the "inverse/reverse" problem, taken as reference. A forward optimization from 122% up to 744% has been achieved with the adjoint importance function introduction in the forward calculations, taken as reference. In the adjoint calculations, the FOM increased up to 8800% of its original value. With the previously discussed geometry and options, optimizing the problem in a way that not all the beads are on the axis, would be penalizing for the beads near the source in terms of FOM when applying a mesh WW. In Table 16, the FOM with respect to the analog continuous estimation for the deeper and not in axis bead is shown. The adjoint importance function introduction in the forward calculation increased the FOM of a factor of 5, similarly to the FOM obtained directly simulating the inverse problem (note that the goal was to optimize the out of axis bead calculation performances and investigate the sensitivity of the dosimeters). If the FOM is doubled with the same simulation time, then the simulation time is divided by a factor of two. If the FOM is quadrupled with the same simulation time, then the simulation time is divided by a factor of four.
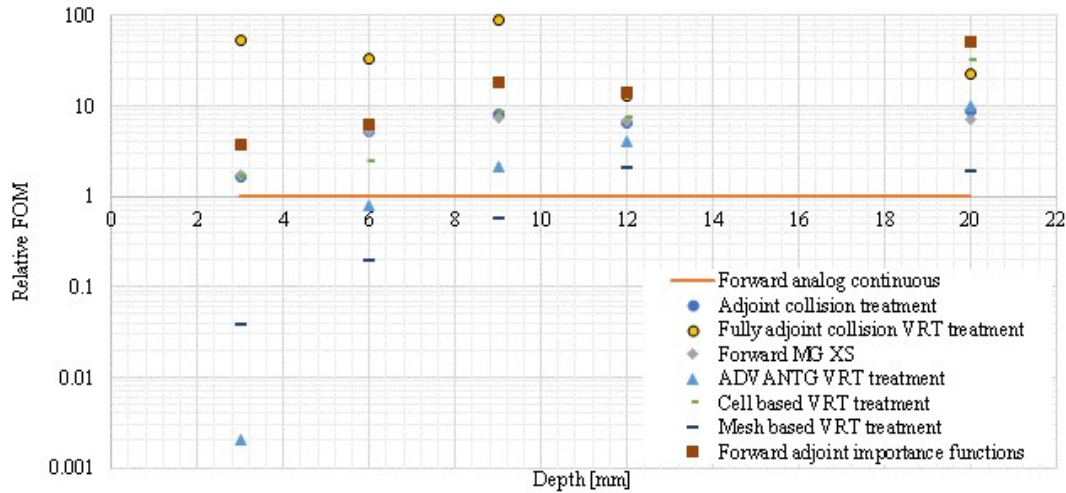
Figure 43. Normalized FOM comparison between the forward mode with WW, the forward mode with the adjoint importance functions, the adjoint calculations and the ADVANTG calculations. Values estimated in depth in the beam axis. Forward analog simulation has been taken as reference [Isolan L., et al., 2020].

Table 16. Normalized FOM calculated for the not in axis and deepest (20 mm in PMMA) bead. FWD analog continuous estimation as reference [Isolan L., et al., 2020].

Simulation treatment	Relative FOM
Forward analog continuous	1.00
Forward MG XS	2.82
Adjoint collision treatment	5.94
Fully adjoint collision VRT treatment	5.79
ADVANTG VRT treatment	1.49
Cell based VRT treatment	1.33
Mesh based VRT treatment	1.56
Forward adjoint importance functions	5.18

Coupling micro-silica beads and forward/adjoint Monte Carlo techniques has been shown to be useful to plan in vivo irradiation illuminating the detector region and in tumor detecting in a patient, simulating his body starting from a CT scan, using a fast and physically biased MCNP model.

Magnetic lens design for focusing the primary electron beam

Moreover, for managing the electron beam shape looking at clinical purposes, a multiple quadrupolar magnetic lens has been designed in such a way to obtain a focal spot of nearly 5 mm diameter as required for patient irradiation instead of the actual 30 mm as designed for cell cultures [Isolan L. and Sumini M., 2020]. As it is known, in a PF device the plasma is pushed by the self-generated Lorentz forces toward the open end of the hollow anode until an implosion occurs, creating the dense magnetized pinch. On the other hands, by looking at a clinical implementation of the technology, some limitations are provided by the Coulomb repulsive forces which spreads the self-collimated electron beam up to tens of mm (suitable for cell culture irradiations) where, for irradiating patient, just few mm are required (not too small in such a way to be able to expose enough tissues but not too big avoiding irradiation also of normal tissues). See Figure 44. Therefore, an in-depth analysis of the angular scatter that occurs during the travel distance between the source (pinch volume) and the target due to the repulsive interaction is aimed at finding a solution to the problem. The main option considered, which is also common in X-ray tubes or accelerators, is to use some focusing equipment. The actual conceptual design of the solution is based on the use of magnetic quadrupoles. The choice of permanent magnets quadrupoles is related to the current avoidance of the introduction of more complex technical equipment. One example is electromagnetic coils for electron beam control in X-ray production. The magnet settings have been analyzed using COMSOL© Multiphysics code and MCNP6 Monte Carlo simulation code (electron spectra recorded through experiments) to investigate deterministic answers to particle trajectories under appropriately designed magnetic fields [Isolan L. and Sumini M., 2020].
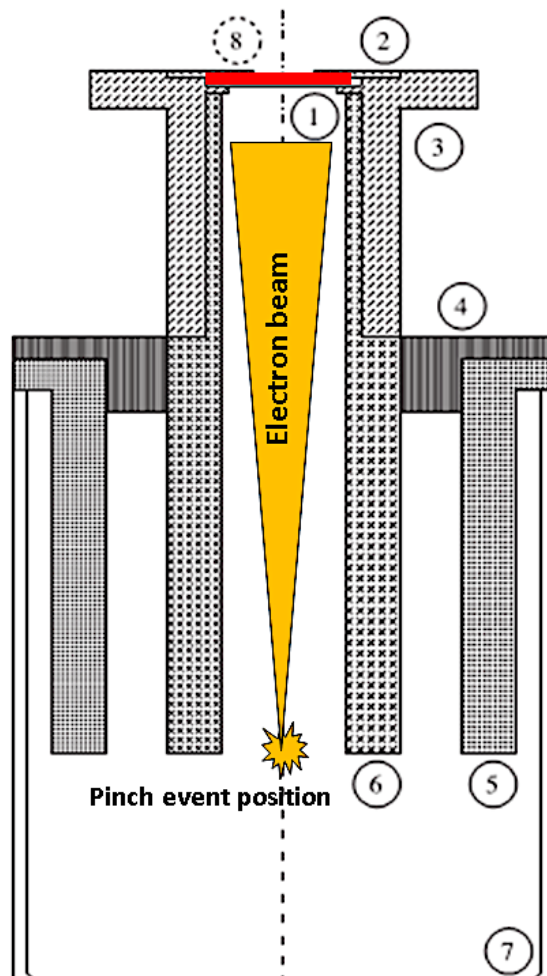
Figure 44. PFMA#3 geometry as shown in [Isolan L. and Sumini M., 2020]. 1, beam target; 2, sealing ring; 3, extraction channel for the particle beam, 4: insulating material between anode and cathode; 5, external electrode; 6, internal electrode; 7, plasma focus vacuum chamber; 8, lead ring collimator (optional). Scale of the not preserved.

A whole PFMA-3 CAD 3D model has been designed and imported into COMSOL©
Multiphysics, Figure 45. A basic design of a triplet of magnetic quadrupoles has been
added to the model, Figure 46. The main components have been isolated and meshed,
Figure 47, Table 17, Table 18. With the support of a parametric sweep, the magnetic
field has been optimized as in Table 19, considering the measured electron spectrum as
measured at 24 kV and 0.40 mbar, splitting the simulations in two steps, one for
calculating the magnetic field lines and the other for transporting particles in it. The
calculated magnetic field lines are shown in Figure 48 while the electrons trajectories
are calculated as in Figure 49 and Figure 50. It can be clearly seen that an effective
focusing effects has been achieved (Table 20).
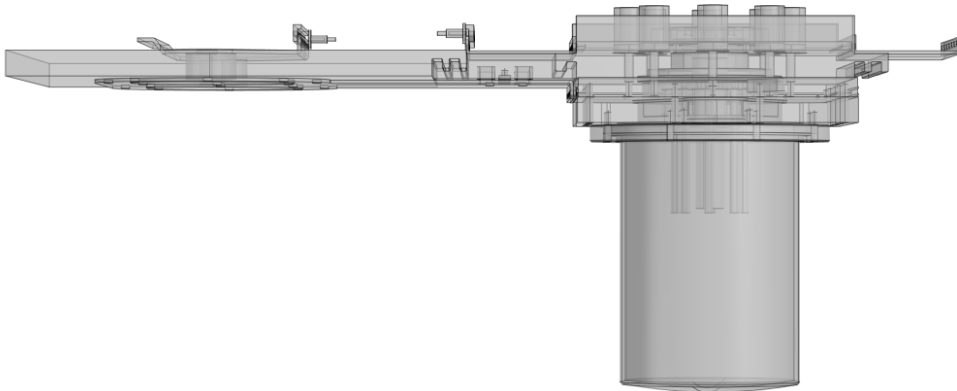
Figure 45. 3D model rendering.
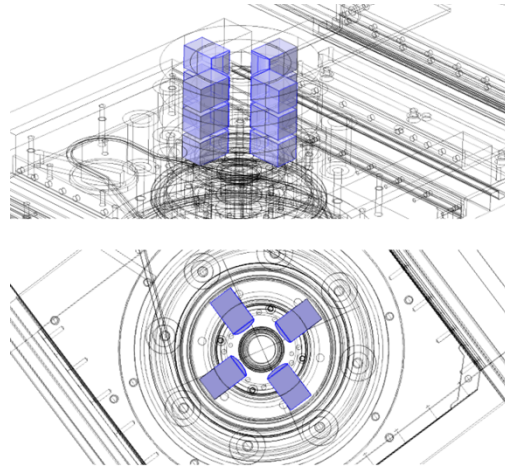
Figure 46. Magnetic quadrupoles on the PFMA-3 model [Isolan L. and Sumini M., 2020].
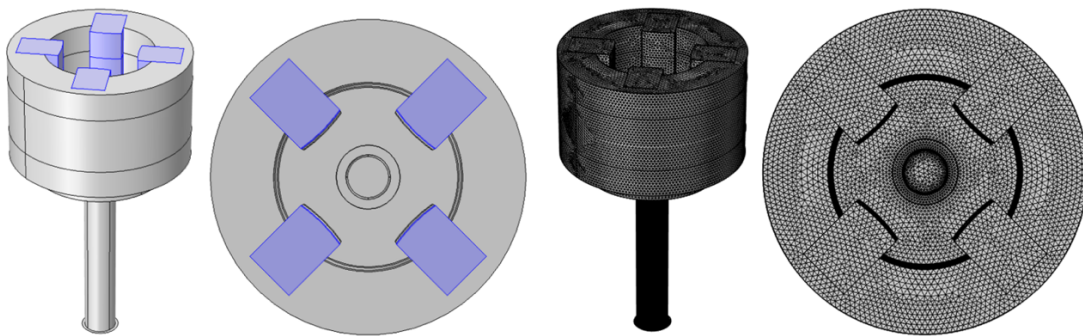
Figure 47. Left, PFMA-3 anode and extraction channel with the quadrupole triplet system (blue, designed magnets). Right, mesh [Isolan L. and Sumini M., 2020].

Table 17. Typical geometric dimension of the quadrupolar triplet system designed in COMSOL Multiphysics [Isolan L. and Sumini M., 2020].

Geometric element	Characteristic dimension
Supports for the upper and lower magnets	8.0 cm, external radius
	5.0 cm, inner radius
	2.4 cm, height
Supports for the central magnets	8.0 cm, external radius
	5.0 cm, inner radius
	4.8 cm, height
Upper and lower magnets	4.32 x 3.36 x 2.4 cm
Central magnets	4.32 x 3.36 x 4.8 cm

Table 18. COMSOL unstructured tetrahedral mesh parameters [Isolan L. and Sumini M., 2020].

Parameter	Value
Mesh general size	Extremely fine
Max Element Size	0.01 m
Minimum Element Size	0.0001 m
Maximum Element Growth Rate	1.3
Curvature Factor	0.2
Resolution of Narrow Region	1.0
Optimization quality	Basic
Tassellation	Automatic
Number of edge elements	172
Number of edge elements	4695
Number of boundary elements	116148
Number of elements	2117489
Minimum element quality	0.1766

Table 19. Magnetic field, particle source and COMSOL simulation principal parameters. MQ, value of the residual magnetic flux for the single magnets. M0, value of the residual magnetic flux along the x and y axes. Xm, initial Maximum Transverse Displacement of the particle beam. Xm' initial Maximum Relative Transverse Velocity. N, number of simulated particles. Em, experimentally measured (with Thomson spectrometer) mean energy of the gaussian spectra for the simulated particles. σ, standard deviation of the electron spectrum. Number of energy bins, the number of the bins for the spectrum discretization (with more than 3 the simulations didn't converge). In the simulation, the coulombian interactions and the relativist treatments were also considered. The simulation followed the electron motion for 3.0E-09 s discretized in 50-time steps [Isolan L. and Sumini M., 2020].

Parameter	Value
MQ [T]	0.296
M0 [T]	0.209
Xm [mm]	12.0
Xm'	0.00
N	1.0E+04
Em [keV]	87.9
σ [keV]	8.5
Number of energy bins	3
Coulomb interactions	Yes
Relativistic treatment	Yes
Formulation	Newtonian
Time step number	50
Time width [s]	3.0E-09
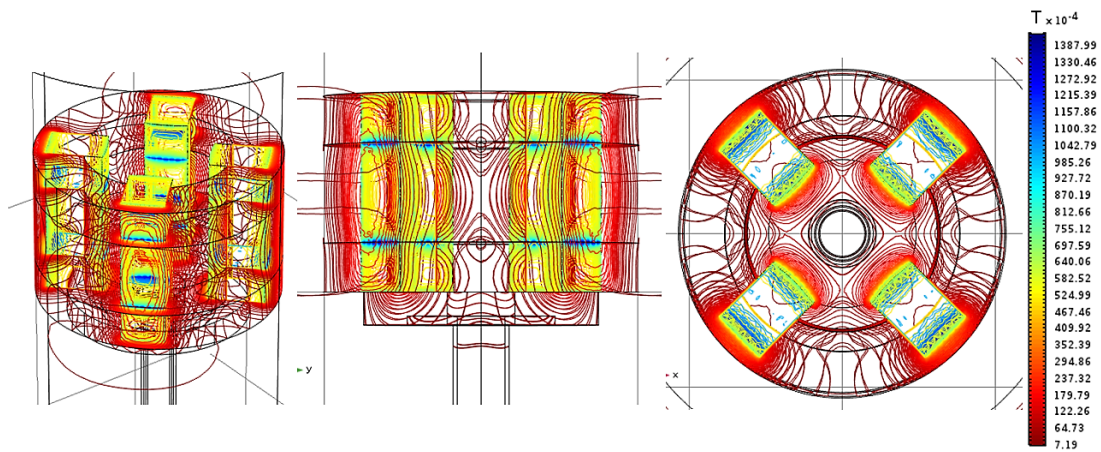
Figure 48.Distribution of the magnetic field lines as calculated in COMSOL Multiphysics [Isolan L. and Sumini M., 2020].
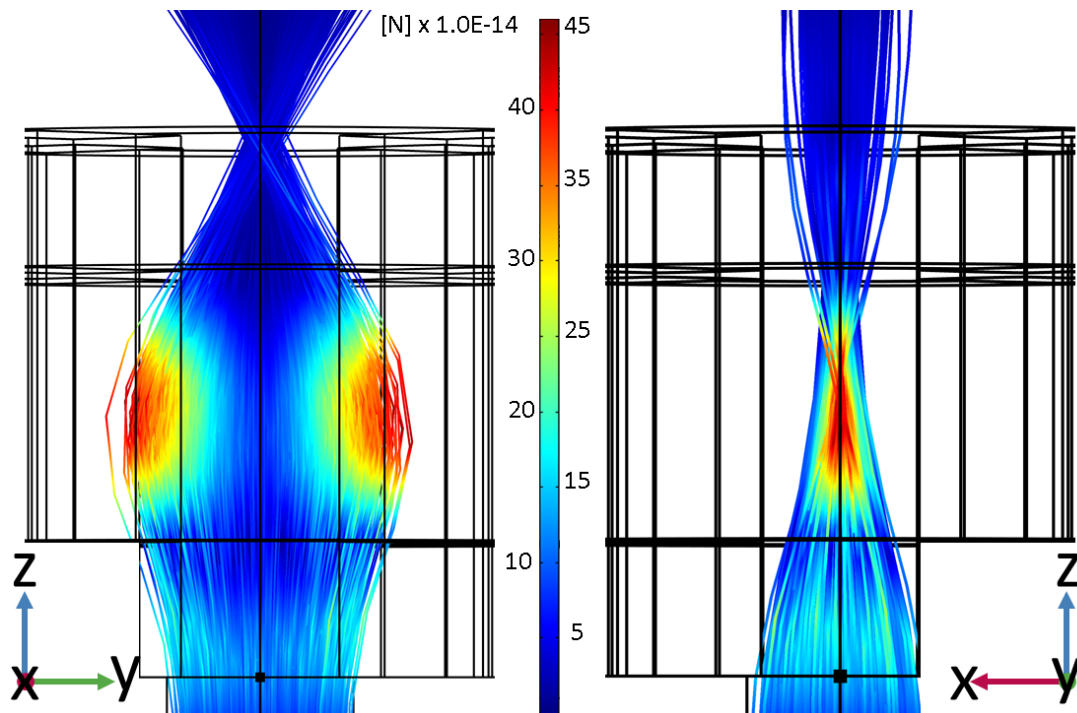
Figure 49. Calculated electron trajectories when interacting with the imposed magnetic field in the COMSOL© Multiphysics simulation. Figure representative of a simulation performed with 10.000 particles. See Figure 4 for dimensions. Left, YZ view. Right, -XZ view [Isolan L. and Sumini M., 2020].
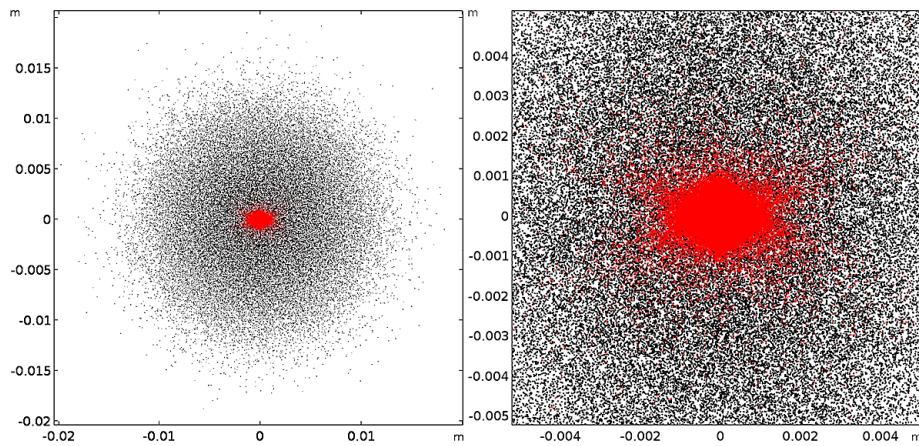
Figure 50. Poincaré maps of the electrons spatial distribution calculated with COMSOL© Multiphysics. Black: electron spatial distribution before entering the quadrupole triplet. Red: electron spatial distribution at the focal spot. Figure representative of a simulation performed with 10.000 particles. Views in the XY plane [Isolan L. and Sumini M., 2020].

Table 20. Magnetic lens focusing efficiency as evaluated thanks to the Poincarè maps, calculated with COMSOL© Multiphysics with a set of Cutting Planes. The focusing factor is calculated as the ratio between the starting beam area and the focal spot area [Isolan L. and Sumini M., 2020].

Starting beam area [cm²]	4.52
Focal spot area [cm²]	0.12
Focusing factor	37.66

The effective COMSOL© Multiphysics designed geometry has been reproduced in MCNP6 also adding details such as lead collimator, brass target (under collimator) and water phantom (Figure 51) [Isolan L. and Sumini M., 2020]. The MCNP electron's source particle spectrum used for the simulation is the one experimentally checked corresponding to a 24 kV power supply of the capacitor bank, that can be considered quite well described by a Gaussian distribution. The sampling from an equivalent Gaussian distribution has also been considered for the particle's initial conditions for the COMSOL simulations. The tallies applied in MCNP include, regarding the standard tallies, the Energy Deposition Tally (F6), the Flux Averaged Over a Cell tally (F4) and, regarding the mesh tallies, the Superimposed Mesh Tally type. The F6 tally has been applied for scoring the photons (particle designator "p") produced by the interaction of the electron beam with a suitable target, estimating the absorbed dose in a water phantom. The F6 tally have been applied with a single energy bin between 1 keV (photon and electron energy cut off as imposed by the Phys card) and 300 keV.

The F4 tally has been used in combination with the Tally Energy (E) card, in order to not have one bin over all energies, that must be introduced in order of increasing values. The F6 tally has been used as dose estimator. In order to verify the focusing effect produced by the designed triplet of quadrupole, the Superimposed Mesh Tally Type A (TMESH, the card that has been chosen) has been applied. The chosen TMESH has been the Type 1 (Track Averaged Mesh Tally) in combination with the FLUX keyword for scoring the average fluence weighted times track length divided by volume in units of #/cm-2.

The application of this card requires also some additional information cards such as CORA data card for mesh coordinate direction #1, CORB data card for mesh coordinate direction #2, CORC data card for mesh coordinate direction #3, ERGSH mesh tally energy or time boundary card, MSHMF response function and the ENDMD block termination card. In the specific case, the RMESH allowed to specify a rectangular mesh described by the coordinate's cards (CORA/B/C) where the bins discretized the space in 100 parts for each 6 cm and in each direction (mesh size equal to 0.06x0.06x0.06 cm).

MCNP6 offers the possibility to apply a magnetic field in the considered geometry and consequently transport the particles in it (see references for other Monte Carlo transport simulations in magnetic fields details), with a direct magnetic field tracking utilizing numerical integration methods.

For models including the quadrupole fields, the user can add the effect of the magnet fringe fields, approximately inserting the hard-edge kicks to the particle entering and leaving the magnetic field cells. It is important to recall the fact that no information about the magnetic fields is written to the output file and particles can get lost, especially for complicated geometries. Due to this reason, the LOST particle control card has been added in the MCNP input file to avoid the run termination by the bad trouble error. The BFLDn card allows the user to create a magnetic field in a specific cell.

In this case, in combination with the BFLDn card, the QUADFF card has been introduced (magnetic field is a quadrupole field with fringe field edge kicks) using a maximum deflection angle equal to 10 mrad, a maximum step size equal to 2 mm and giving the list of surface numbers to which fringe field edge kicks are to be applied.

In the input file, three different BFLD card has been added, one for each group of 4

magnets, in a cell filling the space between them (through the BFLCL in the cell block

part of the input MCNP file, next to the desired cells). The gradient is the one calculated

with Comsol (e.g same geometry and magnetic field) [Isolan L. and Sumini M., 2020].
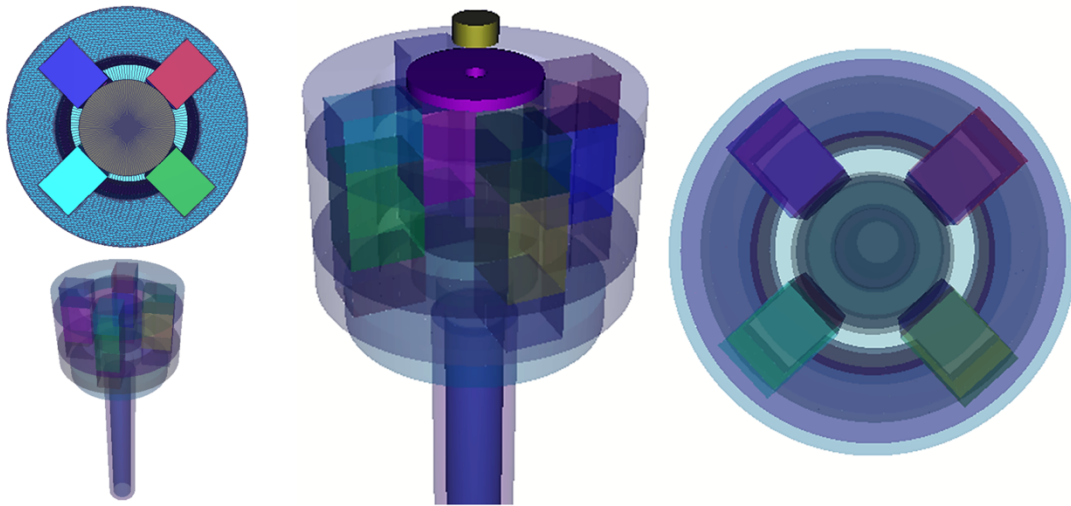
Figure 51. Left, MCNP modelled geometry for reproducing the COMSOL Multiphysics design. Picture plotted by the Vised SW. Center: a lead shield (optional) with a 5 mm hole is visible before the water phantom used for the photon dose estimations (the brass target for the X-rays generation is under the lead shield). Right: plane view of the quadrupole system without the water phantom, the target and the lead shield [Isolan L. and Sumini M., 2020].

An example of used input MCNP file is then reported:

```
10    101    -7.85 -10 11 -12 20   imp:p=1 imp:e=1
20    200 -6e-007 -20 11 -30      imp:p=1 imp:e=1
40    101    -7.85 20 -10 -40 12    imp:p=1 imp:e=1
41    101    -7.85 41 -42 43 -44    imp:p=1 imp:e=1
49    200 -6e-007 -49  imp:p=1 imp:e=1  bflcl 1 $ magnetic field region
50    200 -6e-007 -50  imp:p=1 imp:e=1 bflcl 2 $ magnetic field region
51    200 -6e-007 -51  imp:p=1 imp:e=1  bflcl 3 $ magnetic field region
52      9   -7.874 -52    imp:p=1 imp:e=1 $ first quadrupole
53      9   -7.874 -53    imp:p=1 imp:e=1 $ first quadrupole
54      9   -7.874 -54    imp:p=1 imp:e=1 $ first quadrupole
55      9   -7.874 -55    imp:p=1 imp:e=1 $ first quadrupole
56      9   -7.874 -56    imp:p=1 imp:e=1 $ second quadrupole
57      9   -7.874 -57    imp:p=1 imp:e=1 $ second quadrupole
58      9   -7.874 -58    imp:p=1 imp:e=1 $ second quadrupole
59      9   -7.874 -59    imp:p=1 imp:e=1 $ second quadrupole
60      9   -7.874 -60   imp:p=1 imp:e=1 $ third quadrupole
61      9   -7.874 -61    imp:p=1 imp:e=1 $ second quadrupole
62      9   -7.874 -62    imp:p=1 imp:e=1 $ second quadrupole
63      9   -7.874 -63    imp:p=1 imp:e=1 $ second quadrupole
64     10      -1 -64  imp:p=4 imp:e=1 $ water phantom
65     11   -11.2 65 -66 67 -68 imp:p=1 imp:e=1 $ lead collimator
66    100    -9.7 69 -70 -71 imp:p=1 imp:e=4 $ target
30      0        2000 :4000 :6000 :-1000 :-3000 :-5000  imp:p=0 imp:e=0$ rest of the world
27    200 -6e-007 -2000 -4000 -6000 1000 3000 5000  $ (20 :-
(10 :-11 :12 :-20 )(20 :-11 :30 )(-20 :10 :40 :-12 )
49 50 51
(-41 :42 :-43 :44 )52 53 54 55 56 57 58 59 60 61 62 63 64
(-65 :66 :-67 :68 )(-69 :70 :71 )$(-72 :-73 :-74 :-75 :76 )
```

```
imp:p=1 imp:e=1 $ cell's sense

1000          pz −10
2000          pz 50
3000          px −20
4000          px 20
5000          py −50
6000          py 50
10         cz 2.75
11         pz 0
12         pz 30
20         cz 1.75
30         pz 29.995
40         pz 30.1
41         cz 2.6
42         cz 8.2
43         pz 30.1
44         pz 32.1
49         rcc 0 0 32.2 0 0 2.4 3
50         rcc 0 0 34.6 0 0 4.8 3
51         rcc 0 0 39.4 0 0 2.4 3
52         rpp −6 −3.01 −1 1 32.2 34.6
53         rpp 3.01 6 −1 1 32.2 34.6
54         rpp −1 1 −6 −3.01 32.2 34.6
55         rpp −1 1 3.01 6 32.2 34.6
56         rpp −6 −3.01 −1 1 34.6 39.4
57         rpp 3.01 6 −1 1 34.6 39.4
58         rpp −1 1 −6 −3.01 34.6 39.4
59         rpp −1 1 3.01 6 34.6 39.4
60         rpp −6 −3.01 −1 1 39.4 41.8
61         rpp 3.01 6 −1 1 39.4 41.8
62         rpp −1 1 −6 −3.01 39.4 41.8
63         rpp −1 1 3.01 6 39.4 41.8
64         rcc 0 0 43.9 0 0 1 1
65          pz 41.9
66          pz 42.4
67          cz 0.5
68          cz 3
69          pz 41.895
70          pz 41.900
71          cz 3

mode  p e
…
*tr1 3.7 36.02 3 0 −90 −90 90 −90 0 −90 180 90
SDEF PAR=E POS=0 0 0.00001  ERG=d1 VEC=0 0 1 DIR=1 rad=d2
Si1 H 0.0 0.001689301 0.003362827 0.005599626 0.008392422 0.011732303
0.015608863 0.020010349 0.024923828 0.030335361 0.036230173 0.042592829
0.049407395 0.056657597 0.064326968 0.072398979 0.080857157 0.08968519
0.09886702 0.108386914 0.118229529 0.128379963 0.138823793 0.149547102
0.160536505 0.171779154 0.183262746 0.194975526 0.206906277 0.219044312
0.231379465 0.243902075 0.256602966 0.269473438 0.282505238 0.295690548
0.309021964 0.322492475 0.336095448 0.349824601 0.363673995 0.377638007
0.391711318 0.405888897 0.420165981 0.434538063 0.449000876 0.463550381
0.478182753 0.492894369
SP1 D 0.0 0.000711589 0.000901378 0.001474159 0.002558043 0.004363016
0.007114105 0.010991172 0.015954396 0.022772047 0.030637479 0.039755037
0.050404687 0.061276902 0.072374466 0.081510824 0.090122286 0.094616044
0.093978572 0.085931674 0.07170754 0.053700537 0.037849337 0.025642803
0.014869003 0.00837113 0.003545526 0.00133131 0.000755932 0.000561133
0.001136328 0.000770019 0.000795565 0.000552118 0.000613005 0.000624617
0.00055428 0.000662418 0.000524669 0.000553371 0.000508133 0.000496022
0.00052097 0.000571878 0.001632623 0.001169053 0.001010712 0.000531627
0.00049631 0.000494154
si2 0 1.775
sp2 −21 1
BBREM    1. 1. 46I 100. 100
bfld1 QUAD field=−0.1 vec=1 0 0 axs=0 0 1 MXDEFLC = 10 MAXSTEP = 0.2
bfld2 QUAD field=0.1 vec=0 1 0 axs=0 0 1 MXDEFLC = 10 MAXSTEP = 0.2
bfld3 QUAD field=−0.1 vec=−1 0 0 axs=0 0 1 MXDEFLC = 10 MAXSTEP = 0.2
fmesh24:e geom=xyz
origin −3 −3 29
imesh 3 iints 100
jmesh 3 jints 100
kmesh 43 kints 216
F6:p 64
F4:p 64
f14:e 66
e14 0.001 50i 0.300
TMESH
RMESH21:E FLUX
CORA21 −3 100i 3
CORB21 −3 100i 3
CORC21 29 216i 42
ENDMD
nps 10000000
print
LOST 100000000 10
PRDMP  10000 10000 1 j j
```

The simulation of the particle's transport through a magnetic field in MCNP6 still has some limitations, like i.e. the not really reliable coupled photon transport (i.e. from bremsstrahlung). Then, a formal relationship between the field-lines obtained from COMSOL and the equivalent situation in the MC code is not achievable. Nevertheless, the particle tracking effects can be simulated and the setup in terms of material/geometry allows the scoring of the 3D light charged particles flux spatial distribution with a focusing effect at the same level as in the COMSOL model (see Figure 52). The Monte Carlo simulations allowed also to registering the electron spectrum at the conversion target: as it can be seen from Figure 53 and Table 21, focusing, the X-ray spectrum was noticeably hardened with more high-energy source particles on target, producing a more energetic X-ray shot and a more efficient dose transfer to a phantom (water in the studied configuration), see Table 22.
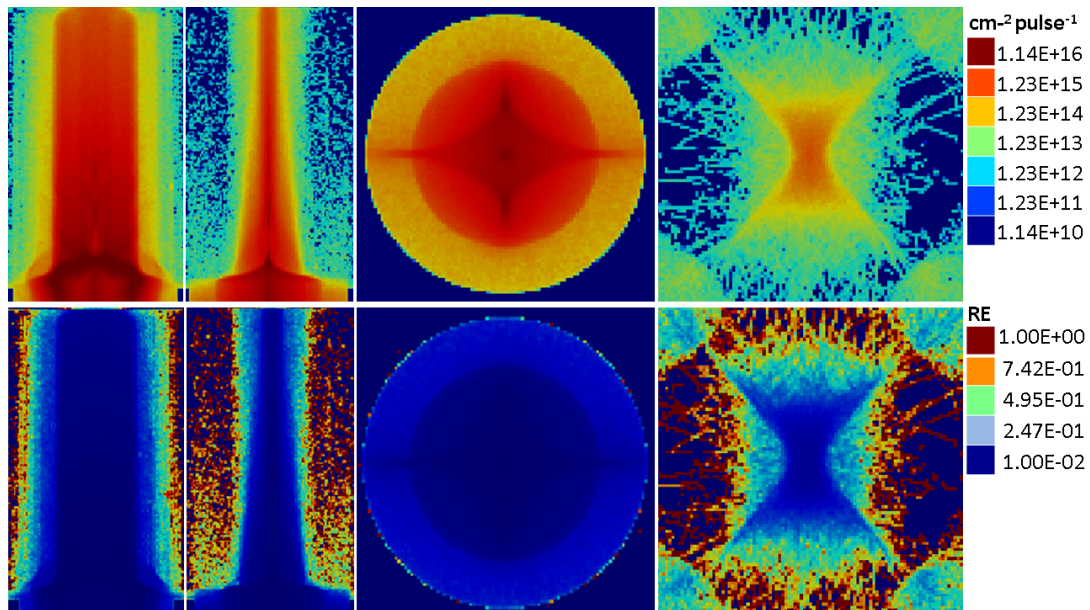
Figure 52. [Isolan L. and Sumini M., 2020] Above: Estimated electron beam when interacting with the magnetic field in the MCNP6 simulations. Logarithmic scale. Below: estimated relative error. 2×10^6 histories result displayed for visualization purposes. From left to right: YZ, -XZ, XY (entering the first quadrupole the spreading effect of the fringe kick is shown), XY (getting out the last quadrupole, at the focal spot) views. Figure generated with the Mesh2Vtk tool (https://github.com/Radiation-Transport/mesh2vtk - ©2019 F4E | European Joint Undertaking for ITER and the Development of Fusion Energy ('Fusion for Energy')), which converts the meshes produced by MCNP and D1S-UNED into a VTK format.
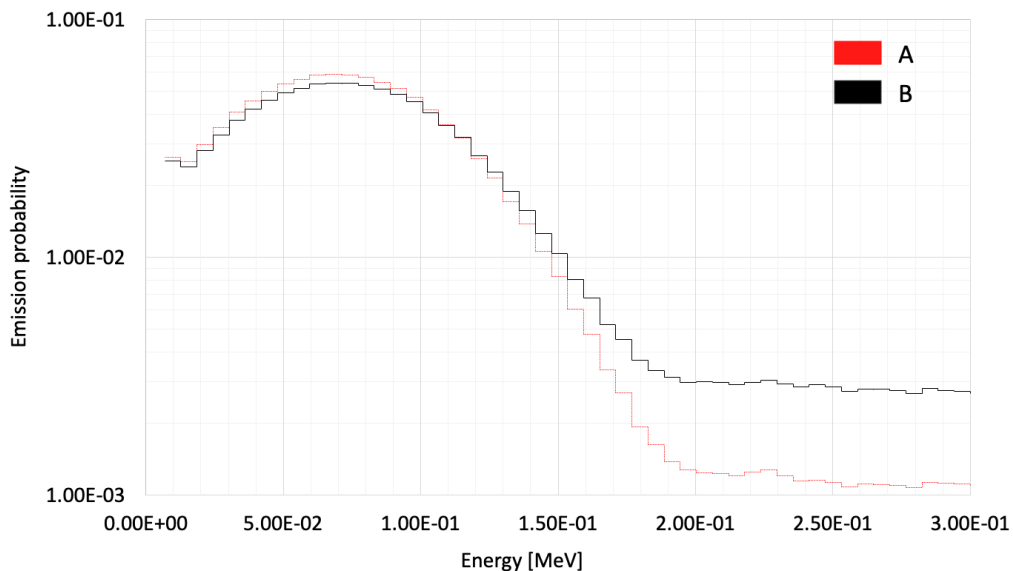
Figure 53. Normalized electron spectra detected at the target. A, spectrum estimated without focusing; B, spectrum estimated with the focusing effect [Isolan L. and Sumini M., 2020].

Table 21. MCNP6 mean electron energy without and with focusing system [Isolan L. and Sumini M., 2020].

	Electron mean energy		
	[keV]	Relative energy increasing [%]	R.E.
A	73.6	Reference value	0.0002
B	83.5	+14	0.0022

Table 22. MCNP6 photon dose estimation in a thick water phantom in configuration A and B [Isolan L. and Sumini M., 2020].

	Photon dose in water phantom	
	Dose [mGy pulse^{-1}] ([%])	Relative Error [%]
A	2.03 (90)	3.18
B	2.25 (100)	5.47

The simulations give a qualitative picture of the effectiveness of the performances of a focus apparatus based on a set of permanent magnets in a quadrupole configuration. The good agreement between the approaches based on COMSOL and on the MCNP6 code, paved the way towards an experimental implementation.

Radiobiological effectiveness evaluation of the flashing photon beam against melanoma cell lines

Finally, a precise idea on the mechanisms of action of UH DR on biological systems is mandatory. New challenges are emerging in terms of updating the well-known mathematical models [Lea DE. and Catcheside DG., 1942] used for the description of the systems evolution (in particular the Surviving Fraction (SF)) caused by the need to have new models capable to support the experimental outcome interpretation when FLASH beams are applied for cell lines or tissues irradiations [Brown JM. and Grave EE., 2014; Pratx G. and Kapp DS., 2019; Carlson DJ., et al., 2008]. To integrate the theoretical models and to support the next generation of biological results, the capability of the Monte Carlo Damage Simulation Software (MCDS) [Stewart R., et al., 2015] has been tested to predict the amount of Double Strand Break (DSB) induced by FLASH sources, referring in particular to the PFMA-3. The MCDS has been then coupled with the MCNP code by exploring the the possible results and correlating FLASH experimental outcomes with the codes inputs and outputs, such as for example the oxygen concentration.

The mechanism behind the radiation damages, at least regarding the determinism of the effects can be described by two different types of interactions. When ionizing radiation (IR) interacts with living matter, ionized particles cause a destabilization that undermines the structure of molecules by two actions called direct interaction and indirect interaction.

1) Direct interaction: results in the direct rupture of a macromolecular structure or DNA.

2) Indirect interaction: the radiation interacts with the water of the molecule producing free radicals such as OH+, OH- and H- (all having an unpaired electron, therefore very responsive). Due to the low stability, the radicals interact with the molecules causing damages and producing other radicals in cascade, going also to ruin the structure of the DNA (deoxyribonucleic acid). Using the usual notation for radical species, "•", and recalling the meaning of (e-)aq as aqueous electron (which is the primary reducing radical formed upon water radiolysis [Herbert JM., 2019]), the cascades are reported by McParland BJ., 2010:

Reaction channel 1: Unstable ions production

$$H20 + IR \rightarrow H2O+• + e-$$

$$H2O + e- \rightarrow H2O-$$
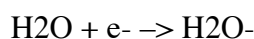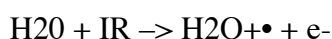
Reaction channel 2:

$$H20 + IR \rightarrow H2O*$$
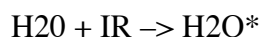
With the free electron recombining as

$$e- + H2O \rightarrow (e-)aq \text{ [Herbert JM., 2019]}$$

Reaction channel 3: The electron ejected by the ionizing radiation can allows the production of H2O+•, highly reactive and unable to recombine with the ejected electron, so:

$$H2O+• \rightarrow H+ + OH•$$

$$H2O+ + H2O \rightarrow H3O+ + OH•$$
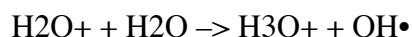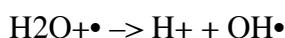
Also the $(e^-)_{aq}$ can interact with water:

$$(e^-)_{aq} + H_2O \rightarrow OH^\bullet + H^+$$
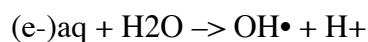
The above-mentioned reactive species have, at maximum, a lifetime of about 10 μs while the ions are characterized by a 0.1 ns lifetime. Such species can diffuse and migrate to the DNA, damaging the helix. On the other hand, the indirect effect must consider the dynamic equilibrium of the ionized organic molecule:

$$RH + IR \rightarrow R^\bullet + H^\bullet$$

It is worth to note that the interaction between $R^\bullet$ and $H^\bullet$ is a function of the amount of oxygen present in the considered system, as oxygen itself is a fee radical scavenger (the radicals interact with it). For this reason, the radioresistance can emerge and arise in hypoxic tissues such as tumors, because the lack of vascularization.

The cell, after the break of macromolecules such as DNA, dies or undergoes mutations in an attempt to repair itself through chemical or enzymatic processes. The cell continually attempts to restore itself but as a result of damage and probable loss of information, both its daughters can go to various fates, depending on the type of damage suffered. If there is only one rupture of the two DNA-forming helices, the repair can be successful because the part of the intact filament is a model for the reconstruction of the damaged tract. It is the case of the Single Strand Break (SSB, less error prone) damage: a propeller breaks and the part of the pattern that contained it is isolated and eliminated. Then there is a polymerization process in which the whole part is reconstructed taking as an example the adjacent patterns. Finally, it is reconnected to the structure and the repair is complete. If both propellers are broken (Double Strand Break, DSB) the information necessary for the cell's recovery is lost and reproduction

could lead to mutation, as well as the case of the rupture of an entire base or a certain number of bridges. If the damage is considerable, the cell will die at the time of reproduction.

Thinking to a biological system, radiation-induced mutations or cell lethality are generated by a single "hit" in which a single ionization event leads to a lesion, or by two independent "hits" in which two separate ionization events occur in close proximity at different times. DSBs are formed when they are physically in close proximity to each other, which can result from the DSBs being produced. One model that can be used for describing the lesions connected at the two different "hits", in terms of Surviving Fraction (SF) is represented by the Linear Quadratic (LQ) model [Lea DE. and Catcheside DG., 1942] (where the SF is linked to the Dose (D) with a description based on α and β parameters, namely the species (two species, from a DSB thanks to the different "hits") [Brenner DJ. and Hall EJ., 1991].

Defining,

- $S(D)$, Surviving;
- α, first-order dose-dependent component to the probability of cell survival;
- β, second-order dose-dependent component to the probability of cell survival;

The LQ model assumes the following form:

$$S(D) = e^{-\alpha D - \beta D^2} \qquad (41)$$

As it is well known, such formalism can be effectively applied when irradiating with conventional sources (adding i.e. the time protractor factor) or assuming an instant enormous transfer of energy, in its simpler description, but could "fails" when FLASH

sources are used, due to oxygen effects, ROS and other physical, chemical and biochemical factors entering in the game. For instance, in Figure 54, an LQ curve, based on the parameters evaluated with conventional sources for SK-Mel28 cell lines is reported for a low dose rate protocol, 0.13 Gy-1 and 0.113 Gy-2 for α and β respectively, 1 minute as half repair time [Brenner DJ. and Hall EJ., 1991].
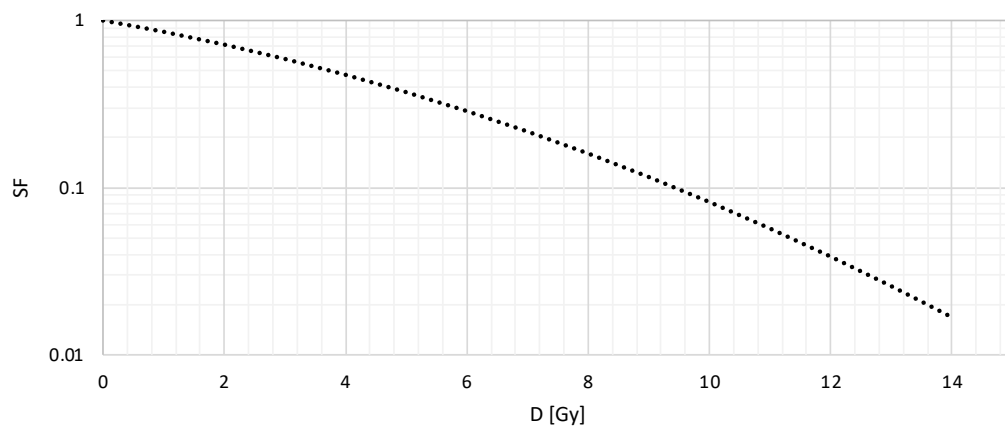
Figure 54. LQ typical model.

The simple model could take also into account the so-called protractor factor G, because if the irradiation is "protracted" in time, the biological system can activate repair mechanisms:

$$G = \frac{2}{D^2} \int\limits_{-\infty}^{+\infty} dt \frac{dD(t)}{dt} \int\limits_{-\infty}^{t} dt' \frac{dD(t')}{dt'} e^{-\mu(t-t')} \qquad (42)$$

The LQ model can be rewritten as the MLQ model (M, modified)

$$S(D) = e^{-\alpha D - G\beta D^2} \qquad (43)$$

$e^{-\mu(t-t')}$ is the repair term of the first DNA damage to produce a DSB, while D is the integral in the $(-\infty, +\infty)$ interval, for the time variable, of the derivative of the dose rate D(t) term. μ is defined as the first order repair constant [Bortfeld T. and Paganetti H., 2006]. The Lea-Catcheside factor can be different depending on how the energy from ionizing radiation is provided to a sample. If the irradiation is extended over time and the dose is a single dose, it can be formulated as

$$S\frac{dD(t)}{dt} = costant = R \qquad (44)$$

and the Lea-Catcheside factor is rewritten as

$$G = \frac{2}{R^2 T^2} \int\limits_{0^-}^{+T} dt R \int\limits_0^t dt' R e^{-\mu(t-t')} = \frac{2}{T^2} \int\limits_{0^-}^{+T} dt \int\limits_0^t dt' e^{-\mu t + \mu t'} \qquad (45)$$

$$= \frac{2}{T^2} \int\limits_{0^-}^{+T} dt e^{-\mu t} \int\limits_0^t dt' e^{\mu t'}$$

By separately solving the two different integrals, for a constant dose rate, the Lea-Catcheside factor is

$$G = \frac{2t_0^2}{T^2}\left(\frac{T}{t_0} + e^{-\frac{T}{t_0}} - 1\right) \qquad (46)$$

With $t_0 = T_{\frac{1}{2}}/\ln(2)$. There are two limit cases to consider, when the irradiation time is long and when is very short, compared to the sample characteristic time.

$$\lim_{T \to +\infty} G(T) = 0 \qquad (47)$$

$$\lim_{T \to 0^+} G(T) = 1 \qquad (48)$$

Other forms can be found by designing the Lea-Catcheside factor (e.g. radioactive decay, see McParland BJ., 2010).

What emerges, is that no simple models well describe the outcomes of FLASH sources. For instance, in the Buontempo F., et al., 2018 work the results on SK-Mel28 and A375 cell lines were modeled with the MLQ formalism but the PFMA-3 results were disaccording (Figure 55) [Isolan L., et al., 2022].
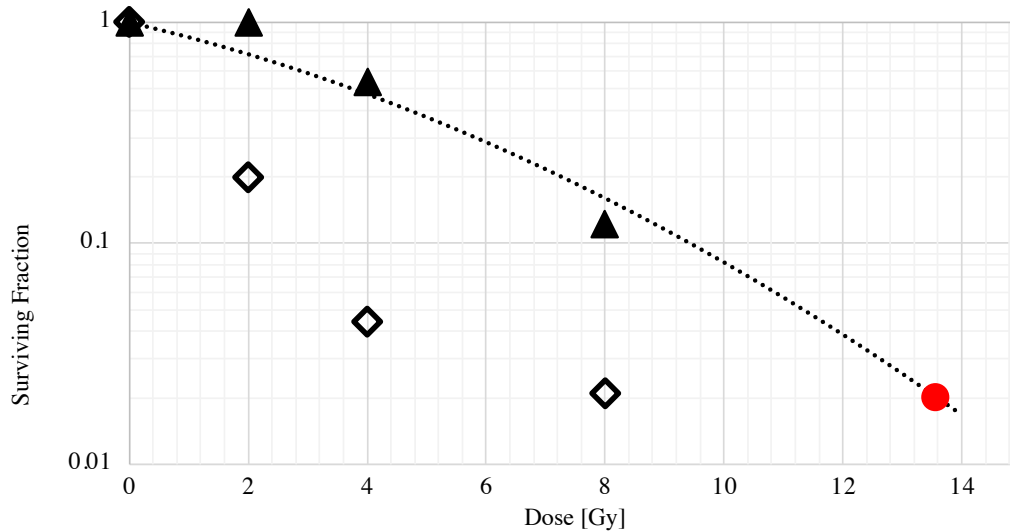
Figure 55. Colony forming unit assay on SK- irradiated with PFMA-3 (rhombus) and XRT (triangles) at 2, 4 and 8 Gy, as published in the Buontempo F., et al., 2018 work. Dashed line, MLQ model. Red dot, MLQ XRT extrapolation up to the same damages produced by the PFMA-3 at 8 Gy [Isolan L., et al., 2022].

In can be clearly seen that FLASH sources and conventional irradiators follow different damage mechanisms and the usual formalism can hardly describe UH-DR outcomes. By extrapolating the MLQ curve, which well describes the XRT experiment results, it is easy to derive that the dose required for conventional sources for replicates the same damage obtained with the PFMA-3 at 8 Gy is 13.6 Gy, e.g., RBE at high doses equal to ~1.7. See Table 23.

Table 23. Radiobiological parameters of SK-Mel28 cell line for PFMA-3 and XRT 2, 4, 8 Gy irradiation [Buontempo F., et al., 2018]. SF2, SF4 and SF8 survival fraction at 2, 4 and 8 Gy respectively. D50, 50% survival dose. The D50 values for XRT device were used as standard reference for the RBE evaluations. The MLQ curve has been built from parameters suggested for SK-Mel28 and for low energy X-ray sources with a correction for the exposure time.

		SF2	SF4	SF8	D(50%) [Gy]	RBE (D(50%))	D(SF=0.02) [Gy]	RBE(SF=0.02)
SK-Mel28	PFMA-3	0.19	0.04	0.02	1.25	3.40	8	1.7
	XRT	1.00	0.53	0.12	4.30	1.00	13.6	Reference

In the same Buontempo F., et al., 2018 work, it is shown that the PFMA-3 resulted to be more effective also in terms of DSB evaluation. See Table 24 and Figure 56 for details. By interpolating the data, it can be seen that the dose required for conventional sources to replicates the same damage obtained with the PFMA-3 at 8 Gy is 13.4 Gy, e.g., RBE at high doses equal to ~1.7 accordingly to what has been found with the SF evaluation. A PFMA-3 saturation effect can be also spotted.

Table 24. DSB obtained with PFMA-3 and XRT for SK-Mel28 cell line at different doses. After irradiation, control and treated cells were seeded on glass slides. Induction of DSB was assessed through detection of phosphorylation of H2A.X at Ser139 (green) [Huang X., et al., 2004; Stope, MB., 2021; Podhorecka M., et al., 2010] by immunofluorescence and microscopy analysis after 4 and 8 Gy treatment. ctrl, control cells. The green "dots" are the cells which experienced a DSB damage. As it can be seen, in the ctrl almost no luminescence can be spotted; on the contrary, in irradiated samples, the cells are clearly visible.

Control samples	Irradiation	Dose [Gy]	Irradiated samples
	PFMA-3	4	
	XRT	4	
	PFMA-3	8	
	XRT	8	
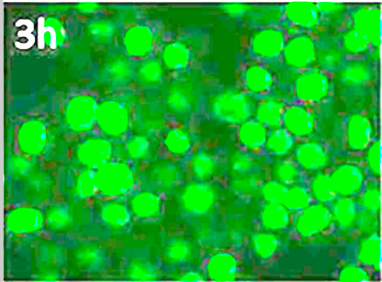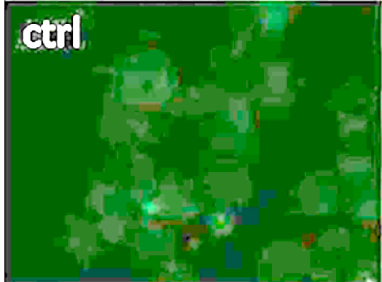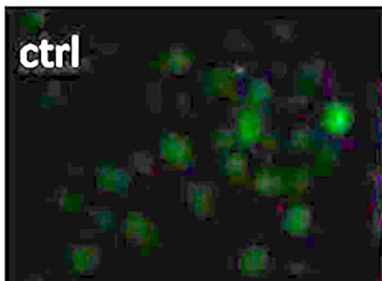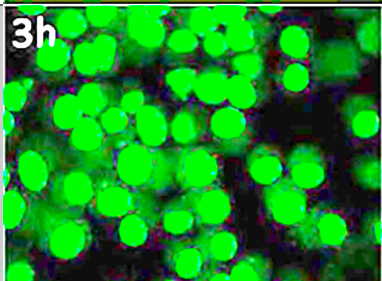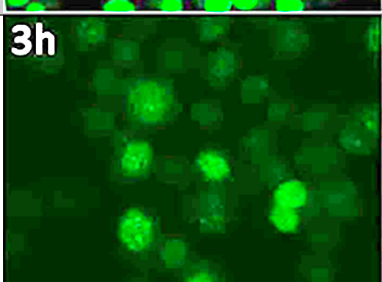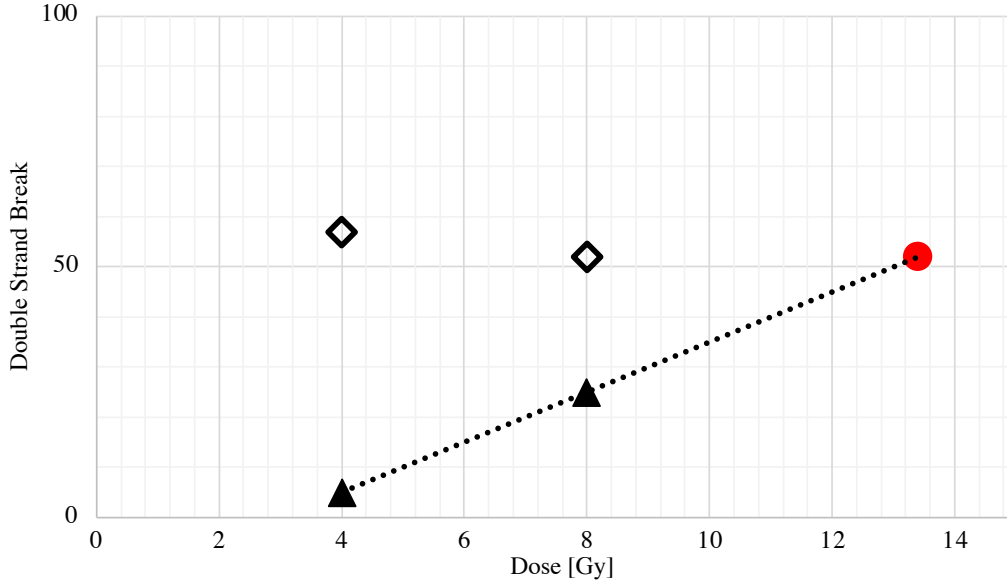
Figure 56. DSB evaluation on SK-Mel28 irradiated with PFMA-3 (rhombus) and XRT (triangles) at 2, 4 and 8 Gy, as published in the Buontempo F., et al., 2018 work. Dashed line, linear interpolation model. Red dot, XRT interpolation up to the same damages produced by the PFMA-3 at 8 Gy [Isolan L., et al., 2022].

The previous results suggested that for high doses RBE(SF) ~RBE(DSB) ~1.7. The Repair Misrepair Fixation (RMF) theory claims that if D≫$\alpha\beta^{-1}$, RBE(SF) ~RBE(DSB) (e.g., the two quantities are similar if the dose is much greater than the ratio of the LQ parameters. In the specific case, $\alpha\beta^{-1}$=1.2 [Brenner DJ. and Hall EJ., 1991] and D(max)=8 [Gy] ≫ $\alpha\beta^{-1}$ [Isolan L., et al., 2022]. The RMF theory can be considered applicable for the studied case.

On the basis of the validation of the RMF theory and considering that it is possible to calculate α and β parameters for a test source (e.g. the PFMA-3) starting from data obtained with conventional source (e.g. XRT) as proposed by Stewart RD., et al., 2018,

$$\alpha_{test} \cong \alpha_{ref} \times RBE_{DSB} \times (1 + X) \qquad (49)$$

$$\beta_{test} \simeq \sqrt{\beta_{ref}} \times RBE_{DSB} \qquad\qquad (50)$$

a simulation strategy has been designed by combining the capability of the MCDS [Stewart et al., 2015; Carlson DJ., et al., 2008] and the MCNP codes. In particular, for finding a way to effectively support the modeling of the experimentally found RBE of the flashing PFMA-3 device, MCDS has been used with MCNP, version 6. MCDS produces a map at the level of the nucleotides in relation to the damage clusters caused by the ionizing radiation interactions with the DNA due to the damage induction in a segment of the DNA uniformly irradiated. The source and geometry details are then incorporated in the simulation by using the MCNP program. For providing information about DNA damages, the Dose Function (DF) was "extracted" from the MCDS and used in MCNP. The basic simulation scheme is shown in Figure 57.
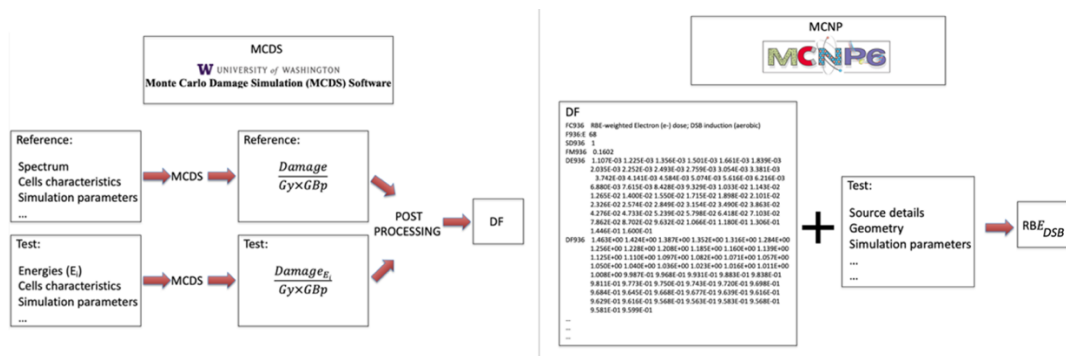
Figure 57. Basic simulation scheme. Left, MCDS data and information flowchart. Right, MCNP data and information flowchart [Isolan L., et al., 2022].

Although MCDS cannot take into account the effects of DR, and the simple LQ model was not well suited to reproduce residual curves in FLASH applications even with a dedicated protractor factor, a computational process was adapted and automated using Python3 by changing:

- the initial cellular conditions of the test source while changing the reference parameters,

- the initial cellular conditions of the reference source while changing the parameters of the same reference,

in such a way to perform a sensitivity analysis variating the Table 25 parameters taken as example of a set and find a "phase space" of possible RBE and SF for supporting experimental results.

The sensitivity analysis can be used to extract one or more RBEs which fits the laboratory data behaviour. The logical scheme is shown in Figure 59 and can be easily extended for other application and sources. However, it can also be extended to test the code under other operative conditions. In Table 25, an example of MCDS parameter "variation table" for one set is shown. The Python3 scripts automated the calculations on 32 different sets and varied the 12 parameters shown in Table 25 per each set in a large range of values. Each of the 32 cases given as output 378 or 388 RBE values. 50 energy bins were used for reproducing the PFMA-3 spectrum, 12 parameters variated and 32 different sets of possible DSB have been evaluated.
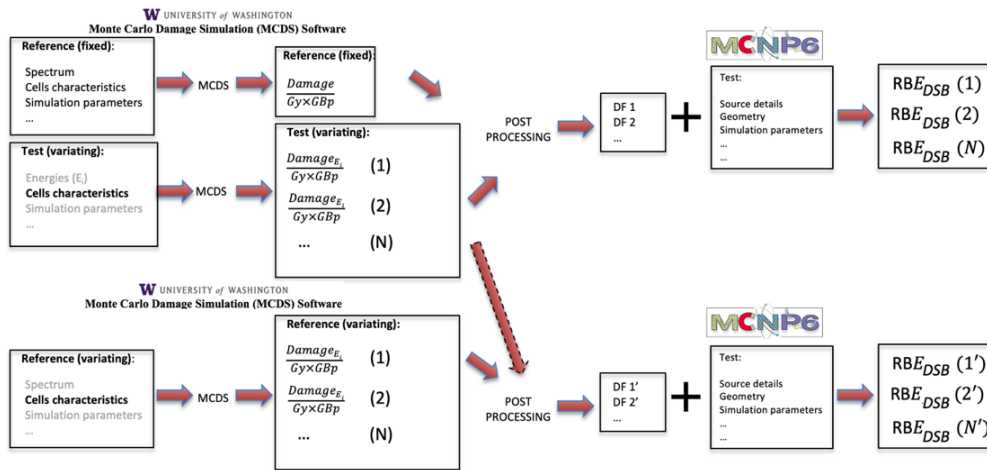
Figure 58. Automatized coupling scheme [Isolan L., et al., 2022].

Table 25. MCDS parameter variation table example per each set. 50 energy points for every PFMA-3 calculation. Globally, 50 MCDS run per every parameter step then repeated for 32 different parameter sets. Variation chosen in order to reach the saturation of the values from a starting point. See Table 26 for the simulation set description related to the values shown below [Isolan L., et al., 2022].

Parameter	Min value	Max value	Intermediate steps	Meaning
NDIA	1	12	5	diameter of cell nucleus (in um) -- used to compute microdosimetric quantities
CDIA	12	20	8	diameter of cell (in um) -- must be greater than or equal to NDIA (default CDIA=NDIA)
WEM	0	1	99	Water-equivalent distance particle must travel to cell surface (mg/cm^2)
pO2	0	100	100	% oxygen concentration (0 to 100%)
m0	0	1000	100	approximate max OER for SSB induction (m0*m0 = approx. max OER for DSB induction)
k	0	100	30	concentration at which half the maximum OER occurs
q	0	1000	2	parameter related to ad hoc correction for radiation quality
r	0	100	4	parameter related to ad hoc correction for radiation quality
fbl	0	1	2	fraction of non-scavengeable DNA damage
CONC	0	5000	2	DMSO concentration (mol dm^-3)
FNSD	0	1	2	concentration at half-level (mol dm^-3)
CHMX	0	10000	10	fraction of total base damage that is an abasic site (site of base loss)

Table 26. One of the simulations set parameters example (other sets with the same presented oxygen initial concentration but different starting nucleus and cell diameters have been also evaluated as 5-5, 6-12, 20-20 [μm] respectively). Values related to the reference and test sources starting condition in the MCDS input files. From the presented starting conditions, the parameters shown in Table 25 have been variated. The number of RBE found for each set is also reported [Isolan L., et al., 2022].

nucleus φ [μm]	cell φ [μm]	%O2 reference source	%O2 test source	[DSB/Gy*GBp] reference source	N. RBE in OUTPUT
12	12	100	100	8.26772E+00	388
12	12	24	24	8.14580E+00	388
12	12	12	12	7.98829E+00	388
12	12	4	4	7.45417E+00	388
12	12	100	100	8.26772E+00	388
12	12	24	100	8.14580E+00	388
12	12	12	100	7.98829E+00	388
12	12	1	100	5.97789E+00	388
12	12	0	100	2.83656E+00	388

The standard use of MCDS was firstly benchmarked against literature data by Stewart RD., et al., 2015, for validating the calculation procedure. A parametric study was performed by varying the incident radiation energy, the material of the anode, and the filter material and thickness, and found a good agreement between data, with some hypothesis introduced in the calculation. See Figure 59.
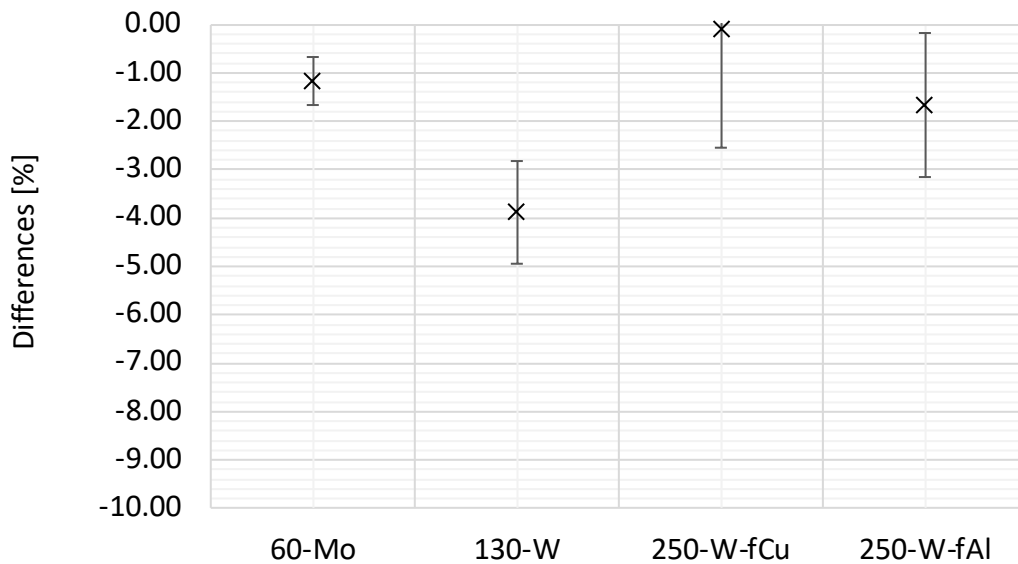
Figure 59. Benchmark with literature data obtained by varying the energy of the X-ray beam from 60 to 250 keV and changing different anode materials and filter characteristics and MCDS option [Stewart RD., et al., 2015; Isolan L., et al., 2021].

For obtaining those results, a standard MCNP model reproducing an X-ray unit has been designed with electrons as particle source (for each case the energy, the filter material and thickness, the anode characteristics, were modified accordingly):

```
c INPUT 0.25 MeV, tungsten anode, copper filter
    1      0          1 :−2 :3 :−4 :5 :−6
    2      1 −0.0012205 −1 2 −3 4 −5 6 (7 :−8 :−9 :10 :−11 )(12 )(13 )(14 )
           (16 :−17 :−18 :19 )(15 )(20 )(21 )
    3      2  −19.25 −7 8 9 −10 11 $ anode
    4      3  −1.848 −12 $ beryllium
    5      1 −0.0012205 −13 $ Score Fluence Detector
    6      4   −8.96 −14 $ Cu filter
    7      5   −1.06 −16 17 18 −19 $ c petri dish side wall
    8      5   −1.06 −15 $ petri dish base
    9      6 −0.998207 −20 $ colture fluid
   10      7         −1 −21 $ cells (monolayer)

    1          px 100
    2          px −100
    3          py 100
    4          py −100
    5          pz 100
    6          pz −100
    7      1  px 0
    8          px −2.5
    9          py −2.5
   10          py 2.5
   11          pz −2.5
   12          rcc 0 0 7 0 0 0.08 6
   13          rcc 0 0 30 0 0 0.5 6
   14          rcc 0 0 31 0 0 0.13 6
   15          rcc 0 0 31.5 0 0 0.1 4
   16          cz 4
   17          cz 3.9
   18          pz 31.6
   19          pz 32.4
   20          rcc 0 0 31.6004 0 0 0.4 3.9
   21          rcc 0 0 31.6 0 0 0.0004 3.9

mode  p e
m1     6000.           −0.000124
       7000.           −0.755268 8000.         −0.231781 18000.         −0.012827
m2     74000.              −1        cond=1
m3     4000.               −1        cond=1
m4     29000.          −1        cond=1
m5     1000.           −0.077421   6000.         −0.922579
m6     1000.           −0.111894   8000.         −0.888106
m7 1000. −0.081192 6000. −0.583442 7000. −0.017798 8000. −0.186381 n12000. −0.130287 17000. −0.0009
*tr1 0 0 0 45 90 −45 90 0 90 135 90 45
imp:p   0               1 8r          $ 1, 10
imp:e   0               1 8r          $ 1, 10
elpt:p j 1e−4
elpt:e j 1e−4
sdef POS=0.05 0 0 AXS=−1 0 0 EXT=0 RAD=d1 PAR=e ERG=0.25
     vec=−1 0 0 DIR=1
si1  0  .01
sp1 −21 1
bbrem 1. 1. 46I 100 3
f4:p 5
e4 0.001 300i 0.25
nps 1e7
```

The photon flux was tallied and used for a new primary X-ray source also applying to

the tally the standard dose functions provided with the MCDS code in such a way to

estimate the RBE and perform the comparison shown in Figure 59:

```
                                                   …
sdef POS=0 0 30.6 AXS=0 0 1 EXT=0 RAD=d1 PAR=p ERG=d2
     vec=0 0 1 DIR=1
si1  0  6.
sp1 −21 1
si2 h 1.0000E−03  1.8272E−032.6545E−03 3.4817E−03 4.3090E−03 5.1362E−03
…
sp2 d 0.0000E+00 1.2666E−04 4.3600E−04 1.0805E−03 1.3060E−03 2.6714E−03
…
fc916   RBE−weighted Electron (e−) dose; DSB induction (aerobic)
f916:e  10
sd916 1
fm916    0.1602
de916    1.000E−05 2.000E−05 3.000E−05 4.000E−05 5.000E−05 6.000E−05
```

```
          7.000e-05 8.000E-05 9.000E-05 1.000E-04 2.000E-04 3.000E-04
          4.000e-04 5.000E-04 6.000E-04 7.000E-04 8.000E-04 9.000E-04
          1.000e-03 2.000E-03 3.000E-03 4.000E-03 5.000E-03 6.000E-03
          7.000e-03 8.000E-03 9.000E-03 1.000E-02 2.000E-02 3.000E-02
          4.000e-02 5.000E-02 6.000E-02 7.000E-02 8.000E-02 9.000E-02
          1.000e-01 2.000E-01 3.000E-01 4.000E-01 5.000E-01 1.000E+00
          1.000e+01 1.000E+02 1.000E+03
df916     3.385E+00 3.354E+00 3.322E+00 3.279E+00 3.235E+00 3.191E+00
          3.140e+00 3.092E+00 3.047E+00 3.002E+00 2.601E+00 2.320E+00
          2.118e+00 1.966E+00 1.852E+00 1.760E+00 1.688E+00 1.627E+00
          1.573e+00 1.314E+00 1.215E+00 1.163E+00 1.129E+00 1.111E+00
          1.094e+00 1.083E+00 1.071E+00 1.062E+00 1.029E+00 1.016E+00
          1.011e+00 1.007E+00 1.006E+00 1.002E+00 1.002E+00 1.003E+00
          9.992e-01 9.963E-01 9.955E-01 9.948E-01 9.944E-01 9.925E-01
          9.910e-01 9.947E-01 9.947E-01
c
fc926     RBE-weighted Electron (e-) dose; DSB induction (anoxic)
f926:e  10
sd926 1
fm926    0.1602
de926    1.000E-05 2.000E-05 3.000E-05 4.000E-05 5.000E-05 6.000E-05
          7.000e-05 8.000E-05 9.000E-05 1.000E-04 2.000E-04 3.000E-04
          4.000e-04 5.000E-04 6.000E-04 7.000E-04 8.000E-04 9.000E-04
          1.000e-03 2.000E-03 3.000E-03 4.000E-03 5.000E-03 6.000E-03
          7.000e-03 8.000E-03 9.000E-03 1.000E-02 2.000E-02 3.000E-02
          4.000e-02 5.000E-02 6.000E-02 7.000E-02 8.000E-02 9.000E-02
          1.000e-01 2.000E-01 3.000E-01 4.000E-01 5.000E-01 1.000E+00
          1.000e+01 1.000E+02 1.000E+03
df926     9.839E+00 9.724E+00 9.590E+00 9.393E+00 9.174E+00 8.929E+00
          8.641e+00 8.359E+00 8.062E+00 7.761E+00 5.123E+00 3.657E+00
          2.887e+00 2.454E+00 2.187E+00 1.996E+00 1.876E+00 1.771E+00
          1.688e+00 1.343E+00 1.232E+00 1.171E+00 1.138E+00 1.118E+00
          1.096e+00 1.086E+00 1.070E+00 1.062E+00 1.030E+00 1.016E+00
          1.009e+00 1.005E+00 1.001E+00 1.001E+00 1.001E+00 1.002E+00
          9.975e-01 9.947E-01 9.951E-01 9.916E-01 9.940E-01 9.919E-01
          9.894e-01 9.946E-01 9.946E-01
c
fc936     Electron (e-) intra-track RMF interaction term (aerobic cells)
f936:e  10
sd936 1
fm936    0.1602
de936    1.000E-05 2.000E-05 3.000E-05 4.000E-05 5.000E-05 6.000E-05
          7.000e-05 8.000E-05 9.000E-05 1.000E-04 2.000E-04 3.000E-04
          4.000e-04 5.000E-04 6.000E-04 7.000E-04 8.000E-04 9.000E-04
          1.000e-03 2.000E-03 3.000E-03 4.000E-03 5.000E-03 6.000E-03
          7.000e-03 8.000E-03 9.000E-03 1.000E-02 2.000E-02 3.000E-02
          4.000e-02 5.000E-02 6.000E-02 7.000E-02 8.000E-02 9.000E-02
          1.000e-01 2.000E-01 3.000E-01 4.000E-01 5.000E-01 1.000E+00
          1.000e+01 1.000E+02 1.000E+03
df936     1.940E-02 3.810E-02 5.605E-02 7.282E-02 8.862E-02 1.035E-01
          1.168e-01 1.295E-01 1.415E-01 1.526E-01 2.291E-01 2.734E-01
          3.039e-01 3.274E-01 3.486E-01 3.671E-01 3.861E-01 4.035E-01
          4.189e-01 5.847E-01 7.486E-01 9.101E-01 1.067E+00 1.226E+00
          1.365e+00 1.495E+00 1.592E+00 1.667E+00 9.033E-01 6.016E-01
          4.692e-01 3.906E-01 3.397E-01 3.014E-01 2.746E-01 2.538E-01
          2.352e-01 1.574E-01 1.320E-01 1.197E-01 1.129E-01 1.017E-01
          1.088e-01 1.235E-01 1.346E-01
c
fc946     Electron (e-) intra-track RMF interaction term (anoxic cells)
f946:e  10
sd946 1
fm946    0.1602
de946    1.000E-05 2.000E-05 3.000E-05 4.000E-05 5.000E-05 6.000E-05
          7.000e-05 8.000E-05 9.000E-05 1.000E-04 2.000E-04 3.000E-04
          4.000e-04 5.000E-04 6.000E-04 7.000E-04 8.000E-04 9.000E-04
          1.000e-03 2.000E-03 3.000E-03 4.000E-03 5.000E-03 6.000E-03
          7.000e-03 8.000E-03 9.000E-03 1.000E-02 2.000E-02 3.000E-02
          4.000e-02 5.000E-02 6.000E-02 7.000E-02 8.000E-02 9.000E-02
          1.000e-01 2.000E-01 3.000E-01 4.000E-01 5.000E-01 1.000E+00
          1.000e+01 1.000E+02 1.000E+03
df946     1.936E-02 3.781E-02 5.517E-02 7.057E-02 8.416E-02 9.567E-02
          1.045e-01 1.118E-01 1.170E-01 1.205E-01 1.050E-01 8.022E-02
          6.669e-02 6.023E-02 5.737E-02 5.572E-02 5.632E-02 5.647E-02
          5.696e-02 7.208E-02 9.081E-02 1.090E-01 1.280E-01 1.465E-01
          1.618e-01 1.775E-01 1.876E-01 1.968E-01 1.069E-01 7.113E-02
          5.519e-02 4.597E-02 3.975E-02 3.554E-02 3.236E-02 2.995E-02
          2.768e-02 1.853E-02 1.557E-02 1.405E-02 1.332E-02 1.199E-02
          1.280e-02 1.458E-02 1.590E-02
c
fc956     Dose-weighted frequency-mean specific energy (ndia=5 um)
f956:e  10
fm956    0.1602
sd956 1
de956    1.000E-05 2.000E-05 3.000E-05 4.000E-05 5.000E-05 6.000E-05
          7.000e-05 8.000E-05 9.000E-05 1.000E-04 2.000E-04 3.000E-04
          4.000e-04 5.000E-04 6.000E-04 7.000E-04 8.000E-04 9.000E-04
          1.000e-03 2.000E-03 3.000E-03 4.000E-03 5.000E-03 6.000E-03
          7.000e-03 8.000E-03 9.000E-03 1.000E-02 2.000E-02 3.000E-02
          4.000e-02 5.000E-02 6.000E-02 7.000E-02 8.000E-02 9.000E-02
          1.000e-01 2.000E-01 3.000E-01 4.000E-01 5.000E-01 1.000E+00
          1.000e+01 1.000E+02 1.000E+03
df956     2.448E-05 4.895E-05 7.343E-05 9.791E-05 1.224E-04 1.469E-04
```

```
          1.713e-04 1.958E-04 2.203E-04 2.448E-04 4.895E-04 7.343E-04
          9.791e-04 1.224E-03 1.469E-03 1.713E-03 1.958E-03 2.203E-03
          2.447e-03 4.892E-03 7.326E-03 9.734E-03 1.209E-02 1.436E-02
          1.649e-02 1.843E-02 2.008E-02 2.137E-02 1.234E-02 8.429E-03
          6.632e-03 5.566E-03 4.853E-03 4.340E-03 3.953E-03 3.649E-03
          3.405e-03 2.293E-03 1.925E-03 1.749E-03 1.650E-03 1.492E-03
          1.601e-03 1.804E-03 1.967E-03
c
fc966    Dose-weighted Electron (e-) stopping power (keV/um)
f966:e   10
sd966 1
fm966    0.1602
de966    1.000E-05 2.000E-05 3.000E-05 4.000E-05 5.000E-05 6.000E-05
          7.000e-05 8.000E-05 9.000E-05 1.000E-04 2.000E-04 3.000E-04
          4.000e-04 5.000E-04 6.000E-04 7.000E-04 8.000E-04 9.000E-04
          1.000e-03 2.000E-03 3.000E-03 4.000E-03 5.000E-03 6.000E-03
          7.000e-03 8.000E-03 9.000E-03 1.000E-02 2.000E-02 3.000E-02
          4.000e-02 5.000E-02 6.000E-02 7.000E-02 8.000E-02 9.000E-02
          1.000e-01 2.000E-01 3.000E-01 4.000E-01 5.000E-01 1.000E+00
          1.000e+01 1.000E+02 1.000E+03
df966    1.632E+01 2.020E+01 2.159E+01 2.213E+01 2.229E+01 2.227E+01
          2.214e+01 2.195E+01 2.172E+01 2.148E+01 1.896E+01 1.695E+01
          1.537e+01 1.412E+01 1.309E+01 1.222E+01 1.148E+01 1.084E+01
          1.028e+01 6.955E+00 5.375E+00 4.428E+00 3.788E+00 3.324E+00
          2.971e+00 2.692E+00 2.465E+00 2.278E+00 1.340E+00 9.811E-01
          7.894e-01 6.693E-01 5.869E-01 5.267E-01 4.807E-01 4.445E-01
          4.153e-01 2.806E-01 2.358E-01 2.144E-01 2.022E-01 1.829E-01
          1.962e-01 2.212E-01 2.420E-01
+f6      10
sd6  1
f16:e    10
sd16  1
f26:p    10
sd26  1
```

The XRT experimental results benchmark by Buontempo, et al., 2018 was done comparing the usual 250 kV reference spectrum [Brenner DJ. and Hall EJ., 1991], finding a positive agreement with the experimental points, (Figure 60). The RBE of the XRT (Comecer SpA device) for H60 beam [ISO 4037-1:2019] was found to be 1.11 relative to the 250 kV reference. The simulations have been run using the standard X-ray input files both for MCNP with DE and DF cards, setting the energy and the filters characteristics accordingly. As it can also be seen in Figure 60, the MLQ formalism has been applied and, as result, it can be said that MCDS allowed to better describe the experimental XRT data.
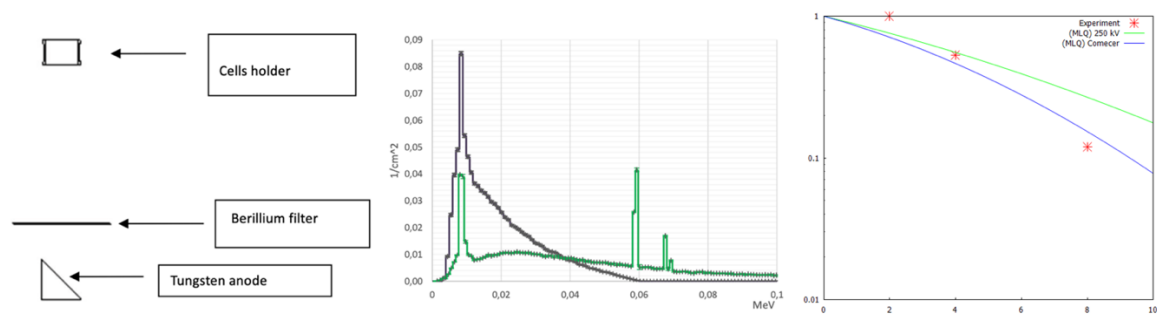
Figure 60. XRT experimental benchmark. Left and center, XRT basic geometry (see also the Stewart RD., et al., 2015 work). Right, LQ fitting of the XRT experimental points, derived with MCDS. The linear and quadratic parameters, personalized for the studied case, were obtained as 0.14 and 0.010 with an R^2 equal to 0.8137 [Isolan L., et al., 2022].

As third step, the comparison between the XRT against the PFMA-3 device has been performed. The modeled geometry is shown in Figure 61 while the MCDS evaluation points have been chosen using a lethargy scale between with 50 discrete energies (for providing more emphasis in the more interesting region).
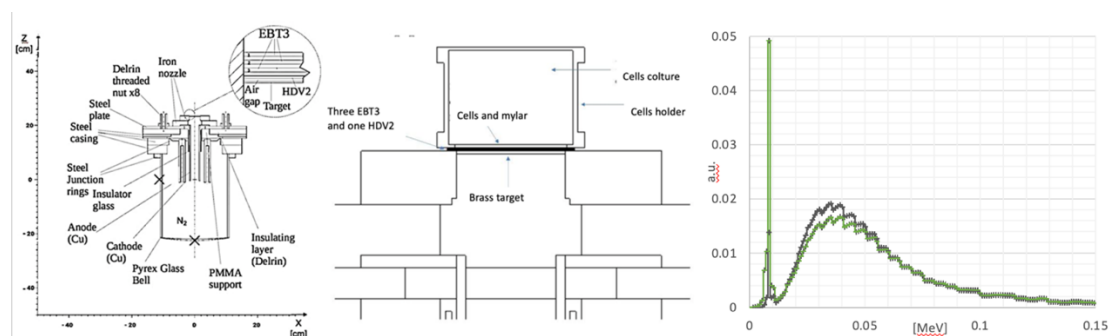
Figure 61. Left, PFMA-3 geometry and spectra targeted before and after the Gafchromic© film dosimeters filter. Right, photon spectra before and after the "filter" [Isolan L., et al., 2022].

The XRT spectrum is represented in MCDS as

```
              Comecer S.p.A.
                   102
e-     1.0000E-03    0.0000E+00
e-     1.9802E-03    1.7058E-02
e-     2.9604E-03    1.6353E-02
e-     3.9406E-03    1.6296E-02
e-     4.9208E-03    1.6677E-02
e-     5.9010E-03    1.7329E-02
e-     6.8812E-03    1.8442E-02
                 ...
e-     1.0000E-01    0.0000E+00
```

While for MCDS the standard input file was used

```
CELL:    DNA=1 NDIA=5 CDIA=5 WEM=0
SIMCON: nocs= seed=987654321
RADX:    FN=sorgente_riferimento.dat
EVO2:    pO2=100 m0=1.74 k=0.3372 q=946.1 r=2.15
MCDS: fbl=0
DMSO: CONC=0 FNSD=0.5 CHMX=0.5
```

The following notation was used:

- CELL: Cell Characteristics and Parameters

    o DNA = DNA content of cell nucleus (in Gbp)

    o NDIA = diameter of cell nucleus (in um) -- used to compute microdosimetric quantities

    o CDIA = diameter of cell (in um) -- must be greater than or equal to NDIA (CDIA=NDIA)

    o WEM = Water-equivalent distance particle must travel to cell surface (mg/cm^2)

- SIMCON: "simulation control" parameters

    o seed = seed for random number generator (default = 987654321)

    o nocs = number of MC simulations (ea. simulation represent damage to one cell)

- RADX: "radiation exposure" parameters

    o FN = {name of a secondary input file specifying a poly-energetic and/or mixed radiation field}

    o PAR = particle type (e.g., e, p, 1H, 2H, 4He, 12C, 56Fe, ...}

    o KE = kinetic energy of particle (MeV)

    o MeV/A = kinetic energy specified as MeV per nucleon (often used for massive ions)

- o AD = absorbed dose (Gy)

  - *NOTE: If a filename is specified, the information associated with the PAR and KE keywords will be ignored*

- EVO2: Environmental O2 Concentration ("oxygen effect")

  - o pO2 = % oxygen concentration (0 to 100%)

  - o mmHg = alternate method to specify the oxygen concentration (760 mmHg= 100%)

  - o m0 = approximate max OER for SSB induction (m0*m0 = approx. max OER for DSB induction)

  - o k = concentration at which half the maximum OER occurs

  - o q = 1st parameter related to ad hoc correction for radiation quality

  - o r = 1st parameter related to ad hoc correction for radiation quality

- DMSO: Parameters related to simulating the effects of DMSO

  - o CONC = DMSO concentration (mol dm^-3)

  - o FNSD = fraction of non-scavengeable DNA damage

  - o CHMX = concentration at half-level (mol dm^-3)

- MCDS: Other adjustable damage simulation parameters

  - o fbl = fraction of total base damage that is an abasic site (site of base loss)

And a typical output (Table 27):

Table 27. Extract of the MCDS output file for the XRT simulation.

Number of lesions	DSB		SSB		OTHER		ALL CLUSTERS	
	Average	SEM	Average	SEM	Average	SEM	Average	SEM
1	---	---	1.0E+2	5.0E-2	3.2E+2	1.3E-1	4.3E+2	1.7E-1
2	4.0E+0	8.0E-3	5.1E1	2.5E-2	7.1E+1	2.9E-2	1.2E+2	3.8E-2
3	2.6E+0	6.6E-3	1.8E+1	1.9E-2	1.5E+1	1.6E-2	3.6E+1	2.9E-2
4	1.2E+0	4.6E-3	6.1E+0	1.1E-2	3.3E+0	8.0E-3	1.0E+1	1.6E-2
5	4.6E-1	2.8E-3	1.9E+0	6.2E-3	7.4E-1	3.6E-3	3.1E+0	8.5E-3
6	1.7E-1	1.7E-3	5.8E-1	3.3E-3	1.6E-1	1.6E-3	9.1E-1	4.4E-3
7	5.9E-2	1.0E-3	1.7E-1	1.7E-3	3.4E-2	7.6E-4	2.6E-1	2.2E-3
8	2.0E-2	5.8E-4	5.1E-2	9.4E-4	7.6E-3	3.5E-4	7.9E-2	1.1E-3
9	6.2E-3	3.2E-4	1.3E-2	4.8E-4	1.7E-3	1.7E-4	2.1E-2	6.1E-4
10	2.2E-3	1.9E-4	4.1E-3	2.6E-4	3.5E-4	7.6E-5	6.6E-3	3.3E-4
11	6.0E-4	9.9E-5	1.1E-3	1.4E-4	6.6E-5	3.3E-5	1.8E-3	1.7E-4
12	2.0E-4	5.7E-5	4.6E-4	8.8E-5	3.3E-5	2.3E-5	7.0E-4	1.0E-4
13	5.0E-5	2.8E-5	6.6E-5	3.3E-5	---	---	1.1E-4	4.4E-5
14	1.6E-5	1.6E-5	5.0E-5	2.8E-5	---	---	6.6E-5	3.3E-5
15	---	---	---	---	---	---	---	---
16	1.6E-5	1.6E-5	---	---	---	---	1.6E-5	1.6E-5
...	...	...	...	...	...	...	...	....
Total	8.6E+0	1.1E-2	1.8E+2	2.9E-2	4.1E+2	1.1E-1	6.1E+2	1.2E-1

Looking at the total DSB obtained with MCDS for the reference source, a series of 50 run for modeling the PFMA-3 spectra in lethargy scale have been run. A lethargy scale was chosen for better describes the lower energies (Figure 62):
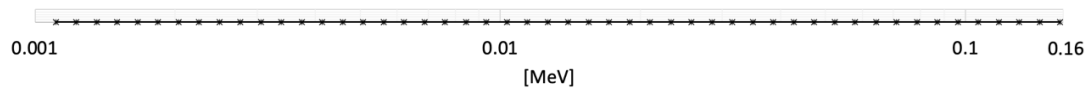
Figure 62. Energy axis discretization. Lethargy scale.

For each energy, an MCDS run has been performed with the goal to build the DE-DF function for the PFMA-3 in MCNP. In particular, by iterating on the KE parameter, with the default MCDS input file setup, a series of 50 run were done (see Table 28 for an extract of an output file of one of the 50 run):

```
CELL:    DNA=1    NDIA=5 CDIA=5 WEM=0
SIMCON:  seed=987654321 nocs=10000
RADX:    PAR=e    KE=0.001106834
EVO2:    p02=100 m0=1.74 k=0.3372 q=946.1 r=2.15
MCDS:    fbl=0
EMSO:    CONC=0 FNSD=0.5 CHMX=0.5
```

Table 28. Extract of the MCDS output file for one energy bin of the PFMA-3 simulation.

Number of lesions	DSB		SSB		OTHER		ALL CLUSTERS	
	Average	SEM	Average	SEM	Average	SEM	Average	SEM
1	---	---	7.4E+1	5.3E-2	2.2E+2	9.3E-2	3.0E+2	1.1E-1
2	3.9E+0	1.4E-2	5.0E+1	4.7E-2	6.9E+1	5.4E-2	1.2E+2	7.2E-2
3	3.7E+0	1.4E-2	2.5E+1	3.5E-2	2.1E+1	3.1E-2	5.0E+1	4.7E-2
4	2.3E+0	1.1E-2	1.1E+1	2.3E-2	6.6E+0	1.8E-2	2.0E+1	3.1E-2
5	1.3E+0	8.2E-3	5.2E+0	1.6E-2	2.0E+0	1.0E-2	8.5E+0	2.0E-2
6	6.7E-1	6.0E-3	2.2E+0	1.0E-2	6.3E-1	5.7E-3	3.5E+0	1.3E-2
7	3.2E-1	4.1E-3	9.2E-1	7.1E-3	1.9E-1	3.2E-3	1.4E+0	8.6E-3
8	1.4E-1	2.8E-3	3.8E-1	4.4E-3	5.9E-2	1.8E-3	5.9E-1	5.5E-3
9	6.5E-2	1.8E-3	1.5E-1	2.9E-3	1.8E-2	1.0E-3	2.4E-1	3.6E-3
10	3.4E-2	1.3E-3	6.1E-2	1.8E-3	5.3E-3	5.4E-4	1.0E-1	2.3E-3
11	1.5E-2	9.2E-4	2.4E-2	1.1E-3	1.8E-3	3.1E-4	4.1E-2	1.5E-3
12	6.7E-3	6.0E-4	8.6E-3	6.8E-4	7.7E-4	2.2E-4	1.6E-2	9.3E-4
13	3.3E-3	4.3E-4	4.5E-3	5.0E-4	2.7E-4	1.2E-4	8.1E-3	6.8E-4
14	7.7E-4	2.0E-4	1.2E-3	2.6E-4	---	---	2.0E-3	3.3E-4
15	4.4E-4	1.5E-4	5.0E-4	1.6E-4	---	---	9.4E-4	2.2E-4
16	2.7E-4	1.2E-4	2.7E-4	1.2E-4	---	---	5.5E-4	1.7E-4
...	...	...	...	...	...	...	...	....
Total	1.2E+1	2.2E-2	1.7E+2	5.3E-2	3.2E+2	7.9E-2	5.0E+2	8.1E-2

And the DE-DF were obtained and used in a dedicated PFMA-3 MCNP input file (see Appendix C).

In such conditions, the RBE of the PFMA-3 has been found to be 1.15 and 1.18 in the anoxic and aerobic cases. As expected, due to the impossibility of considering the DR in MCDS, the RBE of the PFMA-3 and XRT have been found to be "quite similar" and far from the goal of 1.7.

In this case, a dedicated DE and DF cards have been estimated for an accurate description of the phenomena.

The Python3 scripts used the Figure 59 logic, automatizing the simulation processes and performing the MCDS-MCNP sensitivity analysis by varying the code parameters and obtaining three different kinds of results: 1) DSB maps in function of Energy, DSB value, parameter variation; 2) RBE charts per simulation sets, RBE value, parameter variation; 3) SF curves per set, parameter variation, alpha and beta values. An example of a set of estimated DSB is shown for the oxygen variation (Figure 63), the oxygen enhancement ratio (OER, M0 parameter) and water-equivalent distance that particles must travel to cell surface (WEM) in one of the simulated 32 set, Figure 64. In Figure 65 the RBE results for the oxygen are shown with evidence of the set that resulted in an RBE(DSB)=RBS(SF=0.02)≅1.7 fitting the experimental result applying the RMF theory; the same for Figure 66 regarding M0 and WEM. In Figure 67, Figure 68 and Figure 69, the related SF curves span is also shown.
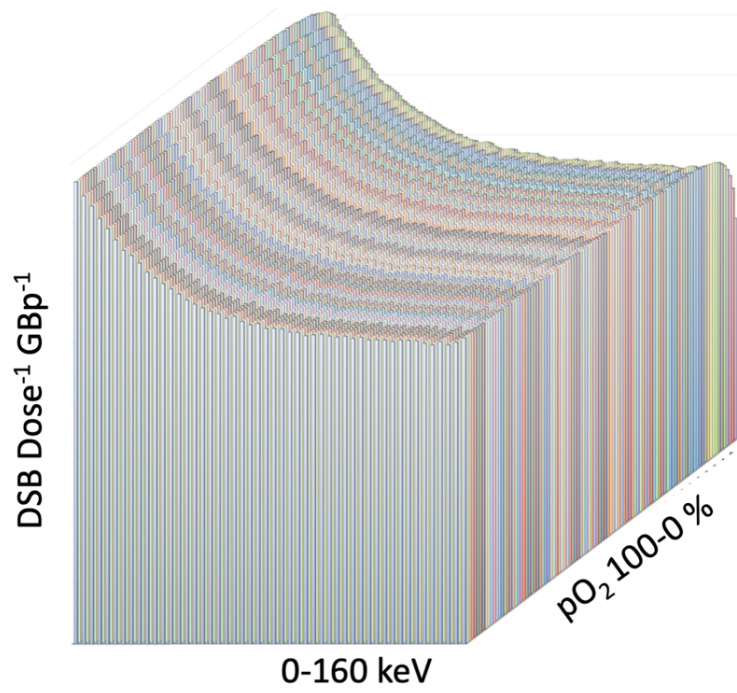
Figure 63. Example of DSB in function of the energy and the O2 variation parameter for one of the simulated sets [Isolan L., et al., 2022].
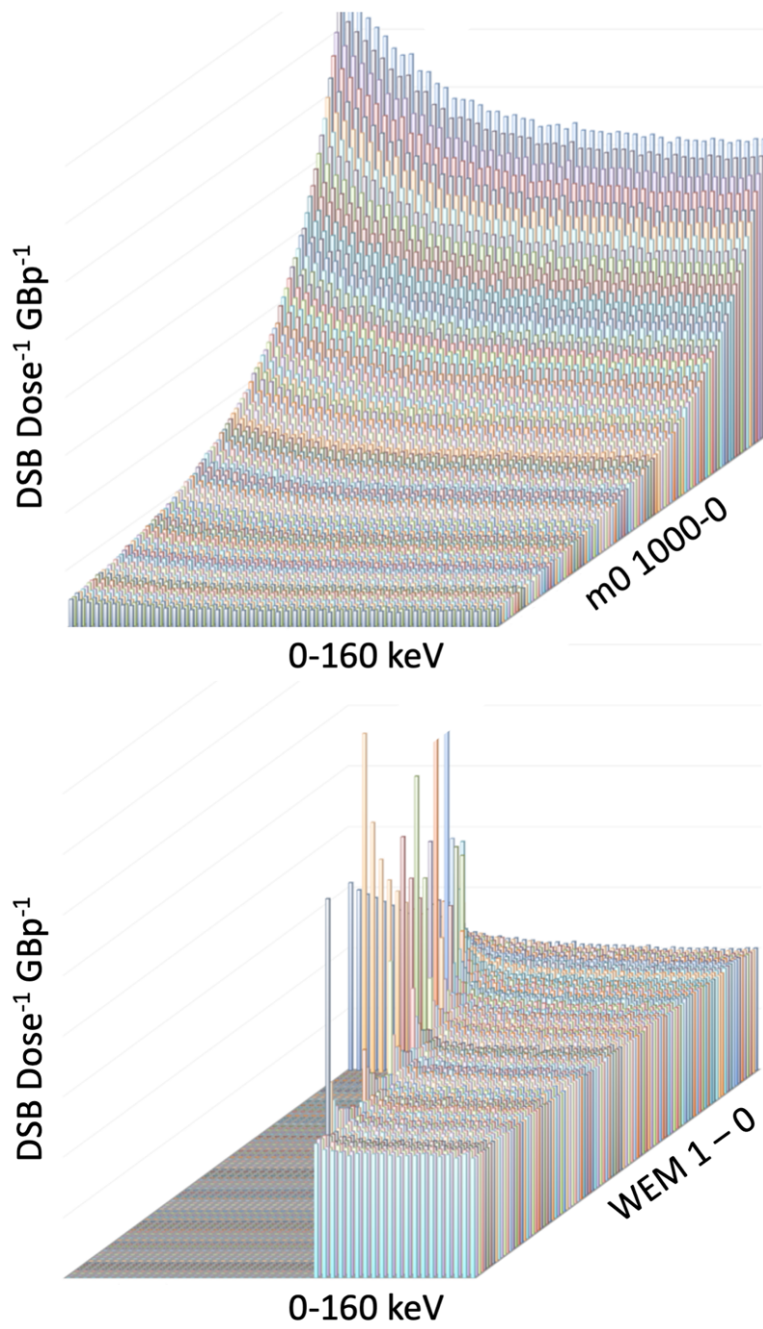
Figure 64. Example of DSB in function of the energy and the M0 and WEM variation parameter for one of the simulated sets [Isolan L., et al., 2022].
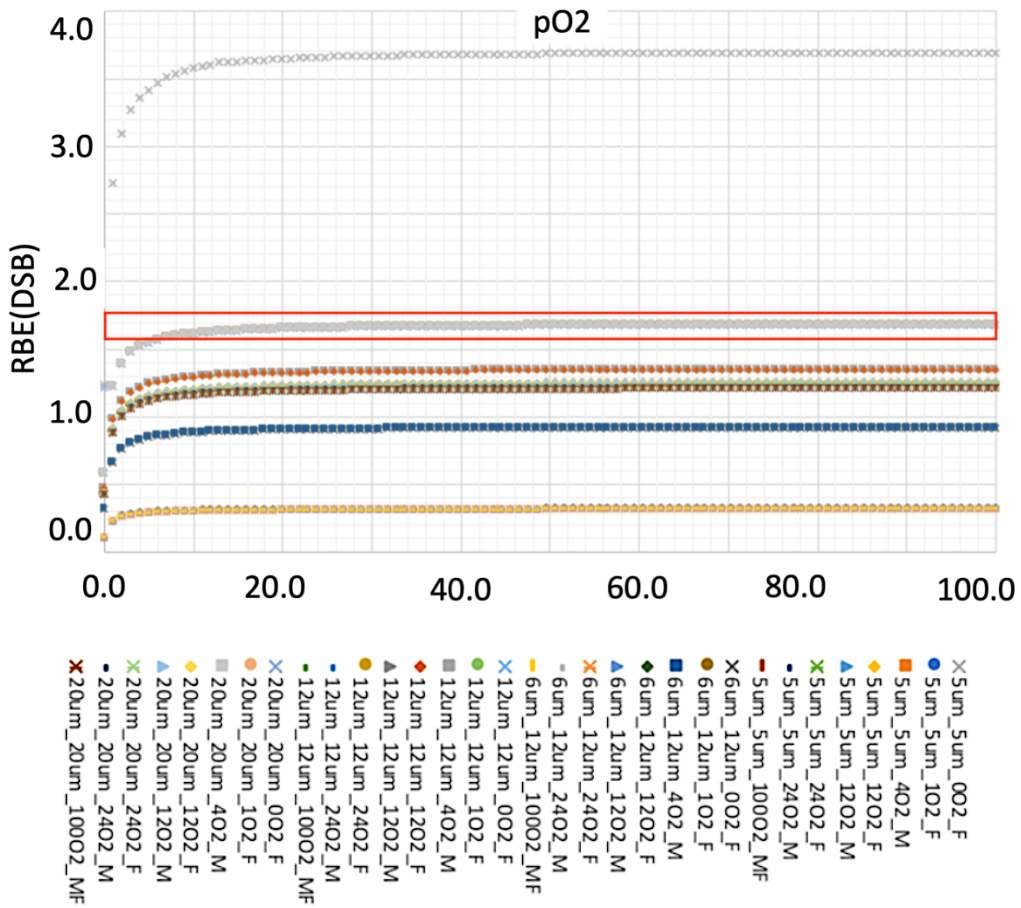
Figure 65. RBE values with respect to the 02 parameter for the simulated sets [Isolan L., et al., 2022].
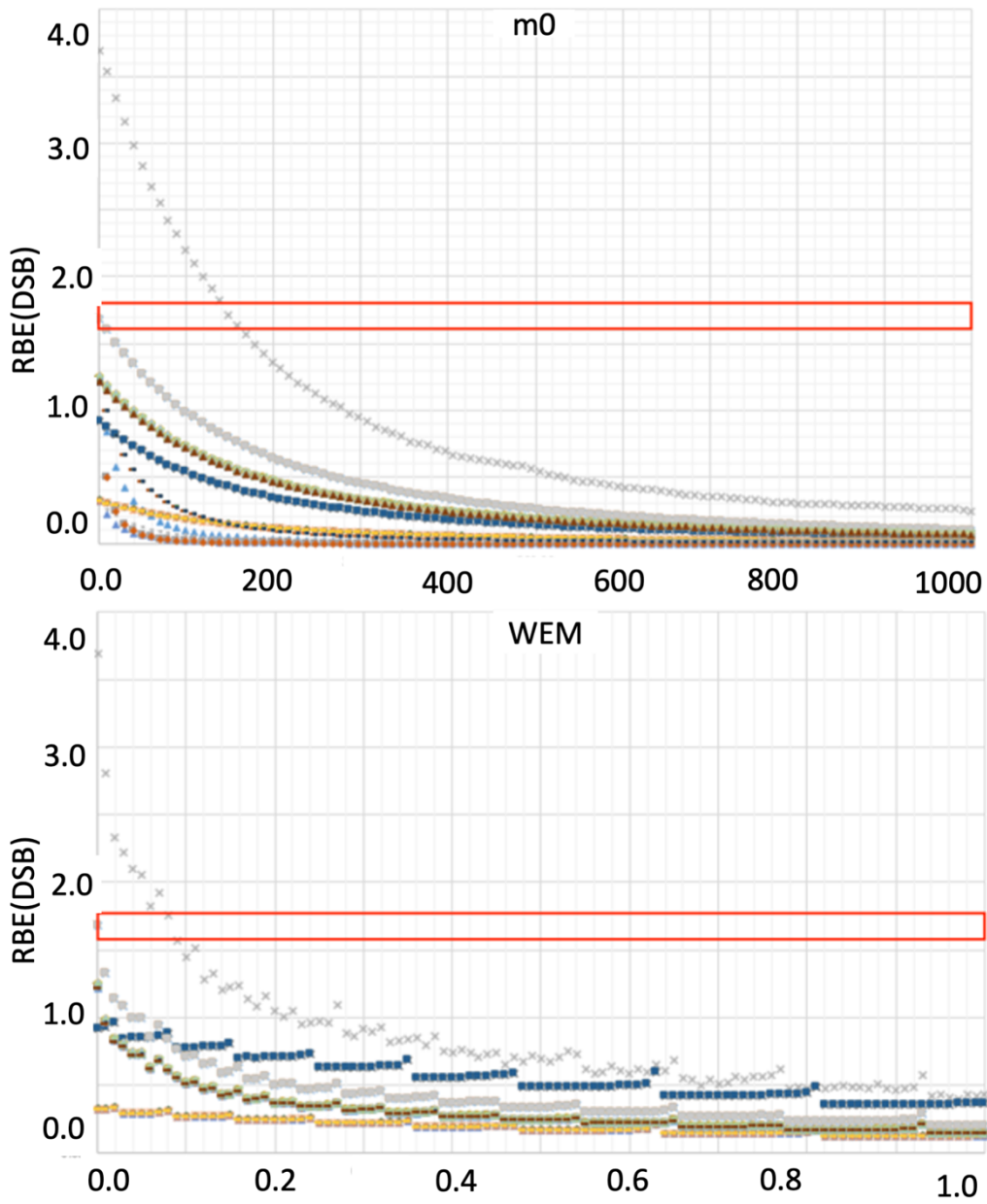
Figure 66. RBE values with respect to the M0 and WEM parameters for the simulated sets [Isolan L., et al., 2022]. Legend in Figure 65.
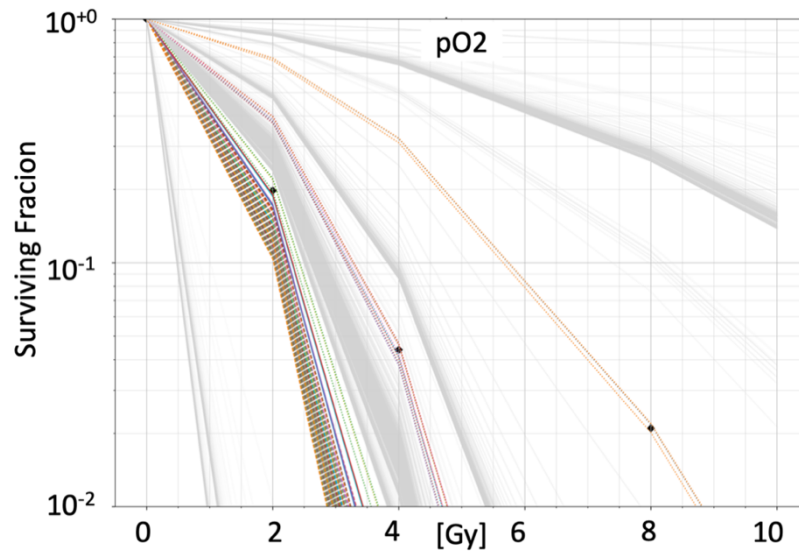
Figure 67. SF "phase space" with respect to the pO2 parameter variation for the simulated sets. Experimental PFMA-3 point also shown for behavior comparison [Isolan L., et al., 2022]. Experimental PF point also shown for behavior comparison. Grey, outside the fitting parameters. Dotted, +-15% from the RBE target value. Dashed, +-15% from the experimental point. Continuous, +-15% from both RBE target value and experimental point. Results obtained from the MCNP output and by applying the LQ formalism. See Appendix D.
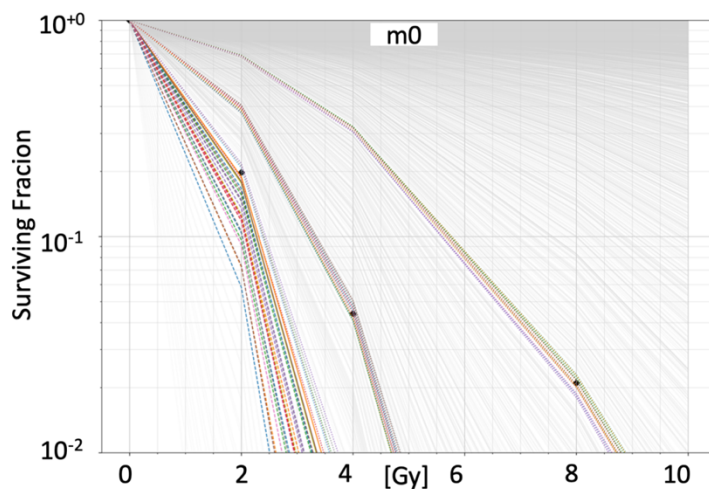
Figure 68. SF "phase space" with respect to the m0 parameter variation for the simulated sets. Experimental PFMA-3 point also shown for behavior comparison [Isolan L., et al., 2022]. Experimental PF point also shown for behavior comparison. Grey, outside the fitting parameters. Dotted, +-15% from the RBE target value. Dashed, +-15% from the experimental point. Continuous, +-15% from both RBE target value and experimental point. Results obtained from the MCNP output and by applying the LQ formalism. See Appendix D.
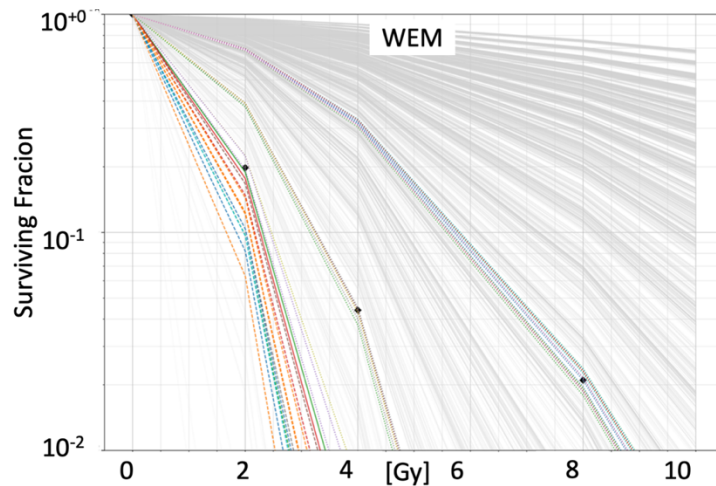
Figure 69. SF "phase space" with respect to the WEM parameter variation for the simulated sets. Experimental PFMA-3 point also shown for behavior comparison [Isolan L., et al., 2022]. Experimental PF point also shown for behavior comparison. Grey, outside the fitting parameters. Dotted, +-15% from the RBE target value. Dashed, +-15% from the experimental point. Continuous, +-15% from both RBE target value and experimental point. Results obtained from the MCNP output and by applying the LQ formalism. See Appendix D.

A full benchmark and sensitivity analysis of the MCDS code have been performed in combination of MCNP and, when required, dedicated Python3 scripts. See Appendix D for further details. The simulations, focused on a PFMA-3 FLASH source model, aimed to support biological clonogenic assay results on melanoma SK-MEL28 and DSB evaluations. A simulation architecture and strategy have been setup and DSBs, RBEs, α and β sets and SF curves have been evaluated with a large amount of parameter variations. A proposal for modeling the experimental data has been outlined, proposing that in FLASH regime more than one SF curve is necessary for fitting the clonogenic assay results. In the next future, on the basis of a combination of available experimental data and results from sensitivity analysis of the MCDS and MCNP codes coupled for radiobiology evaluations, a new strategy for numerically taking into

account the FLASH effect could be defined. A redesign, from the simulation point of view, on how the linear quadratic model is applied is mandatory (e.g. DSB(FLASH) = function(DSB(MCDS))), where function(DSB(MCDS)) could be an empirical model relating Double Strand Break production with the results of experiments with FLASH sources, as a function of dose rate escalation). This work paved the way for approaching an implementation of new simulation models [Isolan L., et al., 2022].

Discussion, conclusion, and future perspective

Since oncological radiation therapy can be considered one of the most adopted therapeutic approaches for the treatment of many cancer's type, it is known that nearly half of all the patients undergo curative or palliative regimen [Isolan L., et al., 2022]. Nevertheless, radio-resistance (which can be intrinsic or acquired) is the main obstacle to the long-term survival. In recent years, research aiming at solving the problem of radio resistance basically followed two approaches: 1) one linked to sensitization of the tumor cell through selective inhibition of oncoproteins with molecularly targeted drugs, combining radiotherapy and targeted therapy; 2) another focused on the generation of intense and modulated ionizing radiation beams, characterized of high DR or even FLASH sources [Favaudon et al., 2014; Buontempo F., et al., 2016; Buontempo F., et al., 2018, Zhang et al., 2020]. The hint is that the higher the DR, the more relevant is the radiobiological effectiveness of the ionizing radiation, as the tumor cells do not have the time to activate those mechanisms to repair the sub-lethal damage, notoriously underlying of the radioresistance [Virelli A., et al., 2015, Ben Kacem et al. 2020]. Newly, it has been found that FLASH sources could probably additionally spare normal tissues respect to conventional treatments, with potential benefits in cancer handling due to effects on oxygen deprecation [Vozenin MC., et al, 2019; Durante M., et al., 2018]. Due to that, flashing devices used as fast sources for radiation therapy applications are collecting a rising consideration from the scientific community, probably becoming the next generations of radiotherapy devices [Vozenin MC., et al, 2019; Durante M., et al., 2018; Kim YE., et al., 2020; Abolfath R., et al., 2020]. New

challenges are also evolving in terms of renewing the mathematical formalisms [Lea DE. and Catcheside DG., 1942] used for the explanation of the systems evolution (the focus is on the SF) caused by the necessity of having new models able to support the experimental results and interpretates the outcomes from FLASH beams on cell lines or tissues [Brown JM. and Grave EE., 2014; Pratx G. and Kapp DS., 2019; Carlson DJ., et al., 2008]. See also Isolan L., et al., 2021.

Different advantages can be achieved also with PLDR treatment, as shown in Jain. J., et al., 2021.

One promising test FLASH source can be represented by devices based on the Plasma Focus (PF) technology.

In this PhD research project, the PFMA-3 has been fully characterized looking mainly at this goal obtaining several results:

1) <u>Spectral and spatial characteristics in function of the operating parameters</u>: relying mainly on a Rogowski coil, the parametric electron spectral measurements carried out have shown the production of electron bunches with an amplitude of a few hundred of ns and maximum currents of the order of 0.5 – 1 kA. It is possible to improve the spectral features and the intensity, namely in the direction of increasing the total current through a reduction of the inductance of the device while keeping unaffected the operating voltage [Sumini M., et al., 2019a]. This result indicated an effective way to optimize the technology toward clinical applications.

2) <u>Analytical modeling of the PFMA-3 discharges for validating the electron beam measurement</u>: experimental results have been analytically validated when operated at 18 kV and 0.4 mbar with a simple model [Lee, 2014] that estimated peak and

pinch currents as 188 kA and 132 kA against measures of 180 kA and 126 kA. The flux has been derived as 1.42E+15 electrons cm^{-2} pulse^{-1} with 18 kA electron current. Such fluence rate corresponds to a calculated transported bunch of electrons of 0.27 mC which is perfectly compliant with the measured quantity of 0.23 mC [Sumini M., et al., 2019a]. The validation of the electron beam data was required due to uncertainties in measuring ultra-fast "quantities".

3) <u>Parametric Monte Carlo (MCNP code, [Goorley T., et al., 2014]) simulations using the measured electron characteristics as model sources and optimizing thickness and material of the target</u>: the key results collected, confirmed that a pulsed X-ray source able to deliver one Gy pulse^{-1} was well characterized and technically feasible [Sumini M., et al., 2019b]. The experimental measurements became a link between the "Lab. reality" and the numerical models.

4) *<u>Punctual dose measurements in PMMA phantoms and MCNP benchmark with numerical optimization and acceleration through adjoint importance functions and CADIS approach (though the ADVANTG tool)</u>*: micro-silica beads dose measurements in a PMMA phantom have been performed and the results benchmarked with MCNP. The problem has been inverted according to the adjoint approach and validated by means of the estimation of the photon flux at different order of scattering. The energy sensitivity analysis of the micro-silica beads dosimeters has been done and the adjoint calculations have been used to generate the importance functions to physically optimize the weight windows to bias the forward calculations performances [Isolan L. et al. 2020] (FOM increased by a factor of ten).

5) *<u>Magnetic lens design for focusing the primary electron beam</u>*: a quadrupole triplet system design has been checked with COMSOL©, by tuning different parameters

up to an optimum configuration. The results have been used as basis for an MCNP model (with applied the magnetic field), which indicated that applying a focusing system could reduce the electron focal spot by a factor of 30 also with benefits in beam hardening (e.g. 14% more) and dose transfer (e.g. 10% more) [Isolan L., and Sumini M., 2020].

6) <u>Radiobiological effectiveness evaluation of the flashing photon beam against melanoma cell lines</u>: based on the clonogenic assay results for the human melanoma cell line SK-Mel28 and A375 showed in Buontempo F., et al., 2018 the SF for the PFMA-3 was 0.02. The dose required by a conventional XRT for obtaining the same damage has been extrapolated at 13.6 with the LQ formalism (parameters derived from MCDS-MCNP codes simulation [Carlson DJ., et al., 2008; Stewart et al., 2015]). In Buontempo F., et al., 2018, the DNA damage induced by the PFMA-3 device has been tested by the H2A.X phosphorylation at Ser139 microscopy fluorescence detection (see also Isolan L., et al., 2021). In this case, the XRT dose capable to provide the same number of fluorescent cells showing DSB, has been evaluated as 13.4 Gy. The RBE calculated for both SF and DSB is $\approx$1.7. In performing a sensitivity analysis on the MCDS-MCNP outcomes (by varying with dedicated Python3 scripts all the MCDS input parameters, e.g., oxygen concentration, among a large set of values), three different types of results have been obtained: 1) DSB 3D charts as a function of energy and parameter variation. 2) RBE 2D charts per simulation set and parameter variation revealing that $\cong$5% of the results were consistent with the RBE(DSB) extrapolated by the experimental data. 3) SF 2D charts per simulation set and parameter variation; this "phase space" showed that a certain number out of 10^4 of the modelled curves hits the PFMA-3 data points experimentally found but none of them fits their trends relative to the

DR increment. The proposed process can be considered as a new approach for the implementation of simulation models suitable for the prediction of biological effects induced by FLASH source irradiation [Isolan L., et al., 2022].

7) <u>Radiation protection</u>: different TLDs have been positioned around the PFMA-3 for collecting ambient doses. A device and laboratory MCNP model have been evaluated and the comparison with the calculated ones has been performed. The spectral characteristics of the radiation interacting with the TLD material has been also estimated with the dose map distribution around the device [Isolan et al., 2021b]. Combining measurements and numerical estimation is crucial when managing FLASH sources, due to the not unknown response to the dosimeters.

The work paved the way to the application of the PF technology at first as an efficient, simple and cost-effective tool for deepening and getting insight in problems related to ultra-fast radiation beams and related radiobiology and, in a future, as an effective clinical device.

References

ABAQUS/CAE Analysis User's Guide. ABAQUS, Inc. https://www.3ds.com/products-services/simulia/products/abaqus/abaquscae/; http://130.149.89.49:2080/v6.14/books/usb/default.htm

Abolfath R., et al. *Oxygen depletion in FLASH ultra‑high‑dose‑rate radiotherapy: A molecular dynamics simulation*. Medical Physics, the international journal of medical physics research and practice, Volume 47, Issue 12 December 2020, Pages 6551-6561. https://doi.org/10.1002/mp.14548

Akel M., et al. *Electron Temperature Measurement of Argon Focussed Plasma Based on Non-local Thermodynamic Equilibrium Model*. J Fusion Energ 32, 350–354 (2013). https://doi.org/10.1007/s10894-012-9576-7

Auluck S., et al. *Update on the Scientific Status of the Plasma Focus*. Plasma. 2021, 4(3):450-669. https://doi.org/10.3390/plasma4030033

Baumann M., et al. *Radiation oncology in the era of precision medicine*. Nat Rev Cancer 16, 234–249 (2016). https://doi.org/10.1038/nrc.2016.18

Bedford JS. and Mitchell JB. *Dose-rate effects in synchronous mammalian cells in culture*. Radiat Res. 1973, May;54(2):316-27. https://doi.org/10.2307/3573709

Begg A., et al. *Strategies to improve radiotherapy with targeted drugs*. Nat Rev Cancer 11, 239–253, 2011. https://doi.org/10.1038/nrc3007

Bennett N., et al. *Development of the dense plasma focus for short-pulse applications*. Phys. Plasmas 24(1), 012702, 2018. https://doi.org/10.1063/1.4973227

Berger MJ., et al. *ESTAR, PSTAR, and ASTAR: Computer Programs for Calculating Stopping-Power and Range Tables for Electrons, Protons, and Helium Ions (version 1.2.3)*. 2005. [Online]. National Institute of Standards and Technology, Gaithersburg, MD. Available: http://physics.nist.gov/Star

Berry RJ. and Stedeford JBH. *Reproductive survival of mammalian cells after irradiation at ultra-high dose-rates: further observations and their importance for radiotherapy*. British Journal of Radiology, 1972, 45, 171-177. https://doi.org/10.1259/0007-1285-45-531-171

Berry RJ. *Effects of radiation dose-rate from protracted, continuous irradiation to ultra-high dose-rates from pulsed accelerators*. Br Med Bull. 1973, Jan;29(1):44-7. https://doi.org/10.1093/oxfordjournals.bmb.a070955

Bhide S. and Nutting, C. *Recent advances in radiotherapy*. BMC Med 8, 25, 2010. https://doi.org/10.1186/1741-7015-8-25

Binwei L., et al. *FLASH Radiotherapy: History and Future*. Frontiers in Oncology, 11, 2021, pag. 1890. https://doi.org/10.3389/fonc.2021.644400

Booth TE. *Automatic Importance Estimation in Forward Monte Carlo Calculations*. Transactions of the American Nuclear Society, 41:308, 1982. https://doi.org/10.13182/FST84-A23082

Booth, TE., et al. *X-5 Monte Carlo Team*. *MCNP - Version 5, Vol. I: Overview and Theory*. LA-UR-03-1987, 2003. https://mcnp.lanl.gov/pdf_files/la-ur-03-1987.pdf

Bortfeld T. and Paganetti H. *The biologic relevance of daily dose variations in adaptive treatment planning*. Int. J. Radiation Oncology Biol. Phys., Vol. 65, No. 3, pp. 899–906, 2006. https://doi.org/10.1016/j.ijrobp.2006.02.036

Bourhis J., et al. *Clinical translation of FLASH radiotherapy: why and how?* Radiother Oncol. 2019a, 139:11–7. https://doi.org/10.1016/j.radonc.2019.04.008

Bourhis J., et al. *Treatment of a first patient with FLASH-radiotherapy*. Radiother Oncol. 2019b, Oct;139:18-22. https://doi.org/10.1016/j.radonc.2019.06.019

Brenner DJ. and Hall EJ. *Conditions for the equivalence of continuous to pulsed low dose rate brachytherapy*. Int J Radiat Oncol Biol Phys. 1991, Jan;20(1):181-90. https://doi.org/10.1016/0360-3016(91)90158-z

Brown JM. and Graves EE., *Tumor Radiation Biology*. Editor(s): Anders Brahme, Comprehensive Biomedical Physics, Elsevier, 2014, 7.06 - Pages 97-119, ISBN 9780444536334, https://doi.org/10.1016/B978-0-444-53632-7.00806-6

Buontempo F., et al. *Characterization of biological effects in radiotherapy applications of ultra-high dose rate pulses from a plasma focus device*. 2016, Eur. J. Cancer 61, Suppl. 1, S9–S218. http://dx.doi.org/10.1016/S0959-8049(16)61563-0

Buontempo F., et al. *Enhancing radiosensitivity of melanoma cells through very high dose rate pulses released by a plasma focus device*. 2018, PLoS ONE 13(6), e0199312. https://doi.org/10.1371/journal.pone.0199312

Carlson DJ., et al. *Combined Use of Monte Carlo DNA Damage Simulations and Deterministic Repair Models to Examine Putative Mechanisms of Cell Killing*. RADIATION RESEARCH, 169, 447–459, 2008. https://doi.org/10.1667/RR1046.1

Casolaro P. *Radiochromic Films for the Two-Dimensional Dose Distribution Assessment*. Appl. Sci. 2021, 11(5), 2132; https://doi.org/10.3390/app11052132

Ceccolini E. Development and performance assessment of a Plasma Focus electron beam generator for Intra-Operative Radiation Therapy. PhD Dissertation thesis, Alma Mater Studiorum University of Bologna, 2012. http://dx.doi.org/10.6092/unibo/amsdottorato/4736

Ceccolini E., et al. *EBT2 dosimetry of X-Rays produced by the electron beam from a Plasma Focus for medical applications*. Journal of Applied Physics, vol. 112, p. 054901-1-054901-5, ISSN: 0021-8979, 2012. https://doi.org/10.1063/1.4748179

Chandra RA., et al. *Contemporary radiotherapy: present and future*. Lancet, 2021; 398: 171–84. https://doi.org/10.1016/S0140-6736(21)00233-6

Chapman B., et al. *Overview of OpenMP*. In Using OpenMP: Portable Shared Memory Parallel Programming (MIT Press) pp 384. Books, Computing and Processing, MIT Press, ISBN-13: 978-0262533027, 2007. https://ieeexplore.ieee.org/servlet/opac?bknumber=6267237

Chen L. *Clinical Applications of Pulsed Low Dose-Rate Radiation Therapy*. Mathews J Cancer Sci. 2021, (6)1:27. https://www.mathewsopenaccess.com/journals/cancer

Chernyshova M., et al. *Interaction of powerful hot plasma and fast ion streams with materials in dense plasma focus devices*. Fus. Eng. Des. 113, 109–118, 2019. https://doi.org/10.1016/j.fusengdes.2016.11.003

Choudhary S. *Deterministic and Stochastic Effects of Radiation*. Canc Therapy & Oncol Int J. 2018, 12(2): 555834. http://dx.doi.org/10.19080/CTOIJ.2018.12.555834

Chow R., et al. *FLASH Radiation Therapy: Review of the Literature and Considerations for Future Research and Proton Therapy FLASH Trials*. Appl Rad Oncol. 2021, 10(2):15-21. https://appliedradiationoncology.com/articles/FLASH-radiation-therapy-review-of-the-literature-and-considerations-for-future-research-and-proton-therapy-FLASH-trials

Chowell D., Napier J., Gupta R., Anderson K. S., Maley C. C., Sayres M. *Modeling the Subclonal Evolution of Cancer Cell Populations*. 2018 Cancer research, 78(3), 830–839. https://doi.org/10.1158/0008-5472.CAN-17-1229

Ciocca M., et al. *In vivo dosimetry using radiochromic films during intraoperative electron beam radiation therapy in early-stage breast cancer*. Radiotherapy and Oncology, 69(3):285–289, 2003. https://doi.org/10.1016/j.radonc.2003.09.001

Damideh V., et al. *Characteristics of Fast ion beam in Neon and Argon filled plasma focus correlated with Lee Model Code*. Vacuum 169, 108916, 2019. https://doi.org/10.1016/j.vacuum.2019.108916

De Matteis A. and Simonini R. *A Monte Carlo biasing scheme for adjoint photon transport*. Nuclear Science and Engineering, 67:3, 309-316, 1978. https://doi.org/10.13182/NSE78-A27251

Deasy JO., et al. *Dose-rate effects in intensity modulated radiation therapy*. 2001, International Journal of Radiation Oncology - Biology – Physics, Abstract, VOLUME 51, ISSUE 3, SUPPLEMENT 1, 400-401. https://doi.org/10.1016/S0360-3016(01)02561-5

Delaney G., et al. *The role of radiotherapy in cancer treatment: Estimating optimal utilization from a review of evidence-based clinical guidelines*. Cancer. 2005, 104, 1129-1137. https://doi.org/10.1002/cncr.21324

Dewey D. and Boag, J. *Modification of the Oxygen Effect when Bacteria are given Large Pulses of Radiation*. Nature 183, 1450–1451, 1959. https://doi.org/10.1038/1831450a0

Doroshow J. and Kummar S. *Translational research in oncology—10 years of progress and future prospects*. Nat Rev Clin Oncol 11, 649–662 (2014). https://doi.org/10.1038/nrclinonc.2014.158

Drumm CR., et al. *Forward and adjoint methods and applications for deterministic electron-photon transport*. Nuclear Science and Engineering; (United States), Journal Volume: 108:1; Journal ID: ISSN 0029-5639, 1991. https://doi.org/10.13182/NSE91-A23805

Dunn WL. and Shultis JK. *Exploring the Monte Carlo Methods*. Elsevier, 398 p., 2011. ISBN:0444515755. https://www.elsevier.com/books/exploring-monte-carlo-methods/dunn/978-0-444-51575-9

Durante M., et al. *Faster and safer? FLASH ultra-high dose rate in radiotherapy*. The British Journal of Radiology, 91 (1082), 2018. https://doi.org/10.1259/bjr.20170628

Evans TM., et al. *DENOVO - A New Three-Dimensional Parallel Discrete Ordinates Code in SCALE*. Nuclear Technology, Volume 171, Issue 8, 2010. https://doi.org/10.13182/NT171-171

Favaudon V., et al. *Ultrahigh dose-rate FLASH irradiation increases the differential response between normal and tumor tissue in mice*. Sci Transl Med, 2014; 6. https://doi.org/10.1126/scitranslmed.3008973

Fernández JE. and Sumini M. *Adjoint calculations for multiple scattering of Compton and Rayleigh effects*. Nuclear Instruments and Methods in Physics Research, B71, 111-115, 1992. https://doi.org/10.1016/0168-583X(92)95311-E

Fernández JE., et al. *Effect of the X-ray scattering anisotropy on the diffusion of photons in the frame of the transport theory*. Nuclear Instruments and Methods in Physics Research Section A: Accelerators, Spectrometers, Detectors and Associated Equipment Volume 280, Issues 2–3, 10, 1989, Pages 212-221, 1989. https://doi.org/10.1016/0168-9002(89)90910-8

Fernandez JE., et al. *Reconstruction of the X-ray tube spectrum from a scattering measurement*. Applied Radiation and Isotopes, 70, 1238–1242, 2012. https://doi.org/10.1016/j.apradiso.2011.11.035

Field SB. and Bewley DL. *Effects of Dose-rate on the Radiation Response of Rat Skin*. International Journal of Radiation Biology and Related Studies in Physics, Chemistry and Medicine, 1974, 26:3, 259-267, https://doi.org/10.1080/09553007414551221

Filippov NV., et al. *Dense high-temperature plasma in a non-cylindrical Z-pinch compression*. Nucl. Fusion Supple. 01, 1962. https://www.semanticscholar.org/paper/DENSE-HIGH-TEMPERATURE-PLASMA-IN-A-NON-CYLINDRICAL-Filippov-Filippova/e4cc8b2ea541a54ee73fbb8b42c5e70d54a678b1?sort=relevance&citationIntent=methodology

Friedl AA., et al. *Radiobiology of the FLASH effect*. Med Phys. 2021, 1–21. https://doi.org/10.1002/mp.15184

Goorley T. *MCNP6.1.1-Beta Release Notes*. LA-UR-14-24680, 2014. https://mcnp.lanl.gov/pdf_files/la-ur-14-24680.pdf

Goorley, T., et al. *Initial MCNP6 Release Overview*. Nuclear Technology, 180, pp 298-315, 2012. http://dx.doi.org/10.13182/NT11-135

Gribkov V.A., et al. *Examination of a chamber of a large fusion facility by means of neutron activation technique with nanosecond neutron pulse generated by dense plasma focus device PF-6*. Fus. Eng. Des. 125, 109–117, 2017. https://doi.org/10.1016/j.fusengdes.2017.10.023

Gribkov VA., et al. *Dense plasma focus: physics and applications (radiation material science, single-shot disclosure of hidden illegal object, radiation biology and medicine, etc.)*. J. Phys.: Conf. Ser. 591, 012020, 2015. https://doi.org/10.1088/1742-6596/591/1/012020

Griffin RJ., et al. *Understanding High-Dose, Ultra-High Dose Rate, and Spatially Fractionated Radiation Therapy*. Int J Radiat Oncol Biol Phys. 2020, Jul 15;107(4):766-778. https://doi.org/10.1016/j.ijrobp.2020.03.028

Haghani S., et al. *Theoretical Study of the Endogenous Production of N-13 in 115 kJ Plasma Focus Device Using Methane Gas*. J Fusion. Energ. 32, 480-487, 2013. https://doi.org/10.1007/s10894-013-9597-x

Hall EJ. *Radiation dose-rate: a factor of importance in radiobiology and radiotherapy*. 1972, Br. J. Radiol. 45 (530), 81–97. https://doi.org/10.1259/0007-1285-45-530-81

Hassan M., et al. Surface modification of AlFe1.8Zn0.8 alloy by using dense plasma focus. Vacuum 81, 291–298, 2006. https://doi.org/10.1016/j.vacuum.2006.05.001

Hebar A., et al. *The impact of molecular targets in cancer drug development: major hurdles and future strategies*. Expert Review of Clinical Pharmacology, 2013, 6:1, 23-34. https://doi.org/10.1586/ecp.12.71

Herbert, JM. *Structure of the aqueous electron*. Phys. Chem. Chem. Phys., 2019, 21, 20538-20565. https://doi.org/10.1039/C9CP04222A

Heredia-Avalos S., et al. *Calculated energy loss of swift He, Li, B, and N ions in SiO2, Al2 O, and ZrO2*. Phys. Rev. A 72, 052902, 2005. https://doi.org/10.1103/PhysRevA.72.052902

Hoogenboom JE. *Adjoint Monte Carlo Methods in Neutron Transport Calculations*. Doctoral thesis. BIBLIOTHEEK TU Delft P11875331, C 303326, Delft University Press/1977. Copyright © 1977 by J. E. Hoogenboom, 1977. http://resolver.tudelft.nl/uuid:6e5cb6b5-ebad-48af-b55e-e5830c842ebf

Hoogenboom JE. *Adjoint Monte Carlo photon transport in continuous energy mode with discrete photons from annihilation*. Proceedings of the PHYSOR, 2000. https://www.ipen.br/biblioteca/cd/physor/2000/physor/054.pdf

Hoogenboom JE. and Légrády D. *A Critical Review of The Weight Window Generator In MCNP*. The Monte Carlo Method: Versatility Unbounded in A Dynamic Computing World. Chattanooga, Tennessee, April 17–21, 2005, on CD-ROM, American Nuclear Society, LaGrange Park, IL. (2005), 2005. https://www.researchgate.net/publication/268421665_A_critical_review_of_the_weight_window_generator_in_MCNP

Huang X., et al. *Detection of histone H2AX phosphorylation on Ser-139 as an indicator of DNA damage (DNA double-strand breaks)*. Curr Protoc Cytom, 2004 Nov;Chapter 7:Unit 7.27. https://doi.org/10.1002/0471142956.cy0727s30

Hyun DH., et al. *History of Radiation Therapy Technology*. Progress in Medical Physics 2020;31(3):124-134. https://doi.org/10.14316/pmp.2020.31.3.124

ICRP, 2007. *ICRP Publication 103*. 2007, The 2007 Recommendations of the International Commission on Radiological Protection. Ann. ICRP 37 (2-4). https://www.icrp.org/publication.asp?id=ICRP%20Publication%20103

Inestrosa-Izurieta MJ., et al. *Deposition of materials using a plasma focus of tens of joules*. J. Phys.: Conf. Ser. 720, 012045, 2016. https://doi.org/10.1088/1742-6596/720/1/012045

ISO 4037-1:2019. *Radiological protection — X and gamma reference radiation for calibrating dosemeters and doserate meters and for determining their response as a function of photon energy — Part 1: Radiation characteristics and production methods*. https://www.iso.org/standard/66872.html

Isolan L. and Sumini M. *Magnetic quadrupole simulations for focusing the electron beams emitted by a plasma focus device*. Radiation Physics and Chemistry, Volume 174, 2020, 108970, https://doi.org/10.1016/j.radphyschem.2020.108970

Isolan L., et al. A Monte Carlo DNA Double Strand Break model for the Assessment of the Relative Biological Effectiveness of Ultra High Dose Rate sources. To be submitted, 2022.

Isolan L., et al. *Analysis of the bias induced by voxel and unstructured mesh Monte Carlo models for the MCNP6 code in orthovoltage applications*. Radiation Effects and Defects in Solids, 2019, 174:5-6, 365-379. https://doi.org/10.1080/10420150.2019.1596104

Isolan L., et al. *Sensitivity analysis via adjoint Monte Carlo calculations of plasma focus irradiation of micro-silica beads in phantoms*. Radiation Physics and Chemistry, Volume 176, 109017, 2020. https://doi.org/10.1016/j.radphyschem.2020.109017

Isolan L., et al. *Un modello radioprotezionistico per la gestione di sorgenti FLASH*. Notiziario di radioprotezione dell'Esperto Qualificato, ANPEQ, 2021b. https://www.anpeq.it

Isolan, L., et al. *Dosimetric analysis and experimental setup design for in-vivo irradiation with a Plasma Focus device*. Radiat. Phys. Chem. 155, 17–21, 2019. https://doi.org/10.1016/j.radphyschem.2018.06.025

Jafari SM., et al. *Energy response of glass bead TLDs irradiated with radiation therapy beams*. Radiation Physics and Chemistry. Vol. 104, P. 208-211, 2014b. https://doi.org/10.1016/j.radphyschem.2014.03.009

Jafari SM., et al. *Glass beads and Ge-doped optical fibres as thermoluminescence dosimeters for small field photon dosimetry*. Phys. Med. Biol. 59, 6875–6889, 2014a. http://dx.doi.org/10.1088/0031-9155/59/22/6875

Jain J., et al. *Characterization of X-Rays pulses from a hundred joules plasma focus to study its effects on cancer cells*. J. Phys. Conf. Ser. 720, 012043, 2016. https://doi.org/10.1088/1742-6596/720/1/012043

Jain J., et al. Hundred joules plasma focus device as a potential pulsed source for in vitro cancer cell irradiation. AIP Adv. 7, 085121, 2017. https://doi.org/10.1063/1.4994655

Jain J., et al. *Hyper-radiosensitivity in tumor cells following exposure to low dose pulsed X-Rays emitted from a kilojoule plasma focus device*. Journal of Applied Physics vol. 130, no. 16, 2021. https://doi.org/10.1063/5.0060710

Jain J., et al. *In vitro irradiation of colorectal cancer cells by pulsed radiation emitted from a hundred joules plasma focus device and its comparison with continuous irradiation*. J. Phys. Conf. Ser. 1043, 012047, 2018. https://doi.org/10.1088/1742-6596/1043/1/012047

Jain J., et al. *Influence of electrode geometry on X-ray emission, plasma inductance, voltage, and current derivative signals obtained from a plasma focus device*. Results in Physics, Volume 23, 2021b, 104016. https://doi.org/10.1016/j.rinp.2021.104016

Jie L., et al. *Safety and efficacy of pulsed low-dose rate radiotherapy for local recurrent esophageal squamous cell carcinoma after radiotherapy*. Medicine: June, 2019, Volume 98 - Issue 26 - p e16176. https://doi.org/10.1097/md.0000000000016176

Johansson KA., et al. *Radiation Therapy Dose Delivery*. Acta Oncologica, 2012, 42:2, 85-91. https://doi.org/10.1080/02841860310004922

Joiner MC. Et al. *Low-dose hypersensitivity: current status and possible mechanisms*. Int J Radiat Oncol Biol Phys. 2001, Feb 1;49(2):379-89. PMID: 11173131. https://doi.org/10.1016/s0360-3016(00)01471-1

Karsch L., et al. *Dose rate dependence for different dosimeters and detectors: TLD, OSL, EBT films, and diamond detectors*. Med. Phys. 39 (5), 2012. https://doi.org/10.1118/1.3700400

Khanna A., et al. *Serratia marcescens- a rare opportunistic nosocomial pathogen and measures to limit its spread in hospitalized patients*. J Clin Diagn Res. 2013, 7(2):243-246. https://dx.doi.org/10.7860%2FJCDR%2F2013%2F5010.2737

Kim MM. et al. *Comparison of FLASH Proton Entrance and the Spread-Out Bragg Peak Dose Regions in the Sparing of Mouse Intestinal Crypts and in a Pancreatic Tumor Model*. Cancers (Basel). 2021, Aug 23;13(16):4244. https://doi.org/10.3390/cancers13164244

Kim YE., et al. *Effects of Ultra-high doserate FLASH Irradiation on the Tumor Microenvironment in Lewis Lung Carcinoma: Role of Myosin Light Chain*. International Journal of Radiation Oncology*Biology*Physics, 2020, ISSN 0360-3016. https://doi.org/10.1016/j.ijrobp.2020.11.012

Klein O. and Nishina Y. *Über die Streuung von Strahlung durch freie Elektronen nach der neuen relativistischen Quantendynamik von Dirac*. Z. Physik 52, 853–868, 1929. https://doi.org/10.1007/BF01366453

Kraft SD., et al. *Dose- dependent biological damage of tumour cells by laser-accelerated proton beams*. New Journal of Physics, 12(8):085003, 2010. https://doi.org/10.1088/1367-2630/12/8/085003

Kraft SD., et al. *Dose- dependent biological damage of tumour cells by laser-accelerated proton beams*. New Journal of Physics, 12(8):085003, 2010. https://doi.org/10.1088/1367-2630/12/8/085003

Labate L., et al. *Lesm: a laser-driven sub-mev electron source delivering ultra-high dose rate on thin biological samples*. Journal of Physics D: Applied Physics, 49(27): 275401, 2016. https://doi.org/10.1088/0022-3727/49/27/275401

Lazzaro G., et al. *Pulsed Dose-Rate Perioperative Interstitial Brachytherapy for Soft Tissue Sarcomas of the Extremities and Skeletal Muscles of the Trunk*. Ann Surg Oncol, 2005, 12: 935. https://doi.org/10.1245/ASO.2005.11.004

Lea DE. and Catcheside DG. *The mechanism of the induction by radiation of chromosome aberrations in Tradescantia*. Journ. of Genetics, 44, 216–245, 1942. https://doi.org/10.1007/BF02982830

Lee G., et al. *Radiotherapy Treatment Review: A Prospective Evaluation of Concordance between Clinical Specialist Radiation Therapist and Radiation Oncologist in Patient Assessments*. Journal of Medical Imaging and Radiation Sciences, 2012, 43 6-10. https://doi.org/10.1016/j.jmir.2011.10.001

Lee S. and Saw H. *Plasma focus ion beam fluence and flux—For various gases*. AIP. 20, 2013. https://doi.org/10.1063/1.4811650

Lee S. and Saw H. *Plasma Focus Numerical Experiments*. 2011. https://www-pub.iaea.org/MTCD/publications/PDF/TE-1713-CD/talks/Saw-paper.pdf

Lee S. *Characterizing the Plasma Focus Pinch and Speed Enhancing the Neutron Yield*. International Centre for Dense Magnetized Plasmas. 2003. https://inis.iaea.org/search/search.aspx?orig_q=RN:36073976

Lee S. *Plasma Focus Radiative Model: Review of the Lee Model Code*. J Fusion Energ 33, 319–335, 2014. https://doi.org/10.1007/s10894-014-9683-8

Lee S., et al. *Numerical Experiments on Radiative Cooling and Collapse in Plasma Focus Operated in Krypton*. J Fusion Energ. 32, 42-49, 2013. https://doi.org/10.1007/s10894-012-9522-8

Lempart M., et al. *Modifying a clinical linear accelerator for delivery of ultra-high dose rate irradiation*. Radiotherapy and Oncology, 2019. https://doi.org/10.1016/j.radonc.2019.01.031

Lewins J. *Importance, The Adjoint Function, The Physical Basis of Variational and Perturbation Theory in Transport and Diffusion Problems*. Copyright @ 1965. Pergamon Press Ltd. Library of Congress Catalog Card No. 65-14223. OSTI ID: 4752764. NSA-24-013266. First edition, 1965. https://www.osti.gov/biblio/4752764-importance-adjoint-function-physical-basis-variational-perturbation-theory-transport-diffusion-problems

Liu C., Lin Q., Yun Z. *Cellular and molecular mechanisms underlying oxygen-dependent radiosensitivity*. 2015 Radiation research, 183(5), 487–496. https://doi.org/10.1667/RR13959.1

Lorence, LJ., et al. *Adjoint electron-photon transport Monte Carlo calculations with ITS*. United States, 1995. https://digital.library.unt.edu/ark:/67531/metadc679031/

Malicki J. *The importance of accurate treatment planning, delivery, and dose verification*. Rep Pract Oncol Radiother. 2012 Mar 6;17(2):63-5. PMID: 24377001; PMCID: PMC3863261. https://doi.org/10.1016/j.rpor.2012.02.001

Marcu LG., et al. *Translational Research in FLASH Radiotherapy-From Radiobiological Mechanisms to In Vivo Results*. Biomedicines. 2021;9(2):181. Published 2021 Feb 11. https://dx.doi.org/10.3390%2Fbiomedicines9020181

Martz RL. *The MCNP6 Book on Unstructured Mesh Geometry: User's Guide*. pp. 8. LA-UR-11–05668 Rev. 8, 2014. https://mcnp.lanl.gov/pdf_files/la-ur-12-25478v1.pdf

Mather JW. *Dense Plasma Focus*. Methods of Experimental Physics, Vol. 9B, Academic Press, New York, pp. 187-250, 1971. https://doi.org/10.1016/S0076-695X(08)60862-5

Mather JW., and Bottoms JP. *Characteristics of the Dense Plasma Focus Discharge*. The Physics of Fluids 11, 611, 1968. https://doi.org/10.1063/1.1691959

Matsuya Y., et al. *Intensity Modulated Radiation Fields Induce Protective Effects and Reduce Importance of Dose-Rate Effects*. Sci Rep 9, 9483, 2019. https://doi.org/10.1038/s41598-019-45960-z

McConn RJ., et al. *Compendium of Material Composition Data for Radiation Transport Modeling*. Report, Richland, Washington. University of North Texas Libraries, UNT Digital Library, https://digital.library.unt.edu; crediting UNT Libraries Government Documents Department. (2011). Publisher Info: Pacific Northwest National Laboratory (PNNL), Richland, WA (United States). Place of Publication: Richland, Washington. PIET-43741-TM-963. PNNL-15870 Rev. 1. https://digital.library.unt.edu/ark:/67531/metadc835293/

McParland BJ. *Nuclear Medicine Radiation Dosimetry (Advanced Theoretical Principles)*. Springer-Verlag London Limited, 2010. Springer, London, ISBN 978-1-84882-125-5, Edition Number 1, Number of Pages: XXXII, 610. https://doi.org/10.1007/978-1-84882-126-2

Mendez LC. and Morton GC. *High dose-rate brachytherapy in the treatment of prostate cancer*. Transl Androl Urol. 2018, 7(3):357-370. https://dx.doi.org/10.21037%2Ftau.2017.12.08

Mitchell JB. and Bedford JS. *Dose-rate effects in synchronous mammalian cells in culture. II. A comparison of the life cycle of HeLa cells during continuous irradiation or multiple-dose fractionation*. Radiat Res. 1977, Sep;71(3):547-60. https://doi.org/10.2307/3574623

Montay-Gruel P., et al. *Irradiation in a FLASH: Unique sparing of memory in mice after whole brain irradiation with dose rates above 100Gy/s*. Radiotherapy and Oncology, Volume 124, Issue 3, 2017, Pages 365-369, ISSN 0167-8140. https://doi.org/10.1016/j.radonc.2017.05.003

Mosher SW., et al. *ADVANTG An Automated Variance Reduction Parameter Generator*. Rev. 1. United States: N. p., 2015. 10.2172/1210162. https://info.ornl.gov/sites/publications/Files/Pub56840.pdf

Niranjan R., et al. *Application of medium energy plasma focus device in study of radioisotopes*. Phys. Lett. A 382, 3365–3368, 2018. https://doi.org/10.1016/j.physleta.2018.09.015

Nuraini R. and Widita R. J. *Tumor Control Probability (TCP) and Normal Tissue Complication Probability (NTCP) with Consideration of Cell Biological Effect*. Phys.: Conf. Ser. 1245 012092, 2019. https://doi.org/10.1088/1742-6596/1245/1/012092

Nüsslin F. *Wilhelm Conrad Röntgen: The scientist and his discovery*. Phys Med. 2020 Nov;79:65-68. Epub 2020 Nov 3. https://doi.org/10.1016/j.ejmp.2020.10.010

Ogawa K., et al. *Radiotherapy targeting cancer stem cells: current views and future perspectives*. Anticancer Res. 2013, Mar; 33(3):747-54. Review. http://www.ncbi.nlm.nih.gov/pubmed/23482741

Patran A., et al. Zakaullah M., Lee S. *Spectral study of the electron beam emitted from a 3 kJ plasma focus*. 2005, Plasma Sources Sci. Technol. 14 549. https://doi.org/10.1088/0963-0252/14/3/018

Paul H., and Schinner A. *An empirical approach to the stopping power of solids and gases for ions from 3Li to 18Ar*. Nucl. Instr. Meth. Phys. Res. B 179, 299, 2001. https://doi.org/10.1016/S0168-583X(01)00576-6

Pavez C., et al. *Potentiality of a table top plasma focus as X-ray source: radiography applications*. J. Phys.: Conf. Ser. 511, 012028, 2014. https://doi.org/10.1088/1742-6596/511/1/012028

Pelowitz DB. *MCNPX Users Manual Version 2.7.0*. LA-CP-11-00438, 2011. https://www.rist.or.jp/rsicc/app/MCNP5_MCNPX_EXE_09.htm#mcnpx270

Peplow DE., et al. *Consistent Adjoint Driven Importance Sampling using Space, Energy, and Angle*. 2012. https://doi.org/10.2172/1052244

Podhorecka M., et al. *H2AX Phosphorylation: Its Role in DNA Damage Response and Cancer Therapy*. Journal of nucleic acids, 2010, 920161. https://doi.org/10.4061/2010/920161

Pouzo JO. and Milanese MM. *Applications of the Dense Plasma Focus to Nuclear Fusion and Plasma Astrophysics*. IEEE Trans Plasma Sci 31, 6, 2003. https://doi.org/10.1109/TPS.2003.821475

Pratx G. and Kapp DS. *A computational model of radiolytic oxygen depletion during FLASH irradiation and its effect on the oxygen enhancement ratio*. Phys. Med. Biol. 64 185005, 2019. https://doi.org/10.1088/1361-6560/ab3769

Rama N., et al. *Improved Tumor Control Through T-cell Infiltration Modulated by Ultra-High Dose Rate Proton FLASH Using a Clinical Pencil Beam Scanning Proton System*. International Journal of Radiation Oncology-Biology-Physics. VOLUME 105, ISSUE 1, SUPPLEMENT, S164-S165, SEPTEMBER 01, 2019. https://doi.org/10.1016/j.ijrobp.2019.06.187

Rashid NA., et al. Effects of Approximation and Close-Fitting Technique of Corona Model on Neon Soft X-Ray Emission in 3-kJ Plasma Focus. IEEE Transactions on Plasma Science, vol. 43, no. 7, pp. 2146-2154, July, 2015. https://doi.org/10.1109/TPS.2015.2433301

Rawat RS., et al. *Effect of insulator sleeve length on soft X-Ray emission from a neon-filled plasma focus device*. Plasma Sources Sci. Technol. 13, 569–575, 2004. https://doi.org/10.1088/0963-0252/13/4/003

Reed JL. *The Genius of Slater's Rules*. Chem. Educ. 1999, 76, 6, 802, Publication Date: June 1, 1999. https://doi.org/10.1021/ed076p802

Rogacki K., et al. *Review of Pulsed Reduced Dose Rate Re-irradiation for Recurrent Tumors*. J Cancer clin Trials, 2018, 3: 143. https://doi.org/10.4172/2577-0535.1000143

Rosenbluth M., et al. *Infinite conductivity theory of the pinch*. Los Alamos Scientific Laboratory. LA-1850, 1954.

Rühm W., et al. *Dose-rate effects in radiation biology and radiation protection*. Annals of the ICRP. 2016, 45(1_suppl):262-279. https://doi.org/10.1177%2F0146645316629336

Samimi M., H., Mahari, A., Farahnakian, M., A., Mohseni, H. A Review on the Rogowski Coil Principles and Applications. IEEE Sensors Journal, vol. 15, no. 2, pp. 651-658, 2015. https://doi.org/10.1109/JSEN.2014.2362940

Saw SH., et al. *A 160 kJ dual plasma focus (DuPF) for fusion-relevant materials testing and nano-materials fabrication*. Plasma Science and Applications (ICPSA 2013). Int. J. Mod. Phys.: Conference Series 32, 1460322, 2014. https://doi.org/10.1142/S2010194514603226

Selzer E. and Kornek G. *Targeted drugs in combination with radiotherapy for the treatment of solid tumors: current state and future developments*. Expert Rev Clin Pharmacol. 2013, Nov;6(6):663-76. Review. https://doi.org/10.1586/17512433.2013.841540

Sheu RJ., et al. *Adjoint acceleration of Monte Carlo simulations using tort/mcnp coupling approach: a case study on the shielding improvement for the cyclotron room of the Buddhist Tzu Chi General Hospital*. Radiation Protection Dosimetry, 2005, Vol. 113, No. 2, pp. 140–151. https://doi.org/10.1093/rpd/nch454

Sinigardi S., et al. *Transport and energy selection of laser generated protons for post acceleration with a compact linac*. Physical Review Special Topics. Accelerators and Beams, vol. 16, p. 031301-1-031301-13, ISSN: 1098-4402, 2013. http://dx.doi.org/10.1103/PhysRevSTAB.16.031301

Skouboe S., et al. *First clinical real-time motion-including tumor dose reconstruction during radiotherapy delivery*. Radiother Oncol. 2019, Oct;139:66-71. https://doi.org/10.1016/j.radonc.2019.07.007

Smyth LML., et al. *Comparative toxicity of synchrotron and conventional radiation therapy based on total and partial body irradiation in a murine model*. Sci Rep 8, 12044, 2018. https://doi.org/10.1038/s41598-018-30543-1

Solomon CJ., et al. *A weighted adjoint source for weight-window generation by means of a linear tally combination*. ANS 2009 International Conference on Advances in Mathematics, Computational Methods, and Reactor Physics. LA-UR-09-01185, 2009. https://permalink.lanl.gov/object/tr?what=info:lanl-repo/lareport/LA-UR-09-01185

Soto L., et al. *Studies on scalability and scaling laws for the plasma focus: similarities and differences in devices from 1 MJ to 0.1 J*. Plasma Sources Sci. Technol. 19, 055017, 2010. https://doi.org/10.1088/0963-0252/19/5/055017

Sterzing F., et al. *Radiobiological Investigation of Dose-Rate Effects in Intensity-Modulated Radiation Therapy*. Strahlenther Onkol 181, 42–48, 2005. https://doi.org/10.1007/s00066-005-1290-1

Stewart RD., et al. A comparison of mechanism-inspired models for particle relative biological effectiveness (RBE). Med. Phys. 45 (11), November, 2018. https://doi.org/10.1002/mp.13207

Stewart RD., et al. *Rapid MCNP simulation of DNA double strand break (DSB) relative biological effectiveness (RBE) for photons, neutrons, and light ions*. Phys. Med. Biol. 60, 2015, 8249–8274. https://doi.org/10.1088/0031-9155/60/21/8249

Stope MB. *Phosphorylation of histone H2A.X as a DNA-associated biomarker (Review)*. World Academy of Sciences Journal, 3, 31, 2021. https://doi.org/10.3892/wasj.2021.102

Sumini M., et al. *A Plasma Focus device as ultra-high dose rate pulsed radiation source. Part I: primary electron beam characterization*. Rad. Phys. Chem. 162, 1-11, 2019a. https://doi.org/10.1016/j.radphyschem.2019.02.027

Sumini M., et al. *A Plasma Focus device as ultra-high dose rate pulsed radiation source. Part II: X-Ray pulses characterization*. Rad. Phys. Chem. 164, 108360, 2019b. https://doi.org/10.1016/j.radphyschem.2019.108360

Sumini M., et al. *Analysis and characterization of the X-ray beam produced by a PF device for radiotherapy applications*. X-Ray Spectr. 44, 289–295, 2015. https://doi.org/10.1002/xrs.2621

Sumini M., et al. *Dose-current discharge correlation analysis in a Mather type Plasma Focus device for medical applications*. Rad. Phys. Chem. 140, 452-457, 2017. https://doi.org/10.1016/j.radphyschem.2017.03.022

Sumini M., et al. *Preliminary design of a 150 kJ repetitive plasma focus for the production of 18-F*. Nucl. Instrum. Methods Phys. Res. Sect. A 562, 1068–1071, 2006. https://doi.org/10.1016/j.nima.2006.02.097

Thwaites D. *Accuracy required and achievable in radiotherapy dosimetry: have modern technology and techniques changed our views?* 2013 J. Phys.: Conf. Ser. 444 012006. https://doi.org/10.1088/1742-6596/444/1/012006

Todd P., et al. *Pulsed High-Intensity Roentgen Rays: Inactivation of human cells cultured in vitro and limitations on usefulness in radiotherapy*. Acta Radiologica: Therapy, Physics, Biology, 1968, 7:1, 22-26. https://doi.org/10.3109/02841866809133174

Town C. *Effect of High Dose Rates on Survival of Mammalian Cells*. Nature 215, 847–848, 1967. https://doi.org/10.1038/215847a0

Trott KR., et al. *Biological mechanisms of normal tissue damage: importance for the design of NTCP models*. Radiother Oncol. 2012, Oct;105(1):79-85. https://doi.org/10.1016/j.radonc.2012.05.008

Ulanowski A., et al. *On prognostic estimates of radiation risk in medicine and radiation protection*. Radiat Environ Biophys 58, 305–319, 2019. https://doi.org/10.1007/s00411-019-00794-1

Venkatesulu BP. et al. *Ultra high dose rate (35 gy/sec) radiation does not spare the normal tissue in cardiac and splenic models of lymphopenia and gastrointestinal syndrome*. Sci Rep, 2019, 9:17180. https://doi.org/10.1038/s41598-019-53562-y

Virelli A., et al. *Early effects comparison of X-rays delivered at high-dose-rate pulses by a plasma focus device and at low dose rate on human tumour cells*. Radiat Prot Dosimetry. 2015, Sep;166(1-4):383-7. Epub 2015 Apr 16. https://doi.org/10.1093/rpd/ncv163

Virelli A.,et al. *A system biology approach to ionizing radiation response by mammalian cell lines*. Sysbiohealth symposium, 14-15 December 2011, Bologna. Conference Proceedings: System Medicine Interfacing Physics, Mathematics and Medicine, 99-104, 2011. https://cris.unibo.it/handle/11585/126280?mode=full.57#.YY5Y8C9aa6s

Vozenin MC, et al. *The advantage of Flash radiotherapy confirmed in mini-pig and cat cancer patients*. Clin. Cancer Res. 1;25(1):35-42, 2019. https://doi.org/10.1158/1078-0432.ccr-17-3375

Wagner JC., et al. *Forward-weighted CADIS method for variance Reduction of Monte Carlo calculations of Distributions and multiple localized Quantities*. International Conference on Mathematics, Computational Methods & Reactor Physics (M&C 2009), 2009. https://www.osti.gov/biblio/1115344-fw-cadis-method-global-semi-global-variance-reduction-monte-carlo-radiation-transport-calculations

Wagner JC., et al. *MCNP: Multigroup/adjoint capabilities*. LA-12704. United States: N. p., 1994. https://doi.org/10.2172/10145615

Weiss H, et al. *Oxygen Depletion in Cells Irradiated At Ultra-High Dose-Rates and At Conventional Dose-Rates*. Int J Radiat Biol Related Stud Phys Chem Med, 1974, 26(1):17–29. https://doi.org/10.1080/09553007414550901

Werner Z., et al. Generation of high-intensity pulsed ion and plasma beams for material processing. Vacuum 63 (4), 701-708, 2001. https://doi.org/10.1016/S0042-207X(01)00261-5

Wiarda, D., et al. 2008. *Development and Testing of ENDF/B-VI.8 and ENDF/B-VII.0 Coupled Neutron-Gamma Libraries for SCALE 6*. ORNL/TM-2008/047, NUREG/CR-

6990. Oak Ridge National Laboratory, Oak Ridge, TN. https://www.nrc.gov/docs/ML0909/ML090990663.pdf

Wilson JD., et al. *Ultra-High Dose Rate (FLASH) Radiotherapy: Silver Bullet or Fool's Gold?* [published correction appears in Front Oncol. 2020 Feb 25;10:210]. Front Oncol. 2020, 9:1563. Published 2020, Jan 17. https://dx.doi.org/10.3389%2Ffonc.2019.01563

Wilson R. *Radiation, Risks and Health Impacts of*. Editor(s): Cutler J. Cleveland, Encyclopedia of Energy, Elsevier, 2004, Pages 223-236, ISBN 9780121764807. https://doi.org/10.1016/B0-12-176480-X/00433-2

Yasar Ay. *Neon soft x-ray yield optimization in spherical plasma focus device*. 2021, Plasma Phys. Control. Fusion 63 115009. https://doi.org/10.1088/1361-6587/ac206d

Yavas G. *Dose Rate Definition in Brachytherapy*. Turk J Oncol 2019, 34(Supp 1):44–55. http://dx.doi.org/10.5505/tjo.2019.1924

Zakaria AM., et al. *Ultra-High Dose-Rate, Pulsed (Flash) Radiotherapy With Carbon Ions: Generation of Early, Transient, Highly Oxygenated Conditions in the Tumor Environment*. Radiat Res, 2020, 194(6):587–93. https://doi.org/10.1667/RADE-19-00015.1

Ziegler JF., et al. *SRIM – The stopping and range of ions in matter*. Nuclear Instruments and Methods in Physics Research B, 268, 1818–1823, 2010. https://doi.org/10.1016/j.nimb.2010.02.091

Zlobinskaya O., et al. *Induction and repair of DNA double-strand breaks assessed by gamma-H2AX foci after irradiation with pulsed or continuous proton beams*. Radiat. Environ. Biophys., 51, 23-32, 2012. https://doi.org/10.1007/s00411-011-0398-1

Appendices

APPENDIX A - Radiation protection issues at the PFMA-3

Thinking to a future installation in a health facility, it was relevant to carefully evaluate the Radiation Protection (RP) issues related to such device which emits charged and neutral particles at ultra-high dose rates [Isolan L., et al., 2021b]. It should be recalled that, at the Montecuccolino Laboratory, the only hazards due to PFMA-3 radiations could be imputed to the photon beam. The gas ion beam, which is collimated and in the plasma motion direction, is completely shielded by the PFMA-3 pyrex glass bell that contains the electrodes [Heredia-Avalos S., et al., 2005; Paul H. and Schinner A., 2001; Ziegler JF., et al., 2010]. On the other hands, the electron beam in the backward direction is collimated through the hollow anode and forced to impact on the metal target which shields the majority of such light charged particles. It should be noted that some electrons can be produced during the interactions with the different materials or even escape the target due to the range. By the way, such electrons are in a negligible quantity, are shielded in the majority of the cases from the pyrex (which covers almost all the directions apart the vertical one) [Berger MG., et al., 2005] or other components and finally are far from the operators which are several meters distance. On the contrary, the photons emitted by the PFMA-3 pulses moves the attention to the radiation protection point of view. Such radiations are characterized for being so intense and so shorts that can be considered hazarding for the operators. The usual active instrumentation designed for RP purposes (e.g. ionization chambers or different) could be insensitive at such fields or, on the contrary, could easily saturate. Due to that, a viable solution which has been implemented at the Montecuccolino Laboratory, it is the usage of passive dosimeters such as TLD (which, in certain cases, are known to be mostly energetic and DR independent [Karsch, L., et al., 2012]) for collecting doses

around the source in an easy, economic, reliable and replicable way. To be confident with the results from the TLD used at the Bologna facility against the PFMA-3 photon beams, a detailed MCNP model of the device has been designed and simulated in the hosting Laboratory benchmarking the experimental outcomes. The validated numerical model has also been used for evaluating doses in other interesting position in the Radiation Controlled Zone (RCZ) and in the Operator Control Room (OCR). Moreover, separately from the standalone in air simulations, the application of the iron cell holder usually used for cell culture irradiations and a PMMA phantom in which dosimetry experiments are typically carried out have been also taken into account.

For obtaining reliable results, the Forward Consistent Adjoint Driven Importance Sampling (FW-CADIS) methodology has been applied with the ADVANTG code in addition to the standalone MCNP code, in such a way to estimate doses in the really small TLD introduced in a very large geometry and radiation field [Mosher SW., et al., 2015]. The detailed geometry of the PFMA-3, as implemented in MCNP, is shown in Figure 70, where also the steel cell holder (cylindrical geometry, steel case and 1 cm radius window) and a typical PMMA phantom (parallelepiped 4x10x2.5 cm) have been taken into account. The shielding cylindrical lead cap consists in a 1.53 cm on the sides and 1.94 cm on the top thick shield, 15 cm high, positioned over and around the target.
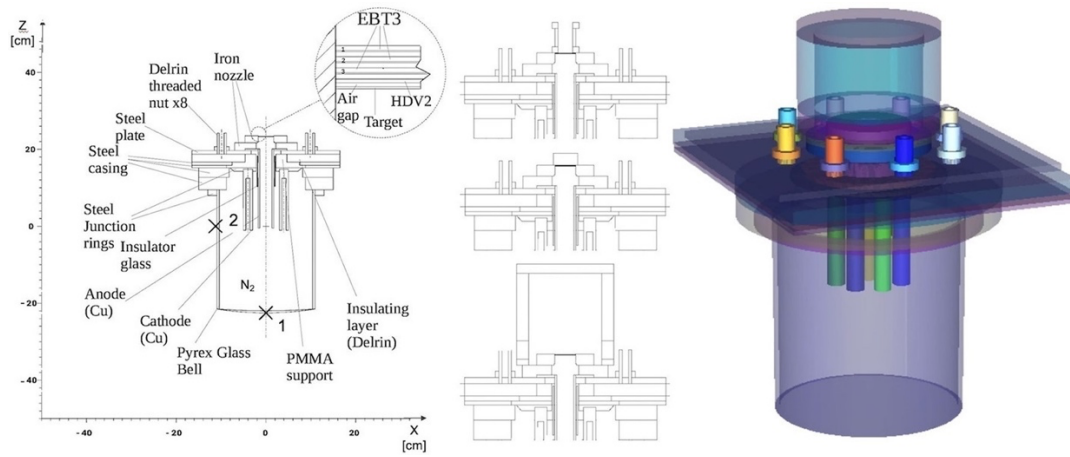
Figure 70. PFMA-3 geometry as implemented in MCNP. Left, XZ axial section. 1), 2): position of two TLD. Centre, from above: with the cell holder, the PMMA phantom and the lead shield. Right, 3D MCNP model [Isolan L., et al., 2021b].

The experimental environment

The Montecuccolino Laboratory Hall of the University of Bologna was originally the main room of an experimental nuclear reactor (Reattore Bologna Due, RB2, managed by AGIP and ENEA), completely decommissioned at the beginning of the nineties of the past Century, then released for ordinary laboratory use.

The actual experimental area is delimited by a gridded metal fence of 2 m high on two sides, by a metallic tubular fence 1 m high on a third side and of a separatory wall between the laboratory hall and the control room (the old control room of the RB2). The wall is mainly constituted by glass but also concrete, iron bars, iron slabs and wooden details. The laboratory access is in the metal fence side. The ceiling of the room is more than 10 m high, and nothing can be located above the source. Pneumatic interlocks, able to operate even in power failure cases, located in the access compartment guarantees immediate inhibition of operation if opened. Two pulsing red lights warn about the risk. Moreover, during the process of charging the capacitor bank, an intermittent acoustic alarm is activated. The control of the device takes place from the console in the Operator Control Room, from which it is possible to visually check the Laboratory Hall. The whole device occupies an area of approximately 2 m^2 while the Laboratory's operational dimensions are 6 m and 10 m respectively. The minimum distance between the device and the fence is approximately 2.55 m. Different TLD have been modeled in positions 1, 2, 3, 4, 5 (Figure 70, Figure 71) while other detectors, for numerical evaluations in points of interests, are referred as 6, 7, 8, 9, 10, 11.
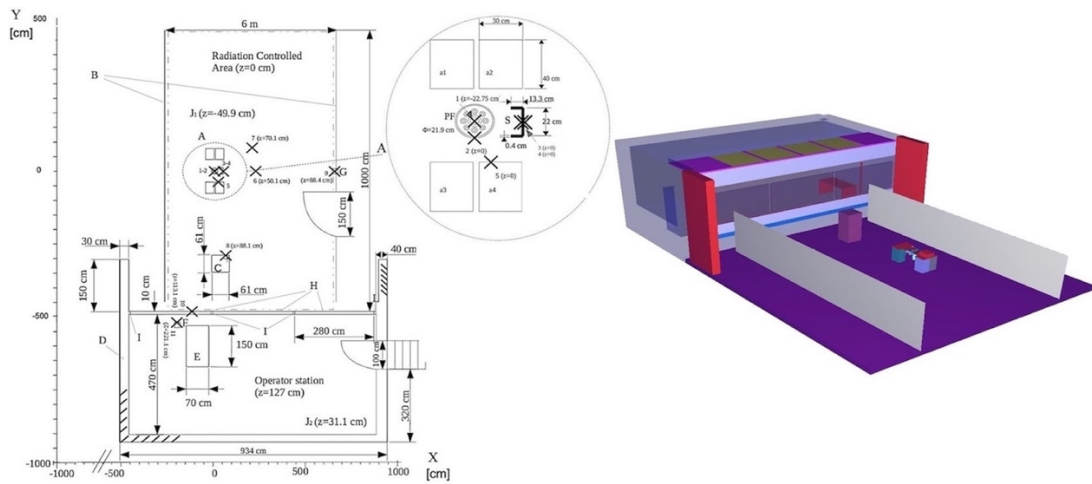
Figure 71. Montecuccolino Laboratory hall and operator room. Left, XY view. The positions of the modeled detectors are shown. 1, 2, 3, 4, 5 referring to numerical points of evaluation. 6-11, numerical detectors in other positions. A, magnification of the PFMA-3 area. a1, a2, a3, a4, capacitors. S, lead shield. B, iron perimeters. C, power supply. D, concrete wall. E, operator desk. F, G, vertical square section poles. H, glass wall above wood and iron panels. I, iron frame. See also Figure 1. J1 and J2, relative heights of the floors of the controlled area and of the control room. The height of the detectors is shown. Right, 3D MCNP model [Isolan L., et al., 2021b].

The TLD setup

The punctual numerical dose estimators have been evaluated reproducing the usual (X+γ) photon dosimeters made of LiF(Mg, Cu, P). The effective and real dosimeters are characterized by a sensitivity range is between 13 keV to 1.25 MeV while the output lower threshold is 0.05 mSv. The angle dependence of response is 10 % and the energy dependence of response is 16 %. The dosimeters are characterized to an overall uncertainty equal to 35 % in the 0.05-0.35 mSv range, 30 % in the 0.35-0.65 mSv range and 25 % for doses greater than 0.65 mSv. The first five numerical TLD have been positioned respectively under the Pyrex glass PFMA-3 bell, at the pinch height on the Pyrex glass PFMA-3 bell, before and after a flat metal shielding panel positioned on the floor in proximity of the PFMA-3 at the pinch height and on a capacitor in front of the Pyrex. The others have been positioned in other interesting coordinates.

Codes and parameters setup

The simulations have been performed with the Monte Carlo Code MCNP release 6.1.1 in four steps, with the support of the ADVANTG tool for variance reduction. Such preparatory work within all the intermediate results is presented in the next sessions.

The source spectrum has been chosen in such a way to test the robustness of the present method and the simulation performances. Due to that, a large range spectrum with also a long "low probability" tail has been considered as primary particle source, taking also into account the divergence of the beam given by the physical processes that occurs during the emission (e.g. the Coulomb interactions between charged streams). Such combination of characteristics, from the Monte Carlo point of view, can be considered critical in terms of convergence and, in general, performances. The implemented primary source characteristics are shown in Figure 71. The photon spectrum, evaluated in the target with an F4 tally [Booth TE., et al., 2003] with a bin width equal to 0.5 keV clearly shows the physics of the interactions that occurs also in comparison with the primary source. The electron and photon energy cutoff have been set to 1 keV (in all the simulation steps).
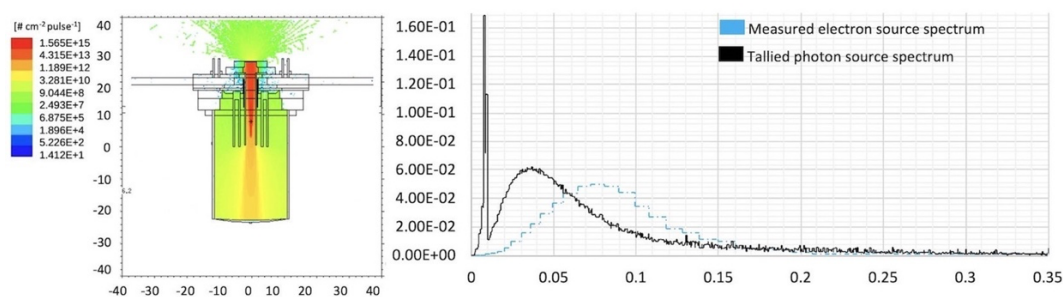
Figure 72. Left, electron source spatial distribution. Length scale in cm. Right, primary electron source spectrum and photons tallied at the target. Energy scale in MeV [Isolan L., et al., 2021b].

The photon spectrum, as tallied at the target, has been used as new primary source for a simulation speed-up. The characteristics of the new source have been benchmarked (with respect to the photons produced by the old ones) against the photon dose in function of the depth in four Gafchromic© film active layers using an F6 tally and against the photon spectra at the different film active layers with an F4 with 5 keV bin width (Figure 72). The benchmark shown a good agreement, at least for the next RP evaluation purposes.
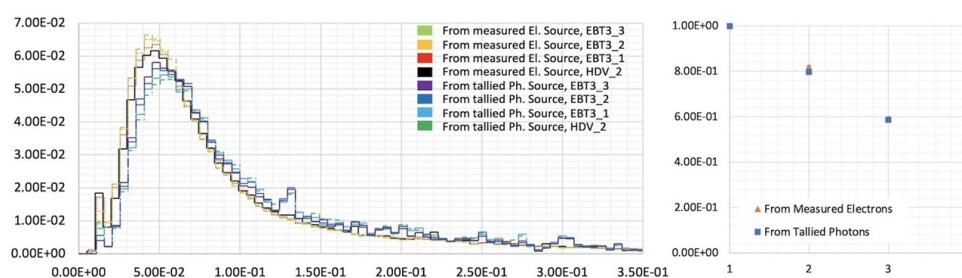
Figure 73. Left, photon spectra estimated starting from the electron primary source interacting with the brass target benchmarked with the ones estimated from the photon primary source. Energy scale in MeV. Right, Percentage Dept Dose (PDD) from photons derived by the interaction with the primary electron source with the target and evaluated at the different Gafchromic© film layers in comparison with the PDD from photons as primary source. See Figure 1 for details [Isolan L., et al., 2021b].

Step 3: variance reduction with ADVANTG

Estimate quantities in the small dosimeters in a so large-scale model or 3D dose distributions on the whole geometry, is really time consuming in a pure analog Monte Carlo calculation. Also with the presence of thick lead shielding, the ADVANTG tool for an optimized VRT, both for evaluating doses at the TLD positions and for performing a global weighting in such a way to estimate quantities (e.g. dose distributions) nearly with a uniform statistical precision on the large tally volume as a mesh-tally covering the entire laboratory, has been used. For the TLD doses estimation, the FW-CADIS methodology has been followed for generating a set of Weight Windows (WW) based on the adjoint flux calculation. The mesh cubic element has a typical size of 4 cm for not being missed by the so-called ray-tracer of ADVANTG but with a reasonable computational time for the biasing parameters build-up. The 200n47g cross section library (a library with 200 neutron groups and 47 gamma groups, respectively in the 1.0E-11:2.0E+01 and 1.0E-02:2.0E+01 MeV ranges, evaluated from the ENDF/B-VII.0 and intended as general-purpose shielding libraries based on a weighting function that consists of a fission spectrum, a 1/E slowing down spectrum, and a Maxwellian distribution; details in Mosher SW., et al., 2015 and Wiarda D., et al., 2008) and 8 polar and 8 azimuthal angles per octant of sphere have been chosen. A Legendre scattering angle expansion (L) equal to 1 has been initially set before moving to 2 and 3. The parameter has a high impact on the DENOVO (the three-dimensional transport code implemented in ADVANTG to obtain the solution of the Boltzmann equation) consumed memory, which scales as $(L+1)^2$. Generally, a high expansion order is recommended for a better physics description of the problem (in particular for photons). Regarding problem scalability, in geometries characterized by a large scale

as the one tested (and where a higher value of L is required) DENOVO could be run in parallel thanks to a multi-threading paradigm (OpenMP) [Chapman B., et al., 2007] libraries. For this reason, a scalability test has been preliminary performed by varying the Legendre scattering angle expansion for studying the behavior of the importance map from the starting point, L=1, up to L=3 and from 128 to 512 angular sectors. An example of 512 directions Adjoint flux (that has the meaning of "importance" [Lewins J., 1965]) and L=3, reflecting the WW applied to the model, is shown. Differences in terms of adjoint flux scales and performances can be spotted. As it can be also seen, with 128 angles several adjoint sources (the detectors) are not well represented. Finally, to optimize the map distribution over the entire geometry on a mesh-tally calculation, a Global Weighting through the FWCADIS spatial treatment has been applied to the model and an example of obtained total adjoint flux (importance map) is also shown with a 10 cm mesh characteristic size, 200n47g cross section library, 8 polar and 8 azimuthal angles per octant of sphere (512 angles) and L3. See Figure 73 and Figure 74.
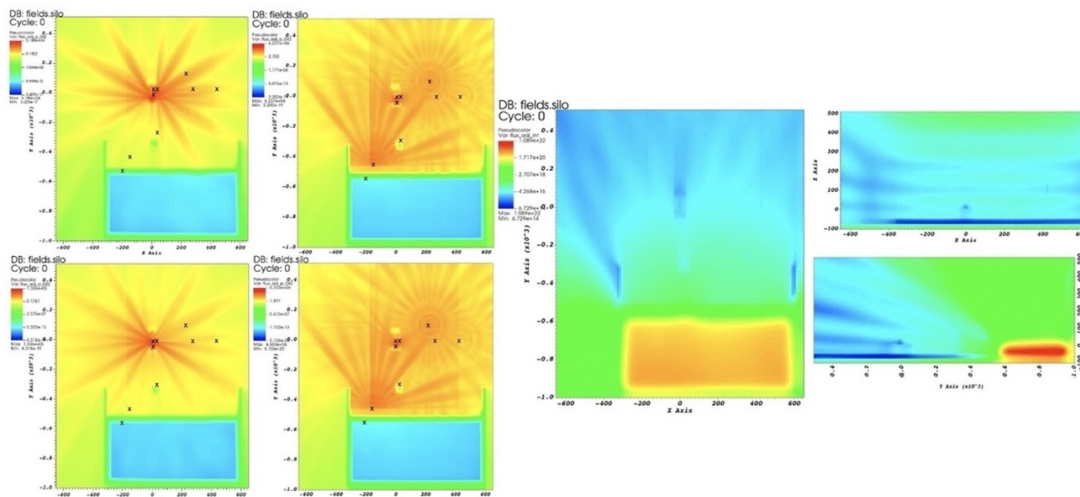
Figure 74. Left, adjoint flux evaluation convergence pattern for the FW-CADIS methodology. From above, L1 and L3 order. From left to right, 128 and 512 directions. Crosses indicate the adjoint source positions in the XY plane. Color maps not

synchronized. Right, Total Adjoint flux for a GVR treatment calculated with the ADVANTG tool, XY plane [Isolan L., et al., 2021b].
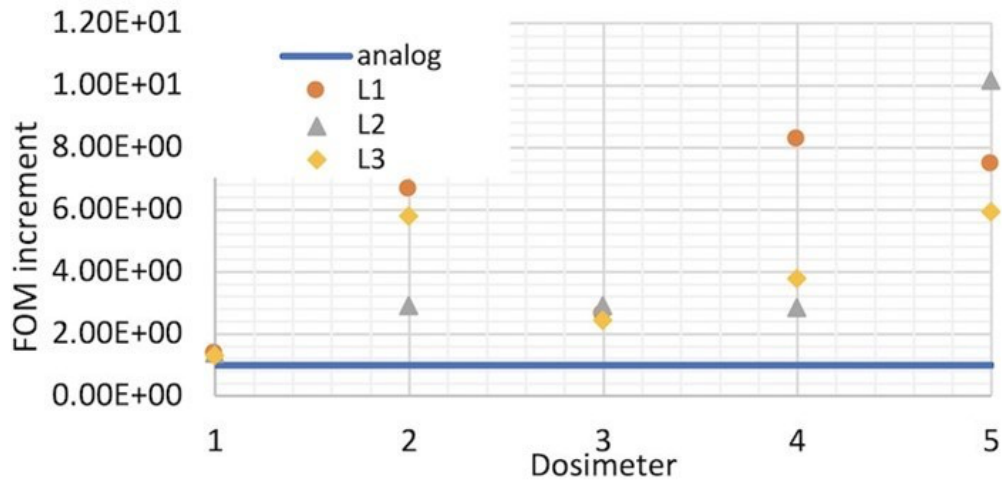
Figure 75. FOM comparison between analog simulations and L1, L2, L3 WW with 512 directions and the FW-CADIS methodology [Isolan L., et al., 2021b].

213

MCNP6.1.1 has been run with a precision target of 10% as relative error, using the WW maps in combination with a Weight Window Parameter and Source Biasing cards for estimating the TLD doses. The spectra at the first set of five TLDs (15 keV bin width) around the source, the doses in other position of RP interests, a dose map around the source with 0.25 cm^3 cubic mesh elements and a complete dose map with discretizing the space in a 10 cm-size cubic mesh for a complete 3D distribution have been estimated. Also, the different experimental tools impact (e.g. the cell's holder, the PMMA phantom and the lead shield) have been evaluated.

In Table 29, the results of the evaluated doses are reported. In Figure75, the results of the first set of five detector is represented comparing the results between analog an biased simulations. The higher dose has been registered in the dosimeter in direction with the target, the # 1, which was positioned at the Pyrex glass bell bottom. Such dosimeter has been subjected to the primary beam from the hollow anode and shielded by the Pyrex. The dosimeter # 2 on the side of the Pyrex glass bell registered a dose smaller than the dosimeter # 1 because even if closer to the source, a higher attenuation occurs before the photons could reach it. The flat shield panel, positioned on the floor, has been found to be highly effective in reducing the dose in the Laboratory entrance direction, with an abatement factor equal to 40 (efficiency of 97 %). Finally, the dosimeter # 5 on the capacitor, confirmed the order of magnitude of the doses. It must be also noted that the four capacitors can be considered as a sort of "natural" heavy shields for the majority of the directions above the device. In Figure 75 The spectral characteristics of the radiation interacting with the TLD material at the different positions around the PFMA-3 has been also estimated thanks to the FW-CADIS methodology. The dosimeter in the position # 1 is subjected to a spectrum similar to the one from the photon source, as expected, while the others result more filtered (as a sum of interaction processes through materials but also of scattering by the floor, the shields, the capacitors and the PFMA-3 structures which occurs in many different ways and also with more "weight" with respect to the dosimeter # 1, mostly subjected to the attenuated primary beam). The dose map distribution around the device, close to the source, is presented in Figure 76, showing also the Relative Error (RE) map of the simulation. The dose distribution in the entire geometry is shown in Figure 77, reporting

the RE distribution map proving the effectiveness of the simulations. As it can be seen, the obtained RE is everywhere low apart a small region outside the RCZ and the OCR, beyond the concrete wall which is effectively the boundary of the model. In Figure, the dose map distributions considering the thick iron cell holder, the PMMA phantom usually used at the Montecuccolino Laboratory and the cylindrical lead shield are also shown within the simulation RE. The cell holder behaves like a symmetrical cylindrical collimator. As expected, the PMMA offers an attenuation to the beam but also a diffusion in the ambient with a beam asymmetry, due to the asymmetry of the phantom itself. The results regarding the application of the thick cylindrical lead shield are shown, proving that the designed configuration is effective in reducing doses.
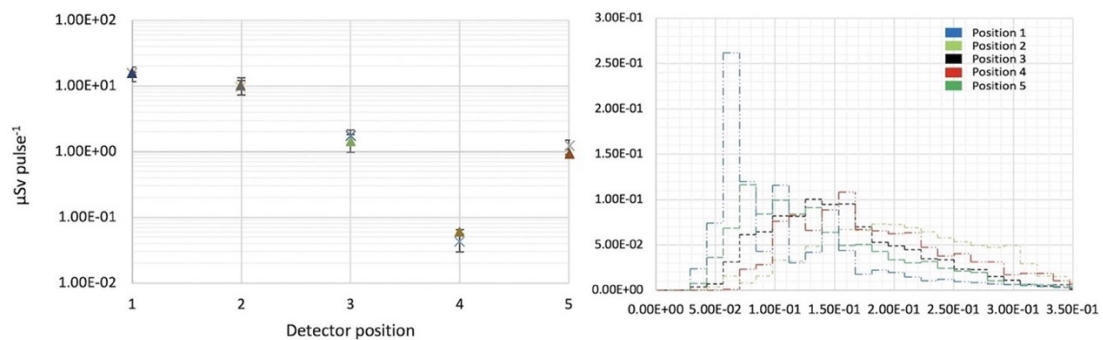
Figure 76. Left, TLD simulation results benchmark. Δ MCNP analog results (very low FOM and unnecessary long simulation time even if near to the source due to the small dimension of the detectors). + biased results. Right, Spectra estimated at the TLD positions. Energy scale in MeV [Isolan L., et al., 2021b].

Table 29. MCNP dose evaluation at the detector positions. See Figure 1 and Figure 2 for details [Isolan L., et al., 2021b].

Detector	[µSv pulse⁻¹]
1	1.56E+01
2	1.03E+01
3	1.41E+00
4	5.98E-02
5	9.43E-01
6	6.33E+01
7	3.40E+00
8	2.76E+00
9	2.53E+00
10	5.41E-01
11	3.23E-01
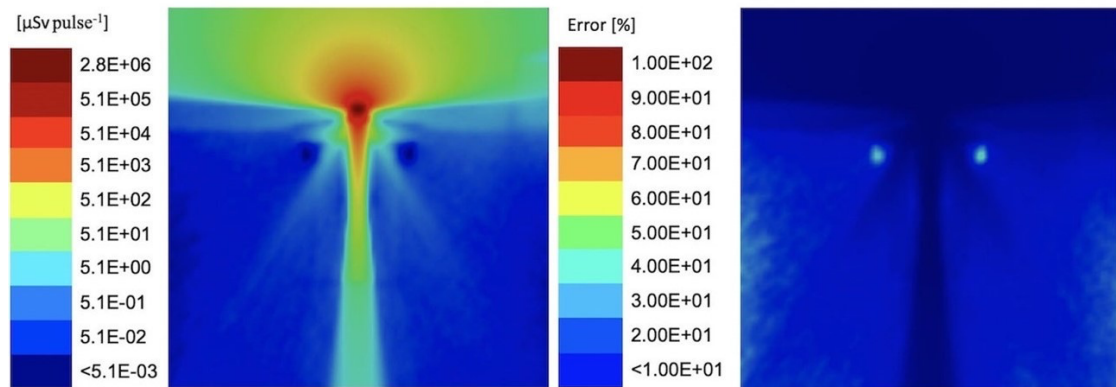
Figure 77. Left, photon dose distribution around the PFMA-3 target on the XZ plane. Right, Relative Error of the calculation [Isolan L., et al., 2021b].
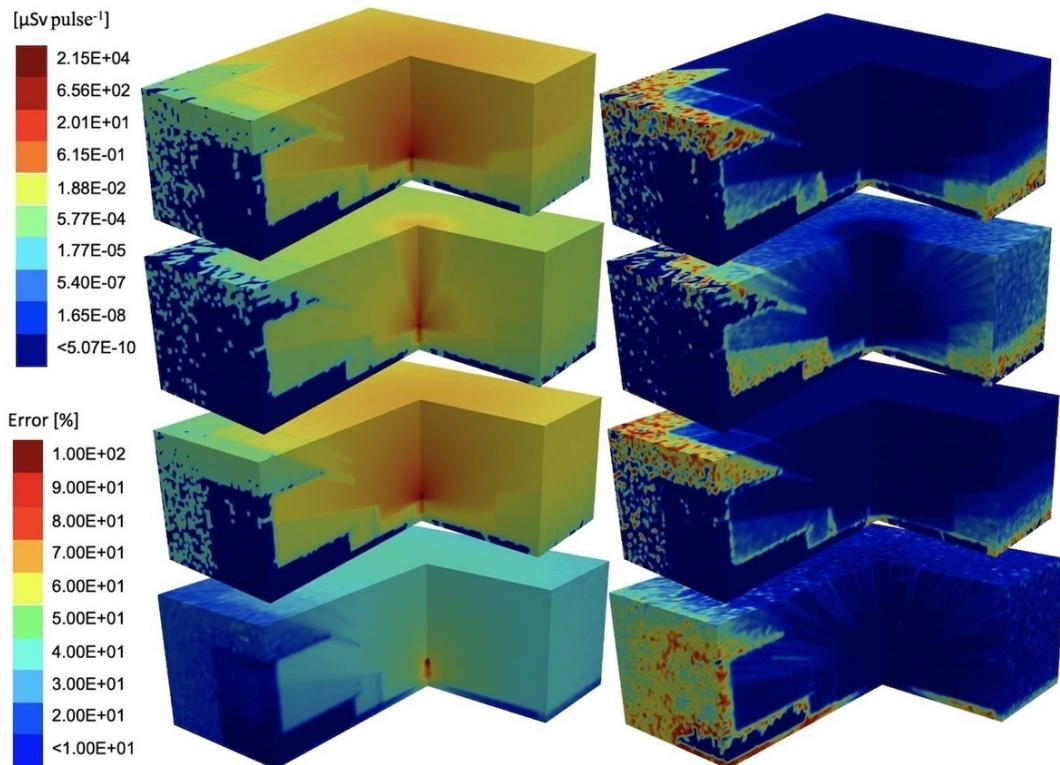
Figure 78. 3D dose distributions and RE on a cut centered on the PFMA-3 target. Results related to the whole model. Left pictures and upper scale refer to doses. Right pictures and lower scale refer to RE. From above, distribution in the entire geometry for in-air beam, with the cell holder, the PMMA phantom and the lead shield [Isolan L., et al., 2021b].

The dose evaluation around a flashing device, e.g. a Plasma Focus source inspired to the PFMA-3 hosted at the Laboratory of Montecuccolino, has been performed with pure numerical techniques for assessing a robust simulation method combining different codes and procedures for both simulation speed-up and keeping reliable the physics of the problem. The MCNP model of the device has been developed considering the whole Laboratory hall and also the Operator Control Room. The simulations have been carried out in four steps for optimization. A first simulation ran with a purely hypothetical primary electron test source. The outcoming photon spectrum and the spectral and PDD characteristics of the X-ray beam in different

Gafchromic© films have been estimated. The target spectrum has been used for a calculation speed-up in a second step. Such secondary source has been also benchmarked against the primary beam effects. As third step, different VRT strategies through the ADVANTG code have been followed with a strong enhance of the performances. As fourth step, the MCNP model has been used for estimating the spectral characteristics of the photons at the TLD positions, the doses in other different points of interest and also dose maps around the source and in the entire Monte Carlo geometry (even considering experimental tools such as cell holders, PMMA phantoms and thick cylindrical lead shields). In particular, the simulations proved the effectiveness of the designed lead shield which has been thought for reducing doses around the device and to follow the ALARA principle. It must be noted that the shields are usually designed for attenuating photon beams and without a proper VRT, as it should be, no particles should be easily transported outside the barrier and so no analog results could be obtained in reasonable amount of time or without heavily parallelized codes and machines (e.g., supercomputers). A conclusion for this part can be given: a numerical simulation dedicated strategy suitable for flashing source (but not only) to be hosted in large facilities/laboratories/hospitals, with the MCNP code and the ADVANTG tool, have been outlined and followed to achieve optimized results in term of evaluation of quantities of interest, shielding design and performances. The same strategy could be considered of relevance in the RP practice, making viable the investigation of very complex sources and environments in a fast, robust and reliable numerical modeling where measures the radiation fields could not be easily done. Such techniques could be used by the Radiation Protection Expert for supporting its preliminary radiation protection evaluations and estimate doses for workers or design proper shielding.

APPENDIX B - Electron measured source spectra data for MCNP

```
c 12kV. 0.40 mbar


Si1 H 0.0 0.001689301 0.003362827 0.005599626 0.008392422 0.011732303
      0.015608863 0.020010349 0.024923828 0.030335361 0.036230173 0.042592829
      0.049407395 0.056657597 0.064326968 0.072398979 0.080857157 0.08968519
      0.09886702 0.108386914 0.118229529 0.128379963 0.138823793 0.149547102
      0.160536505 0.171779154 0.183262746 0.194975526 0.206906277 0.219044312
      0.231379465 0.243902075 0.256602966 0.269473438 0.282505238 0.295690548
      0.309021964 0.322492475 0.336095448 0.349824601 0.363673995 0.377638007
      0.391711318 0.405888897 0.420165981 0.434538063 0.449000876 0.463550381
      0.478182753 0.492894369 0.507681796
SP1 D 0.0 0.001346207 0.002185518 0.004550224 0.008715847 0.015363109
      0.024839352 0.037350349 0.052645965 0.069810514 0.086985721 0.10000745
      0.104220496 0.091686425 0.06240326 0.037782468 0.035296102 0.04445687
      0.04098651 0.02569869 0.018424632 0.017292172 0.017434085 0.005192772
      0.00308702 0.002532123 0.001528881 0.002341466 0.001878322 0.001721434
      0.003015161 0.002391242 0.005358237 0.002943015 0.003045748 0.002440937
      0.002997895 0.011891786 0.002191933 0.003925853 0.00284091 0.002907726
      0.002845056 0.003419076 0.004902739 0.005413698 0.003402414 0.003304294
      0.004180652 0.005471217 0.003346428


c 14kV. 0.40 mbar


SI1 H 0.0 0.001666215 0.003330301 0.005557767 0.008341365 0.01167221
      0.015539918 0.019932758 0.024837815 0.030241166 0.036128049 0.042483037
      0.049290204 0.05653328 0.0641958 0.072261235 0.080713111 0.089535113
      0.098711176 0.108225563 0.118062923 0.128208346 0.138647401 0.149366164
      0.160351238 0.171589769 0.183069443 0.194778497 0.206705703 0.218840368
      0.231172317 0.243691879 0.256389872 0.269257586 0.282286762 0.295469575
      0.308798615 0.322266864 0.33586768 0.349594781 0.363442217 0.377404363
      0.391475895 0.405651776 0.419927239 0.434297773 0.448759108 0.4633072
      0.477938221 0.492648545 0.507434735 0.522293535
SP1 D 0.0 0.001173282 0.001921425 0.003933163 0.00737462 0.01313036
      0.020997784 0.031962833 0.044993054 0.060184123 0.075400612 0.087895677
      0.097486937 0.09974295 0.093416385 0.079888511 0.059282338 0.044682723
      0.033306568 0.025546645 0.019633566 0.01365803 0.012496658 0.008719605
      0.004764639 0.003068211 0.001402502 0.001657002 0.00155977 0.001701345
      0.001688526 0.001751641 0.001980585 0.002149224 0.001508778 0.001470264
      0.001926668 0.002143395 0.002203461 0.002130551 0.002156393 0.002337987
      0.002360727 0.002500635 0.002303939 0.002974154 0.002623088 0.002280737
      0.002675958 0.002430841 0.002537382 0.00288375


c 16kV. 0.40 mbar


SI1 H 0.0 0.001666215 0.003330301 0.005557767 0.008341365 0.01167221
      0.015539918 0.019932758 0.024837815 0.030241166 0.036128049 0.042483037
      0.049290204 0.05653328 0.0641958 0.072261235 0.080713111 0.089535113
      0.098711176 0.108225563 0.118062923 0.128208346 0.138647401 0.149366164
      0.160351238 0.171589769 0.183069443 0.194778497 0.206705703 0.218840368
      0.231172317 0.243691879 0.256389872 0.269257586 0.282286762 0.295469575
      0.308798615 0.322266864 0.33586768 0.349594781 0.363442217 0.377404363
      0.391475895 0.405651776 0.419927239 0.434297773 0.448759108 0.4633072
      0.477938221
SP1 D 0.0 0.000905262 0.001461757 0.002892127 0.005273538 0.00906297
      0.014215737 0.021189162 0.029614951 0.038703335 0.048439839 0.058630791
      0.067120002 0.073833778 0.074939785 0.072152025 0.064417755 0.057211554
      0.051576187 0.047437237 0.043496686 0.038400166 0.035118218 0.030930569
      0.026710126 0.021517808 0.016110225 0.011671554 0.010256841 0.002610075
      0.000528114 0.00049775 0.000523253 0.000635119 0.000642802 0.000931387
      0.000932186 0.001017416 0.00104675 0.001009723 0.001605388 0.004916931
      0.001360812 0.001346684 0.001755085 0.000965693 0.00114935 0.001343588
      0.00189191


c 18 kV. 0.45 mbar


SI1 H 0.0 0.001689301 0.003362827 0.005599626 0.008392422 0.011732303
      0.015608863 0.020010349 0.024923828 0.030335361 0.036230173 0.042592829
      0.049407395 0.056657597 0.064326968 0.072398979 0.080857157 0.08968519
      0.09886702 0.108386914 0.118229529 0.128379963 0.138823793 0.149547102
      0.160536505 0.171779154 0.183262746 0.194975526 0.206906277 0.219044312
      0.231379465 0.243902075 0.256602966 0.269473438 0.282505238 0.295690548
      0.309021964 0.322492475 0.336095448 0.349824601 0.363673995 0.377638007
```

```
        0.391711318 0.405888897 0.420165981 0.434538063 0.449000876 0.463550381
        0.478182753 0.492894369
SP1 D 0.0 0.000506137 0.00066953 0.001105696 0.001841899 0.002928607
        0.004487925 0.006576291 0.009244587 0.012556984 0.016383505 0.02090279
        0.025716789 0.030825608 0.035465822 0.040811164 0.044320955 0.047370694
        0.048755617 0.048156081 0.046673199 0.04541434 0.044960487 0.044672026
        0.04497688 0.044580073 0.043331288 0.041223653 0.038918739 0.036490813
        0.033781247 0.030194165 0.026207253 0.02329284 0.019546874 0.016401549
        0.01224224 0.003534458 0.000566933 0.000414801 0.000377885 0.000386539
        0.000364582 0.000372002 0.000431581 0.000359397 0.000360634 0.000359397
        0.000363313 0.000574129


c 18 kV. 0.5 mbar


Si1 H 0.0 0.001689301 0.003362827 0.005599626 0.008392422 0.011732303
        0.015608863 0.020010349 0.024923828 0.030335361 0.036230173 0.042592829
        0.049407395 0.056657597 0.064326968 0.072398979 0.080857157 0.08968519
        0.09886702 0.108386914 0.118229529 0.128379963 0.138823793 0.149547102
        0.160536505 0.171779154 0.183262746 0.194975526 0.206906277 0.219044312
        0.231379465 0.243902075 0.256602966 0.269473438 0.282505238 0.295690548
        0.309021964 0.322492475 0.336095448 0.349824601 0.363673995 0.377638007
        0.391711318 0.405888897 0.420165981 0.434538063 0.449000876 0.463550381
        0.478182753 0.492894369
SP1 D 0.0 0.000436285 0.000556614 0.000890941 0.001489671 0.002433132
        0.003776433 0.005588475 0.00790243 0.010704349 0.013993593 0.017811279
        0.022446715 0.02702857 0.032395097 0.036610604 0.040736494 0.044481011
        0.047483773 0.048254646 0.048033636 0.046060726 0.043294462 0.041378267
        0.040711362 0.04062275 0.040097129 0.039778914 0.038542824 0.037142158
        0.035629185 0.033224457 0.030632053 0.027568061 0.024164564 0.0206662
        0.017464025 0.01391942 0.009356214 0.002933844 0.000460468 0.000482235
        0.00032561 0.000325271 0.000378792 0.000375659 0.000325164 0.000337751
        0.000366266 0.000382423


c 18 kV. 0.6 mbar


Si1 H 0.0 0.001689301 0.003362827 0.005599626 0.008392422 0.011732303
        0.015608863 0.020010349 0.024923828 0.030335361 0.036230173 0.042592829
        0.049407395 0.056657597 0.064326968 0.072398979 0.080857157 0.08968519
        0.09886702 0.108386914 0.118229529 0.128379963 0.138823793 0.149547102
        0.160536505 0.171779154 0.183262746 0.194975526 0.206906277 0.219044312
        0.231379465 0.243902075 0.256602966 0.269473438 0.282505238 0.295690548
        0.309021964 0.322492475 0.336095448 0.349824601 0.363673995 0.377638007
        0.391711318 0.405888897 0.420165981 0.434538063 0.449000876 0.463550381
        0.478182753 0.492894369
SP1 D 0.0 0.000453866 0.00060358 0.00099096 0.00163822 0.002631447 0.00401317
        0.005827875 0.008145289 0.010976929 0.014291064 0.018301127 0.022468267
        0.027191083 0.031665656 0.035145077 0.038344815 0.041087243 0.042041083
        0.042825561 0.042594458 0.043040104 0.04413909 0.045131531 0.0456123
        0.045571097 0.04573463 0.045214305 0.043741692 0.042228258 0.039376612
        0.036255839 0.032712364 0.028300275 0.025022212 0.019745253 0.014010769
        0.004834266 0.002656715 0.001352336 0.000467507 0.000513249 0.000469206
        0.000390395 0.000380556 0.000478301 0.000350778 0.000349559 0.000343539
        0.000340476


c 20kV. 0.40 mbar


SI1 H 0.0 0.001689301 0.003362827 0.005599626 0.008392422 0.011732303
        0.015608863 0.020010349 0.024923828 0.030335361 0.036230173 0.042592829
        0.049407395 0.056657597 0.064326968 0.072398979 0.080857157 0.08968519
        0.09886702 0.108386914 0.118229529 0.128379963 0.138823793 0.149547102
        0.160536505 0.171779154 0.183262746 0.194975526 0.206906277 0.219044312
        0.231379465 0.243902075 0.256602966 0.269473438 0.282505238 0.295690548
        0.309021964 0.322492475 0.336095448 0.349824601 0.363673995 0.377638007
        0.391711318 0.405888897 0.420165981 0.434538063 0.449000876 0.463550381
        0.478182753 0.492894369
SP1 D 0.0 0.001043078 0.001613007 0.003118367 0.005699569 0.009701416
        0.015405003 0.022746302 0.031593848 0.042072521 0.052720107 0.062977337
        0.072416554 0.079760259 0.083494979 0.081709995 0.075563764 0.066707319
        0.056974526 0.048511792 0.039753669 0.031746575 0.0240386 0.018177946
        0.014281595 0.011113984 0.007759156 0.006221297 0.002282964 0.001586954
        0.001113849 0.001282897 0.00131754 0.001314972 0.00205037 0.001383349
        0.001361796 0.001384239 0.001378788 0.001507499 0.001328061 0.001654655
        0.001388021 0.001268293 0.001658979 0.001680629 0.001503115 0.001461949
        0.0017818 0.001386717


c 22kV. 0.40 mbar


Si1 H 0.0 0.001689301 0.003362827 0.005599626 0.008392422 0.011732303
        0.015608863 0.020010349 0.024923828 0.030335361 0.036230173 0.042592829
        0.049407395 0.056657597 0.064326968 0.072398979 0.080857157 0.08968519
        0.09886702 0.108386914 0.118229529 0.128379963 0.138823793 0.149547102
```

```
        0.160536505 0.171779154 0.183262746 0.194975526 0.206906277 0.219044312
        0.231379465 0.243902075 0.256602966 0.269473438 0.282505238 0.295690548
        0.309021964 0.322492475 0.336095448 0.349824601 0.363673995 0.377638007
        0.391711318 0.405888897 0.420165981 0.434538063 0.449000876 0.463550381
        0.478182753 0.492894369 0.507681796 0.522541779
SP1 D 0.0 0.000590567 0.000755646 0.001255068 0.002292367 0.004123567
        0.007161738
        0.011864424 0.018243589 0.026340106 0.036197818 0.047443591 0.059318681
        0.070074394 0.079384091 0.086332922 0.090535326 0.090580085 0.085256225
        0.072808261 0.056343133 0.040723843 0.027994135 0.019653241 0.013860738
        0.004959563 0.005755028 0.003353114 0.002079817 0.001461742 0.001196398
        0.001273663 0.001208773 0.001192836 0.001544037 0.002522935 0.002974776
        0.001180806 0.001217993 0.001408122 0.001794405 0.003059126 0.001660663
        0.001501846 0.001598955 0.001435143 0.000985455 0.000664143 0.000596879
        0.001682334 0.001157193 0.001400699


c 24kV, 0.40 mbar


Si1 H 0.0 0.001689301 0.003362827 0.005599626 0.008392422 0.011732303
        0.015608863 0.020010349 0.024923828 0.030335361 0.036230173 0.042592829
        0.049407395 0.056657597 0.064326968 0.072398979 0.080857157 0.08968519
        0.09886702 0.108386914 0.118229529 0.128379963 0.138823793 0.149547102
        0.160536505 0.171779154 0.183262746 0.194975526 0.206906277 0.219044312
        0.231379465 0.243902075 0.256602966 0.269473438 0.282505238 0.295690548
        0.309021964 0.322492475 0.336095448 0.349824601 0.363673995 0.377638007
        0.391711318 0.405888897 0.420165981 0.434538063 0.449000876 0.463550381
        0.478182753 0.492894369
SP1 D 0.0 0.000711589 0.000901378 0.001474159 0.002558043 0.004363016
        0.007114105 0.010991172 0.015954396 0.022772047 0.030637479 0.039755037
        0.050404687 0.061276902 0.072374466 0.081510824 0.090122286 0.094616044
        0.093978572 0.085931674 0.07170754 0.053700537 0.037849337 0.025642803
        0.014869003 0.00837113 0.003545526 0.00133131 0.000755932 0.000561133
        0.001136328 0.000770019 0.000795565 0.000552118 0.000613005 0.000624617
        0.00055428 0.000662418 0.000524669 0.000553371 0.000508133 0.000496022
        0.00052097 0.000571878 0.001632623 0.001169053 0.001010712 0.000531627
        0.00049631 0.000494154
```

APPENDIX C - PFMA-3 input file for MCDS-MCNP simulations analysis

```
1     0           1 :−2 :3 :−4 :5 :−6
2    15 −0.0012205 −1 2 −3 4 −5 6 (7 :−8 )(9 :−10 )(11 :−12 )(13 :−14 )
           (15 :−16 )(17 :−18 )(19 :−20 )(21 :−22 )(23 :−24 :25 :−26 )27 28 29
            30 31 32 33 34 35 36 37 (−38 :39 :−40 :41 )(−42 :43 :40 :−44 )
           (45 :−46 :−47 :48 )(49 :−50 )(51 :−52 )(53 :−54 )(55 :−56 )
           (57 :−58 )(−59 :60 )(−60 :61 )(−62 :63 )(−63 :64 )(−65 :66 )
           (−66 :67 )(−68 :69 )(−69 :70 )(−71 :72 )(−72 :73 )(−74 :75 )
           (−75 :76 )(−77 :78 )(−78 :79 )(−80 :81 )(−81 :82 )#49 #47 #48 (90 )
           (91 )111 113 (100 :−101 )#56 (105 )(106 )(107 )#51 #52 #53 #54 #59
            #60 #66 (206 )(208 )(207)
3    10    −8.96 −7 8
4    10    −8.96 −9 10
5    10    −8.96 −11 12
6    10    −8.96 −13 14
7    10    −8.96 −15 16
8    10    −8.96 −17 18
9    10    −8.96 −19 20
10   10    −8.96 −21 22
11   10    −8.96 −23 24 −25 26
12   500    −1.2 −27
13   12    −1.38 −28
14   12    −1.38 −29
15   500    −1.2 −30
16   12    −1.38 −31
17   12    −1.38 −32
18   500    −1.2 −33
19   12   −1.385 −34
20   12   −1.385 −35
21   500    −1.2 −36
22   12    −1.38 −37
23    4    −2.23 38 −39 40 −41
24    4    −2.23 42 −43 −40 44
25    4    −2.23 −45 46 47 −48
26    8    −7.82 −49 50
27    8    −7.82 −51 52
28    5    −1.41 −53 54
29    5    −1.41 −55 56
30    5    −1.41 −57 58
31    5    −1.41 59 −60
32    5    −1.41 60 −61
33    5    −1.41 62 −63
34    5    −1.41 63 −64
35    5    −1.41 65 −66
36    5    −1.41 66 −67
37    5    −1.41 68 −69
38    5    −1.41 69 −70
39    5    −1.41 71 −72
40    5    −1.41 72 −73
41    5    −1.41 74 −75
42    5    −1.41 75 −76
43    5    −1.41 77 −78
44    5    −1.41 78 −79
45    5    −1.41 80 −81
46    5    −1.41 81 −82
47    8    −7.82 −83 84 (−59 :60 )(−62 :63 )(−65 :66 )(−68 :69 )(−71 :72 )
           (−74 :75 )(−77 :78 )(−80 :81 )
48    8    −7.82 −184 85 #49
49   10    −8.96 86 −87 −88 89
51    8    −7.82 −92 −93 94 96 (7 :−8 )(9 :−10 )(11 :−12 )(13 :−14 )
           (15 :−16 )(17 :−18 )(19 :−20 )(21 :−22 )(23 :−24 :25 :−26 )
           (26 :−24 :114 )
52    5    −1.41 93 −95 96 −97
53    5    −1.41 −98 96
54    5    −1.41 −99 96
55    3    −1.19 −100 101
56    8    −7.82 −102 103 104
57    7    −8.07 −105
58    5    −1.41 −106 :−107
59   11 −6e−007 −38 44 −42 −47 (7 :−8 )(9 :−10 )(11 :−12 )(13 :−14 )
           (15 :−16 )(17 :−18 )(19 :−20 )(21 :−22 )(23 :−24 :25 :−26 )
60   11 −6e−007 47 −48 −38 (7 :−8 )(9 :−10 )(11 :−12 )(13 :−14 )(15 :−16 )
           (17 :−18 )(19 :−20 )(21 :−22 )(23 :−24 :25 :−26 )
61   11 −6e−007 48 −108 −50 (7 :−8 )(9 :−10 )(11 :−12 )(13 :−14 )(15 :−16 )
           (17 :−18 )(19 :−20 )(21 :−22 )#11 (100 :−101 )
62   11 −6e−007 108 −93 −52 (7 :−8 )(9 :−10 )(11 :−12 )(13 :−14 )(15 :−16 )
           (17 :−18 )(19 :−20 )(21 :−22 )#11 (100 :−101 )#51
63   11 −6e−007 −112 #11 (100 :−101 )
64   11 −6e−007 −84 #11 (100 :−101 )
65   11 −6e−007 −113 (−86 :87 :88 :−89 )(23 :−24 :25 :−26 )(82 :−83 :−84 )
           (184 :−85 )#56
66   17   −1.06 −200 (−201 :202 )(203 )(204 )(205 )(206 )(208 )
67   16   −1.38 −206
68   19      −1 −208
69   18 −0.998207 −207
```

```
 1        px 100
 2        px −100
 3        py 100
 4        py −100
 5        pz 100
 6        pz −100
 7        rcc 4 0 −1 0 0 15.8 1
 8        rcc 4 0 −1 0 0 13.5 0.5
 9        rcc 2.8284 2.8284 −1 0 0 15.8 1
10        rcc 2.8284 2.8284 −1 0 0 13.5 0.5
11        rcc 0 4 −1 0 0 15.8 1
12        rcc 0 4 −1 0 0 13.5 0.5
13        rcc −2.8284 2.8284 −1 0 0 15.8 1
14        rcc −2.8284 2.8284 −1 0 0 13.5 0.5
15        rcc −4 0 −1 0 0 15.8 1
16        rcc −4 0 −1 0 0 13.5 0.5
17        rcc −2.8284 −2.8284 −1 0 0 15.8 1
18        rcc −2.8284 −2.8284 −1 0 0 13.5 0.5
19        rcc 0 −4 −1 0 0 15.8 1
20        rcc 0 −4 −1 0 0 13.5 0.5
21        rcc 2.8284 −2.8284 −1 0 0 15.8 1
22        rcc 2.8284 −2.8284 −1 0 0 13.5 0.5
23        cz 1.7
24        pz −0.5
25        pz 20.1
26        cz 1.4
27        rpp −2 2 −2 2 23.4335 23.4432
28        rpp −2 2 −2 2 23.4432 23.444
29        rpp −2 2 −2 2 23.444 23.4565
30        rpp −2 2 −2 2 23.4565 23.4595
31        rpp −2 2 −2 2 23.4595 23.472
32        rpp −2 2 −2 2 23.472 23.4845
33        rpp −2 2 −2 2 23.4845 23.4875
34        rpp −2 2 −2 2 23.4875 23.5
35        rpp −2 2 −2 2 23.5 23.5125
36        rpp −2 2 −2 2 23.5125 23.5155
37        rpp −2 2 −2 2 23.5155 23.528
38        cz 10.4
39        pz 9.5
40        pz −21.5
41        cz 10.95
42         z −21.5 10.4 −21.95 0 0 57.401316
43         z −21.5 10.95 −22.5 0 0 58.351316
44        pz −22.5
45        cz 12.95
46        cz 10.95
47        pz 8
48        pz 9.5
49        rcc 0 0 9.5 0 0 3.25 15
50        cz 8.8
51        rcc 0 0 12.75 0 0 2.45 15
52        cz 8.2
53        rpp −19 19 −16.5 16.5 15.2 15.85
54        cz 8.8
55        rpp −19 19 −16.5 16.5 15.85 16.68
56        cz 7.5
57        rpp −19 19 −16.5 16.5 16.68 18.7
58        cz 4.7
59        rcc 9.85 0 18.7 0 0 5.5 0.525
60        rcc 9.85 0 18.7 0 0 5.5 1.025
61        rcc 9.85 0 19.7 0 0 1 1.625
62        rcc 6.965 6.965 18.7 0 0 5.5 0.525
63        rcc 6.965 6.965 18.7 0 0 5.5 1.025
64        rcc 6.965 6.965 19.7 0 0 1 1.625
65        rcc 0 9.85 18.7 0 0 5.5 0.525
66        rcc 0 9.85 18.7 0 0 5.5 1.025
67        rcc 0 9.85 19.7 0 0 1 1.625
68        rcc −6.965 6.965 18.7 0 0 5.5 0.525
69        rcc −6.965 6.965 18.7 0 0 5.5 1.025
70        rcc −6.965 6.965 19.7 0 0 1 1.625
71        rcc −9.85 0 18.7 0 0 5.5 0.525
72        rcc −9.85 0 18.7 0 0 5.5 1.025
73        rcc −9.85 0 19.7 0 0 1 1.625
74        rcc −6.965 −6.965 18.7 0 0 5.5 0.525
75        rcc −6.965 −6.965 18.7 0 0 5.5 1.025
76        rcc −6.965 −6.965 19.7 0 0 1 1.625
77        rcc 0 −9.85 18.7 0 0 5.5 0.525
78        rcc 0 −9.85 18.7 0 0 5.5 1.025
79        rcc 0 −9.85 19.7 0 0 1 1.625
80        rcc 6.965 −6.965 18.7 0 0 5.5 0.525
81        rcc 6.965 −6.965 18.7 0 0 5.5 1.025
82        rcc 6.965 −6.965 19.7 0 0 1 1.625
83        rpp −15 15 −16.5 16.5 18.7 19.7
84        rcc 0 0 18.7 0 0 1 3.3
184        rcc 0 0 19.7 0 0 2 7
85        cz 2.2
86        cz 1.7
87        cz 4.7
88        pz 20.1
89        pz 19.7
90        rpp −331 −301 −465 −315 −49.9 373.1
91        rpp 573 603 −465 −315 −49.9 373.1
```

```
 92        kz 6.6 0.8711 1
 93        pz 15.2
 94        pz 14.28
 95        pz 15.85
 96        cz 2.2
 97        cz 8.8
 98        rcc 0 0 15.85 0 0 0.83 7.5
 99        rcc 0 0 16.68 0 0 2.02 4.7
100        rcc 0 0 10.3 0 0 8 2.05
101        rcc 0 0 10.3 0 0 8 1.85
102        rcc 0 0 21.7 0 0 1.7335 4.7
103        rcc 0 0 21.7 0 0 0.2 1.85
104        rcc 0 0 21.9 0 0 1.6 1.7
105        rcc 0 0 23.3285 0 0 0.005 1.7
106        rpp −19 −15 −16.5 16.5 18.7 22.7
107        rpp 15 19 −16.5 16.5 18.7 22.7
108         pz 12.75
109        rpp −19 19 −16.5 16.5 15.2 19.7
110        rcc 0 0 21.7 0 0 1.6435 4.7
111        rcc 0 0 9.5 0 0 10.2 15
112        rcc 0 0 15.2 0 0 3.5 2.2
113        rcc 0 0 19.7 0 0 3.6285 2.2
114         pz 20.095
115         pz 15.57
116         pz 14
117         cz 5.88
118         pz 20.2
200        rcc 0 0 23.528 0 0 3.2 2.3
201        rcc 0 0 24.028 0 0 2.2 2.1
202        rcc 0 0 24.028 0 0 2.2 2.3
203        rcc 0 0 23.628 0 0 0.0945 1.95
204        rcc 0 0 23.7225 0 0 2.9055 1.95
205        rcc 0 0 23.528 0 0 0.1 1.75
206        rcc 0 0 23.628 0 0 0.003 1.95
207        rcc 0 0 23.6314 0 0 2.9966 1.95
208        rcc 0 0 23.631 0 0 0.0004 1.95

mode  p e
m3     1000.12p      −0.080538
       6000.12p      −0.599848 8000.12p      −0.319614
m4     5000.         −0.040064
       8000.12p      −0.539562 11000.        −0.028191 13000.        −0.011644
       14000.        −0.37722 19000.         −0.003321
m5     1000.12p      −0.066667
       6000.12p         −0.4 8000.12p        −0.533333
m7     26000.        −0.00087
       29000.        −0.665382 30000.        −0.325697 50000.        −0.002673
       82000.        −0.005378
        cond=1
m8     6000.12p       −0.005
       26000.         −0.995
        cond=1
m10    29000.            −1
        cond=1
m11    7000.12p          −1
m12    1000.12p       −0.04196
       6000.12p      −0.625016 8000.12p      −0.333024
m15    6000.12p      −0.000124
       7000.12p      −0.755268 8000.12p      −0.231781 18000.        −0.012827
m16    1000.12p       −0.04196
       6000.12p      −0.625016 8000.12p      −0.333024
m17    1000.12p      −0.077421
       6000.12p      −0.922579
m18    1000.12p      −0.111894
       8000.12p      −0.888106
m19    1000.12p      −0.081192
       6000.12p      −0.583442 7000.12p      −0.017798 8000.12p      −0.186381
       12000.12p     −0.130287 17000.12p      −0.0009
m500   1000.12p       0.0978
       3000.          0.009 6000.12p          0.587 7000.12p         0.0023
       8000.12p        0.28 17000.           0.0175 19000.           0.0064
imp:p  0            1 66r       $ 1, 68
imp:e  0            1 66r       $ 1, 68
sdef X=d1 Y=d2 Z=d3 ERG=d4 TME=5 PAR=P CEL=57
si1 −1.7 1.7
sp1 0 1
si2 −1.7 1.7
sp2 0 1
si3 23.3285 23.3335
sp3 0 1
si4 h 1.00E−03  5.94e−03 1.09e−02 1.58e−02 2.08e−02 2.57e−02 3.06e−02 3.56e−02 4.05e−02 4.55e−02
5.04e−02 5.53e−02 6.03e−02 6.52e−02 7.02e−02 7.51e−02
…
       0.00e+00
c
FC16    Electron (e−) dose;
F16:E    68
SD16     1
FM16     0.1602
FC936    RBE−weighted Electron (e−) dose; DSB induction (aerobic)
F936:E  68
SD936    1
```

```
FM936    0.1602
DE936    1.107E-03 1.225E-03 1.356E-03 1.501E-03 1.661E-03 1.839E-03
         2.035E-03 2.252E-03 2.493E-03 2.759E-03 3.054E-03 3.381E-03
         3.742E-03 4.141E-03 4.584E-03 5.074E-03 5.616E-03 6.216E-03
         6.880E-03 7.615E-03 8.428E-03 9.329E-03 1.033E-02 1.143E-02
         1.265E-02 1.400E-02 1.550E-02 1.715E-02 1.898E-02 2.101E-02
         2.326E-02 2.574E-02 2.849E-02 3.154E-02 3.490E-02 3.863E-02
         4.276E-02 4.733E-02 5.239E-02 5.798E-02 6.418E-02 7.103E-02
         7.862E-02 8.702E-02 9.632E-02 1.066E-01 1.180E-01 1.306E-01
         1.446E-01 1.600E-01
DF936    1.463E+00 1.424E+00 1.387E+00 1.352E+00 1.316E+00 1.284E+00
         1.256E+00 1.228E+00 1.208E+00 1.185E+00 1.160E+00 1.139E+00
         1.125E+00 1.110E+00 1.097E+00 1.082E+00 1.071E+00 1.057E+00
         1.050E+00 1.040E+00 1.036E+00 1.023E+00 1.016E+00 1.011E+00
         1.008E+00 9.987E-01 9.968E-01 9.931E-01 9.883E-01 9.838E-01
         9.811E-01 9.773E-01 9.750E-01 9.743E-01 9.720E-01 9.698E-01
         9.684E-01 9.645E-01 9.668E-01 9.677E-01 9.639E-01 9.616E-01
         9.629E-01 9.616E-01 9.568E-01 9.563E-01 9.583E-01 9.568E-01
         9.581E-01 9.599E-01
nps 1e9
prdmp j 9.99e8
```

APPENDIX D - MCNP-MCDS DSB legend and results

The color tables for Figure 67, Figure 68, Figure 69 are shown in Figure 79, Figure 80, Figure 81.

In specific, each symbol represents a SF curve satisfying the described fitting parameters.

The first value represents the estimated RBE, the second group of values is the set and the setup used for simulations (see legend in Figure 65 Supplement 3), the third is the scanned parameter (e.g. 0.59_551F_0.0 means that the plotted SF curve is representing of an irradiation condition in which an RBE of 0.59 has been obtained with 5 μm for nucleus and cell diameters, 1% of oxygen concentration, pO_2, fixed for the XRT reference source and 100% as starting point for the PF flash test source; then, the scan begun and the PF pO2 has been set to 0.0).

Other parameter's results are shown (Figure 82, Figure 83, Figure 84, Figure 85, Figure 86, Figure 87, Figure 88, Figure 89, Figure 90).

Figure 79. Legend for Figure 67, pO2 parameter. The values fitting both conditions described in Figure 67 caption have been evidenced [Isolan L., et al., 2022].

227

Figure 80. Legend for Figure 68, m0 parameter. The values fitting both conditions described in Figure 68 caption have been evidenced [Isolan L., et al., 2022].

Figure 81. Legend for Figure 69, WEM parameter. The values fitting both conditions described in Figure 69 caption have been evidenced [Isolan L., et al., 2022].
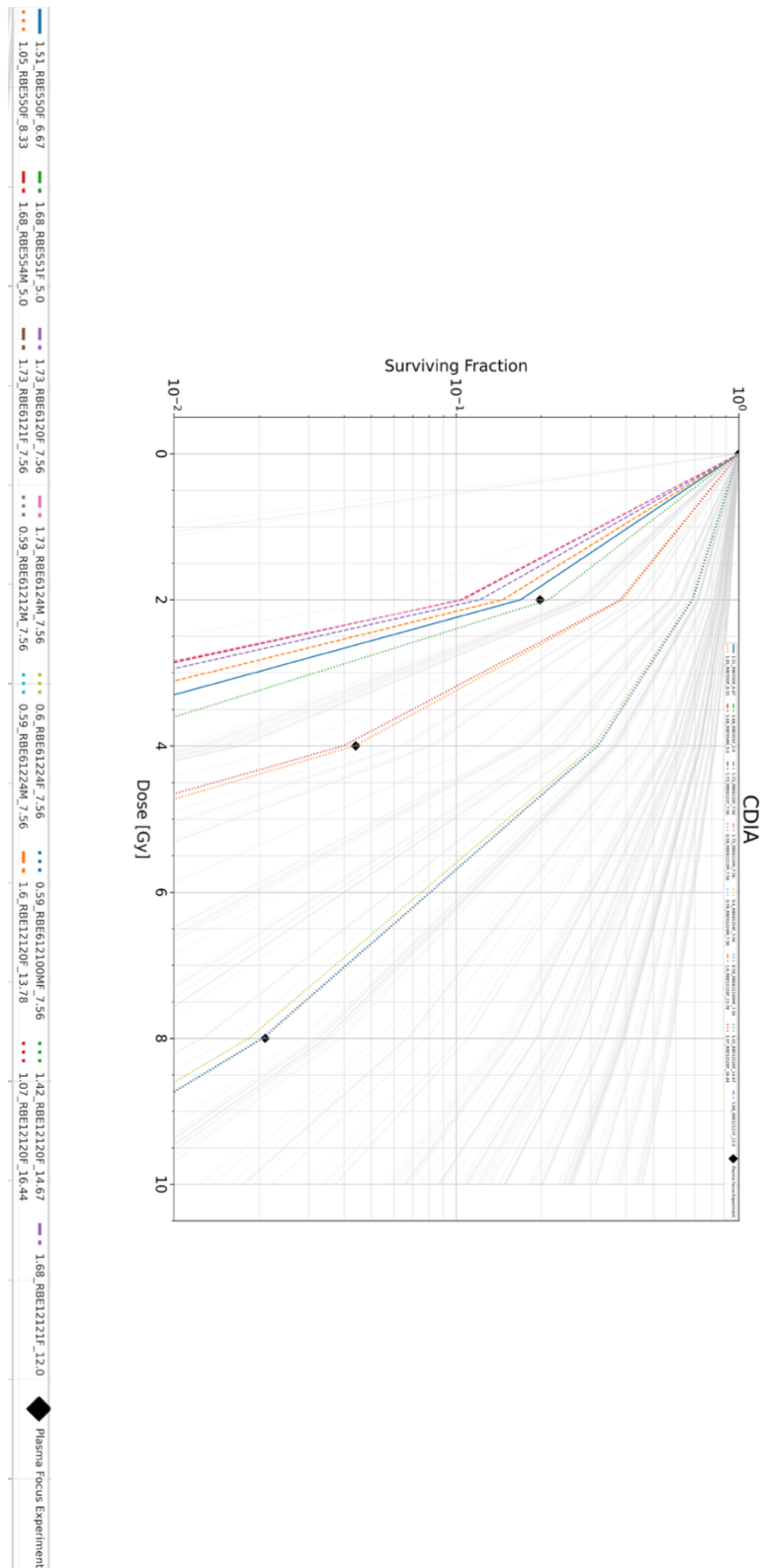
Figure 82. DSB simulation results for the CDIA parameter.
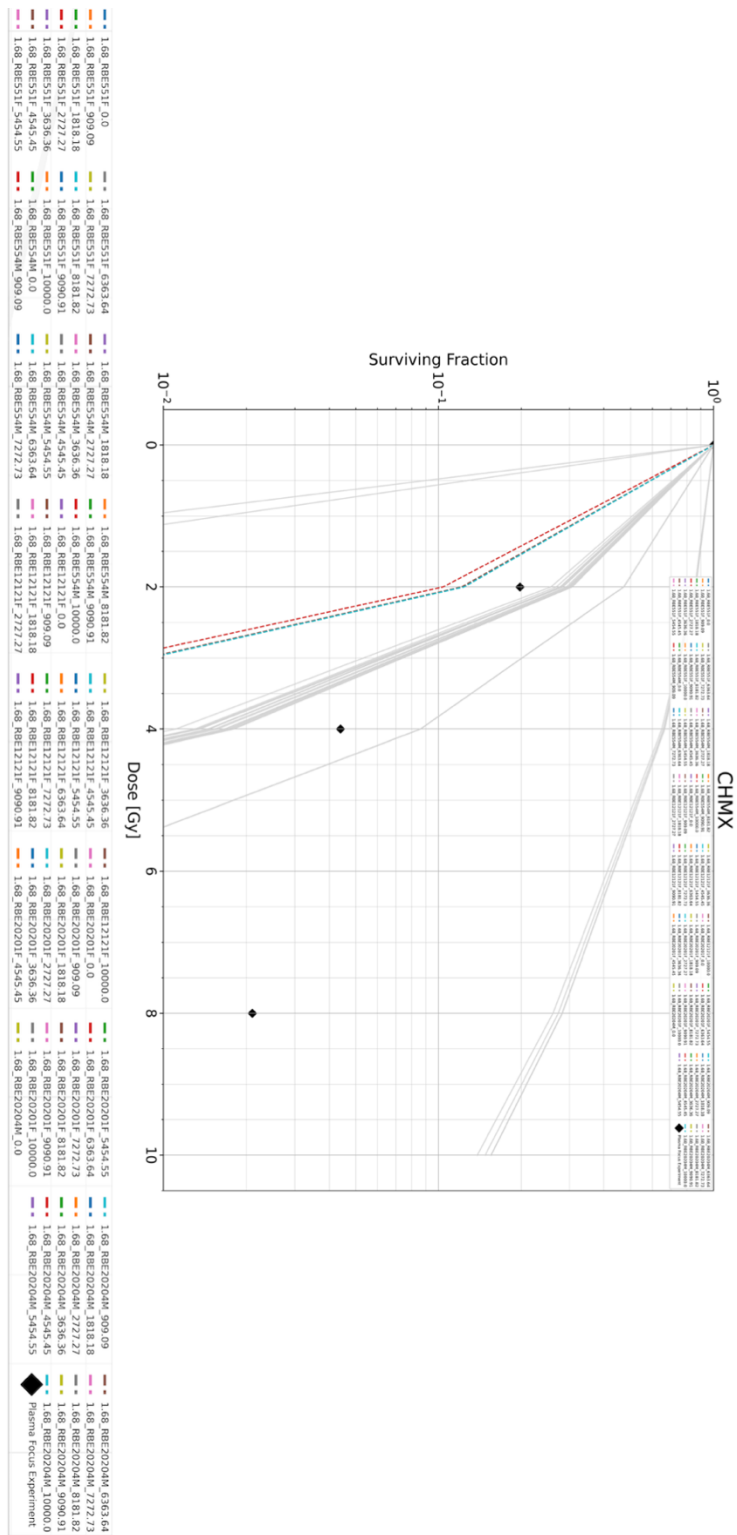
Figure 83. DSB simulation results for the CHMX parameter.
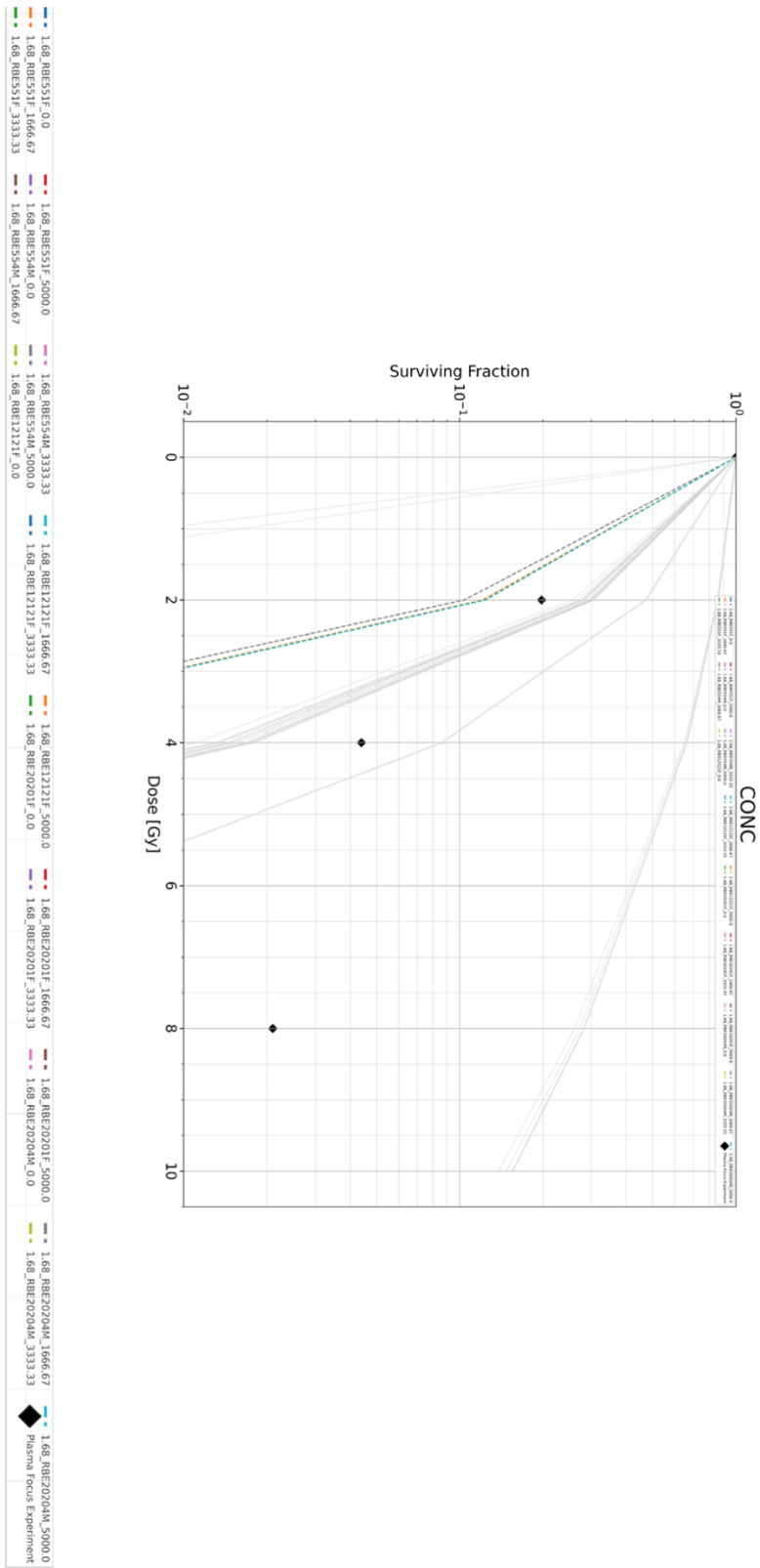
Figure 84. DSB simulation results for the CONC parameter.

Figure 85. DSB simulation results for the fbl parameter.

Figure 86. DSB simulation results for the FNSD parameter.

Figure 87. DSB simulation results for the k parameter.

Figure 88. DSB simulation results for the NDIA parameter.

Figure 89. DSB simulation results for the q parameter.

Figure 90. DSB simulation results for the r parameter.

LIST OF FIGURES

LIST OF TABLES

LIST OF SYMBOLS

Definition	Symbol
Ambient gas density	ρ_0
Angular photon flux	$f(\boldsymbol{r}, \boldsymbol{\omega}, \lambda)$
Bias source distribution	$\hat{q}(\boldsymbol{r}, \boldsymbol{\omega}, E)$
Bremsstrahlung term	$\dfrac{dQ_b}{dt}$
Capacitance	C_0
Capacitor voltage	V_0
Caracteristic axial transit time of the CS	t_a
Cathode radius/anode radius	$c = b/a$
Characteristic axial transit speed	v_a
Characteristic period of the shot measured in µs	T
Characteristic radial transit time	t_r
Characteristic speed of the radial inward shock to reach focus axis [Lee S., 2014]	v_r
Computational time	T
CS position	r_p
Current factor	f_{cr}
Current factor (or current sheet, CS)	f_c
Decond-order dose-dependent component to the probability of cell survival	β
Detector-tally response	R
Dffective nuclear charge	Z_{eff}
Dhock pressure	P
Dhock speed	v_s
Direction of flight	$\boldsymbol{\omega}$
Figure of Merit	FOM
First-order dose-dependent component to the probability of cell survival	α
Forward integro-differential operator	$\hat{L}$
Iinteraction kernel	k
Inductance	L_0
Joule term	$\dfrac{dQ_j}{dt}$
Line loss term	$\dfrac{dQ_l}{dt}$
Mass factor	f_m
Mass number of gas	M
Multiplier factor for pinch current calculation	f
Particle flux	J_b
Particle source distribution	q
Particle weight	$w(\boldsymbol{r}, \boldsymbol{\omega}, E)$
Peak current	I_{peak}
Pease-Braginskii current	I_{p-b}
Permeability	μ
Pinch current	I_{pinch}

Pinch time	t_p
Position	**r**
Position of the axial CS [Lee S., 2014]	z_f
Position of the current sheet	z
Position of the inward moving shock front driven by the piston at position	r_s
Protractor factor	G
Radial phase mass swept-up	f_{mr}
Radius of the pinch	$pinch_{radius}$
Reflected Shock (RS) position [Lee S., 2014]	r_r
Specific heat ratio of the gas	γ
Statistical error	σ
Sum of the power in input for joule effect and the power in output for the bremsstrahlung and the line radiation	Q
Surviving	$S(D)$
Total power gains/loss of the plasma column	$\dfrac{dQ}{dt}$
Wavelengt	λ

LIST OF ACRONYMS

ADVANTG, AutomateD VAriaNce reducTion Generator
CAD, Computer Aided Design
CADIS, Consistent Adjoint Driven Importance Sampling
CS, Current Sheet
CT, Computed Tomography
D, Dose
DE, Dose Energy
DF, Dose Function
DICOM, Digital Imaging and Communications in Medicine
DNA, DeoxyriboNucleic Acide
DR, Dose Rate
DSB, Double Strand Break
FIB, Fast Ion Beam
FOM, Figure of Merit
FPS, Fast Plasma Streams
FW-CADIS, Forward CADIS
IORT, Intra Operative Radiation Therapy
IR, Ionizing Radiation
LDHR, Low Dose Hyper Radiosensitivity
LET, Linear Energy Transfer
LINAC, LINear ACelerator
LQ, Linear Quadratic
MC, Monte Carlo
MCDS, Monte Carlo Damage Simulation software
MCNP, Monte Carlo N-Particle transport
MG, Multi-Groups
MHD, Magneto Hydro Dybamic
MLQ, Modified Linear Quadratic
NTCP, Normal Tissue Complication Probability
OCR, Operator Control Room
OER, Oxygen Enhancement Radio
PF, Plasma Focus
PFMA-3, Plasma Focus Device for Medical Applications #3
PLD, Pulsed Low Dose
PLDR, Pulsed Low Dose Radiotherapy
PMMA, PolyMethylMethAcrylate (Acrylic)
RBE, Radio-Biological Effectiveness
RCZ, Radiation Controlled Zone
RE, Relative Error
ROS, Reactive Oxygen Species
RP, Radiation Protection
RS, Reflected Shock
RT, Radiation Therapy (Radiotherapy)
SF, Surviging Fraction,

SSB, Single Strand Break
TCP, Tumor Control Probability
TLD, Thermo-Luminescent Dosimeter
TS, Transition Switching
UH, Ultra-High
UM, Unstructured Mesh
VRT, Variance Reduction Techniques
WEM, Water Equivalent Distance that Particle Must Travel to the Sourface
WW, Weight Windows
XR, X-Rays
XRT, X-ray Tube